ABSTRACT

NEUTRON TIME-OF-FLIGHT DIFFRACTION
AND
STRUCTURAL ANALYSIS OF GLASSY CARBON

by
David Francis Raymond Mildner

Chairman: John M. Carpenter

A sample of glassy carbon prepared by Hucke from furfuryl alcohol resin, heat treated at 2000°C, has been studied by neutron time-of-flight diffraction techniques. A total diffraction pattern S(Q) has been acquired for wave vector transfers $Q = 4\pi/\lambda \sin \theta/2$ from 0.06Å^{-1} to 25 Å^{-1}. The data have been corrected for multiple scattering by Monte Carlo techniques, by which the data are used to correct themselves. The high value of the maximum wave vector transfer allows a spatial resolution of 0.15 Å in the radial distribution function. This should be sufficient to resolve the first coordination peaks for trigonally bonded atoms (at 1.42 Å) and for tetrahedrally bonded atoms (at 1.54 Å).

There was no evidence of any significant amount of tetrahedrally bonded atoms. On the other hand, there is a correspondence with in-plane correlations of graphite, though there is no definite ordering of the graphitic planes. The widths of the first two diffraction peaks have been interpreted as corresponding to crystallite sizes with values $L_c \sim 31$ Å and $L_a \sim 50$ Å; these have also been confirmed by wide angle X-ray diffraction. The spacing between the planes is 3.46 Å, obtained from the position of the first diffraction peak.

The radial distribution function shows peaks which correspond closely to those of graphitic planes; but to explain the difference in strength between glassy carbon and turbostratic graphite, an amorphous two-dimensional quinoid model (distorted hexogonal layers) has been proposed. A computer model has been built with randomly oriented layers

of 6-fold rings with randomly distributed double bonds. These arrays have been allowed to relax, and an ensemble average has been used to compute the radial distribution function.

The intense small angle scattering from this carbon has been measured, and for $Q < 0.4$ $Å^{-1}$ the data may be approximated by an exponential with a characterisitic void dimension of 13.6 Å. A Guinier plot for lamellar voids suggests a mean thickness of 11.8 Å, and a mean diameter of the order of L_a. It is more likely that the voids are polydisperse and a Debye plot suggests characteristic length of 11.6 Å in the voids, and a length of the order of L_c in the solid. The Porod plot suggests that there are sharp density transitions from the voids to the solid. It would seem therefore as though the disc-shaped voids act as spacers between crystalline cylinders of height L_c and diameter L_a.

Also introduced into this particular carbon during its preparation were large-scale pores with dimensions of the order of 250 Å, as measured by mercury porosimetry. It is assumed that these large scale voids are distributed randomly throughout the substance, with solid regions comprising of crystallites and small scale voids. The scattering appears to be separable into three distinct regions; (1) very low angle diffraction ($Q < 0.025$ $Å^{-1}$) characteristic of large-scale voids; (2) small angle diffraction (0.025 $Å^{-1} < Q < 1.$ $Å^{-1}$) characteristic of small-scale voids; and (3) the extended diffraction ($Q > 1$ $Å^{-1}$) characteristic of interference between neighboring atoms. The transforms of each diffraction region may be correlated with the macroscopic density measurements.

NEUTRON TIME-OF-FLIGHT DIFFRACTION AND STRUCTURAL ANALYSIS OF GLASSY CARBON

by
David Francis Raymond Mildner

A dissertation submitted in partial fulfillment
of the requirements for the degree of
Doctor of Philosophy
(Nuclear Engineering)
in The University of Michigan
1974

Doctoral Committee:

Professor John M. Carpenter, Chairman
Professor Edward E. Hucke
Professor John S. King
Professor George C. Summerfield

ACKNOWLEDGMENTS

This thesis ought to be dedicated to the many friends made, and lost, during the course of a long sojourn in Ann Arbor! The author would like to extend his thanks and appreciation to both the faculty and the now mostly former students of the Nuclear Engineering Department for their friendship and encouragement over the years, and hopes that these associations may continue in the future.

The thesis has been written with financial support from the National Science Foundation. Gratitude is also due to Eugene Leppanen for the illustrations and Debra A. Racine, Kathy J. McKenzie, and Freddie M. Brewster for the typing. All have been helpful to me. I also thank the staff of the Phoenix Library for their liberal borrowing policies. I should add my gratitude to the operators of the Ford Nuclear Reactor, under the supervision of Bob Martin, for providing all the neutrons. I wish I could have made use of a larger percentage of them.

I wish to thank my committee for the help that they have been. A good committee is one that you can have a drink with and this has been a great committee. John King has not only been of scientific assistance but a great provider of financial support for me as a graduate student. Ed Hucke has provided the sample and drawn my attention to the results from various other groups. His understudy, William Leslie, has gone

beyond the call of duty, and provided a most critical review of the thesis. For this, I am most thankful. George Summerfield has helped with many useful discussions, especially during some dark days when he has been a source of encouragement. Jack Carpenter is thanked for his guidance and support of this project, and for the many discussions and work we have done together.

The author appreciates the help given by so many scientists from elsewhere who have sent me preprints and permission to reproduce figures. These include Sabri Ergun for sending reports before publication, Pol Duwez for sending his unpublished data, Cornelius Pings for sending his report before publication, Art Bienenstock for having R. W. Lindberg's thesis sent to me, Adrian Wright for his discussions and permission to reproduce figures from his thesis (British theses are yet to be available on a world-wide basis), Nikki Orlandea for modifying his computer program for dynamical systems and teaching me how to use it, Mike Rowe for sending a copy of his program, and John Copley for both giving me a copy of his Monte Carlo program and explaining how it works, and the many others who have discussed the problems within this thesis, especially those whom I met in Europe, including Jack Powles, John Dore, Alan Leadbetter, Adrian Wright, Slade Cargill, Gerard Janninck, Tito Williams, and George Stirling. Unwittingly they have helped me to get down and actually write the thesis.

Closer to home, I appreciate the pioneering work on the time-of-flight diffractometer done by John Sutton and Jack Carpenter, and the many useful discussions and help with the computer programs from Chuck Pelizzari. Without the unfailing assistance of my colleagues, George Summerfield and Chuck Pelizzari, this thesis would have proved even more difficult to finish; but without the constant supervision of Jack Carpenter it would never have got off the ground. His advice is gratefully acknowledged, and his ability to draw on past experience has helped me to avoid some of the difficulties both in the work, and with the machine, which over years has not been troublefree. I return his major counsel in a more "in" idiom; "spinning rotors will get you through times of no neutrons better than neutrons will get you through times of no machine."

TABLE OF CONTENTS

TABLE OF CONTENTS (Concluded)

LIST OF TABLES

LIST OF FIGURES

LIST OF FIGURES (Continued)

LIST OF FIGURES (Continued)

LIST OF FIGURES (Concluded)

CHAPTER I. THE PROBLEM

1.1 INTRODUCTION

A large number of non-graphitizing carbons have been prepared possessing great strength and hardness and low permeability to gases. It appears that the properties of these carbons may be varied by their method of preparation and starting material, and that judicious combinations of their attributes might solve many technological problems. A study of the structure of these carbons might yield information for the understanding of their characteristics.

Originally they were called glassy, vitreous or glasslike, since they had a shiny surface similar to glass. In addition, like glass it seemed that their structures were amorphous or non-crystalline. Unfortunately there is no satisfactory set of criteria by which the structure of glassy carbons may be characterized uniquely. In fact it might be best to describe these materials as massive disordered carbons to distinguish them from other non-graphitizing carbons such as carbon black; for it was thought originally that these bulk carbons possessed little graphitic structure. However we shall keep the earlier name of glassy carbon.

Although these carbons are fundamentally similar in their properties, it is expected that the diversity in the density, strength, and conductivity are due to different structures produced by the various

methods of preparation. Most of these carbons have been prepared by the controlled thermal degradation of certain cross-linked polymers including phenolic and furfuryl resins. The properties of resulting material have been found to depend on the starting material and the maximum heat treatment temperature. During the preparation, it is probable that a cross-linked structure is formed which is related to the particular polymer precursor. In addition there may be changes in the structure during further treatment at higher temperatures. Fitzer et al., (1969) has listed three processes that might be major contributors to the structure; viz.,

(1) polymerization,
(2) decomposition,
(3) pyrolysis.

In fact it is difficult to characterize the structure of glassy carbons in a unique way as for crystalline substances.

1.2 THE PROPERTIES OF GLASSY CARBON

Glassy carbon was originally developed as a cladding material for fuel elements for high temperature gas-cooled nuclear reactors, for glassy carbon is compatible with alkali metals and is impermeable to gases. Since the atomic motions in glassy carbon are similar to those in graphite (Carpenter, 1973), there is no great difference other than density between glassy carbon and graphite from the point of view of neutron thermalization which is insensitive to the small differences in the total cross section and elastic scattering probabilities. Other applications of glassy carbons are in the fields of electrical engineering, metallurgy, and chemical engineering. These are mainly due to their high stren th and low density, low permeability to all gases, and their inertness to more environments than any other solid.

The properties (and preparation) of various glassy carbons have been reviewed by Yamada (1968). While glassy carbons have been formed with widely varying properties, the general trends are:

(1) Glassy carbon is much stronger and harder than graphite; and it can scratch ordinary glass and cannot be machined easily.

(2) These carbons are generally stable up to at least 3000°C, and at kbar pressures.

(3) The density is in the range of 1 44 - 1 55 $gm\ cm^{-3}$ (although some carbons have densities around 1.3 $gm\ cm^{-3}$, and others as high as 1.9 $gm\ cm^{-3}$). This is about 2/3 of the crystallographic density of graphite.

(4) Glassy carbons possess extremely low permeability to gases which is surprising in view of their low densities. Since the densities in helium and krypton are similar to those measured by mercury porosimetry, the materials must have a high degree of inaccessible porosity.

(5) They have low electrical resistance of the order of 10^{-3}-10^{-2} ohm-cm.

(6) They have excellent corrosion resistance and low oxidation rate and are biologically inert.

(7) They have also a high resistance to attack from many reagents and acids.

A large number of disordered carbons have been prepared artifically and it has been usual to compare their properties with the two naturally occurring allotropes of carbon; viz., diamond and graphite. The density of diamond is 3.52 gm cm^{-3} and density of a single crystal of graphite is 2.26 gm cm^{-3}. However, the density of a polycrystal of the latter is usually about 1.6 gm cm^{-3}, which is close to the density of most glassy carbons. Graphites exhibit varying degrees of anisotropy depending on the method of processing, whereas glassy carbon is believed to be isotropic. Diamond is the hardest naturally occurring substance and comes from the Greek $\alpha\delta\alpha\mu\alpha\varsigma$ meaning 'invincible.' It has a hardness value of 10 on the Moh's scale whereas graphite (which comes from the Greek $\gamma\rho\alpha\phi\epsilon\iota\nu$ meaning 'to write') is soft with a Moh's value of 1. Glassy carbon has a value of 7 on the Moh's hardness scale. Additionally, diamond is a poor conductor, whereas graphite is a good conductor, with similar electrical resistivity to glassy carbon.

1.3 THE STRUCTURE OF CRYSTALLINE CARBONS

The carbon atom has four orbitals in the valence shell; one 2s orbital with a bond strength of unity, and three 2p orbitals with a bond strength of 1.732. Pauling (1960) has shown that if the four bonds of carbon are assumed to be equivalent and directed with equal strength towards the corners of a tetrahedron, then the sp^3 (tetrahedral) bonds have a strength of 2. On the other hand, if we assume that each carbon atom has three strong bonds at 120° to each other in a plane perpendicular to the c-axis, Pauling has shown that the sp^2 (trigonal) bonds have a strength of 1.605. These are the covalent bondings in diamond and graphite, respectively.

Glassy carbon has some properties similar to those of graphite, but tetrahedral bonding is held responsible for high strength and hardness, the low gas permeability and the low graphitization tendency of glassy carbon. Consequently, it is natural to compare the atomic structure of glassy carbon with those of diamond and graphite, since the physical properties are dependent on the nature of the bonding between the atoms of the substance.

The diamond lattice consists of carbon atoms located at the corners of regular tetrahedra and linked together by covalent bonds with an interatomic distance of 1.54 Å (Bragg and Bragg, 1913). A summary of the diamond structure which is cubic is found in Appendix A.1 together with pertinent diffraction data. The high strength and melting point

of diamond is explained by the high coordination number of covalently bonded carbon atoms. This also explains the high density of diamond.

On the other hand, the carbon atom in graphite which is also bonded covalently has only three other adjacent carbon atoms, with an interatomic distance of 1.42 Å (Bernal, 1924). These covalent bonds are stronger, and the atoms form a linked hexagonal planar structure. The hexagonal arrays form parallel sheets which are 3.35 Å apart and are linked by weaker Van der Waals forces. A summary of the 'hexagonal graphite' structure is given in Appendix A.2, together with pertinent diffraction data. Since the forces between the planes are relatively weak, the strength of graphite is less than that of diamond, and graphite tends to shear rather easily along the planes. Graphite is the stable allotrope, and the surfaces of diamond begin to transform into graphite in an inert environment at high temperatures. Industrial carbons are generally imperfect forms of graphite, and the diffraction patterns of these carbons are very diffuse. They are usually described in terms of a disordered (turbostratic) structure of graphite-like hexagonal layers with no orientation between the adjacent layers.

The layers in hexagonal graphite, however, are arranged such that one half of the atoms in a given plane lie above and below the hexagon centers of the planes on either side. This is called the 'ababab' arrangement. Anomalous diffraction lines for graphite (Lipson and Stokes, 1942) suggest that graphite may also be found in another

crystalline form which is similar to hexagonal graphite in dimensions, but with a different arrangement of layers, viz, 'abcabc.' A summary of the 'rhombohedral graphite' structure is given in Appendix A.3, together with pertinent diffraction data. Comparison is also made with the hexagonal unit, and it will be seen that there are some diffraction lines which are common to both, and others which are peculiar to each.

Not only may graphite come in two crystalline forms, but the suggestion has been made that diamond exists in two forms (Ergun and Alexander, 1962) The regular linking of tetrahedra yields hexagonal close packed layers in which layers are spaced alternately by one bond length, and by 1/3 bond length. The simple forms of hexagonal close packed layered structures are the diamond-type lattices and the hexagonal wurzite-type lattices. The layers are formed by the (111) planes in the cubic lattice, and the (00.2) planes in the hexagonal lattice . Adjacent layers separated by a bond-length have atom positions which are identical; and the two structures differ in the arrangement of the adjacent layers which are separated by a 1/3-bond length. The cubic structure has an arrangement A-A-B-B-C-C-A-A, and the hexagonal structure has A-A-B-B-A-A. The analogy may be made to the graphite lattice in the rhombohedral and hexagonal forms.

The argument is made that, since other tehahedral structures such as ZnS exist in both the cubic (sphalerite) and hexagonal (wurzite)

forms, perhaps diamond can exist in the two forms also. A summary of the 'hexagonal diamond' structure is given in Appendix A.4, together with pertinent diffraction data. It will seem that most of the cubic reflections have corresponding reflections in the hexagonal lattice, which, having less symmetry, gives rise to many additional reflections.

1.4 THE STRUCTURE OF GLASSY CARBON

Since the density of glassy carbon is low, any proposed structure which is based upon that of graphite must include a high degree of porosity. These pores must be non-interconnecting since the material is impermeable to gases. The high strength of glassy carbon makes the existence of these voids very interesting. They may strongly influence the local environment of many of the atoms of the material in such a manner as to increase its strength. Hence it would seem reasonable to compare the diffraction pattern of non-crystalline carbons with the crystalline forms.

Crystals are described by lattice structures with various symmetries. Non-crystalline materials lack a high degree of symmetry, and cannot be described by equilibrium atom positions within a unit cell. Instead they are characterized by a 'radial distribution function' which gives a time-averaged characterization of the atomic densities as a function of the distances between the atoms in the substance. In a crystal, such a function would be highly peaked; but in a non-crystalline material these peaks are broadened because of the lack of long range order, and at large distances the effect would be such that the average atomic density would approach a constant value.

To understand the features of the RDF, it is necessary to construct a model of the bonding of the constituent atoms, and to consider the average environment of the individual atoms. Consider that the valence

of a given atom, i, is n_i, and that each valence corresponds to a covalent bond with n_i other atoms. Then the contribution to the area under the first peak in the RDF from this particular atom is proportional to n_i, since it has n_i nearest neighbors. If the total number of atoms in the sample is N, then the contribution to the area under t the first peak is simply the sum of the individula contributions, i.e., $\sum_i^N n_i$. But since the RDF is an average function, the area under the first peak is identically equal to $n_i = N^{-1} \sum_i^N n_i$, the average coordination number for the bonding between neighboring atoms. Similar further extensions may be made for the areas under subsequent peaks in the RDF.

Since the areas are proportional to the average coordination numbers, analysis of the RDF should yield information regarding the bonding between neighboring atoms. Consequently the relative amounts of trigonally and tetrahedrally coordinated carbon atoms may be determined. For diamond, the bonding is sp^3 (tetrahedral), and the coordination number is 4. For graphite, the bonding is sp^2 (trigonal), and the coordination number is 3, while the bonding between planes is weak and attributed to Van der Waals forces. The number and distance of the first four coordination spheres of diamond and graphite are shown in Table I. Models for glassy carbon in which the trigonally and tetrahedrally bonded atoms are found are proposed in section 5.2, and the areas under the first few peaks examined.

TABLE I

2000°C HUCKE SAMPLE

Coordination Sphere	Diamond r(Å)	n	Graphite r(Å)	n
1	1.54	4	1.42	3
2	2.53	12	2.46	6
3	2.96	12	2.83	3
4	3.89	12	3.75	6

A comparison with crystalline forms of carbon was performed originally for the diffraction pattern of fine carbon blacks (Warren and Biscoe, 1941) which have rather broad diffuse peaks. After Fourier inversion, it was found that the distribution of neighboring atoms was exactly the same as in a single layer of graphite. The diffraction lines of general form (00.ℓ) and (hk.0) could be correlated with the diffraction pattern but the general lines (hk.ℓ) were missing. This suggests a random layered structure in which the single graphite layers are stacked parallel and equidistant with each layer having a random orientation relative to the other layers; that is, there is a random rotation of layers about the layer normal. This is called 'turbostratic graphite' and may be considered as a two-dimensional crystal.

The atomic bonding of glassy carbon has also been analyzed by comparison with the types of bonding found for the crystalline forms of carbon. Noda and Inagaki (1964) have acquired the X-ray diffraction pattern of a glassy carbon from Tokai of Japan, obtained from an initial resin of furfuryl alcohol. Diffraction patterns were taken for various carbons after treatment at various temperatures and the peaks tend to

sharpen at higher temperatures. The first peak of the radial distribution function, which is equivalent to the position of the nearest neighbor atoms, has an area corresponding to the a mean coordination number of between 3 and 4. They assume, therefore, that the glassy carbon is composed mainly of two types of carbon bonding in some proportion which varies from sample to sample. One type has tetrahedral (sp^3) coordination between the carbon atoms as in diamond, and the other trigonal (sp^2) bonding like graphite (see Figure 1.1).

They further separate the first observed peak into two components which correspond to the different types of carbon atoms, using the assumption that the curve for each type was Gaussian. The amount of trigonal carbon atoms was increased by raising the heat treatment temperature, and the positions of the observed maxima in the RDF also approached those found for graphite. They assume that the trigonal carbon atoms form a two-dimensional layers, whereas the tetrahedral carbon atoms have no regular arrangement. Their structural model therefore has the tetrahedral carbon domains cross-lining the regions of graphite-like layers in a random fashion. The extend of the domains of these types of bonding cannot be determined by analysis of the radial distribution function which shows detail out to only a few interatomic distances. This structural model is based on that consisting of domains of graphite interspersed by disordered regions, which was first proposed by Franklin (1950) for amorphous carbon films.

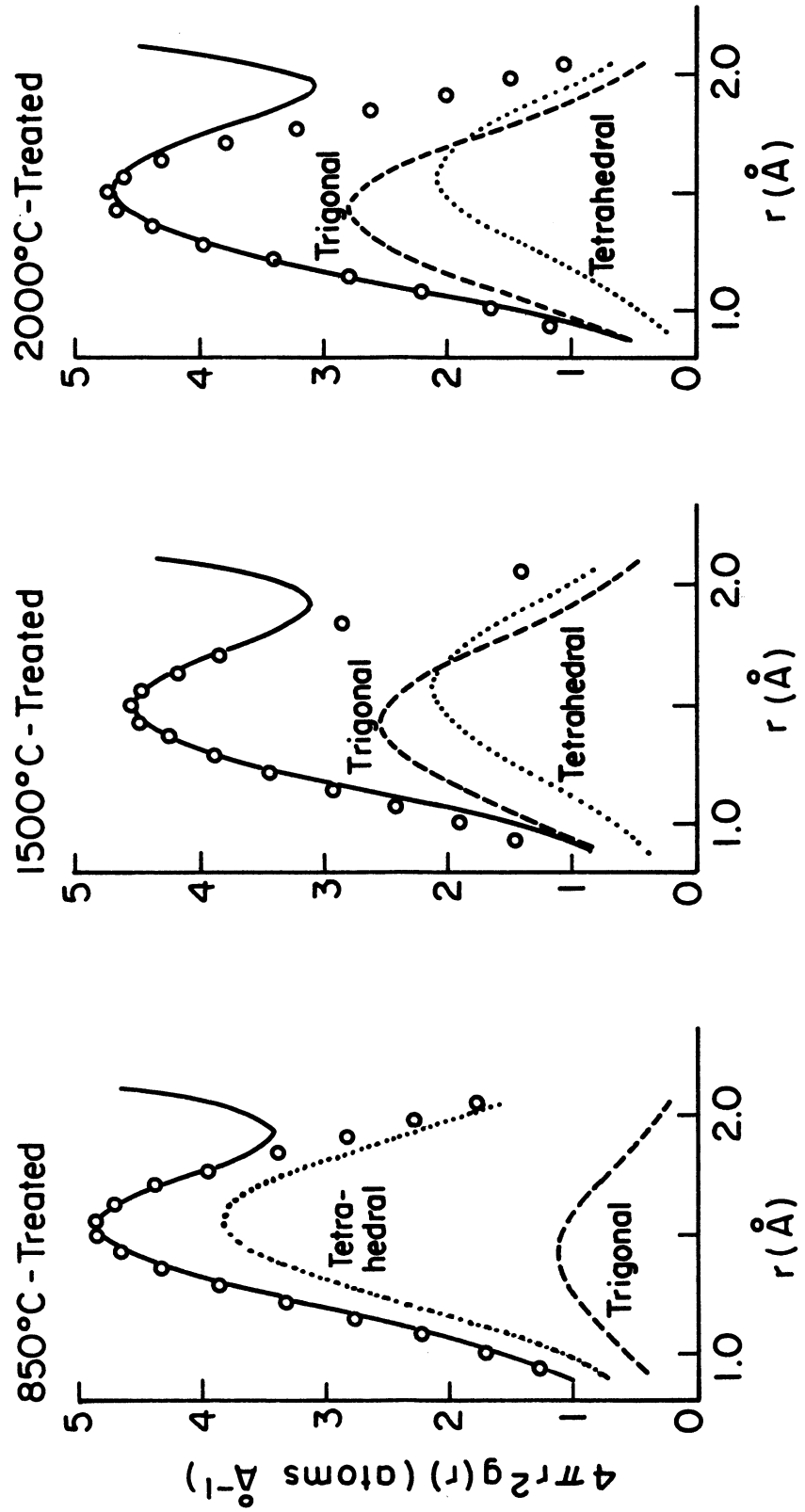

Figure 1.1. The separation of the first peak of the radial distribution function into component curves, Noda and Inagaki (1964).

The radius of the first coordination sphere of amorphous carbon films lies around 1.50 Å between the values of graphite and diamond.

Kakinoki et al. (1960) studied the structure of evaporated carbon films of thickness ~ 100 Å by electron diffraction techniques and obtained a diffraction pattern out to 33 $Å^{-1}$. They found that the radial distribution function's first two peaks both acquired the corresponding distances in diamond and graphite with nearly equal statistical weight. The first peak could be decomposed into these two peaks, whereas the second peak required the third nearest neighbor of graphite and diamond to be taken into account.

The discrepancy between the observed density and that calculated using the Noda-Inagaki model has led Furukawa (1964) to propose a different model. Noda and Inagaki assumed trigonal islands linked together in a random way by tetrahedral bonds. Furukawa proposed a three-dimensional irregular network of carbon atoms involving all kinds of carbon-carbon bonds. This model is disordered with no more than three hexagonal units in a row in any direction; this allows small regions, about 10 Å in size, of planar hexagonally linked carbon atoms.

For low-temperature heat treated samples, these two models are similar, since the Noda-Inagaki model has little trigonal bonding and the Furukawa model consists mainly of tetrahedral and planar double bonds. On the other hand the specific heat of glassy carbon heat treated at 3000°C shows a T^2-dependence (Takahashi and Westrum (1965))

which is characteristic of a two-dimensional layered lattice. More recently (Salinger, 1973) there has been found a linear anomaly in the specific heat at the lowest temperatures around 4°K.

Kakinoki (1965) further proposed a model in which oxygen atoms are added as bridges between the various tetrahedral and trigonal domains. The oxygen bridges are then assigned the responsibility for the low density of glassy carbon. However, it was later found that the oxygen content necessary for this model was greater than that reported originally (Noda et al., 1968).

The structural model of Noda and Inagaki is generally believed to be the best of the three; that is, small domains of graphite-like layers cross-linked randomly by tetrahedral carbon atoms to form a continuous, isotropic, low-density material. They claim further that this model is valid for the different types of glass-like materials. The large number of cross-linking atoms are held responsible for the non-graphitizability of glass-like carbons. These graphite-like layers have a very small size (of the order of 15-100 Å) with an average layer spacing of 3.55 Å (perfect graphite has a spacing of 3.35 Å), the layers being randomly stacked as in turbostratic carbon.

More recently, Kasatochkin et al. (1973) have also proposed a model in which the carbon atomic orbitals may exist in three hybridizations, sp^3, sp^2, and sp. The carbon atoms are bonded such that there are many graphite-like regions linked by atoms of the other types of bonding,

including polyene (- C ≡ C -) and cumulene (= C = C =). Consequently their model includes all possible forms of carbon bonding. This agrees with Whittaker and Wolten (1972) who made electron diffraction measurements on glassy carbon and found small regions in which carbon is bonded in all its crystal forms.

A K-emission band study of glassy carbon by Saxena and Bragg (1973) tends to support the Noda-Inagaki model. They studied not only glassy carbon heat treated at various temperatures, but also diamond and graphite. They concluded that glassy carbon contains both trigonal and tetrahedral bonding, and that the amount of trigonal bonding increases with increasing heat treatment temperature. They do not state the relative amounts, but it seems that they believe that the amounts of tetrahedral bonding is not negligible even at the highest (2700°C) temperature.

In contrast, Kammereck and Nakamizo (1973) performed laser raman studies on graphite and on glassy carbons prepared from polyfurfuryl alcohol, heat treated between 500°C and 2000°C. They conclude from their spectra and there is little tetrahedral bonding even for the lower temperature carbons, and that the raman band attributed to graphitic layers increases in intensity and becomes more narrow with increasing heat treatment temperature.

In summary, therefore, it is fair to say that the structure of glassy carbon is not well known. Yamada (1968) believes that the

different forms of amorphous carbon may have the same short-range structure with differences which depend on the starting material and on the heat treatment temperature. The first and second coordination spheres have coordination numbers which lie between those of graphite (3,6) and those of diamond (4,12). The particular values depnd on the method of preparation, and they affect the physical and chemical properties of the resulting carbon. To account for the low density, there are non-communicating pores, 25-40 Å in diameter which are observable by transmission electron microscopy. The presence of these voids can be detected by small angle X-ray scattering (Bragg and Hammond, 1965; and Perret and Ruland, 1972).

The investigation of the structure of bulk disordered carbons is performed directly by diffraction methods. It will be seen (section 5) that the Fourier inversion of diffraction data gives an RDF with spatial resolution inversely proportional to the maximum value of reciprocal lattice space scanned. If the resolution width is less than the differences in the positions of the peaks for diamond and graphite, then the differences in the coordination numbers should be sufficient to deduce the amounts of the two types of bonds. It is specially true for the area of the first peak which is independent of the type of model proposed for carbon.

The X-ray diffraction pattern of Noda and Inagaki out to $Q = 10.25$ $Å^{-1}$ does not extend to large enough values of wave vector change for a

determination of the type of bonding in glassy carbon. Their data gives a resolution of only about .63 Å in the RDF which is insufficient to resolve the closely spaced peaks (Figure 1.1). It is unrealistic to attempt to separate the first peak into two peaks having a separation of 0.12 Å. Consequently, it is necessary to use diffraction techniques which allow sufficient resolution in the RDF to determine the amounts of trigonal and tetrahedral bonded atoms, in order to test the Noda-Inagaki model.

Since carbon has a low atomic number the scattering power for X-rays is small. Consequently, there is merit to considering neutron diffraction (section 3.6). Additionally if the diffractometer can be designed to collect data at very large wave vector transfers, then the results may have sufficient resolution to determine the form of bonding between atoms.

CHAPTER II. THE THEORY

2.1 INTRODUCTION

In this section the relationship between the atomic structure of an amorphous material and its neutron diffraction pattern is developed. More complete discussions of the basic theory of neutron scattering are given by Lomer and Low (1965) and by Windsor (1973), and its application to amorphous materials by Leadbetter (1973) and by Wright (1974). Here the scattering by a target system of only monoatomic nuclei is considered, although the results may be generalized for a polyatomic system.

Since the wavelength of thermal neutrons and the interatomic distances of materials are comparable (~1Å), the intensity of scattered neutrons as a function of scattering angle, that is the diffraction pattern, will have properties which depend upon the arrangement of the atoms within the scattering system. This is analogous to X-ray diffraction. Additionally the frequency of scattered radiation for thermal neutrons is comparable to the vibrational frequencies of the scattering system, and therefore the vibrational frequency spectrum of the system may be analyzed by thermal neutrons. In fact, this introduces a difficulty with neutron diffraction compared to X-ray diffraction, where the energy changes are small in comparison to the incident X-ray energy. However, while X-rays interact with the atomic electrons which have a spatial extent 1Å, neutrons interact with the nucleus of extent ~10 Å.

Hence the neutron-nuclear interaction is localized, and in addition the scattering amplitude of this interaction varies with the specific nuclear isotope. (In fact, it varies quite randomly unlike X-ray scattering whose amplitudes increase monotonically with the atomic number Z.) Also, the scattering cross section can be divided into coherent and incoherent parts, and it is the coherent total scattering cross section which gives information about the distribution of interatomic distances in the target system.

2.2 THE PHYSICS OF NEUTRON DIFFRACTION

Consider a beam of neutrons of initial wave vector $\underline{k}_o$ which are scattered by a system of nuclei through an angle θ, with a scattered wave vector $\underline{k}$. The interaction between a neutron and a nucleus is governed by the laws of conservation of momentum and energy, so that there is a net transfer of momentum $\hbar\underline{Q}$ and energy $\hbar\omega$ to the system given by

$$\hbar\underline{Q} = \hbar(\underline{k}_o - \underline{k}) \tag{2.1}$$

$$\hbar\omega = \frac{\hbar^2}{2m_n}(k_o^2 - k^2). \tag{2.2}$$

The neutron wave vector $\underline{k}$ is related to its velocity $\underline{v}$ by $\hbar\underline{k} = m_n\underline{v}$, where m_n is the neutron mass, and $\hbar$ is Planck's constant divided by 2π. The scalar momentum transfer is given by

$$Q = |\underline{Q}| = (k_o^2 + k^2 - 2k_o k \cos\theta)^{1/2}. \tag{2.3}$$

Eliminating the final wave vector $\underline{k}$ gives

$$Q^2 = 2k_o^2[1 - (m_n\omega/\hbar k_o^2) - \cos\theta(1 - (2m_n\omega/\hbar k_o^2))^{1/2}]. \tag{2.4}$$

For elastic scattering, there is no energy change; i.e., $\omega = 0$ and $k_o = k$. Then

$$Q = \sqrt{2}k(1 - \cos\theta)^{1/2} = 2k \sin\theta/2 = \frac{4\pi}{\lambda}\sin\theta/2 \tag{2.5}$$

where $\lambda = 2\pi/k$ is the wavelength of a neutron with an associated wave number k. It will be shown that for amorphous materials and for

polycrystalline substances, the diffraction pattern is the intensity of scatter as a function of Q, the scalar wave vector transfer.

The scattering amplitude of a nuclear interaction is denoted by b, the bound-atom scattering length. This is related to the free atom scattering length by $b = a(M + m_n)/M$, where M is the mass of the scattered nucleus. For thermal neutrons, b is independent of momentum transfer $\underline{Q}$, and the differential cross section $d\sigma/d\Omega$ is isotropic for a rigid single nucleus. Hence the total cross section σ_T may be found by integrating over all solid angles; viz., for a single bound nucleus

$$\sigma_T = \int_{4\pi} \frac{d\sigma}{d\Omega} d\Omega = 4\pi b^2. \qquad (2.6)$$

For a system of nuclei, the scattering amplitude is given by $\sum_j b_j \exp(i\underline{Q}.\underline{r}_j)$, where the sum extends over all nuclei with position vector $\underline{r}$. This may cause a transition in the radiation from a initial energy state E_o to a final energy state E, with an energy transfer of $\hbar\omega$. Details of the derivations of the scattering cross section are found elsewhere (Summerfield *et al.*, 1968) but the main result is that the cross section for scattering is proportional to the following;

(1) the product of the matrix elements of the scattered amplitude between the initial i and final f states,

$$\sum_{j,k} < i|b_j e^{-i\underline{Q}.\underline{r}_j}|f >< f|b_k e^{+i\underline{Q}.\underline{r}_k}| \ i >$$

(2) the probability that the initial state is occupied at a temperature T,

$$P_i = \frac{e^{-E_i/k_BT}}{\sum_\ell e^{-E_\ell/k_BT}}$$

where k_B is the Boltzmann constant,

(3) an energy conserving delta function,

$$\delta(E_i + E_o - E_f - E) = \delta(E_f - E_i - \hbar\omega),$$

(4) the ratio of the scattered and incident wave vectors,

$$\frac{k}{k_o}.$$

Then the double differential cross section, which is the probability that neutrons are scattered into a solid angle $d\Omega$ with a neutron energy in the range dE, is

$$\frac{d^2\sigma}{d\Omega dE} = \frac{k}{k_o} \sum_{if} P_i \sum_{jk} < i|b_j e^{-i\underline{Q}\cdot\underline{r}_j}|f > < f|b_k e^{+i\underline{Q}\cdot\underline{r}_k}|i > \delta(E_f - E_i - \hbar\omega) \qquad (2.7)$$

The energy sum may be transformed into a time integral to give

$$\frac{d^2\sigma}{d\Omega dE} = \frac{k}{k_o} \frac{1}{2\pi\hbar} \int_{-\infty}^{\infty} dt e^{-i\omega t} \sum_{j,k} < b_j e^{-i\underline{Q}\cdot\underline{r}_j(0)} b_k e^{+i\underline{Q}\cdot\underline{r}_k(t)} > \qquad (2.8)$$

Where the angular brackets indicate a thermal average over the different

energy states of the system.

The Van Hove space-time correlation function (1954) is introduced as

$$G(\underline{r},t) = \frac{1}{N}\sum_{jk}\int d\underline{Q} e^{-i\underline{Q}\cdot\underline{r}} < e^{-i\underline{Q}\cdot\underline{r}_j(0)} e^{+i\underline{Q}\cdot\underline{r}_k(t)} > \qquad (2.9)$$

where N is the total number of scattering nuclei. For a classical system $G(\underline{r},t)$ may be described as the probability of finding a nucleus at $\underline{r}$ at time t given that a nucleus was at $\underline{r} = 0$ at time $t = 0$.

By separating the sum of equation (2.9) into sums for $j = k$ and $j \neq k$, $G(\underline{r},t)$ may be divided into a self-correlation function $G_s(\underline{r},t)$ describing correlations between positions at different times for the same particle, and a distinct correlation function $G_d(\underline{r},t)$ describing correlations between positions between pairs of different particles. That is

$$G(\underline{r},t) = G_s(\underline{r},t) + G_d(\underline{r},t) \qquad (2.10)$$

where

$$G_s(\underline{r},t) = \frac{1}{N}\sum_{j}\int d\underline{Q} e^{-i\underline{Q}\cdot\underline{r}} < e^{-i\underline{Q}\cdot\underline{r}_j(0)} e^{+i\underline{Q}\cdot\underline{r}_j(t)} > \qquad (2.11)$$

and

$$G_d(\underline{r},t) = \frac{1}{N}\sum_{j\neq k}\int d\underline{Q} e^{-i\underline{Q}\cdot\underline{r}} < e^{-i\underline{Q}\cdot\underline{r}_j(0)} e^{+i\underline{Q}\cdot\underline{r}_k(t)} >. \qquad (2.12)$$

The division of the double sum on j and k in (2.9) into separate

sums for $j = k$ and $j \neq k$ may also be performed for equation (2.8). Since there is no correlation between b_i and b_k, then $< b_i b_k > = < b >^2$, where this average is performed over the nuclear isotopes and spins of the system, and equation (2.8) becomes

$$\frac{d^2\sigma}{d\Omega dE} = \frac{k}{k_o}\frac{1}{2\pi\hbar}\int_{-\infty}^{\infty} dt e^{-i\omega t} \left\{ < b^2 > \sum_j < e^{-i\underline{Q}\cdot\underline{r}_j(0)} e^{+i\underline{Q}\cdot\underline{r}_j(t)} > + < b >^2 \sum_{j\neq k} < e^{-i\underline{Q}\cdot\underline{r}_j(0)} e^{+i\underline{Q}\cdot\underline{r}_k(t)} > \right\} \quad (2.13)$$

or

$$\frac{d^2\sigma}{d\Omega dE} = N\frac{k}{k_o}\frac{1}{2\pi\hbar}\iint d\underline{r}dt\, e^{i(\underline{Q}\cdot\underline{r} - \omega t)} \left\{ < b^2 > G_s(\underline{r},t) + < b >^2 G_d(\underline{r},t) \right\} \quad (2.14)$$

However, it is customary to divide the cross section into two parts: viz., (1) coherent scattering which accounts for correlations in positions of nuclei, and (2) incoherent scattering which accounts for difference in the scattering lengths for either different isotopes or different spin configurations. The differential coherent scattering cross section is $b_{coh}^2 = < b >^2$, the square of the average scattering length of the nucleus; and the differential incoherent scattering cross section is

$$b_{inc}^2 = < (b - < b >)^2 > = < b^2 > - < b >^2 \quad (2.15)$$

the mean square deviation of the average scattering length. If in (2.14) we add and subtract $< b >^2 G_s(\underline{r},t)$, we obtain

$$\frac{d^2\sigma}{d\Omega dE} = N \frac{k}{k_o} \frac{1}{2\pi\hbar} \iint d\underline{r}dt e^{i(\underline{Q}.\underline{r} - \omega t)} \left\{ (< b^2 > - < b >^2) G_s(\underline{r},t) + < b >^2 G(\underline{r},t) \right\} \qquad (2.16)$$

which may be written

$$\frac{d^2\sigma}{d\Omega dE}\text{coh} = \frac{Nb^2_{\text{coh}}}{2\pi\hbar} \frac{k}{k_o} \iint d\underline{r}dt\, e^{i(\underline{Q}.\underline{r} - \omega t)} G(\underline{r},t) \qquad (2.17)$$

and

$$\frac{d^2\sigma}{d\Omega dE}\text{inc} = \frac{Nb^2_{\text{inc}}}{2\pi\hbar} \frac{k}{k_o} \iint d\underline{r}dt\, e^{i(\underline{Q}.\underline{r} - \omega t)} G_s(\underline{r},t) \qquad (2.18)$$

The scattering functions $S(\underline{Q},\omega)$ and $S_s(\underline{Q},\omega)$ are introduced as the Fourier transforms of $G(\underline{r},t)$ and $G_s(\underline{r},t)$. Therefore

$$S(\underline{Q},\omega) = \frac{1}{2\pi} \iint d\underline{r}dt e^{i(\underline{Q}.\underline{r} - \omega t)} G(\underline{r},t) \qquad (2.19)$$

and

$$S_s(\underline{Q},\omega) = \frac{1}{2\pi} \iint d\underline{r}dt e^{i(\underline{Q}.\underline{r} - \omega t)} G_s(\underline{r},t) \qquad (2.20)$$

such that (2.14) may be written as

$$\frac{d^2\sigma}{d\Omega d\omega}\text{coh} = Nb^2_{\text{coh}} \frac{k}{k_o} S(\underline{Q},\omega) \qquad (2.21)$$

$$\frac{d^2\sigma}{d\Omega d\omega}\text{inc} = Nb^2_{\text{inc}} \frac{k}{k_o} S_s(\underline{Q},\omega) \qquad (2.22)$$

By definition, the scattering law $S(\underline{Q},\omega)$ depends only on the properties of the scattering system, and not upon the scattered radiation.

2.3 THE STATIC APPROXIMATION

The structure factor $S(\underline{Q})$ of an atomic system is defined as the integral of the scattering law over all energy transfers

$$S(Q) = \int_{-\infty}^{+\infty} S(\underline{Q},\omega)d\omega \tag{2.23}$$

which after substitution of (2.19) reduces to

$$S(Q) = \int G(\underline{r},0)e^{i\underline{Q}\cdot\underline{r}}d\underline{r} \ . \tag{2.24}$$

Now

$$G(\underline{r},0) = G_s(\underline{r},0) + G_d(\underline{r},0) = \delta(\underline{r}) + g(\underline{r}) \tag{2.25}$$

where $g(\underline{r})$ is the static pair correlation function, or the average atomic density at a distance $\underline{r}$ from an atom located at the origin. Then

$$S(Q) = 1 + \int g(\underline{r})\ e^{i\underline{Q}\cdot\underline{r}}d\underline{r} \ . \tag{2.26}$$

Similar treatment for the incoherent scattering law shows that

$$S_s(Q) = \int_{-\infty}^{\infty} S_s(Q,\omega)d\omega = \int G_s(\underline{r},0)e^{i\underline{Q}\cdot\underline{r}}d\underline{r} = 1 \ . \tag{2.27}$$

The coherent angular differential cross section is given by

$$\frac{d\sigma_{coh}}{d\Omega} = Nb^2_{coh} \int_{-\infty}^{\infty} \frac{k}{k_o} S(\underline{Q},\omega)d\omega \ . \tag{2.28}$$

If the assumption is made that $k_o \simeq k$, then

$$\frac{d\sigma_{coh}}{d\Omega} = Nb_{coh}^2 S(Q). \qquad (2.29)$$

This is true for X-ray scattering in which the integration over energy transfers is performed at constant Q, since the energy transfers are small compared with the incident energy. In the ideal scattering experiment to measure the structure factor S(Q), the scattered intensity I(Q), which is proportional to the differential cross section $d\sigma/d\Omega$, is measured as a function of momentum transfer Q (usually with a constant k_o and therefore as a function of scattering angle θ), regardless of any energy transfers involved. This is called the static approximation and is valid for conventional X-ray diffraction.

For neutrons, on the other hand, the static approximation does not hold, since the neutron energy is comparable with energy transitions of the scattering system. Hence in a diffraction experiment in which the integrated intensity I of scattered neutrons measured at a given scattering angle θ, the integration over energy transfers is performed, but not at constant Q. The integration path in Q-ω space is along a path of constant scattering angle θ, which deviates from a constant Q path, especially at high energy transfers $\hbar\omega$. Additionally there is a minimum ω integration limit defined when the energy loss $\hbar\omega$ is equal to the incident neutron energy E_o. Hence the measured differential cross section $(d\sigma/d\Omega)_m$ is now given by

$$I \propto \left(\frac{d\sigma}{d\Omega}\right)_m = \left| Nb_{coh}^2 \int_{-E_o/\hbar}^{\infty} \frac{k}{k_o} S(\underline{Q},\omega) d\omega \right|_{\text{const } \theta} \qquad (2.30)$$

where we have neglected an additional weighting factor with energy dependence accounting for the incoherent scattering and the detector efficiency.

Now the structure factor S(Q) is less easy to obtain. If, however, a constant - Q neutron scattering experiment could be performed, with the static approximation able to be invoked by adequate corrections, then the total scattered intensity I(Q) is proportional to S(Q), and is given by

$$I(Q) \propto \left(\frac{d\sigma_{coh}}{d\Omega}\right)_{total} = Nb_{coh}^2 \int G(\underline{r},0) e^{i\underline{Q}\cdot\underline{r}} d\underline{r}$$

$$= Nb_{coh}^2 (1 + \int g(\underline{r}) e^{i\underline{Q}\cdot\underline{r}}) . \qquad (2.31)$$

Another technique is to perform an elastic neutron scattering experiment, with a double energy analysis, so that the <u>elastic</u> coherent scattering differential cross section is measured and given by

$$\left(\frac{d\sigma_{coh}}{d\Omega}\right)_{elastic} = Nb_{coh}^2 \int G(\underline{r},\infty) e^{i\underline{Q}\cdot\underline{r}} d\underline{r} . \qquad (2.32)$$

The correlation function $G(\underline{r},\infty)$ is the time averaged value of $G(\underline{r},t)$, and may be described in terms of static equilibrium positions $G_e(\underline{r})$ and thermal displacements about the equilibrium positions. For harmonically bound atoms, this gives a Debye-Waller factor of the form $\exp(-2W)$, where

$$W = 1/6 < u^2 > Q^2 \qquad (2.33)$$

for isotropic mean square displacements $< u^2 >$. Then

$$G(\underline{r},\infty) = G_e(\underline{r}) \exp(-2W), \tag{2.34}$$

and the elastic scattering cross section (2.32) becomes

$$\left(\frac{d\sigma_{coh}}{d\Omega}\right)_{elastic} = Nb_{coh}^2 \int G_e(\underline{r})\, e^{-2W} e^{i\underline{Q}\cdot\underline{r}} d\underline{r} . \tag{2.35}$$

If the equilibrium correlation function $G^e(\underline{r})$ may be expressed by

$$G_e(\underline{r}) = \delta(\underline{r}) + g_e(\underline{r}), \tag{2.36}$$

where $g_e(\underline{r})$ is the pair distribution function for equilibrium atomic positions, then

$$\left(\frac{d\sigma_{coh}}{d\Omega}\right)_{elastic} = Nb_{coh}^2 (1 + \int g_e(\underline{r}) e^{i\underline{Q}\cdot\underline{r}} d\underline{r}) e^{-2W} . \tag{2.37}$$

Hence elastic scattering experiments may give information about the thermal displacements which are averaged out in the total scattering measurements.

If the same separation is also made for the static pair correlation function, giving

$$g(\underline{r}) = g_e(\underline{r})\, e^{-2W} , \tag{2.38}$$

then the total scattering cross section equation (2.37) becomes

$$\left(\frac{d\sigma_{coh}}{d\Omega}\right)_{total} = Nb_{coh}^2 (1 + \int g_e(\underline{r}) e^{-2W} e^{i\underline{Q}\cdot\underline{r}} d\underline{r}) . \tag{2.39}$$

Hence the relationship between the total and elastic scattering cross sections is simply

$$\left(\frac{d\sigma_{coh}}{d\Omega}\right)_{total} = \left(\frac{d\sigma_{coh}}{d\Omega}\right)_{elastic} + Nb^2_{coh}(1 - e^{-2W}) . \qquad (2.40)$$

2.4 THE RADIAL DISTRIBUTION FUNCTION

Equation (2.31) expresses the relationship between the diffraction pattern (or the intensity I(Q) of scatter as a function of scalar momentum transfer) and the static pair correlation function $g(\underline{r})$ (or the number of atoms in a volume element $d\underline{r}$ at a distance $\underline{r}$ from an atom located at the origin).

$$I(Q) = Nb_{coh}^2 \left(1 + \int g(\underline{r})\, e^{i\underline{Q}\cdot\underline{r}}\, d\underline{r}\right). \qquad (2.31)'$$

For large distances, $g(\underline{r})$ approaches a constant value g_o which is the average atom density in the sample. We add and subtract g_o from $g(\underline{r})$ to give

$$I(Q) = Nb_{coh}^2 \left(1 + \int_V (g(\underline{r}) - g_o)\, e^{-i\underline{Q}\cdot\underline{r}}\, d\underline{r} + g_o \int_V e^{-i\underline{Q}\cdot\underline{r}}\, d\underline{r}\right) \qquad (2.41)$$

where V is the sample volume.

For isotropic systems the vector $\underline{r}$ may take on all orientations in space with equal probability to give the density fluctuation $(g(\underline{r}) - g_o)$ spherical symmetry. For distances greater than a few atomic distances, $(g(r) - g_o)$ approaches zero, except near the sample surface; and for distances less than the closest interatomic distance, $g(r) = 0$. Hence the orientation average for the second term may be performed, and is $\int 4\pi r^2 (g(r) - g_o) \sin Qr/Qr\, dr$. This second term basically involves only interactions between atoms which are closely separated. The third term involves interactions between distant points within the sample, and

gives rise to forward angle scattering (see section 2.5). Provided that the sample size is great enough, this term may be ignored, and the coherent scattered intensity I(Q) is given, neglecting absorption and multiple scattering as well as incoherent and inelastic scattering, by

$$I(Q) = Nb_{coh}^2 \left(1 + 4\pi \int_o^\infty (g(r) - g_o) \frac{\sin Qr}{Qr} r^2 dr\right). \qquad (2.42)$$

We define the radial density function (RDF) as

$$D(r) = 4\pi(g(r) - g_o) \qquad (2.43)$$

that is, the fluctuation in the atomic density about its mean value as a function of r. This may be obtained by Fourier inversion of equation (2.42). Note that at large Q, I(Q) approaches $Nb_{coh}^2 = I(\infty)$, the "structure independent" coherent scattering intensity at large momentum transfers. Then define i(Q) as the "normalized intensity" obtained from the experimental diffraction pattern I(Q) by

$$i(Q) = (I(Q) - I(\infty))/I(\infty). \qquad (2.44)$$

By substitution in equation (2.42), this becomes

$$Qi(Q) = 4\pi \int_o^\infty r(g(r) - g_o) \sin Qr \, dr. \qquad (2.45)$$

The Fourier transform then gives

$$r(g(r) - g_o) = \frac{1}{2\pi^2} \int_o^\infty Qi(Q) \sin Qr \, dQ \qquad (2.46)$$

or

$$r^2D(r) = 4\pi r^2(g(r) - g_o) = \frac{2r}{\pi}\int_o^\infty Qi(Q)\sin Qr\, dQ \qquad (2.47)$$

which is one form of the formula of Zernicke and Prins (1927).

The function Qi(Q) may be obtained from neutron scattering data, and the evaluation of the integral in equation (2.47) yields the RDF, D(r), which gives the structure of liquids and non-crystalline materials. This formula is also valid for polyatomic substances, except that the densities g(r) and g_o are averages weighted by the coherent scattering lengths of the various isotopes according to the composition of the system.

In an amorphous materials, the function g(r) has peaks which become less distinct and more broad with increasing r, until g(r) approaches a constant value equal to g_o. The distances between the peaks and the origin correspond to the distances between the atoms. Additionally, the area A_m under the m^{th} peak in the function $r^2D(r)$ gives a measure of the number n_m of atoms at a distance r_m from a typical origin atom. That is

$$A_m = \int_{m^{th}\ peak} 4\pi r^2(g(r) - g_o)dr = n_m . \qquad (2.48)$$

The RDF is therefore analogous to the Patterson function for solids and crystals, which is a correlation function giving the position of every atom relative to every other atom. It is directly proportional to the square of the atomic structure factor, as is the RDF via the Zernicke-Prins formula (2.47) and the Van Hove space-time correlation function (2.9).

2.5 FORWARD ANGLE SCATTERING

For small crystallites the intensity of scattered radiation in a region around each reflection point in the reciprocal lattice may be described as a function whose form depends upon the external crystal and not upon its internal structure. These diffraction regions extend in reciprocal space out to distances Q from the reflection center of the order of $2\pi/d$ where d is the linear dimension of the crystallite (Guinier (1963)). Hence the Scherrer formula $\Delta Q \simeq 2\pi/L$ relates the width ΔQ (after subtraction of resolution) in reciprocal space of a particular reflection to the apparent size L of the crystallite in a direction perpendicular to the plane spacing corresponding to that reflection or node. Reflections of the indices (000) at the center of the reciprocal lattice are also describable by the same function, and hence small crystallites give rise to small angle scattering around the incident beam. For a homogeneous substance, the diffraction pattern may contain some reflections for which an interpretation may be found by analogy to the crystalline form. However, around $Q = 0$, there certainly exists a node center with the same characteristics as the crystallite of the same external form.

In the derivation of the intensity of scattered radiation for amorphous substances (section 2.4), we ignored the third term in equation (2.41), viz.,

$$I(Q) = Nb_{coh}^2 g_o \int_V e^{-i\underline{Q}\cdot\underline{r}} \, d\underline{r} \qquad (2.49)$$

which involves interactions between distant points within the sample and gives rise to forward angle scattering. For large distances r, the static pair correlation function $g(\underline{r})$ approaches a constant g_o, the average atomic density within the sample. Hence by equation (2.25)

$$g_o = \underset{\text{large } \underline{r}}{\text{Limit}} \; G(\underline{r},0) . \tag{2.50}$$

Also in the limit of large r, there are no correlations between distant atoms, so that the space time correlation function (equation (2.9)) becomes

$$\underset{\text{large } \underline{r}}{\text{Limit}} \; G(\underline{r},0) = N \int_V d\underline{Q} \; e^{-i\underline{Q}\cdot\underline{r}} . \tag{2.51}$$

Hence by the substitution of

$$N = g_o \int_V e^{+i\underline{Q}\cdot\underline{r}} \, d\underline{r} \tag{2.52}$$

into equation (2.49) gives

$$I(Q) = b_{coh}^2 g_o^2 \left| \int_V e^{-i\underline{Q}\cdot\underline{r}} \, d\underline{r} \right|^2 . \tag{2.53}$$

The integral is taken over the entire volume of the sample which has been considered to be homogeneous.

Moreover, if the sample consists of N_D homogeneous domains, then under the assertion that individual contributions to the small angle scattering are independent, they may be summed together so that equation (2.53) becomes

$$I(Q) = N_D \, b_{coh}^2 \, g_o^2 \left| \int_D e^{-i\underline{Q}\cdot\underline{r}} \, d\underline{r} \right|^2 \qquad (2.54)$$

where the integral extends over a typical domain. Hence the small angle scattering will be characteristic of the domain sizes within the sample, and independent of the atomic structure of the individual domains.

On the other hand, let us consider a homogeneous sample with independent but similar voids. This assumes that the voids are oriented randomly within a material of constant density g_o, with sufficient dilution that their separation is large compared with the interatomic spacing, since large r limits were taken for the orientation averaging of the second term in equation (2.41). We make no assumption about the relative number and size of the voids and the material, other than that the void volume is much smaller than the sample volume. It is then possible to analyze the small angle scattering data, not in terms of domains of material, but in terms of voids within the material.

Hence the voids are treated as scattering domains with a negative atomic density $-g_o$ within a material of uniform zero density, with negligible interference between the waves scattered by the individual voids. The observed intensity is the sum of the diffracted intensities produced by the individual voids, which for N_v identical voids, each of volume V_v, distributed at random with a material of constant density g_o is given by

$$I(Q) = N_v \, b_{coh}^2 \, g_o^2 \left| \int_{V_v} e^{-i\underline{Q}\cdot\underline{r}} \, d\underline{r} \right|^2 . \qquad (2.55)$$

2.6 INHOMOGENEOUS POROUS MEDIUM

In the previous section, it is assumed that the voids in the material are not only independent but also similar. However Debye and Bueche (1949) have demonstrated that the small Q diffraction from an inhomogeneous porous material may be characterized more generally by the fluctuations in the scattering property of the medium. The Debye theory may be applied to the case of neutron scattering.

Define a correlation function $\gamma(r)$ by the equation

$$\gamma(\underline{r}) = \frac{\int_V \xi(\underline{r}-\underline{r}')\xi(\underline{r}')d\underline{r}'}{\int_V \xi^2(\underline{r})d\underline{r}}, \qquad (2.56)$$

where $\xi(\underline{r})$ is the local fluctuation at the point $\underline{r}$ in the atomic density from the average value g_o in the bulk material. Let the true local atomic density of the solid regions of the material be g_3; (the reason for this subscript will become apparent in Chapter 6). Then the local fluctuations of the density in the solid regions and in the voids from the average density are given by $(g_3 - g_o)$ and $-g_o$, respectively. Let the void fraction by volume of the substance be ϕ; then the denominator in equation (2.56) is given by

$$\int_V \xi^2(\underline{r})d\underline{r} = \langle\xi^2\rangle = (g_3 - g_o)^2(1-\phi) + (-g_o^2)\phi. \qquad (2.57)$$

The void fraction is defined by

$$\phi = 1 - \frac{g_o}{g_3}, \qquad (2.58)$$

so that equation (2.57) becomes

$$\langle \xi^2 \rangle = g_o(g_3 - g_o) \ . \tag{2.59}$$

The small Q scattering term in equation (2.41) has the implicit assumption that the material is homogeneous, and we rewrite equation (2.49) as

$$I(Q) = b^2 V \int_V g_o^2 \, e^{-i\underline{Q} \cdot \underline{r}} \, d\underline{r} \ , \tag{2.60}$$

where the number of scattering atoms may be defined by

$$N = g_o V. \tag{2.61}$$

However to treat an inhomogeneous medium with sharp boundaries between regions of material and void, we must consider local fluctuations in the atomic density. Hence we replace g_o^2 in equation (2.60) by $\gamma(\underline{r})\langle \xi^2 \rangle$. The intensity of scatter for small Q from an inhomogeneous medium is therefore given by

$$I(Q) = b_{coh}^2 \, V \int_V \langle \xi^2 \rangle \, \gamma(\underline{r}) \, e^{-i\underline{Q} \cdot \underline{r}} \, d\underline{r}. \tag{2.62}$$

For an isotropic medium, $\gamma(\underline{r})$ has spherical symmetry, so that equation (2.62) becomes

$$I(Q) = 4\pi b_{coh}^2 \, V \, g_o(g_3 - g_o) \int_o^\infty r^2 \, \gamma(r) \frac{\sin Qr}{Qr} \, dr. \tag{2.63}$$

Debye further showed that the functional form of $\gamma(r)$ for a random scatterer may be given by

$$\gamma(r) = \exp(-r/a) \tag{2.64}$$

where a is a correlation length. The substitution of equation (2.64) allows the integral in equation (2.63) to be performed, to give

$$I(Q) = \frac{8\pi b_{coh}^2 V g_o (g_3 - g_o) a^3}{(1 + a^2 Q^2)^2} \tag{2.65}$$

as the intensity of scattering at small Q for an inhomogeneous porous medium.

CHAPTER III. THE EXPERIMENT

3.1 TIME-OF-FLIGHT DIFFRACTOMETRY

In diffractometry the intensity of scattered radiation is measured as a function of wave vector transfer Q; and it is useful to extend the measurements to as high a value, Q_{max}, as possible in order to increase the spatial resolution $\Delta r = 2\pi/Q_{max}$. It is seen from equation (2.5) that Q depends on two factors, the wave length λ of the radiation and the scattering angle θ. In conventional diffractometry a monochromatic incident beam of neutrons or X-rays is used, and the intensity of scattered radiation is measured as a function of scattering angle. This method therefore has a maximum Q-range determined by the wavelength used. Presently a practical limit is $Q_{max} \sim 23$ Å^{-1} for X-rays, and ~15 Å^{-1} for neutrons. An alternative method is to keep the scattering angle fixed, and Q is varied by using a white beam of radiation, that is, a wide range of wavelengths. For neutrons this may be accomplished by time-of-flight diffractometry which has been reviewed by Turberfield (1970).

A pulsed neutron beam containing a broad distribution of neutron energies, with a flux per unit wave number at time t_o given by $\phi(k_o,t_o)$, is emitted by the source. Neutrons are scattered with a probability given by equation (2.29); viz., $Nb^2S(Q)$ in the static approximation. A detector which subtends a solid angle $\Delta\Omega_D$ at the target counts scattered

neutrons with an efficiency $\eta(k)$. The observed count rate $C(\theta,t)$ at the detector at a scattering angle θ and at a time t is determined by neutrons with a velocity v which were emitted by the source at a time $t' = t - (L_o + L)/v$, where L_o and L are the distances traversed by the neutrons between the source and the target, and between the target and the detector, respectively. Then, neglecting finite target effects, and in the static approximation,

$$C(\theta,t) = \int \phi(k,t_o) Nb^2 S(Q)\ \Delta\Omega_D \eta(k)\ \delta(t - t_o - (L_o + L)/v) dt_o dk \qquad (3.1)$$

where the delta function ensures an integration of neutrons arriving at the detector at the same time t, that is, recorded in the same time channel.

Since a pulsed source is used, $\phi(k,t_o)$ may be represented as $\phi(k)\ \delta(t_o)$, so that the time integral may be performed, and the observed count rate $C(\theta,t)$ is given by

$$C(\theta,t) = \int \phi(k)\ Nb^2 S(Q)\ \Delta\Omega_D \eta(k)\ \delta(t - (L_o + L)/v) dk\ . \qquad (3.2)$$

Since $\hbar k = m_n v$, and the momentum transfer Q is a function of k and θ by equation (2.5), then the integral may be performed in principle, and the observed count rate $C(\theta,t)$ is proportional to the observed intensity as a function of Q. However this includes two unknown functions, the transmitted neutron flux $\phi(k_o)$ and the detector efficiency $\eta(k)$. These may be eliminated by performing an identical experiment on a material with a known cross section.

If we now consider the possibility of inelastic scattering, then the count rate C(t') includes all combinations of initial and final velocities, v_o and v, for which $(L_o/v_o + L/v)$ is a constant; that is, those velocities which have the same time of arrival at the detector. Each combination of v_o and v (or wave numbers k_o and k) has a corresponding energy change $\hbar\omega$ and wave vector transfer $\hbar\underline{Q}$ for a given scattering angle θ given by equations (2.1) and (2.2). Hence the diffractometer integrates all scattering events along a path in Q-ω space corresponding to each time of arrival. The path intersects the $\omega = 0$ axis at a momentum transfer which corresponds to elastic scattering.

The ideal integration path in (Q-ω) space is the constant - Q path so that the structure factor S(Q) may be obtained directly via equation (2.31). However time-of-flight diffractometry will always have inelastic contributions to the scattered intensity and Carpenter and Sutton (1972) have considered the integration paths in Q-ω space as a function of the ratio of the flight paths, L/L_o. They show that with equal flight paths, $L = L_o$, the integration path crosses $\omega = 0$ tangent to the line of constant Q. Hence in equal flight path time-of-flight diffractometry, the constant Q integration requirement is better approximated than in the case with a choice of unequal paths, and also for conventional crystal diffractometry. However this arrangement of equal flight paths causes a minimum in the counting rates.

3.2 UNIVERSITY OF MICHIGAN TIME-OF-FLIGHT NEUTRON DIFFRACTOMETER

The extended neutron diffraction pattern of the glassy carbon was obtained on the University of Michigan Time-of-Flight Neutron Diffractometer which is located at beam port J of the two megawatt Ford Nuclear Reactor. A schematic drawing is shown in Figure 3.1. The original machine was described by Sutton (1971); but many modifications have been made since that time, and the present diffractometer with nearly equal flight paths has been described by Carpenter et al. (1974).

The beam port looks radially at the heavy water tank adjacent to the reactor core, which enhances the leakage flux from the core. The neutron beam is defined by a plug composed of graphite, lead and concrete, before it passes through two rotors. The first is a fiber-glass-resin rotating collimator with a wide divergent slit designed to transmit a relatively broad pulse of both thermal and fast neutrons. The second is a curved-slit chopping rotor of Nimonic - 90 alloy, with a thin coating of gadolinium along the surfaces of the slits such that only slow neutrons are transmitted. The neutron beam is further collimated between the chopper and the target by an aperture of dimensions 1 in. (vertical) x 3/8 in. (horizontal). Together with the chopper, this aperture defines the beam size at the target position to be 1-1/2 in. x 1/2 in.

The rotor transmission characteristics, which define the distribution of neutron energies transmitted by the machine, are a

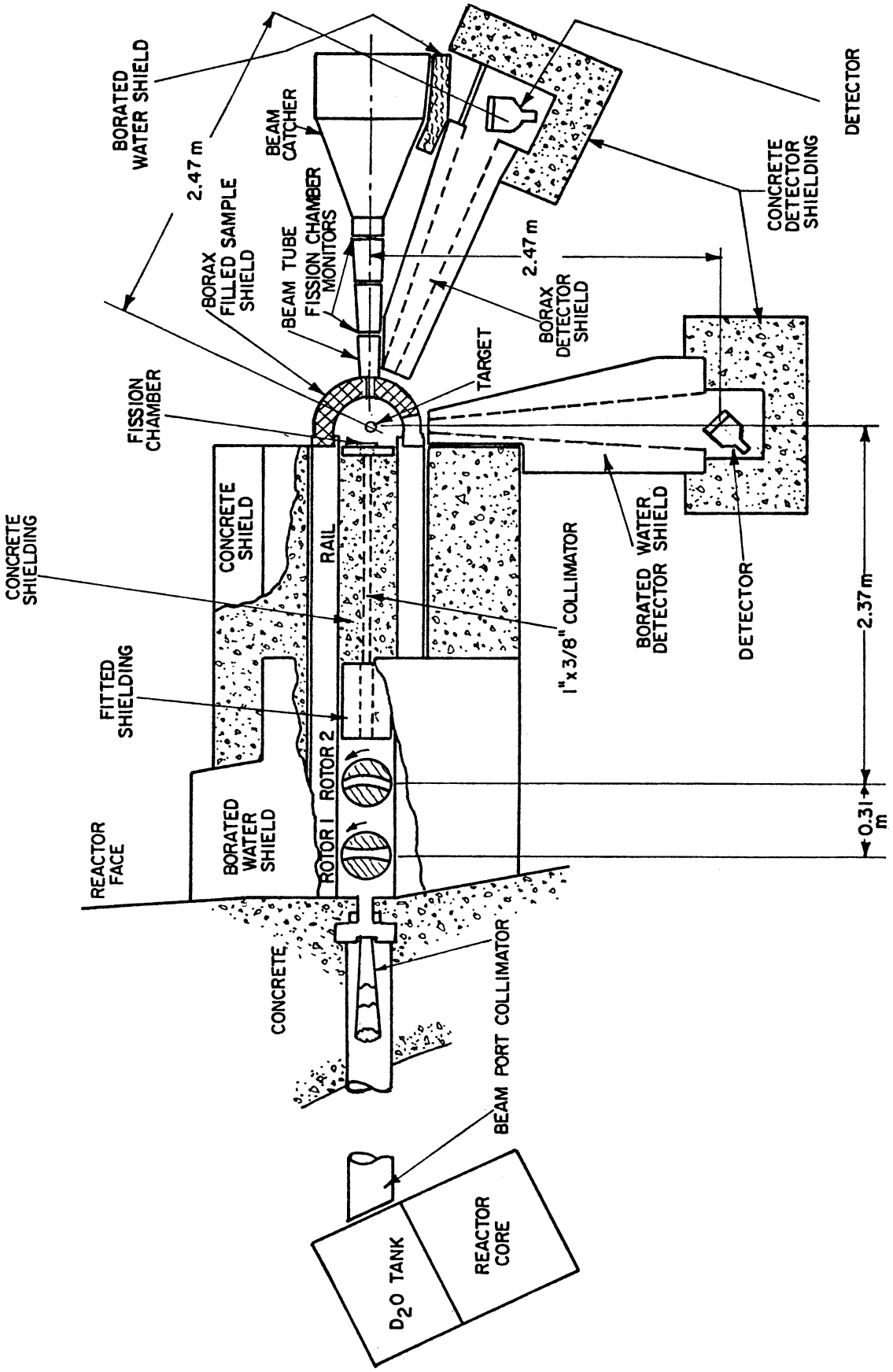

Figure 3.1. A schematic drawing of the University of Michigan Time-of-Flight Neutron Diffractometer.

function of the speed of rotation of the rotor and the curvature of its slit; while the resolution is a function of the slit width also. The 10-in. diameter Nimonic rotor has three 1/4-in. slits with a 40-in. radius of curvature. This gives a value of the ratio of the optimum transmitted neutron speed (NS) to the rotor tip speed (TS) of 16; that is $NS/TS = v_o/R\omega = 16$, where v_o is the optimum neutron velocity for a rotor of radius R rotating at an angular frequency ω. For the rotor frequencies used in the experiment 140 Hz, 240 Hz and 480 Hz, the optimum neutron energies are 17 meV, 49 meV and 197 meV, and the optimum neutron time-of-flights are 559 μs/m, 326 μs/m and 163 μs/m, respectively.

The rotor's performance does not appreciably diminish even at 1 ev, and using equation (2.5) a neutron energy of 0.934 ev gives a wave vector transfer of 30 $Å^{-1}$ for 90° scattering. The fall-off of the reactor neutron spectrum at high energies, however, is the practical limitation to the range of Q scanned by the machine. For this study the highest wave vector transfer for which reasonable data are obtained is about 25 $Å^{-1}$ at a rotor frequency of 480 Hz and scattering angle of 90°; and the lowest, 0.9 $Å^{-1}$ at a rotor frequency of 140 Hz and scattering angle of 20°.

The rotors are each driven by a Harwell type (Pickles and Hazlewood, 1961) three phase hysteresis synchronous drive motor (Figure 3.2). The amplifiers are driven at any of 13 frequencies between 140 and 480 Hz

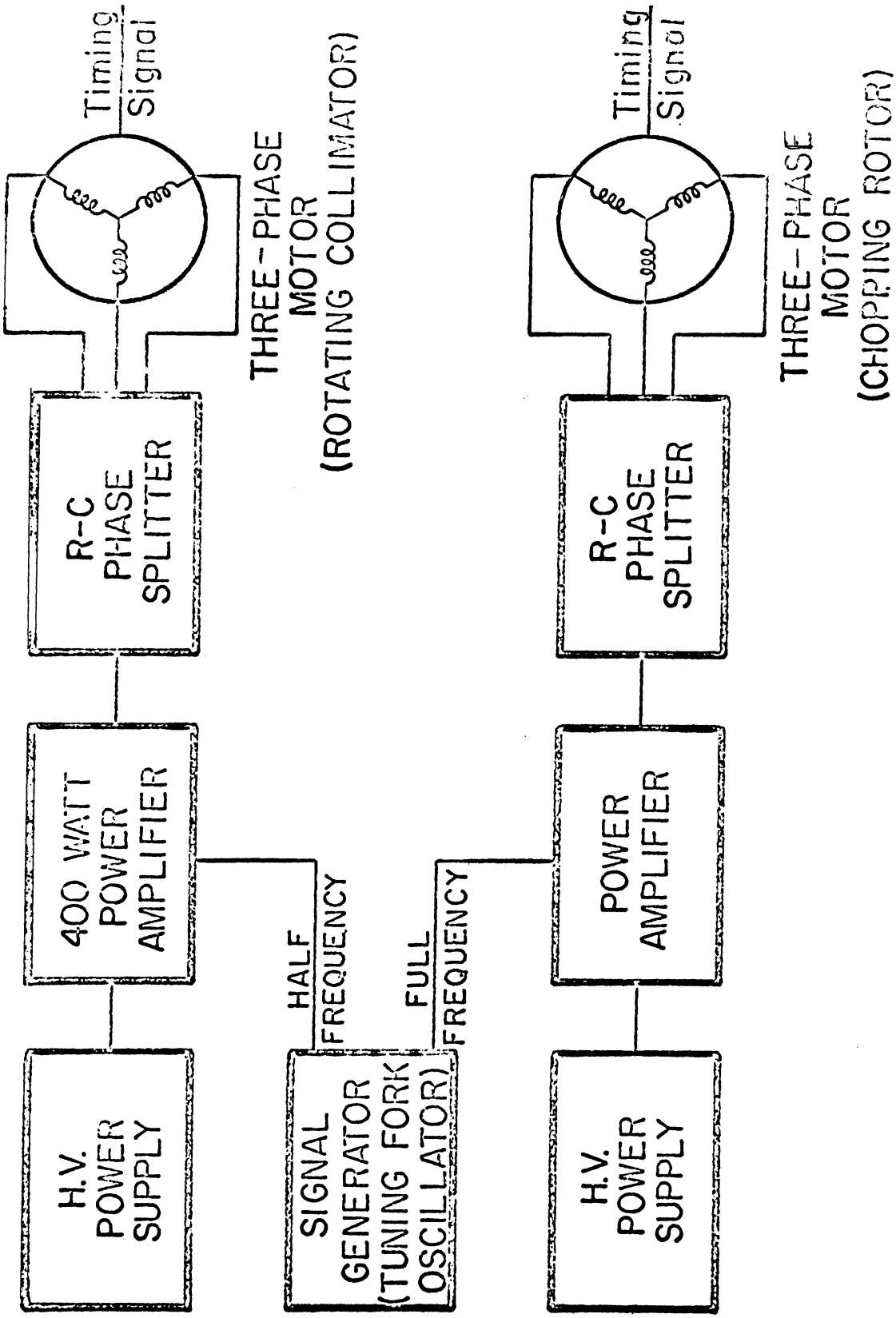

Figure 3.2. The rotor driving power system block diagram.

by a signal generator controlled by a precision tuning-fork oscillator. Timing signals emantate through a magnetic pick-up for each rotor system. The second rotor triggers the starting of a time-of-flight multichannel analyzer after a pre-set delay. Together with a suitable channel width, this allows the scattered thermal neutron spectrum to be analyzed efficiently. By selecting a suitable phase difference between the two rotors, the fast neutron background may be eliminated in the time-of-flight region of the scattered thermal neutrons. Four scattered intensity distributions are analyzed in 256 channel memory segments; those from the sample and the reference at two different scattering angles.

Neutron detectors are mounted in banks at scattering angles of 20° and 90°. The 20° bank of four detectors subtends an azimuthal angle of 14.7° and solid angle of 3×10^{-3} steradian; and the 90° bank of seven detectors subtends an azimuthal angle of 27.8° and solid angle of 1.5×10^{-2} steradian. Each detector has a 5 in. x 5 in. Stedman type (1961) thin Li^6F - ZnS(Ag) scintillator bonded to a boron glass plate. Neutrons cause the reaction $Li^6(n,\alpha)H^3$, and consequent excitation of ZnS produces photons which are collected by a photomultiplier tube via a polymethyl methacrylate (PMMA) light guide. The pulses are transmitted by an emitter follower output circuit, and are passed through a pulse shape discriminator for the elimination of gamma pulses and background noise, before finally arriving at the analyzer. The high

voltage characteristics of the detectors are matched to produce a maximum signal to background ratio for detected neutrons.

The momentum resolution ΔQ of the machine is determined by various parameters which include:

(1) the beam angular divergence,

$$\left(\frac{\Delta Q}{Q}\right)_{\Delta\theta} = \cot\left(\frac{\theta}{2}\right) \Delta\left(\frac{\theta}{2}\right), \tag{3.3}$$

(2) the time width of the neutron burst,

$$\left(\frac{\Delta Q}{Q}\right)_{\Delta t} = \frac{\Delta t}{t} , \tag{3.4}$$

and

(3) the flight path uncertainties,

$$\left(\frac{\Delta Q}{Q}\right)_{\Delta L} = \frac{\Delta L}{L} . \tag{3.5}$$

However Carpenter (1967) has shown that, for a point source and point scatter, and for detectors of finite extent, that $(\Delta Q/Q)_{\Delta L}$ (and hence $\Delta Q/Q$) is minimized if the scintillator surfaces are located on a constant time-of-arrival surface. The effect of time focussing on the resolution of aluminum and graphite polycrystals diffraction lines has been measured. The slab target was placed at an angle of 45° to the incident beam, and the angle between the scattered beam direction and the normal to the detector face was vained. A schematic drawing is shown in Figure 3.3, with the results of the resolution (measured as a

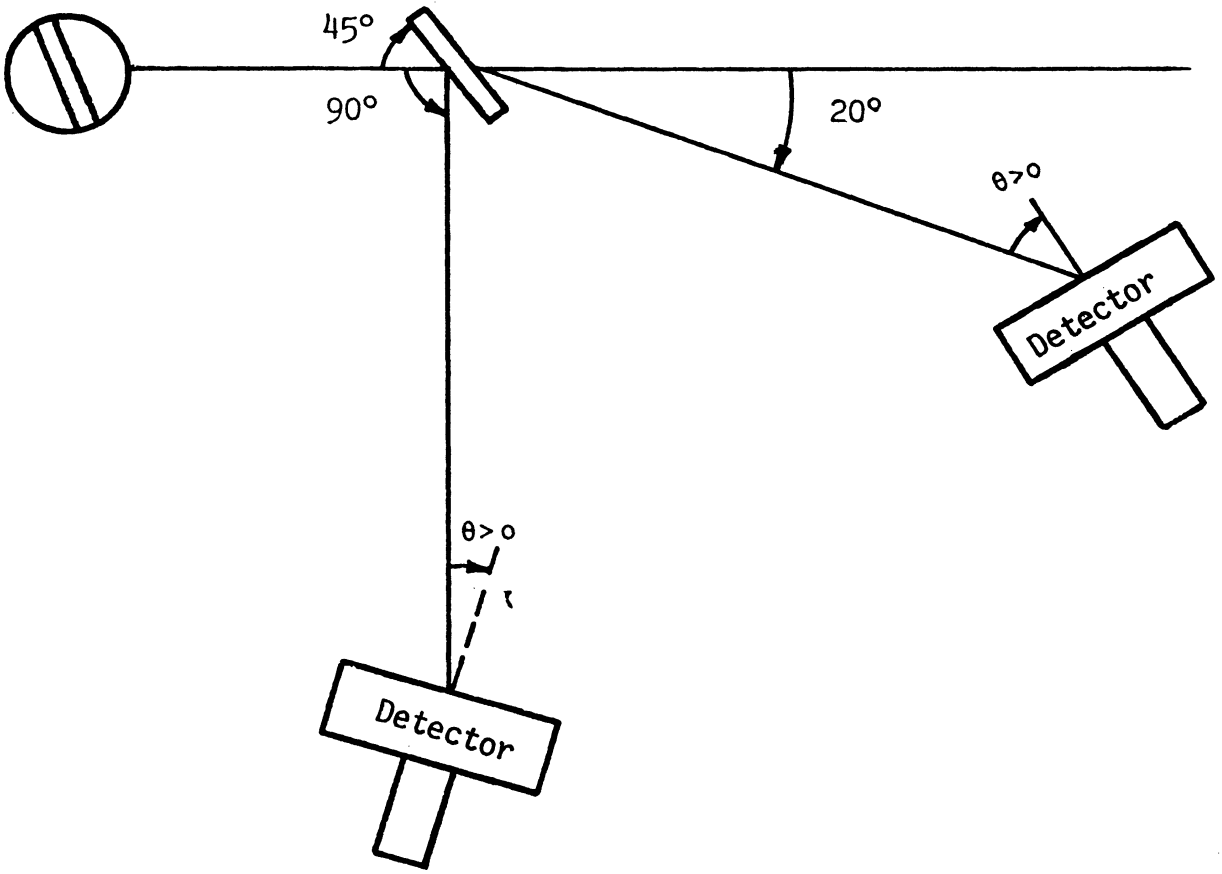

Figure 3.3. A schematic drawing for time focussing of detectors.

function of the detector angle for the two scattering banks in Figures 3.4 and 3.5 On the basis of these measurements, the detector angles for the time-focussed diffractometer were chosen as 80° for the 20° scattering angle bank, and as 45° for the 90° scattering angle bank. These angles are the same as those predicted by the time-focussed geometry, that is, the focus for optimum resolution.

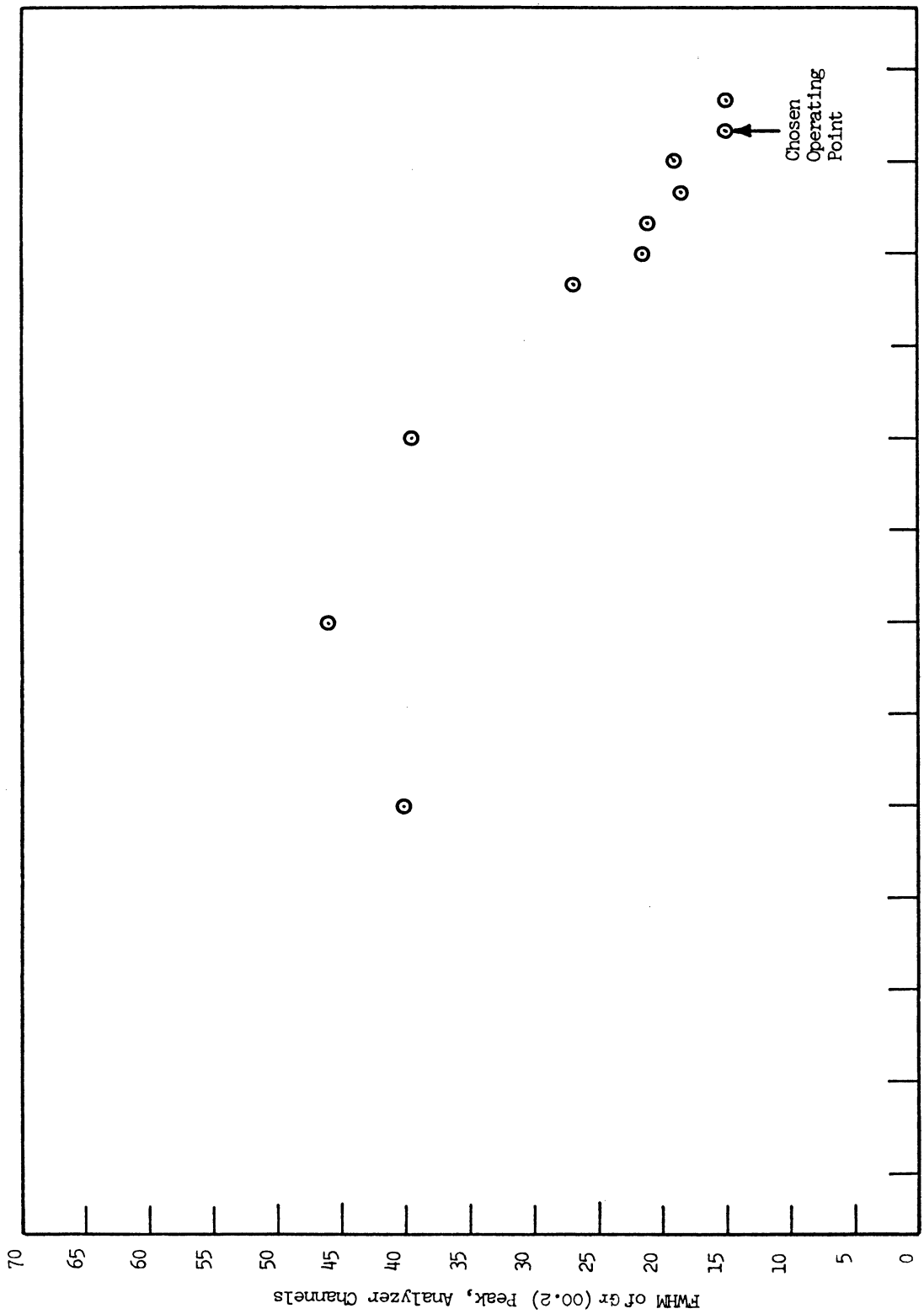

Figure 3.4. The diffraction line resolution as a function of detector angle for the 20° scattering bank, obtained from the graphite (00.2) peak, using a rotor speed of 400 Hz.

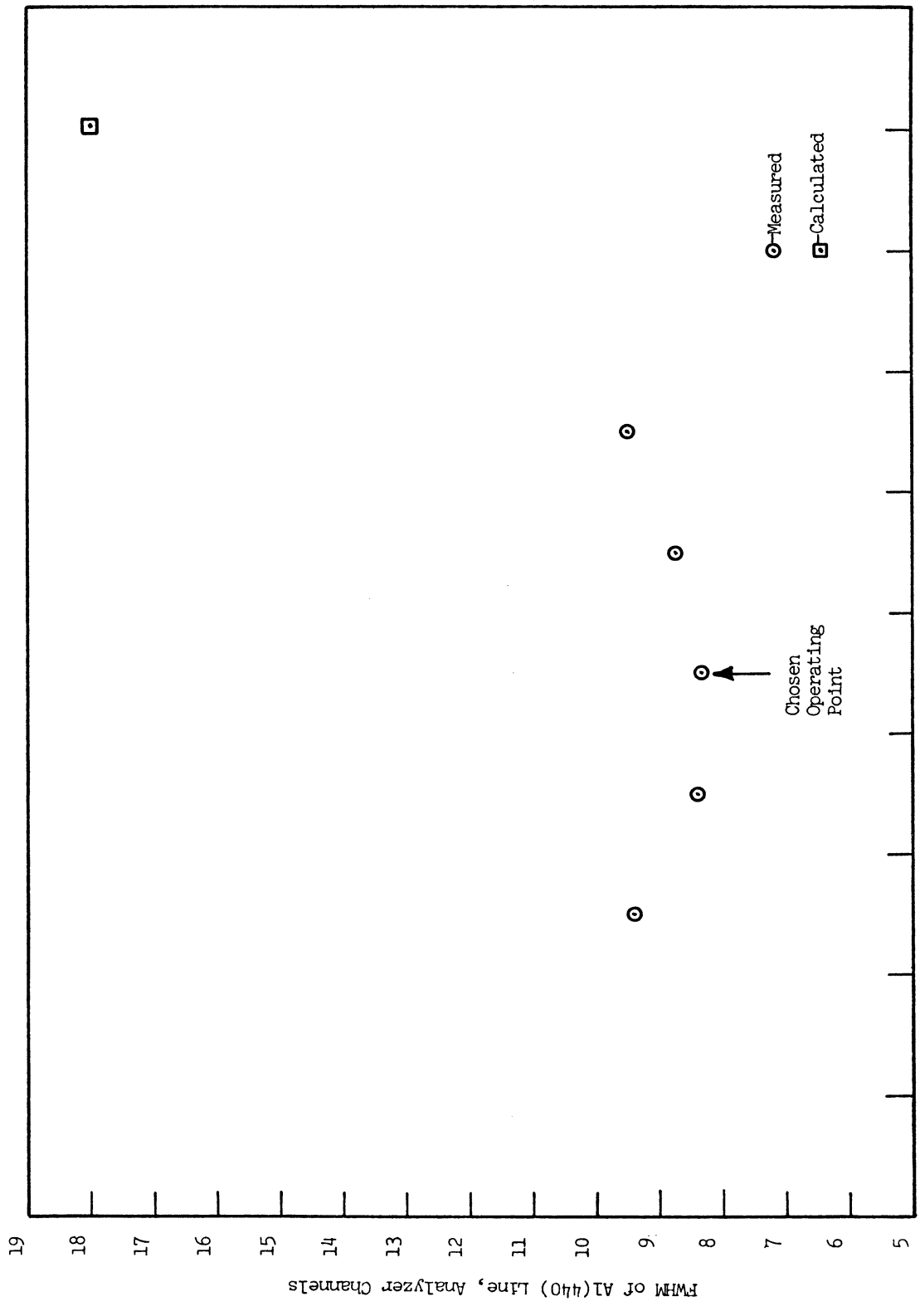

Figure 3.5. The diffraction line resolution as a function of detector angle for the 90° scattering bank, obtained from the aluminum (440) peak, using a rotor speed of 400 Hz.

3.3 THE CALIBRATION PROCEDURE

The count rate at a given time after the triggering of the analyzing system determines the observed intensity at a particular wave vector transfer Q, and is given by equation (3.2). A useful calibration requires an accurate determination of the flight-path lengths, L_o and L, and the scattering angle θ, so that the time-of-flight analyzer channel number n may be expressed as a function of Q, or in fact its inverse. A more accurate method is to use a polycrystalline target whose plane spacings $d_{hk\ell}$ are known, and to perform a calibration run for each detector bank. Aluminum is a useful calibration target, and its structure and diffraction parameters are given in Appendix B.1.

For a given scattering angle θ, and plane spacing $d_{hk\ell}$, neutrons are diffracted if they have a wavelength λ given by the Bragg equation

$$\lambda = 2d_{hk\ell} \sin(\theta/2) = \frac{2\pi}{k} = \frac{2\pi\hbar}{m_n v} \qquad (3.6)$$

where v is the neutron velocity corresponding to a wavelength λ. If t_{err} is the timing error of the magnetic pick-up of rotor (positive if the pick-up pulse is later than the time of the opening of the rotor), t_{del} is the pre-set delay before the analyzer actuates, and $\Delta\tau$ is the time width of each channel of the analyzer, then the channel number n corresponds to a time t after the trigger from rotor 2 given by

$$t = t_{err} + t_{del} + (n - 1.5)\Delta\tau \qquad (3.7)$$

The factor 1.5 expresses a delay time in the time-of-flight analyzer, measured to the midpoint of the analyzer channel. Since the neutron velocity is simply given by the distance travelled divided by the time taken, then the calibration equation is given by

$$2d_{hk\ell} \sin(\theta/2) = \frac{2\pi\hbar}{m_n(L_o+L)} (t_{err} + t_{del} + (n - 1.5)\Delta t) \quad (3.8)$$

Hence the channel number n is a linear function of the plane spacings $d_{hk\ell}$, or the inverse of the reciprocal lattice vectors $|\underline{q}_{hk\ell}| = 2\pi/d_{hk\ell}$.

A typical calibration run for aluminum is given in Figure 3.6, in which many peaks are shown as a function of channel number. The problem is then reduced to determining which peaks correspond to which plane spacings. A plot of $d_{hk\ell}$ versus n (Figure 3.7) will give a straight line only if the correct peaks and spacings are matched. The slope of such a plot will yield a value of $(L_o + L) \sin \theta/2$, while the intercept will also give a value of $(t_{err} + t_{del})$. This is sufficient information needed to calibrate a specific run; that is to determine the momentum transfer Q as a function of channel number n, since from equations (2.5) and (3.6)

$$Q = 4\pi/\lambda \sin \theta/2 = 2\pi/d_{hk\ell}(n) \quad (3.9)$$

It turns out that the greatest spacing for aluminum corresponds to $Q = 2.678\ \text{Å}^{-1}$ which is fine for the 90° detector bank. However, for the 20° bank, it is necessary to find a polycrystalline target with a larger

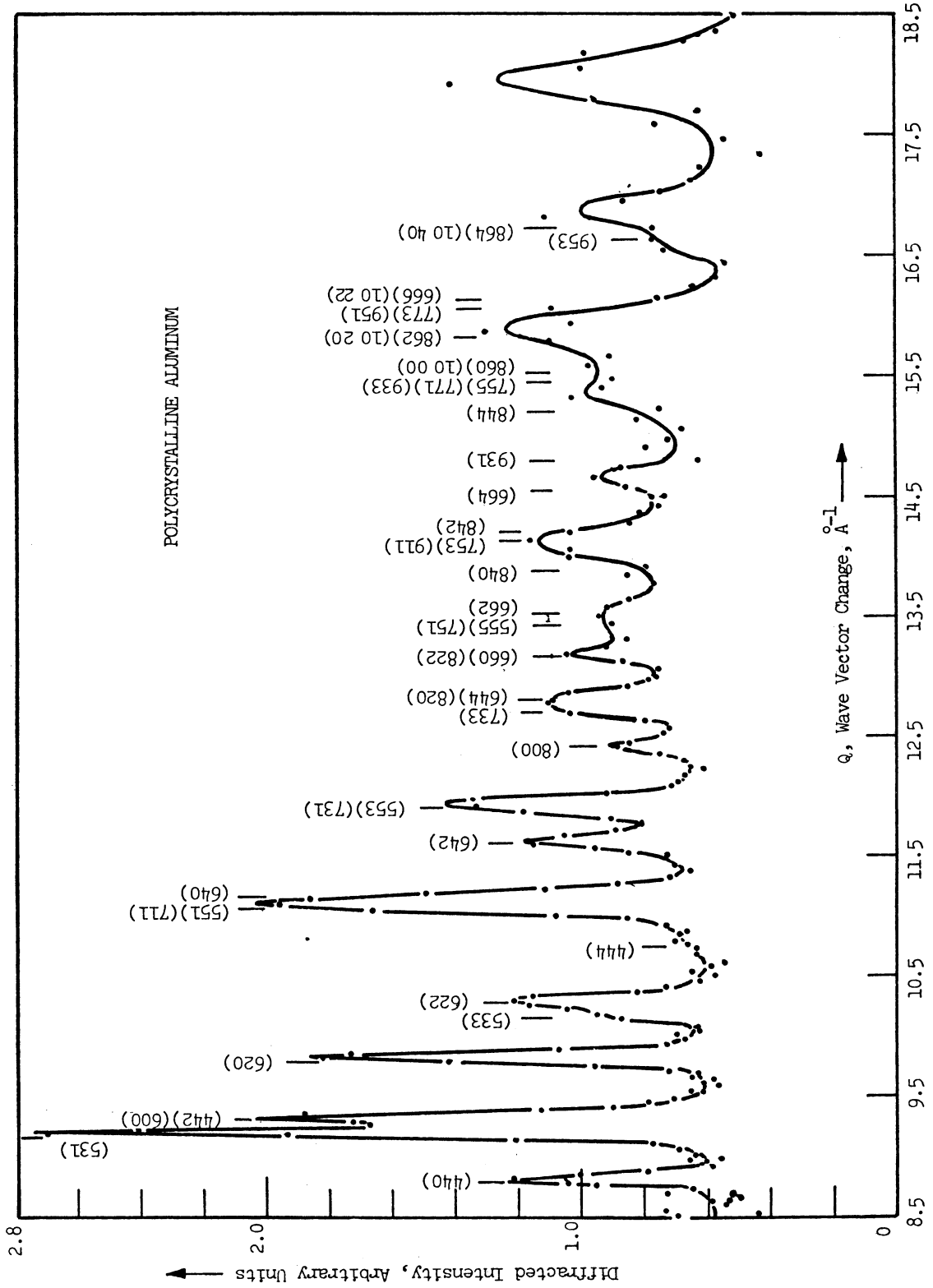

Figure 3.6. A neutron diffraction pattern for polycrystalline aluminum taken with the 90° scattering bank.

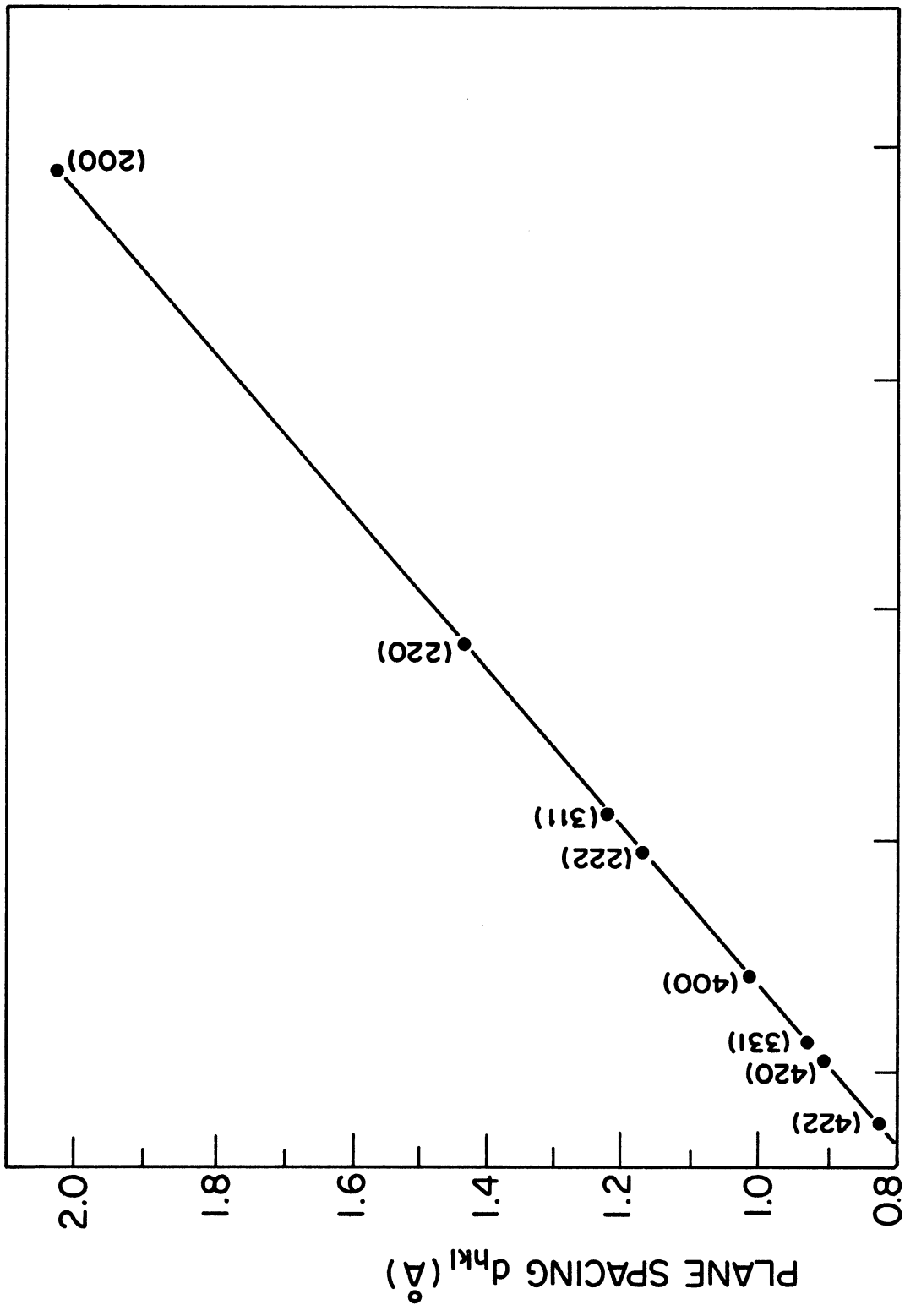

Figure 3.7. A typical calibration run with an aluminum polycrystal target for the 90° scattering bank.

spacing so that there might be a reliable calibration at lower values of Q. Lead has a face-centered cubic structure similar to aluminum with a lattice constant about 20% greater, giving the lowest Q value of 2.198 $Å^{-1}$ (see Appendix B.2). However, the 20° bank diffraction pattern was unable to be interpreted uniquely.

Reactor grade graphite is a suitable sample for calibration at low Q, for though it has a very large density of diffraction lines, the lowest Q value is 1.877 $Å^{-1}$ (see Appendix A.2). Often only two other peaks are seen at 20° scattering; viz., Q = 2.954 $Å^{-1}$ and 3.140 $Å^{-1}$. The paucity of lines at low Q introduce a possibility of inaccuracy of calibration for this particular detector bank, especially due to the absence of clear peaks for (10.0) and (10.2).

A check of the diffraction from graphite shows that (hh.ℓ) peaks for even ℓ are expected to be very strong, and for odd ℓ are absent. Strong peaks are indeed found for (00.2), (00.4), and (00.6), and for (11.0), (11.2), (11.4), etc. Though the general peak (hk.ℓ) should be much weaker, some are much weaker than expected. The odd ℓ peaks are greater than the even ℓ peaks as expected for the (20.ℓ) and (21.ℓ) peaks, but it is found the (10.ℓ) peaks are much weaker than expected. No explanation is offered by the presence of rhombohedral graphite (see Appendix A.3), since only (hh.ℓ) planes are common to both forms of graphite. The inability to locate the second peak due to (10.0) planes clearly, and the lack of other lines at low Q introduces a possibility

of inaccuracy of calibration for the 20° detector bank. However, since the detector circuits in each bank are similar, the same value of $(t_{del} + t_{err})$ is used for the calibration equation (3.8) for each bank. Hence the 20° bank has an extra point on the calibration line. Perhaps an additional usefulness of having graphite for calibration in the study of glassy carbon is that it shows the effect of crystallinity on the breadth of the diffraction lines.

From the aluminum calibration runs, it is possible to obtain the resolution $\Delta Q/Q$ of the machine from the full-width at half-maximum for the diffraction peaks. The results, shown in Figure 3.8, demonstrate, as expected, that the resolution for measurements at the 90° detector bank is superior to that at the 20° bank. Although the resolution for 90° scattering becomes progressively worse for higher values of Q, the diffraction pattern of amorphous materials have less pronounced features at high Q anyway. In practice, the value of $\Delta Q/Q$ is less than 0.025 over the whole range of Q scanned by this detector bank. The resolution for the 20° scattering is such that ΔQ is always less than 0.12 $Å^{-1}$.

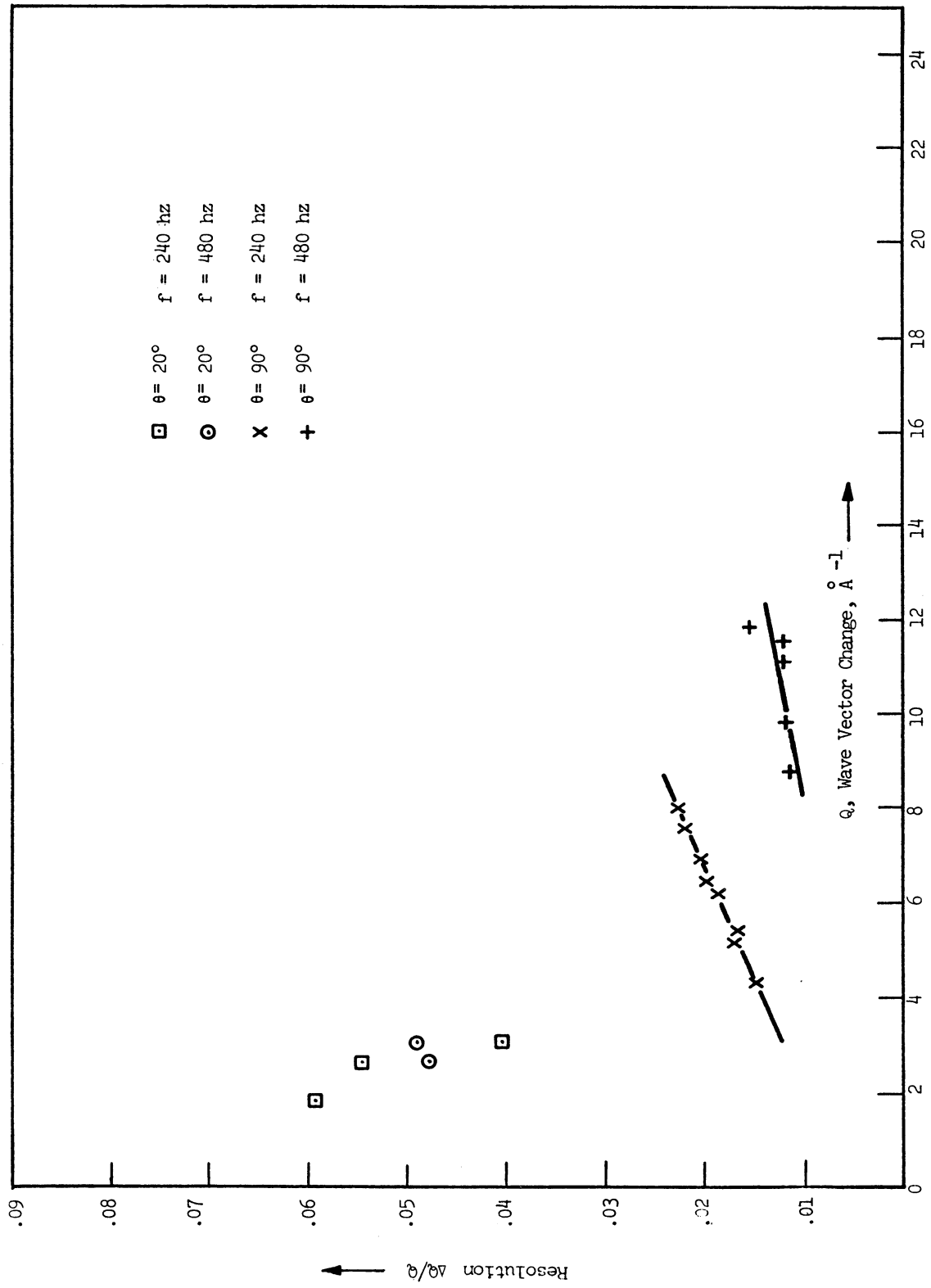

Figure 3.8. The resolution of the University of Michigan Time-of-Flight Neutron Diffractometer as a function of momentum transfer.

3.4 THE VANADIUM REFERENCE METHOD

In the lowest order of approximation we ignore both the effects of attenuation and multiple scattering, and contributions from inelastic scattering events, and we assume that the experimental integration path in the Q-ω plane is along paths at constant Q, so that the static approximation holds. Then the scattering cross section for the sample is given by equation (2.29). The observed scattered intensity $I_{obs}(Q)$ recorded by a bank of detectors with an efficiency η (which may have an unknown neutron energy dependence which we neglect for the time being), and with a solid angle $\Delta\Omega_D$ subtended at the sample is given by

$$I_{obs}(Q) \simeq I_o \eta b^2 S(Q) \Delta\Omega_D \eta \qquad (3.10)$$

where I_o is the beam intensity incident upon the sample of η atoms per unit area in the direction $\underline{\Omega}_o$. This is shown schematically in Figure 3.9, where the cross section per scattering nucleus is given by $\partial\sigma/\partial\Omega(Q) = b^2 S(Q)$.

The factors I_o, $\Delta\Omega_D$ and η may be determined by measuring the scattering intensity from a reference material for which the cross section is known. Vanadium is a suitable reference material since it is an almost totally incoherent elastic scatter of neutrons. The coherent scattering length b_{coh} is -0.52 fermis, and cross section σ_{coh} is 0.034 barns (Willis, 1973), whereas the incoherent scattering cross section σ_{inc} is 5.13 barns (Hughes and Schwartz, 1957). Note from

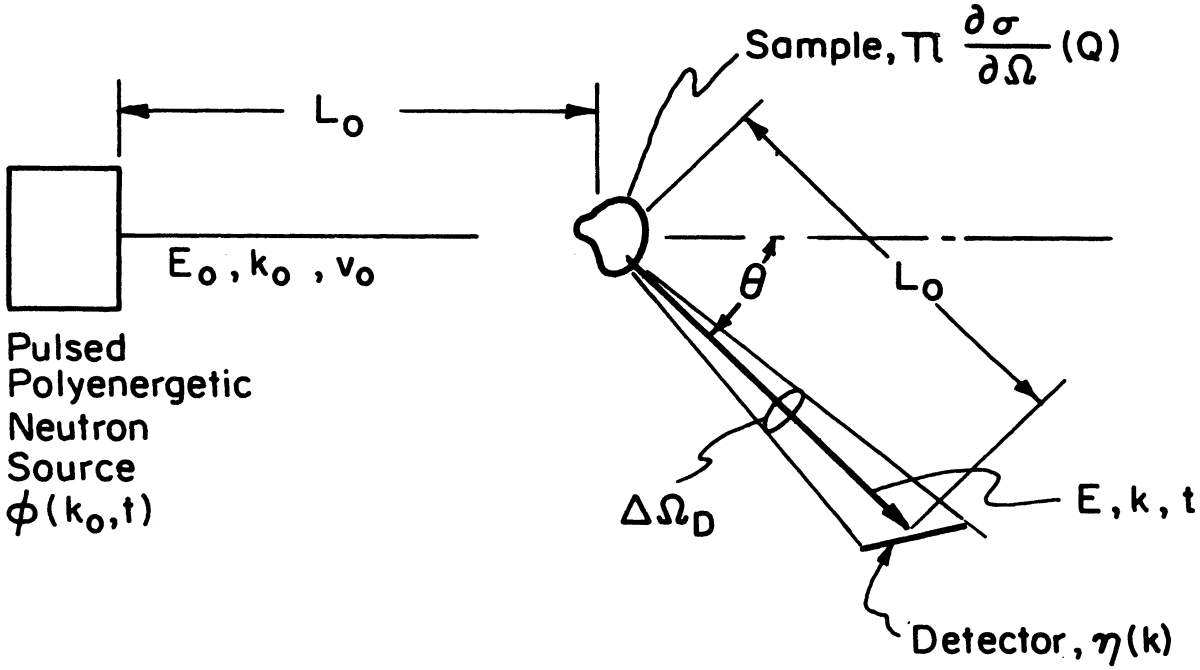

Figure 3.9. A schematic drawing of time-of-flight diffractometry.

equation (2.27) that S(Q) for an incoherent scatter is unity, so that the observed scattered intensity from vanadium is isotropic and is given by

$$I^{v}_{obs} \simeq I_o \eta_v b^{v\,2}_{inc} \Delta\Omega_D \eta \qquad (3.11)$$

If the vanadium reference method is used, the material under study and the vanadium target are cycled continuously into the sample position, so that any slow variations in the neutron flux or detector efficiency will be time-averaged equally in the observed intensities corresponding to each position. The analyzer therefore records counts alternately from the sample (S) and vanadium (V), and in the lowest order of approximation, the ratio of the observed intensities gives

$$\frac{I^{s}_{obs}}{I^{v}_{obs}}(Q) \simeq \frac{\eta_s}{\eta_v} \frac{b^{s\,2}_{coh}}{b^{v\,2}_{inc}} S(Q) \qquad (3.12)$$

Hence the sample cross section per scattering nucleus as a function of momentum transfer is

$$\left(\frac{\partial\sigma}{\partial\Omega}(Q)\right)_s = b^{s\,2}_{coh} S(Q) \simeq \left(\frac{I^{s}_{obs}}{I^{v}_{obs}}(Q)\right) \frac{\eta_v}{\eta_s} b^{v\,2}_{inc} \qquad (3.13)$$

3.5 FINITE TARGET EFFECTS

The detectors provide a measure of all the radiation scattered by the target into the detector directions, including those neutrons which are scattered more than once. Again ignoring inelastic contributions, the observed intensity may be expressed by

$$I_{obs} = I_o(P_1 + P_M)\eta \tag{3.14}$$

where P_1 and P_M are the probabilities of single and multiple scattering from the incident direction $\underline{\Omega}_o$ into $\Delta\Omega_D$ about the detector direction $\underline{\Omega}_D$.

In the ideal experiment (that is, with no finite target effects), there will be no multiple scattering, such that $P_M = 0$. In this case P_1 will tend towards the ideal probability of scatter, P_I, which is seen from equations (3.10) and (3.14) to be

$$P_I = \pi\zeta b^2 S(Q)\ \Delta\Omega_D = \pi\zeta \frac{\partial\sigma}{\partial\Omega}(Q)\ \Delta\Omega_D . \tag{3.15}$$

It is then convenient to rewrite equation (3.14) as

$$I_{obs} = I_o P_I \eta \left(\frac{P_1 + P_M}{P_I} \right). \tag{3.16}$$

such that the factor, $C_o = (P_1 + P_M)/P_I$, is now the multiplicative correction factor that is necessary to be applied to the ideal scattered intensity to account for the finite thickness of the target.

If we assume that other correction factors are either negligible or that they are included in C_o which may be calculable for both the sample and the reference, then the expression for the sample cross sec-

tion (equation (3.13)) becomes

$$\left(\frac{\partial\sigma}{\partial\Omega}(Q)\right)_s = \frac{I^s_{obs}(Q)}{I^v_{obs}}\frac{\eta_v}{\eta_s}\left(\frac{C^v_o(Q)}{C^s_o}\right) b^{v2}_{inc} \qquad (3.17)$$

In a well-devised experiment, the correction factors C_o will be close to unity, and may be calculated with an adequate accuracy using approximate cross sections.

It is useful to observe that C_o can be written

$$C_o = \frac{P_1 + P_M}{P_I} = \frac{P_1}{P_I}\left(1 + \frac{P_M}{P_1}\right), \qquad (3.18)$$

where the ratio $C_A \equiv P_1/P_I$ has the significance of an attenuation correction factor, and $C_M \equiv (1 + P_M/P_1)$ might be called a multiple scattering correction factor. The effects of attenuation are also present in P_M, of course, so that strictly speaking, "multiple scattering correction factor" is a misnomer. However, for various reasons it is appropriate to discuss the attenuation correction factor separately.

We refer to Figure 3.10. The incident radiation is attenuated as it travels a distance $l_1(\underline{r})$ in a direction $\underline{\Omega}_1$ to the point of scatter, and the emerging radiation is similarly attenuated traveling a distance $l_D(\underline{r})$ in a direction $\underline{\Omega}_D$ out of the target. If we assume that the scattering interaction is elastic, then the attenuation coefficient Σ_T is a constant before and after scattering. The probability of single scatter into $\underline{\Omega}_D$ per neutron is given by

$$P_1(\underline{\Omega}_D) = \frac{1}{V}\int_V dV \exp(-\Sigma_T l_1(\underline{r}))\exp(-\Sigma_T l_D(\underline{r}))N\frac{\partial\sigma}{\partial\Omega}(\underline{\Omega}_1 \to \underline{\Omega}_D)\Delta\underline{\Omega}_D \qquad (3.19)$$

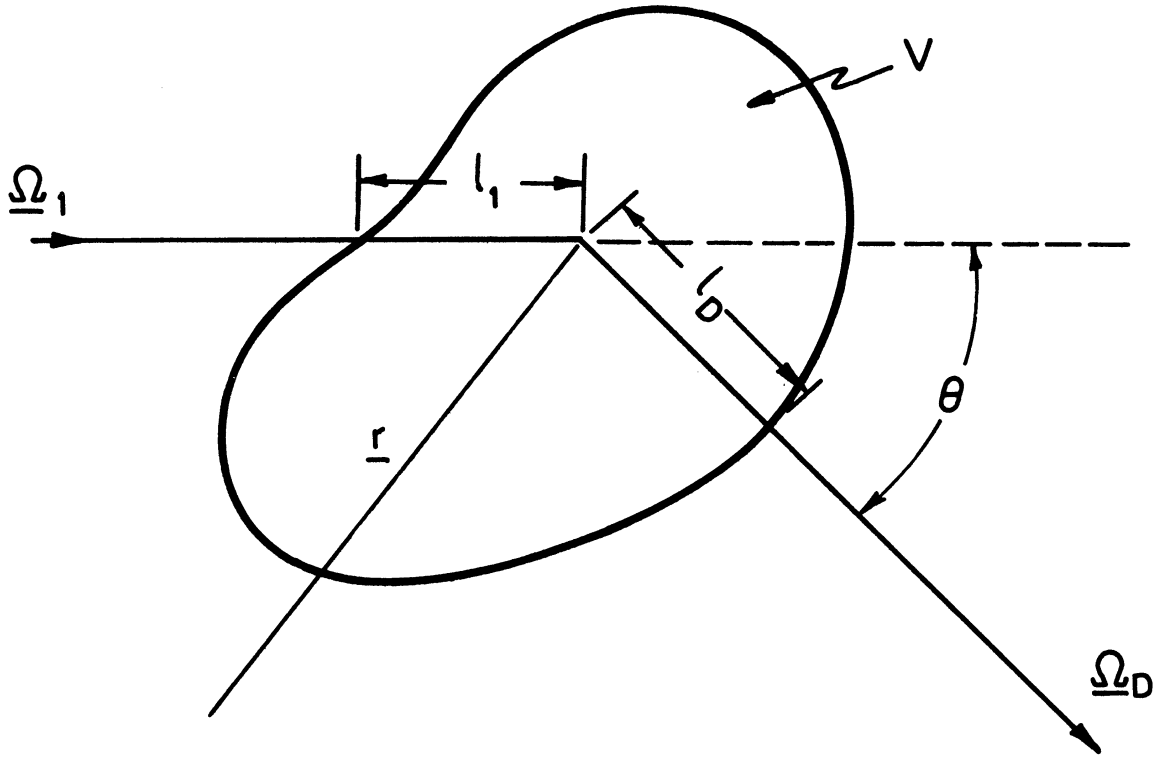

Figure 3.10. The general case of target attenuation in a neutron scattering experiment.

where the integration is over the volume V of the target which is bathed by the incoming beam (which is assumed to have a uniform profile). Then the target attenuation correction factor is

$$C_A = \frac{P_1}{P_I} = \frac{1}{V} \int_V dV \exp(-\Sigma_T l_1(\underline{r})) \exp(-\Sigma_T l_D(\underline{r})) \qquad (3.20)$$

and is independent of the unknown differential cross section, although dependent on the total cross section.

The multiple scattering correction factor C_M, on the other hand, is dependent on the differential cross section, which is both unknown and is to be measured. Consequently special methods are required when the differential cross section cannot be expressed analytically. It should be stressed that finite target effects are often severe, and that corrections must be made for these geometric factors. Without these adjustments the Fourier transform of the observed diffraction pattern may lead to poor conclusions of the local ordering from an incorrect radial distribution function.

3.6 THE GLASSY CARBON SAMPLE

The isotopes of carbon found in nature are C^{12} with an abundance of 98.89%, and C^{13} with an abundance of 1.11%. Willis (1973) gives the coherent scattering length b_{coh} for the two as 6.65 fermis and 6.0 fermis, respectively. The coherent cross section for carbon may be written as the sum of the individual cross sections for the isotopes weighted by their abundances.

$$\sigma_{coh} = 4\pi \sum_i n_i \, b^i_{coh} \qquad (3.21)$$

where n_i is the percentage abundance of the i^{th} isotope. Then the coherent cross section for carbon is 5.545 barns. The incoherent cross sections for each isotope are 0.0 and 1.0 barns, respectively, so that the incoherent cross section for carbon is 0.011 barns, by equation (2.15). Additionally the thermal absorption cross section is 0.0034 barns. Carbon is therefore an excellent choice for a neutron scattering experiment, since it has a reasonably high coherent cross section and a negligibly small incoherent cross section; and moreover it is a monatomic substance.

It is useful in a neutron scattering experiment to have a large target to increase the scattered intensity, since neutron fluxes are much smaller that those in X-ray sources. However, an increased target size increases the problems of attenuation and multiple scattering, and a good rule of thumb has often been a target with thickness t such that

there is about 10% scatter. Hence 0.1 = $g\sigma t$ where g is atomic number density of the target. The density of most carbons is of the order of 1.5 gm/cc, so that g ~ 0.075 atoms/$Å^3$. Hence an ideal thickness would be about 0.244 cm, or 1/10 in. Additionally the ideal target would be in the form of a slab which completely covers the neutron beam, so that corrections may be applied more easily later.

Our sample was provided by Hucke (1972) and was prepared by the carbonization of polyfurfuryl alcohol resin which leave the carbon in a disordered amorphous state. The bulk material was formed in a long cylinder of diameter 2 cm, and heat treated at 2000°C. The bulk density of the material is 0.923 gm/cc because of the large-scale pores which were introduced into the sample during preparation. However helium pycnometry, which measures the density of the material between these large-scale pores, gives a value of 1.41 gm/cc, and mercury intrusion to 60,000 psi gives a real density of 1.49 gm/cc.

This particular sample (312-31) has been thoroughly characterized by numerous measurements by Hucke (1973). Wide angle X-ray diffraction analysis was performed on a 3 mm thick disc of the sample. The (002) peak is smooth and quite broad which shows that the carbon is of a single phase. Further results of the analysis are given is section 4.8. Select area electron diffraction has also been employed. Bright and dark field transmission electron microscopy has been used to examine the microstructure. The micrographs show irregularly shaped platelets

containing granular texture whose size suggest that they correspond to small paracrystalline regions. Small angle X-ray scattering shows that the carbon is polydisperse, since large-scale voids were introduced during the preparation in addition to the small-scale voids characteristic of all glassy carbons. The large-scale voids have a mean pore diameter of about 250 Å and an intrusion pore volume of 0.4118 cc/gm as measured by mercury porosimetry. Further discussion of the voids in this carbon is found in Chapter 6.

Another sample of glassy carbon was provided by Bokros (1972) and was prepared by pyrolytic deposition of the carbon in a fluidized bed. The deposition temperature was 1180°C ± 10°C as measured by a thermocouple. The sample was heat treated for 1 hr at a temperature ~ 2000°C (maximum 2025°C). The density of the sample is 1.86 gm/cc and is in the form of 55 pieces, each of dimensions 1/4 in. x 1/4 in. x 1/64 in. These have been placed in a holder to form a sample of size 1/2 in. x 1 in. x 7/64 in. surrounded by .003 in. aluminum. This is approximately an ideal target. No measurements have been made of this particular target as yet, but it is intended that a neutron diffraction pattern will be taken as a comparison to the data taken from the Hucke sample, which was prepared by different method but with a similar heat treatment temperature.

In the analysis of the diffraction results it will be necessary to take into account contributions due to the sample container. However,

the Hucke sample, which was about 1-1/2 in. long could be held in the target position with screws. This eliminated a container, though not with a background measurement.

CHAPTER IV. DATA ANALYSIS

4.1 DATA REDUCTION

It was found convenient to take diffraction data of the glassy carbon sample at three different rotor frequencies; viz., 140 Hz (the lowest available frequency), 240 Hz, and 480 Hz (the highest available frequency). For each rotor frequency and detector bank, this allows the scattered radiation to be measured for the sample and the reference over a large range of wave vector transfer Q. Reasonable statistics were obtained in the following ranges:

Frequency	Scattering Angle	Range of Q Space
140 Hz	20°	1.0 - 2.5 $Å^{-1}$
240 Hz	20°	1.5 - 3.0 $Å^{-1}$
480 Hz	20°	2.5 - 3.5 $Å^{-1}$
140 Hz	90°	2.8 - 12.0 $Å^{-1}$
240 Hz	90°	4.5 - 15.0 $Å^{-1}$
480 Hz	90°	9.0 - 25.0 $Å^{-1}$

The data sets have a large amount of overlap in the range of Q scanned, which increases the confidence of the measurement. The real test occurs at the overlap of data for the same range of wave vector transfer from different scattering angles, for which the magnitudes of the corrections will be different. Better statistics have been obtained on the 90° bank, since not only is the resolution much better, but also the solid angle $\Delta\Omega_D$ subtended by the detectors at the sample is five times greater than that at the 20° degree bank (Carpenter, et al., 1973).

A rotor of a magnesium-cadmium alloy with different transmission characteristics (NS/TS = 8) from the Nimonic rotor has also been used at a frequency of 180 Hz with a scattering angle of 90° to obtain better data for the range of Q below 3.0 $Å^{-1}$. However, the composition of this alloy is such that the removal cross section for fast neutrons is so low that there are background problems, and the data has not been used.

Reliable data has therefore been obtained for the carbon sample and the vanadium reference for a range of wave vector transfer between about 1.0 $Å^{-1}$ and 25.0 $Å^{-1}$. These data have been reduced by computing the ratio of the observed intensities, I^{s}_{obs}/I^{v}_{obs}, of the two samples at each channel, accounting for the length of time taken for the counting of of each sample. In practice the fractions of the total counting time for the sample and reference were 0.74671 and 0.25329 for the 240 Hz and 480 Hz data, and 0.48831 and 0.51169 for the 140 Hz data which was taken at a later time. By taking the ratio for similar channels, the factors (k_o), the neutron flux, and $\eta(k)$, the detector efficiency, in equation (3.2) are eliminated, and the differential cross section of the sample is given by (3.13).

In each of the data runs, there are contributions due to the background which can never be entirely eliminated. It is of course minimized by large amounts of shielding, and by judicious phasing of the two rotors. Background has been compensated by two methods; first, by taking a separate background measurement, and secondly, by a linear interpolation beneath the data between points where the observed

intensity is effectively constant. A separate background measurement is obviously more desirable, in case the background has some analyzer channel or time dependence as is true for fast neutron background. However the present analyzer and sample cycler capabilities prevent this from being performed simultaneously with the other measurements. A background measurement performed at a later time may have errors in the neutron flux and detector efficiency. The interpolation procedure on the other hand does not allow for any time-dependent background. However it is usual to arrange the phasing of the rotors, and the time delay and channel width such that the edges of the fast neutron background are just seen. Consequently the interpolation is performed between the two minima in the observed intensity at each end of the observed spectrum. It is found in practice that little difference exists between the two procedures, and the interpolation method has been used in the final analysis.

While the counting times used in this study have been reasonably lengthy, statistical variations may still occur in the data. The diffraction spectra have been smoothed by using a formula such that counts in a particular channel are averaged over a few side channels. For the sample data, this averaging has been over 5 channels with a ratio of 1:4:6:4:1. For the vanadium data which are expected to be more smooth, the averaging has been over 7 channels with a ratio of 1:6:15:20:15:6:1. These ratios have also been taken into account to the computation

of the standard deviation for the ratio of the counts in each channel. This first stage in the analysis is performed by the program DATRED, for "Data Reduction."

Having obtained ratios of the diffracted intensities for the sample and the vanadium reference, corrections for attenuation and multiple scattering in equation (3.17) must be computed. The vanadium finite target corrections are performed first since they are easier to compute than for the sample. The sample corrections require a knowledge of the total cross section for attenuation purposes, and the differential scattering cross section for the multiple scattering calculation. Preliminary values of the latter are obtained from a partially (i.e., vanadium) corrected diffraction pattern which has been normalized. After the sample corrections have been made, the fully corrected diffraction pattern is normalized again. A second iteration of the sample corrections should be made from the fully corrected diffraction pattern to ensure the convergence of the corrections computed in this way. The diffraction pattern is then transformed by equation (2.47) to give the radial distribution function. After termination error removal, the analysis of the RDF proceeds by comparison with models for the sample.

4.2 VANADIUM REFERENCE CORRECTIONS

The vanadium slab has a thickness t of 0.3175 cms, and a density of 6.1 gm/cc. It is approximately a 10% scatter of neutrons when it is placed perpendicularly to a beam of incident neutrons. In this experiment the slab was inclined at an angle ϕ of 45° to the incoming beam direction $\underline{\Omega}_o$, as shown in Figure 3.3, so that the 90° detector bank is in a time-focussed geometry. Not only is vanadium an incoherent scatterer with a total scattering cross section σ_t of 5.13 barns (Hughes and Schwartz, 1957), but it is also a 1/v neutron absorber with a 0.0253 ev cross section σ_a of a 5.06 barns (Hughes and Schwartz, 1958). Consequently, severe attenuation corrections are expected in addition to multiple scattering corrections; moreover these corrections are required to be made for accurate measurements.

Since the effective size of the vanadium slab is 4 in. by 2-1/4 in., which is much greater than the size of the beam at the sample (1-1/2 in. by 1/2 in.), the vanadium corrections are computed easily using a transport calculation for an infinite slab, as originally suggested by Vineyard (1954). The assumptions are that the incoming neutron beam is uniform, that the scattering is entirely elastic and incoherent, so that the angular distribution of primary scattered neutrons is isotropic. Hence the vanadium scattering is treated in the elastic approximation, since the incoherent scattering cross section is much greater than the inelastic scattering cross section which is of the order of millibarns.

However in the lowest order of approximation, the measurement senses the total (elastic and inelastic scattering), so that no Debye-Waller correction has been applied.

Normally vanadium scattering is treated as completely incoherent and therefore isotropic, so that the diffraction spectrum is an image of the reactor spectrum, $\Phi(k_o)$, modified by the machine transmission characteristics, and the detector efficiency $\eta(k)$. However it has been found that the diffraction spectrum for vanadium has little peaks due to the small coherent scattering cross section (0.034 barns) of vanadium. A lack of cognizance of this fact may cause small dips in the computed diffraction pattern at Q values corresponding to the vanadium crystal structure (see Appendix B.3). In fact a number of peaks or anomalous points found in the 90° scattering data were attributed to the following planes; for 140 Hz, (200) and (211); for 240 Hz, (220), (310), and (321); and for 480 Hz, (400) and (420).

X-ray diffraction from the polycrystalline vanadium sample used in these measurements showed that it had no preferred orientation. It therefore seems to be a valid assumption that the crystalline grains of the sample are randomly oriented, and that the coherent scattering is azimuthally symmetric and cannot be reduced substantially. Since the amount of coherent scattering cannot be assessed easily, it is found convenient to simply interpolate beneath these coherent peaks which appear in the vanadium data, and to analyze the results thereafter as

for a totally incoherent scatterer.

The program used to account for the vanadium corrections is an adaption of that due to Rowe (1973). Define the following probabilities, P_I and P_N, as the probability of an incident neutron being scattered from the incident direction $\underline{\Omega}_o$ into a solid angle $\Delta\underline{\Omega}_D$ about a detector direction $\underline{\Omega}_D$ by the target per unit atom scatterer, in the ideal case (i.e., neglecting attenuation), and after N scattering events. Let L_D and L_N be the distances travelled by the neutron in the target in the directions $\underline{\Omega}_D$ towards the detector after the last scatter, and $\underline{\Omega}_N$ before the Nth scatter. Hence $\underline{\Omega}_o$ and $\underline{\Omega}_1$ are identically equal. Then

$$P_I(\underline{\Omega}_D) = \int_o^{t/\sin\phi} dL_o \frac{d\sigma}{d\Omega}(\underline{\Omega}_o \rightarrow \underline{\Omega}_D)\, \Delta\Omega_D , \tag{4.1}$$

$$P_1(\underline{\Omega}_D) = \int_o^{t/\sin\phi} dL_1\, e^{-\Sigma_T L_1} \frac{d\sigma}{d\Omega}(\underline{\Omega}_1 \rightarrow \underline{\Omega}_D)\, e^{-\Sigma_T L_D}\, \Delta\underline{\Omega}_D, \tag{4.2}$$

and

$$P_2(\underline{\Omega}_D) = \int_o^{t/\sin\phi} dL_1\, e^{-\Sigma_T L_1} \int_o^{4\pi} d\Omega_2 \frac{d\sigma}{d\Omega}(\underline{\Omega}_1 \rightarrow \underline{\Omega}_2)$$

$$\int_o^{L} dL_2\, e^{-\Sigma_T L_2} \frac{d\sigma}{d\Omega}(\underline{\Omega}_2 \rightarrow \underline{\Omega}_D)\, e^{-\Sigma_T L_D}\, \Delta\underline{\Omega}_D , \tag{4.3}$$

where Σ_T is the total macroscopic cross section of the target for neutrons of a given wave vector. Note that P_I is not really a probability but rather a ratio of the detected to incident neutrons in the ideal case.

The plane of the vanadium slab is inclined at angle ϕ to the neutron beam direction $\underline{\Omega}_o$ (see Figure 4.1). For each detector point with azimuthal angle β at a scattering angle θ, define a parameter $\tau = \sin\theta \cos\beta \cot\phi - \cos\theta$. For $\theta > \phi$ (i.e., reflection geometry), $\tau > 0$; this applies to the 90° bank. For $\theta < \phi$ (i.e. transmission geometry), $\tau < 0$; this applies to the 20° bank. Fortunately for vanadium $d\sigma/d\Omega = \Sigma_s/4\pi$, and being isotropic has no angular dependence. Consequently the ratios of the probabilities reduce to

$$\frac{P_1}{P_I}(\underline{\Omega}_D) = \frac{1}{t/\sin\phi} \int_o^{t/\sin\phi} dL_1 \exp(-\Sigma_T L_1) \exp(-\Sigma_T L_D) \qquad (4.4)$$

where

$$L_D = \dot{L}_1/\tau \qquad \text{for } \tau > 0$$

$$= (L_1 - t/\sin\phi)/\tau \qquad \tau < 0$$

and

$$\frac{P_2}{P_I}(\underline{\Omega}_D) = \frac{\Sigma_s}{t/\sin\phi} \int_{-1}^{+1} \int_o^{2\pi} d\mu d\alpha \int_o^{t/\sin\phi} dL_1 \exp(-\Sigma_T L_1)$$

$$\int_o^{L} dL_2 \exp(-\Sigma_T L_2) \exp(-\Sigma_T L_D) \qquad (4.5)$$

where μ is the scattering cosine of the first scatter angle ψ, and α is the azimuthal angle of the first scattering direction relative to the incoming beam; and where

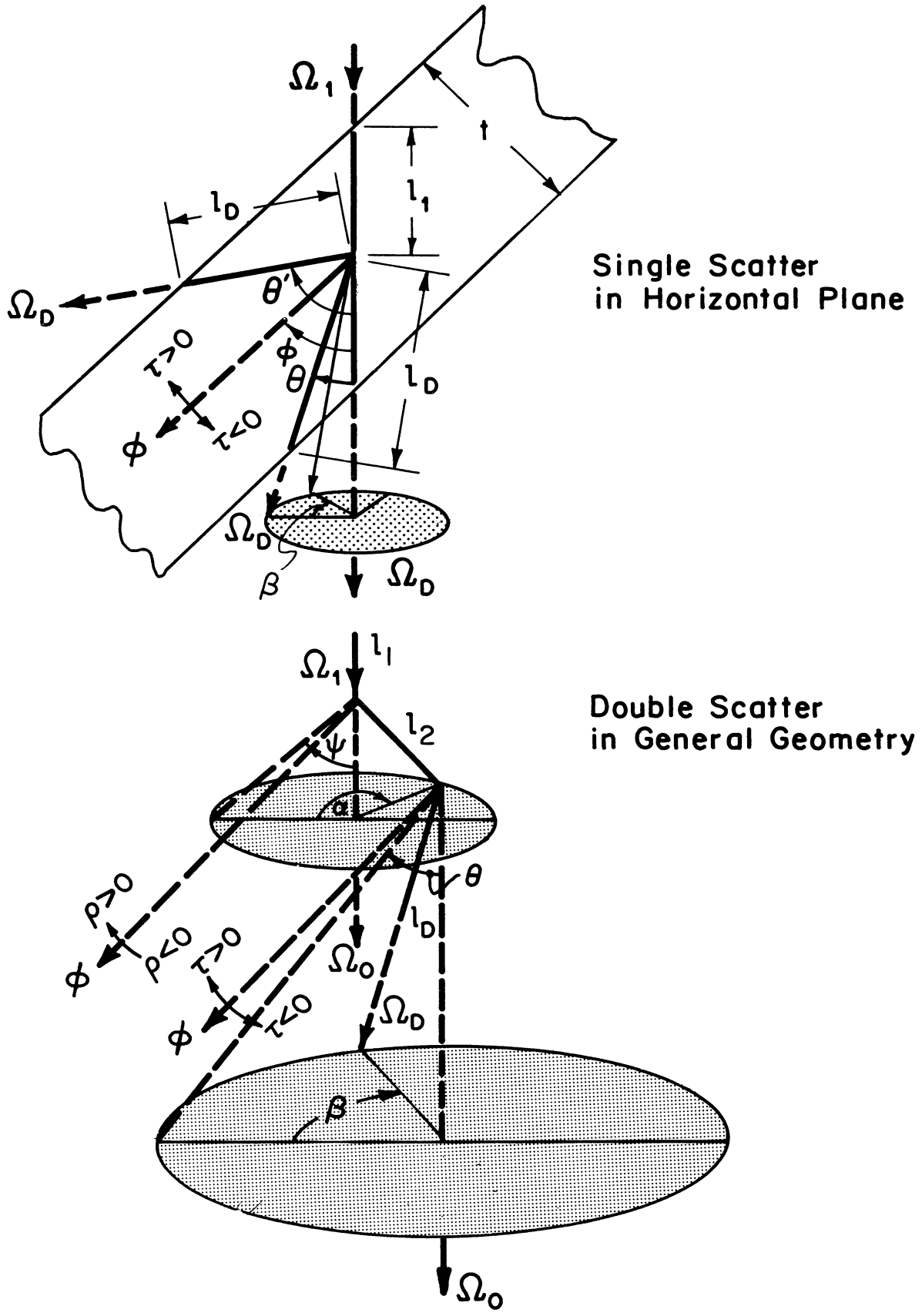

Figure 4.1. Schematic drawings for the vanadium correction program.

$$L = L_1/\rho \qquad \text{for } \rho > 0$$

$$= (L_1 - t/\sin\phi)/\rho \qquad \rho < 0$$

with

$$\rho = \sin\psi \cos\alpha \cot\phi - \cos\psi \tag{4.6}$$

and where

$$L_D = (L_1 - L_2\rho)/\tau \qquad \text{for } \tau > 0$$

$$= (L_1 - L_2\rho - t/\sin\phi)/\tau \qquad \tau < 0$$

with

$$\tau = \sin\theta \cos\beta \cot\phi - \cos\theta \tag{4.7}$$

The first integral can be performed analytically, and in the general case for all scattering angles $\theta > 0$,

$$\frac{P_1}{P_I}(\underline{\Omega}) = \frac{1 - \exp(-\Sigma_T t/\sin\phi\ (1 + 1/\tau))}{\Sigma_T t/\sin\phi\ (1 + 1/\tau)} \exp\left(\frac{\Sigma_T t z}{\sin\phi\ \tau}\right) \tag{4.8}$$

where

$z = 0$ for $\theta > \phi$ (reflection geometry)

$z = 1$ for $\theta < \phi$ (transmission geometry).

The second integral cannot be computed analytically, but must be

performed by summing over segments of α, the azimuthal scattering angle, and μ, the cosine of the first scattering angle ψ. ρ is exactly analogous to τ, and $\rho > 0$ when the first scatter is towards the reflection surface, and $\rho < 0$ when the first scatter is towards the transmission surface. The integration for the first scatter is taken over all values of ρ, and is performed by a numerical integration. In general, for all scattering angles $\theta > 0$

$$\frac{P_2}{P_I}(\underline{\Omega}_D) = \frac{\Sigma_s}{\Sigma_T} \frac{1}{N_\alpha N_\mu} \sum_{\mu}^{N_\mu} \sum_{\alpha}^{N_\alpha} \frac{\exp\left(\frac{\Sigma_T t z}{\sin\phi\ \tau}\right)}{\Sigma_T t/\sin\phi} \frac{1}{1 - \rho/\tau}$$

$$\left[\frac{1 - \exp\left(-\frac{\Sigma_t t}{\sin\phi}(1 + 1/\tau)\right)}{(1 + 1/\tau)} - R \frac{1 - \exp\left(-\frac{\Sigma_T t}{\sin\phi}(1 + 1/\rho)\right)}{(1 + 1/\rho)} \right] \qquad (4.9)$$

where

$$\rho = 1 \qquad \text{for } \rho > 0$$

$$= \exp\left(\frac{\Sigma_r t}{\sin\phi}\left(\frac{1}{\rho} - \frac{1}{\tau}\right)\right) \qquad \rho < 0$$

and, as before,

$$z = 0 \qquad \text{for } \theta > \phi \qquad \text{(reflection geometry)}$$

$$z = 1 \qquad \text{for } \theta < \phi \qquad \text{(transmission geometry).}$$

Hence for neutrons of a given wave number k (and therefore a given total cross section Σ_T), values of $P_1/P_I(\underline{\Omega}_D)$ and $P_2/P_I(\underline{\Omega}_D)$ may be easily

computed. In practice it is found that values of N_μ and N_α equal to 10 and 20, respectively, are sufficient for convergence with adequate statistics.

The finite extent of the detectors in a bank of scattering angle θ is analyzed by treating the detectors as points at different azimuthal angles β. Due to the horizontal symmetry of the targets, azimuthal angles β may be examined from 0° (horizontal) to a maximum value β_{max} (appropriate to the particular detector bank) with suitable weightings U_D to account for the actual location of the detectors, so that for any detector bank

$$P_N(\theta) = \sum_D U_D \, P_N(\underline{\Omega}_D) \, , \tag{4.10}$$

where the sum extends over the detectors of the bank. Hence for a given scattering angle θ, values are computed for $P_1(\theta)$ and $P_2(\theta)$, the probabilities per neutron of single and double scatter by the target into the detector bank.

The probability of an incident neutron being scattered more than once by the target into a detector is given by

$$P_M = P_2 + P_3 + P_4 + \ldots\ldots \, . \tag{4.11}$$

In cases where the scattering isotropic, Vineyard (1954) has shown that it is reasonable to assume that the ratio of successive scattering probabilities is a constant; i.e., successive probabilities form a

geometric progression,

$$\frac{P_2}{P_1} \simeq \frac{P_3}{P_2} \simeq \frac{P_4}{P_3} \simeq \ldots = r = \frac{P_2/P_I}{P_1/P_I} \quad . \tag{4.12}$$

then

$$\frac{P_M}{P_1} \simeq \frac{r}{1 - r} \quad . \tag{4.13}$$

Hence the attenuation correction factor, C_A, and the multiple scattering correction factor, C_M, which are defined in section 3.5, may be determined for the vanadium slab target, and are given by

$$C_A(Q) = \frac{P_1}{P_I}(\theta,k) \tag{4.14}$$

and

$$C_M(Q) = 1 + \frac{P_M}{P_1}(\theta,k). \tag{4.15}$$

Hence the overall correction factor, C_o, defined by equation (3.18), is given by

$$C_o^V(Q) = \frac{P_1(\theta,k) + P_M(\theta,k)}{P_I(\theta,k)} \tag{4.16}$$

Values of C_A, C_M, and C_o^V computed in this way are shown as a function of Q for each of the scattering banks in Figure 4.2. The correction factor $C_o^V(Q)$ may be applied to equation (3.17) to provide a 'vanadium-corrected' diffraction pattern of the sample, or a differential cross section as a function of Q. This second stage in the analysis is performed by the program VANCOR, for "Vanadium Correction."

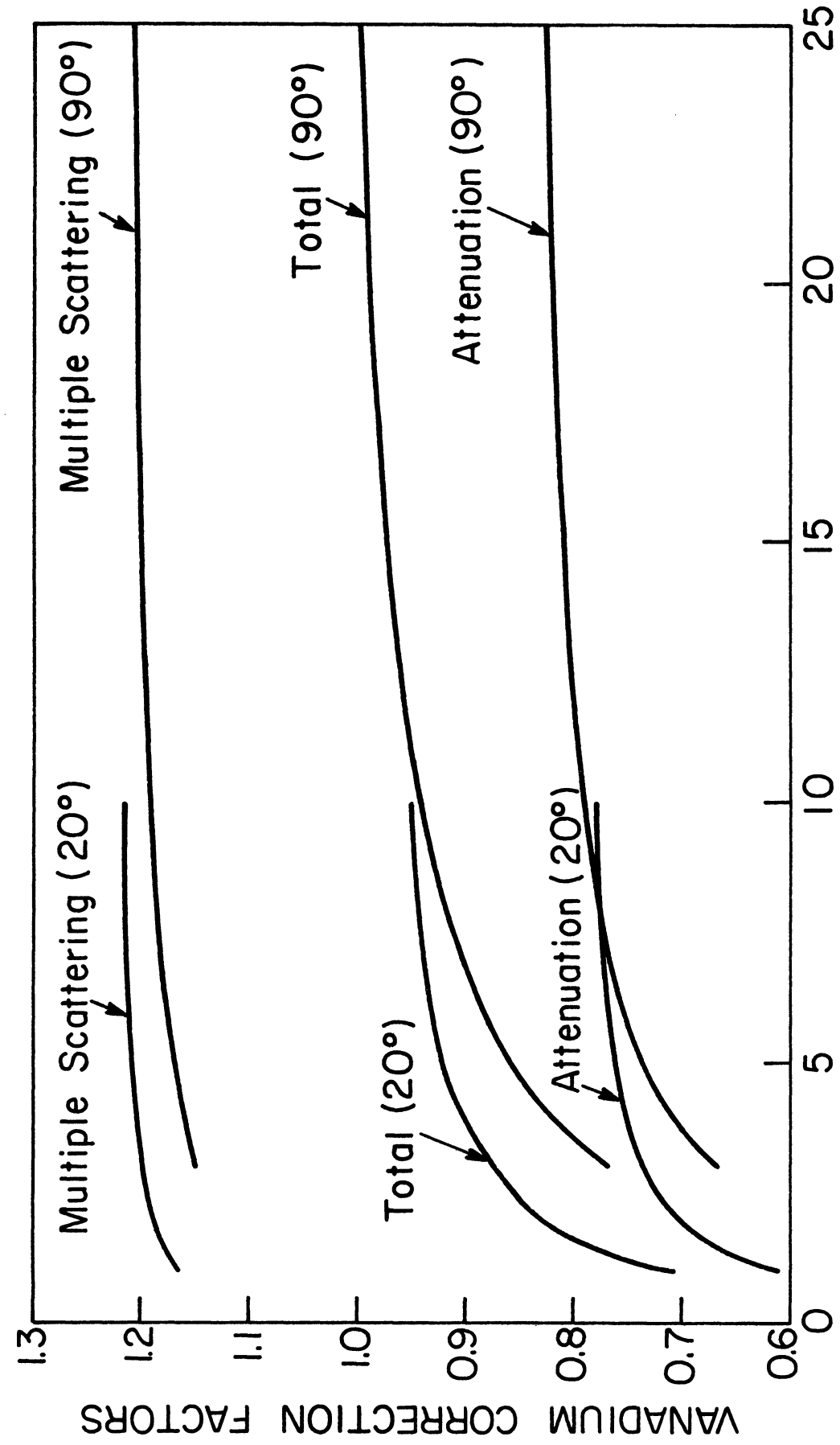

Figure 4.2. Vanadium correction factors for the two detector banks as a function of momentum transfer.

4.3 TOTAL NEUTRON CROSS SECTION

In order to apply finite target corrections for the sample itself, it is necessary to know its total neutron cross section as a function of wave number. Hence, it is usual to make a transmission measurement on the sample, using the same transmitted neutron energy spectrum as in the diffraction measurements; that is, using the same rotor frequencies. The transmitted neutrons may be measured by a fission chamber further down stream from the target. By the physical measurement of the distances L_o, from the Nimonic rotor to the sample, and L, from the sample to fission chamber, the transmission experiment may be calibrated using equation (3.7). The timing error t_{err} may be obtained from a calibration run as for the diffraction experiment. Hence the channel number n of the analyzer is inversely proportional to the wave number k of the neutron, and is given by

$$\frac{m_n}{\hbar k} = \frac{1}{v} = \frac{t}{L_o+L} = \frac{1}{L_o+L}(t_{err} + t_{del} + n - 1.5)\Delta\tau. \quad (4.17)$$

With no sample present, the count rate $C_o(n)$ in the fission chamber corresponding to channel number n is determined by the incident neutron flux $\phi(k)$ and the detector efficiency $\eta(k)$; that is

$$C_o(n) \sim \phi(k)\ \eta(k). \quad (4.18)$$

However with a sample present, a certain proportion of the flux is removed from the transmitted beam which is determined by the total cross

section $\sigma_T(k)$ of the sample. Ignoring any scattering into the fission chamber, the count rate with the sample present is given by

$$C_s(n) \sim \phi(k)\ \eta(k)\ e^{-g\sigma_T(k)x} \qquad (4.19)$$

where x is the thickness of the target. Hence the measured cross section may be determined from the ratio of the incident flux to the transmitted flux; that is,

$$\sigma_T(k) = \frac{1}{gx} \log \frac{C_o}{C_s}(n) \qquad (4.20)$$

where equation (4.17) gives the relationship between channel number η and wave number k.

Such a measurement was attempted without success; it will be described here, together with the reason for its failure. The carbon target was placed with its cylindrical axis along the neutron beam so that its effective thickness x was 1-1/2 in. The beam area was stopped down by a thick cadmium sheet so that only those neutrons transmitted through the target were measured. A fission chamber of diameter of 7 cms was placed at a distance L of 1.2509 m downstream fron the target, so that the solid angle $\Delta\Omega_{FC}$ presented to the fission chamber by the target was 0.00246 ster. With an expected total cross section $\sigma_T \sim 5.5$ barns, the transmitted beam would be about 38% which should be sufficient for reasonable results. However the experiment gave a measured cross section of the order of 3 barns. Even with the fission chamber

stopped down further with cadmium sheeting, this value did not change significantly. A difference between σ_T and the measured cross section of the order of 2 barns in 5 is a very large discrepancy in the transmission results.

If we take into account scattering into the fission chamber, then equation (4.19) becomes

$$C_s(n) \sim \phi(k)\ \eta(k)\ e^{-g\sigma_T x} + \phi(k)\ \eta(k)\ g \int_{\Delta\Omega_{FC}} \frac{\partial\sigma}{\partial\Omega}(k)d\Omega\ x(\underline{\Omega})\ f(\underline{\Omega}) + \text{multiple scattering terms.} \qquad (4.21)$$

Considering only single scatter into the small solid angle $\Delta\Omega_{FC}$, so the attenuation correction $f(\underline{\Omega})$ may be approximated by

$$f \approx e^{-g\sigma_T x}. \qquad (4.22)$$

Then equation (4.21) becomes

$$C_s(n) \sim \phi(k)\ \eta(k)\ e^{-g\sigma_T x}\left(1 + gx\int_{\Delta\Omega_{FC}} \frac{\partial\sigma}{\partial\Omega}(k)d\Omega\right)$$

$$\sim \phi(k)\ \eta(k)\ e^{-g\sigma_T x}\ e^{gx \int_{\Delta\Omega_{FC}} \frac{\partial\sigma}{\partial\Omega}(k)d\Omega}, \qquad (4.23)$$

and equation (4.20) becomes

$$\sigma_T(k) - \int_{\Delta\Omega_{FC}} \frac{\partial\sigma}{\partial\Omega}(k)d\Omega = \frac{1}{gx}\log\left(\frac{C_o}{C_s}(n)\right). \qquad (4.24)$$

Hence the total cross section σ_T is decremented by an amount $\int_{\Delta\Omega_{FC}} \partial\sigma/\partial\Omega\ d\Omega$ to give the measured cross section σ_{meas}; i.e.,

$$\sigma_T(k) = \sigma_{meas}(k) + \int_{\Delta\Omega_{FC}} \frac{\partial\sigma}{\partial\Omega}(k)\,d\Omega \qquad (4.25)$$

For an isotropic scatterer with no absorption, an experiment with this geometry would give a discrepancy of only 0.02% by equation (4.25). Although the assumption of no absorption is valid for carbon, the scattering is certainly not isotropic since the incoherent scattering is negligible compared to the coherent scattering. Let us assume that for all wave numbers the forward scattering that reaches the detector has been produced by a constant differential cross section $d\sigma/d\Omega|_F$ over the angular range $\Delta\Omega_{FC}$, and that the remaining scattering is isotropic, and equal to 0.442 barn/ster, the 'structure independent' value. The average value of $d\sigma/d\Omega|_F$ required to produce the observed 2-barn discrepancy is of the order of 800 barn/ster from equation (4.25). Just such intense forward scattering is a characteristic feature of glassy carbons (Bragg and Hammond, 1965), and has been measured in detail (section 4.9).

Since it is not possible to measure the total cross section directly by a simple transmission measurement, if there is any appreciable amount of forward angle scattering another method must be found. In theory cross sections may be computed, but for low energy neutrons the cross section is dependent upon the structure of the material. Consequently any assumptions made about the atomic structure for the determination of cross sections will bias the final result of the diffaction measurements. Obviously then, the best estimate of the details of the cross section may be obtainable from the diffraction pattern

itself, which is of course characteristic of the structure of the material (equation (2.31)).

In the static approximation, the scattering cross section is given by the integral of equation (2.29) over all solid angles; viz.,

$$\sigma_s(k) = b^2 \int_{4\pi} S(Q)\, d\Omega. \tag{4.26}$$

Using the elastic scattering equation (2.5)

$$Q^2 = 2k^2(1 - \mu) \tag{4.27}$$

where μ is the cosine of the scattering angle θ. Differentiation of equation (4.27) gives

$$Q\, dQ = - k^2\, d\mu. \tag{4.28}$$

Substitution of equation (4.27) into equation (4.26) yields

$$\begin{aligned} \sigma_s(k) &= 2\pi b^2 \int_o^{\pi} S(Q) \sin\theta\, d\theta \\ &= 2\pi b^2 \int_{-1}^{+1} S(Q)\, d\mu \\ &= \frac{2\pi}{k^2} b^2 \int_o^{2k} S(Q)\, Q\, dQ. \end{aligned} \tag{4.29}$$

Placzek corrections (Placzek, 1952; Wick, 1954) which are due in this relationship on account of inelastic contributions, have been ignored.

Hence for a particular neutron wave number k, the scattering cross section may be estimated from the partially corrected diffraction pattern by integrating its product with Q from zero to 2k, as in equation

(4.29). To employ this method, a diffraction pattern is required beyond Q_{max}, the maximum value of Q for which data were taken. At high k, the cross section becomes constant and independent of the structure of the material; so that at high Q, $\partial\sigma/\partial\Omega$ tends towards b^2 (equal to 0.442 barns/ster for carbon). It is assumed that this constant value has been reached in this study at $Q_{max} = 25$ Å^{-1}.

At the low Q end of the diffraction pattern ($Q < 1$ Å^{-1}), the small Q diffraction pattern (section 4.9) joined to the large Q diffraction pattern ($Q > 1$ Å^{-1}). Hence a total neutron cross section as a function of wavenumber for the glassy carbon may be obtained using

$$\sigma_T(k) = \sigma_s(k) + \frac{k_{th}}{k}\,\sigma_a(k_{th}) \qquad (4.30)$$

where $\sigma_a(k_{th})$ is the absorption cross section at a wave number k_{th} equivalent to the thermal energy, 0.0253 ev. For carbon this is 0.0034 barns, so that the total neutron cross section is essentially the same as the scattering cross section which is shown in Figure 4.3. This has been performed by the program TOTALX for total cross section.

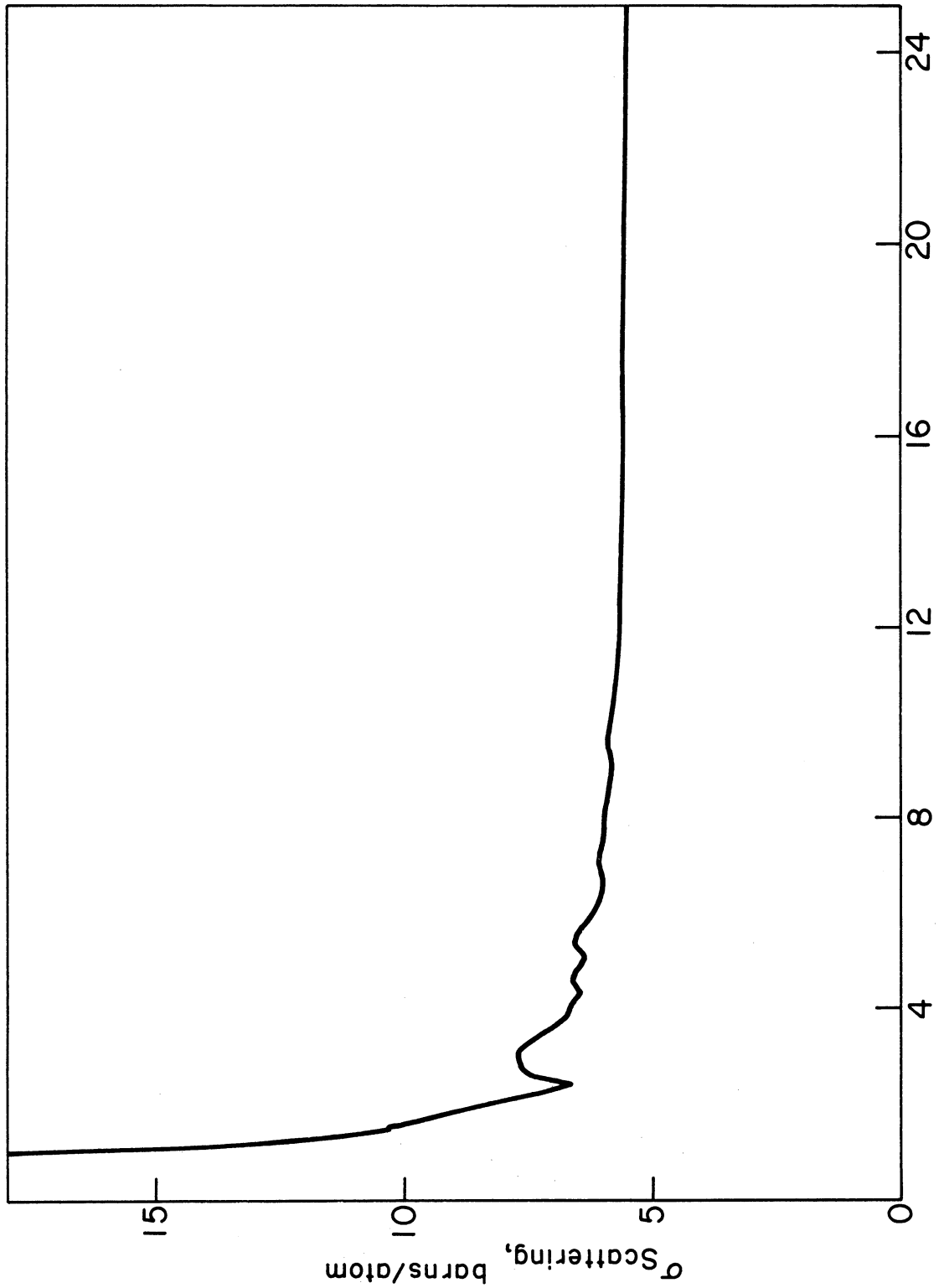

Figure 4.3. Glassy carbon scattering cross section as a function of neutron wave number.

4.4 DATA UNIFICATION AND NORMALIZATION

Effectively there are seven sets of diffraction data each covering overlapping regions in Q space, which must be joined together and normalized. The first region is the small Q diffraction pattern (see section 4.9) which was obtained between Q = 0.065 $Å^{-1}$ and 2.0 $Å^{-1}$ using 4.06 Å wave length neutrons. These data have been extrapolated to Q = 0 $Å^{-1}$ by fitting an exponential to the data for Q less than 0.3 $Å^{-1}$. The data sets obtained for the extended Q diffraction pattern and their effective Q-range are listed in section 4.1. They cover a range of Q between 1.0 $Å^{-1}$ and 25 $Å^{-1}$.

The problem is to unify these data and to normalize them. In fact this procedure has to be performed twice. The first time uses 'vanadium-corrected' data to provide a normalized partially-corrected diffraction pattern which must be extended out to Q = 50 $Å^{-1}$ in order to provide cross sections for the attenuation and multiple scattering corrections. The second time uses 'carbon-corrected' data to provide a normalized diffraction pattern for Fourier inversion to the pair correlation function.

Each of the data sets taken on the UMTOFND machine gives the ratio of the observed intensities, $I^{s}_{obs}/I^{v}_{obs}(Q)$, as a function of Q for each analyzer channel. These data are the results of the program DATRED and have had no corrections for attenuation and multiple scattering for either sample or vanadium; nor has account been taken for the sample

thicknesses and atomic densities. The program VANCOR computes the overall correction factor $C_o^v(Q)$ for vanadium, and gives a vanadium-corrected differential cross section, using $b_{inc}^{v\ 2} = 5.13/4\pi$ as the vanadium differential cross section, but with the factors η_s, the number of scatterers per unit area in the sample, and $C_o^s(Q)$, the overall correction factor for sample, both equal to unity in equation (3.17). However it is possible to multiply the result by an arbitrary factor which accounts for η_s and $C_o^s(Q)$; i.e., the assumption is that the sample corrections are independent of momentum transfer Q. This is done for all the sets of data but with different scaling factors such that within a region of Q of overlap, one data set matches the previous set. Consequently using arbitrary scaling factors, the various sets of data may be made internally consistent.

Fortunately there are two occasions for putting the data on an absolute basis. First the Thermal Neutron Time-of-Flight Spectrometer (TNTOFS) machine (Kleb et al., 1973), on which the small Q scattering data of glassy carbon were taken (Mildner and Carpenter, 1973), is calibrated against a vanadium standard, so that the vanadium-corrected small-Q diffraction was obtained using $C_o^s(Q) \simeq 1$. Secondly the highest Q data set was normalized such that around Q = 25 $Å^{-1}$ where the diffraction pattern is reasonably flat, the vanadium-corrected differential cross section was made equal to 0.442 barns/ster, the carbon 'structure independent' differential cross section. This is plausible provided

that the diffraction pattern has been taken to sufficiently high Q. It is believed that this criterion has been fulfilled by our data, since there are no large ripples in the data beyond Q = 20 $Å^{-1}$.

Hence the 480 Hz - 90° vanadium-corrected data has been normalized by using an arbitrary factor $\eta_s C_o^s(Q)$ to account for the sample attenuation and multiple scattering corrections in equation (3.17). Since there is a region of overlap of the 240 Hz - 90° and 480 Hz - 90° data, these may be matched over a region that is relatively flat, so that another arbitrary scaling factor may be determined for the 240 Hz - 90° data. This matching procedure may be performed for all the data sets down to the 140 Hz - 20° data which must be joined also to the independently normalized small-Q diffraction data.

Since the attenuation and multiple scattering correction $C_o^s(Q)$ is dependent on the behaviour of S(Q), it is expected that the assumption that $C_o^s(Q)$ may be approximated by a constant becomes progressively worse at smaller values of Q, where S(Q) becomes more sharply varying. Hence it is not unexpected that the matching of the UMTOFND data and the TNTOFS data at small Q was not perfect, since it is obvious that this factor $C_o(Q)$ varies not only with Q but with scattering angle θ. This mismatching becomes more noticeable for the regions of the large Q data where both 20° and 90° data were obtained with different geometries; viz., in transmission and reflection, respectively. The scaling factors for the 90° data were approximately the same; and for the 20° data too.

However the particular scaling factor for each angle was very different since again the correction factor is not only dependent on Q, but also varies markedly with scattering angle. Therefore in practice two different correction factors corresponding to each scattering angle are used, but each is constant, that is independent of Q.

Values of $\partial\sigma/\partial\Omega(Q)$ were selected in the following regions from the data:

0 - 1.0 $Å^{-1}$	the TNTOFS small-Q diffraction data
1.0 - 2.0 $Å^{-1}$	a combination of the small-Q data and the UMTOFND 140 Hz - 20° data
2.0 - 2.5 $Å^{-1}$	a combination of the 140 Hz - 20° data and the 240 Hz - 20° data
2.5 - 3.0 $Å^{-1}$	a combination of the 240 Hz - 20° data and the 480 Hz - 20° data
3.0 - 3.5 $Å^{-1}$	a combination of the 480 Hz - 20° data and the 140 Hz - 90° data which have very different correction factors
3.5 - 6.3 $Å^{-1}$	the 140 Hz - 90° data
6.3 - 7.3 $Å^{-1}$	a combination of the 140 Hz - 90° data and the 240 Hz - 90° data
7.3 - 11.0 $Å^{-1}$	the 240 Hz - 90° data
11.0 - 14.0 $Å^{-1}$	a combination of the 240 Hz - 90° data and the 480 Hz - 90° data
14.0 - 25.0 $Å^{-1}$	the 480 Hz - 90° data
25.0 - 50.0 $Å^{-1}$	no data with sufficient statistics are available.

The region about 25.0 $Å^{-1}$ has been assumed to be constant, and has been given the 'structure independent' value, the same estimate used to normalize the data at high Q.

Hence a vanadium-corrected and normalized diffraction pattern for values of Q from 0 $Å^{-1}$ to 25 $Å^{-1}$ has been obtained (see Figure 4.4). Analysis of this is left until later (see section 4.8). Values of $\partial\sigma/\partial\Omega(Q)$ were computed in steps of $\Delta Q = 0.02$ $Å^{-1}$ from 0 to 50 $Å^{-1}$, so that the total cross section $\sigma(k)$ might be obtained in steps of $\Delta k = 0.01$ $Å^{-1}$ up to $k = 25$ $Å^{-1}$, using the equations (4.29) and (4.30), where $b^2S(Q)$ is approximated by $\partial\sigma/\partial\Omega(Q)$.

The small Q diffraction data were corrected for the sample attenuation and multiple scattering first, since the corrections are most severe at small Q. The results therefrom were again combined with the other data. Then the UMTOFND data were corrected for the sample attenuation and multiple scattering. Now we have again seven sets of data which have been corrected for the sample finite targets effects and which must be joined together. The same procedure as before was used, with the value of $\partial\sigma/\partial\Omega$ at $Q = 25$ $Å^{-1}$ made equal to $\sigma/4\pi = 0.442$ barns/ster. The rest of the UMTOFND data was then matched to this, while the small-Q data was already normalized.

In normalizing the data at high Q, there remains a problem of determining where on the scale of the unnormalized diffraction pattern lies the value of the 'structure-independent' differential cross section.

Krogh-Moe (1956) has suggested a normalization procedure which is based on the effective exclusion of an atom from the immediate neighbourhood of another atom. Hence for r less than the closest interatomic distance, the static pair correlation function $g(\underline{r})$ is zero; i.e., in the limit $Qr \to 0$, equation (2.46) reduces to

$$-2\pi^2 g_o = \int_o^\infty Q^2 i(Q) dQ . \tag{4.31}$$

In practice, for all values of Q greater than a certain value Q_{max}, which is usually the limit of the diffraction pattern for which the data support reasonable statistics, i(Q) is set equal to zero. Then over the range of Q for which data have been obtained, equation (4.31) is evaluated which may be written, using equation (2.44), as

$$-2\pi^2 g_o = \lim_{Q_{max} \to \infty} \int_o^{Q_{max}} \frac{I(Q) - I(\infty)}{I(\infty)} Q^2 dQ . \tag{4.32}$$

It has been found that the value of g_o obtained by this integration is very sensitive to small changes in $I(\infty)$. The proper value of g_o in the case of this carbon sample is 0.07471 atoms $Å^{-3}$, equivalent to a bulk density of 1.49 gm cc^{-1}, which ignores the large scale (~ 250 Å) pores.

If on the other hand, equation (4.31) is solved explicitly for $I(\infty)$, we obtain

$$I(\infty) = \lim_{Q_{max} \to \infty} \frac{3 \int_o^{Q_{max}} I(Q)\, Q^2 dQ}{Q_{max}^3 - 6\pi^2 g_o} . \tag{4.33}$$

If the value of Q_{max} is sufficiently high, then the value of $I(\infty)$ is relatively insensitive to the choice of g_o. However it was found that if the data were normalized at high Q to the 'structure independent' cross section and a value of g_o was obtained by equation (4.32), then substitution of g_o into equation (4.33) yields a different $I(\infty)$. Since equations (4.32) and (4.33) are equivalent, this apparent inconsistency is explained by integration difficulties, especially at high Q and in regions where I(Q) is wildly varying.

In order to obtain a normalized diffraction pattern which is consistent with known values of g_o and $I(\infty)$, values of I(Q) are changed slightly around Q_{max} until equations (4.33) and (4.34) are equivalent. Instead of applying a modification function which is unity for $Q < Q_{max}$, and zero for $Q > Q_{max}$, the function I(Q) is forced to approach $I(\infty)$ smoothly; i.e., the modification function varies monotonically from unity to zero in a region less than 0.4 $Å^{-1}$ around Q_{max}. The effects of this procedure on the transform is discussed in section 5.1. The normalization method is performed by the program KROGHM, for the "Krogh-Moe normalization."

4.5 SAMPLE TARGET CORRECTIONS

The target attenuation correction factor C_A^S is independent of the differential cross section from equation (3.20). Hence it can be found easily by a transport calculation, similar to that for vanadium, provided that the sample geometry in the scattering plane is relatively simple (Mildner et al., 1974). However it is often the case that the target is not totally bathed by the incoming beam, so that a direct integration has to be performed to obtain the attenuation correction factor. Provided that the total cross section is known as a function of neutron wave number, this may be performed in principle for any target geometry.

The sample multiple scattering correction C_M^S, on the other hand, is dependent on the differential cross section whose relationship to momentum transfer we wish to measure. In general we can make no easy assumptions about the differential cross section for the sample as were able to be made for vanadium which is primarily an isotropic scatterer. The partially corrected data (Figure 4.4) shows how bad is an assumption of isotropic scattering. Consequently the calculation of the multiple scattering contribution to be detected events will be more difficult than that for vanadium, for which the ratio of successive scattering probabilities is approximately constant (equation (4.12)). In theory numerical integrations for orders of scatter higher than two can be performed, though it would be necessary to ensure that the results converge

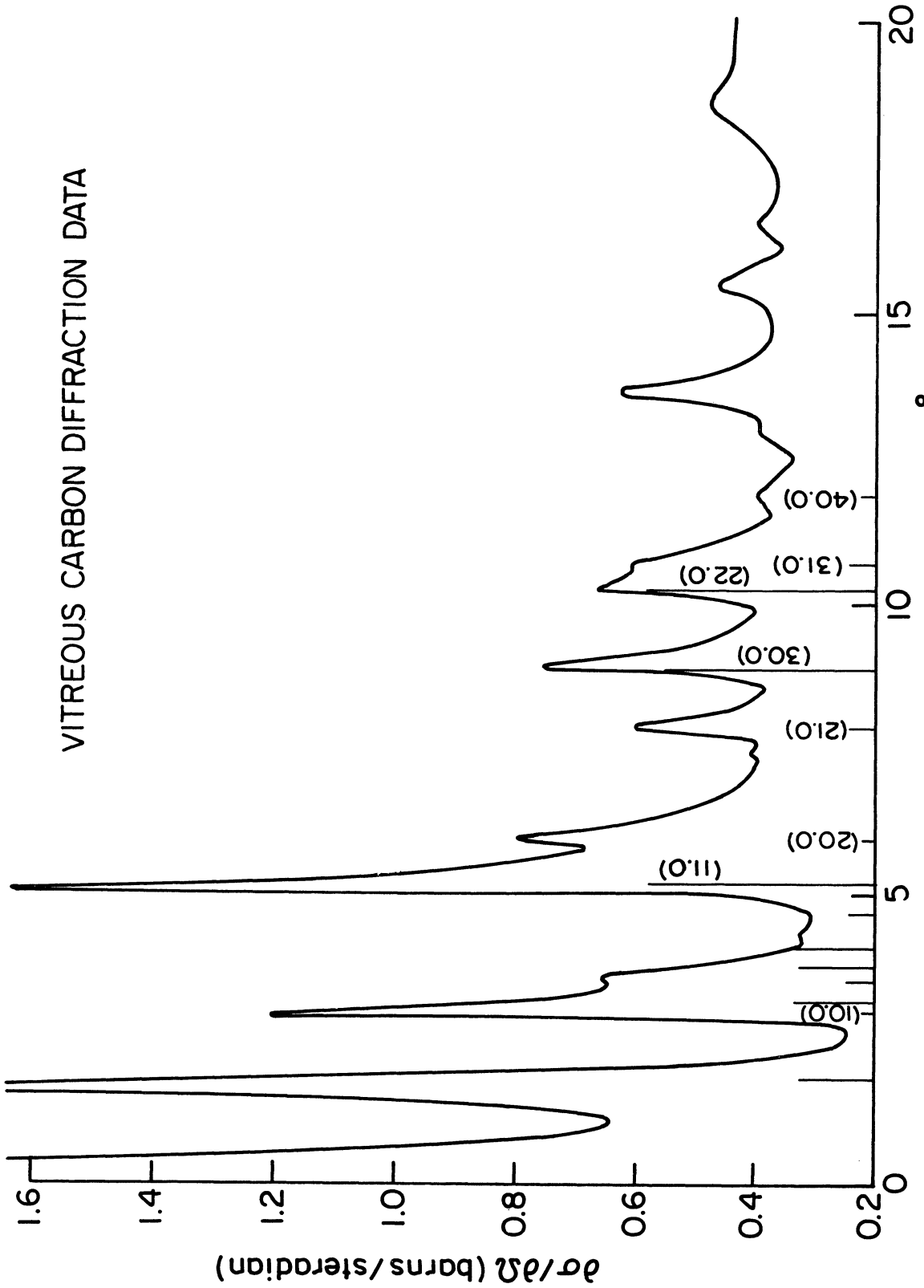

Figure 4.4. The partially corrected diffraction pattern of glassy carbon. The in-plane correlations for graphite are shown up to 12 $Å^{-1}$, and the out-of-plane correlations up to 5 $Å^{-1}$.

rapidly. In practice however, we perform a Monte Carlo calculation.

The procedure of the Monte Carlo simulation follows the work of Bischoff (1970) and Copley (1973). The program has been adapted for the time-of-flight diffractometer, in which we consider only elastically scattered neutrons. The reason for this is twofold. Although inelastic neutron scattering measurements have been performed on this sample by Carpenter (1973), values of $S(Q,\omega)$ are unknown for much of the Q-ω plane. Additionally the scattering events for carbon are predominantly elastic (section 3.6), and hence inelastic contributions are a very small perturbation upon a purely elastic model. Consequently the vanadium corrected data are a reasonable approximation to $S(Q)$ for the carbon. The Monte Carlo calculation is first described briefly, and then in more detail in the following section.

The simulation was performed by the program entitled MSCATD for Multiple Scattering for Diffraction. This program presently requires the writing of only one subroutine called TARGET which gives the particular geometry of the experiment as well as that of the sample. That is, it gives the beam profile and the detector positions relative to the target, in addition to the sample configuration. Various subroutines in lieu of TARGET have been written for the UMTOFND machine including UNICYL for a lone cylinder centrally located in the beam with its axis vertical, as in the present experiment, and UNISLAB for a slab material placed in the beam, as for the vanadium reference measurement. In

addition the program also calls upon a file containing the diffraction pattern from which the scattering probabilities are estimated.

The angular scattering distribution of neutrons is required for both the scoring of detected neutrons and for following the paths of the neutrons within the sample. Angles of scatter, Θ and ϕ, randomly selected from the cumulative distribution of scattering angles,

$$f(\Theta) = \frac{\int_0^{\Theta} S(Q) \sin \Theta' \, d\Theta'}{\int_0^{\pi} S(Q) \sin \Theta' \, d\Theta'} \qquad (4.34)$$

and

$$f'(\phi) = \frac{\phi}{2\pi} , \qquad (4.35)$$

since the scattering is independent of azimuthal scattering angle. The partially corrected differential cross section gives the best approximation to the angular scattering distribution. This will be valid provided that the variation of the correction factors with Q is not too large for a given scattering angle, since the normalization procedure for the partially corrected data assumes that the sample correction factor C_o is independent of Q. This model is certainly superior to one using a diffraction pattern derived from some other model independent of the data obtained from the sample, since it will tend to bias the result towards that of the model.

Since scattering events are exclusively of interest (only neutrons which have been scattered are measured in the real experiment while

absorbed and unscattered neutrons are undetected), scattering collisions are forced to occur in the computer simulation. This technique allows every neutron at every collision to contribute to the angular scattered intensity, and improves the convergence of the calculation. This is performed by assigning a statistical weight to the neutron at each collision points are then chosen at random from the cumulative distribution function for path lengths

$$F(L) = \frac{\int_o^L \exp(-g\sigma_T(k)x)\,dx}{\int_o^t \exp(-g\sigma_T(k)x)\,dx}, \qquad (4.36)$$

where t is the maximum distance from the last scattering point to the surface of the sample in the direction of scatter.

In practice the calculation proceeds one neutron energy at a time, with the scoring for all the detector angles, though in our measurements there are only two. Consequently values of the sample multiple scattering correction $C_M^S(Q)$ are determined for a large number of Q values for the two different scattering angles, with an increased density of points around the regions of Q for which there are large variations in the diffraction pattern. Judicious choice of neutron energies reduces computing time. A smooth curve of $C_M^S(Q)$ for each scattering angle is computed using spline functions. Hence values of $C_M^S(Q)$ may be determined by interpolation from the results of the Monte Carlo simulation, and values of $C_A^S(Q)$ by direct integration (Figures 4.5 and 4.6).

Values of the overall correction factor $C_o^S(Q)$ for the sample finite

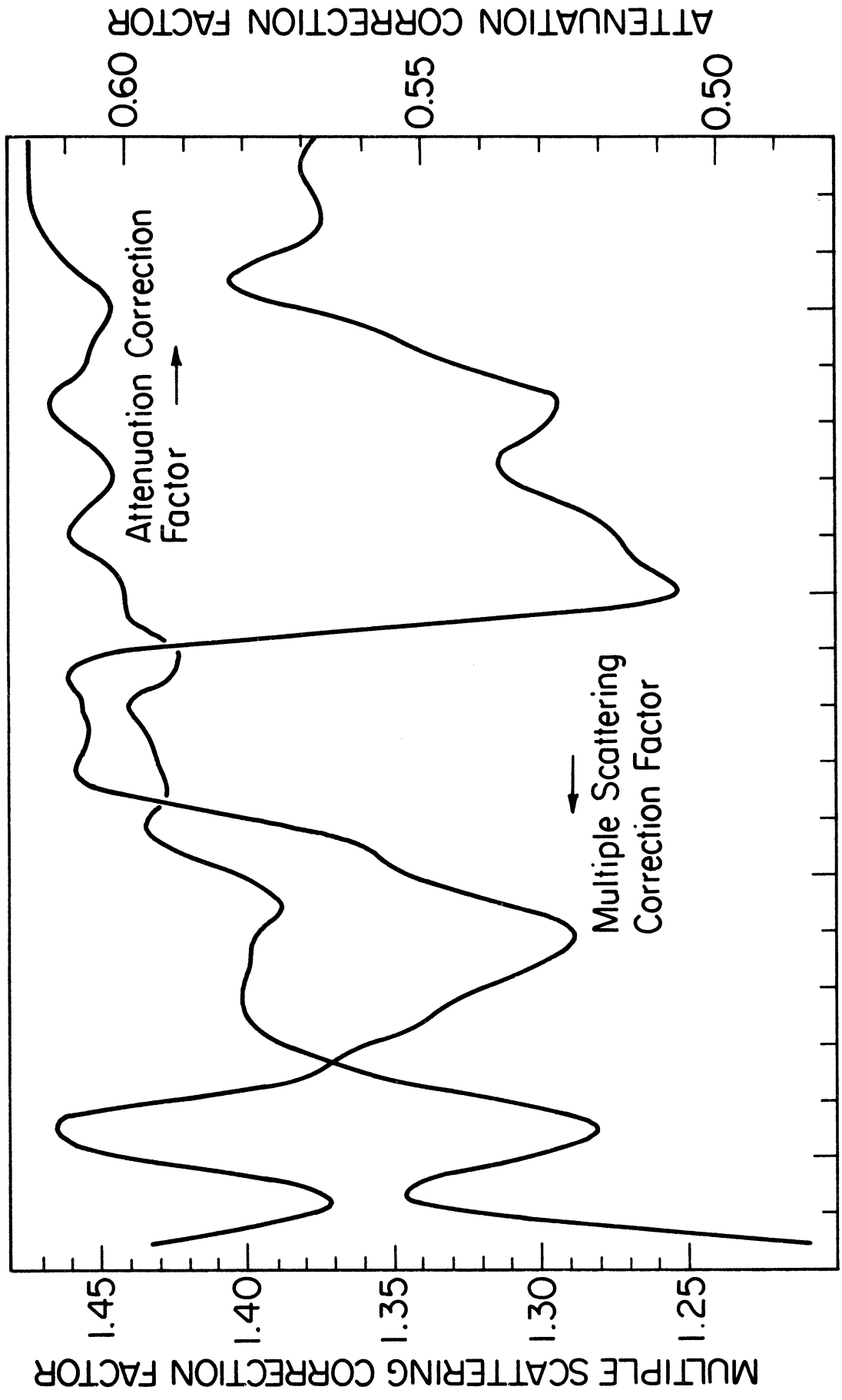

Figure 4.5. Multiple scattering and attenuation correction factors for the 20° scattering bank.

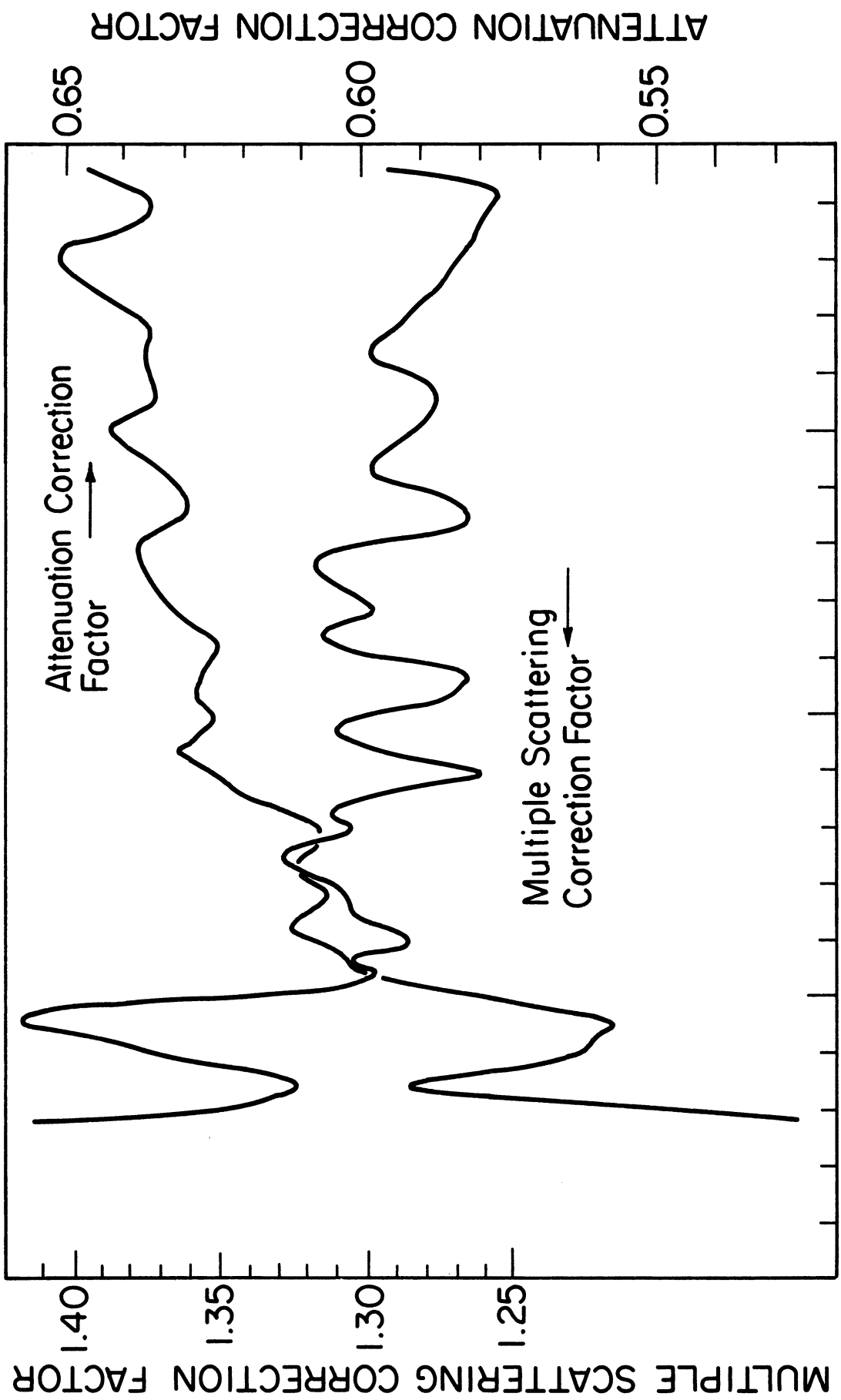

Figure 4.6. Multiple scattering and attenuation correction factors for the 90° scattering bank.

thickness as defined by equation (3.17) are used to adjust the data to yield a fully corrected diffraction pattern. This has been performed using the program CARCOR for Carbon Correction. It has been assumed that the ratio of the true multiple scattering correction factor and that computed by one iteration through the Monte Carlo simulation is relatively insensitive to Q. The overlap of the data sets is good, though small scaling adjustments had to be applied. Even in the overlap region between Q = 1, $Å^{-1}$ and 2 $Å^{-1}$ with data from two different diffractometers, the values of $\partial\sigma/\partial\Omega$ (Q) had remarkable agreement. The normalization procedure has already een outlined in section 4.4.

Due to the variation in resolution of the various segments of the data, the best resolution regions of the data were used throughout in deciding which data to accept. In fact no corrections for resolution have been made at this stage in our analysis, nor have attempts been made to account for the Placzek corrections which are due to the inelastic contributions. The resulting scattered intensity distribution is shown in Figure 4.7. The effect of multiple scattering is to decrease the peaks in the spectrum and to fill in the minima. By comparison with the partially corrected date in Figure 4.4, it can be seen that the application of the multiple scattering correction factor is such that the peaks are enhanced. The value of Q_{max} = 25 $Å^{-1}$ is sufficiently high that the diffracted intensity is slowly varying.

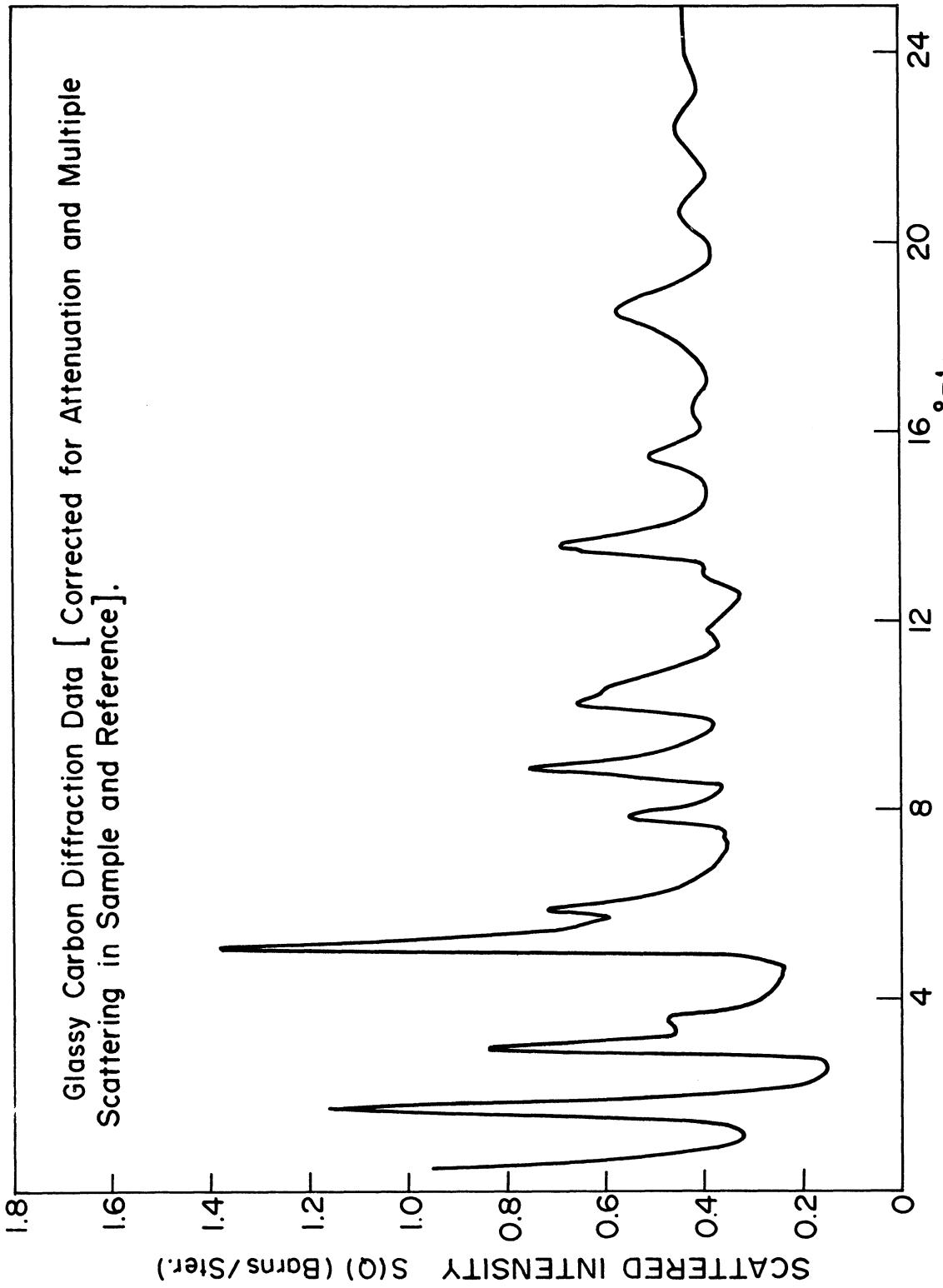

Figure 4.7. The neutron diffraction of Hucke glassy carbon.

4.6 MONTE CARLO SIMULATION

The purpose of these calculations is to make estimates of the overall correction factor which is defined by equation (3.18). The probability that a neutron is scattered into a detector direction as defined in section 4.2 is obtained from the 'score' accumulated by neutrons scattered into that detector direction. In fact many histories are traced in the simulation for neutrons of the same incident energy, and the eventual score is normalized to 'per incident neutron per unit area.' The method of averaging and estimating the variances of the parameters determined by the simulation are shown below. But first the algorithm for following a neutron's history is given.

Each neutron used in the calculation is given an initial weight W_o of unity, and an initial direction $\underline{\Omega}_1$ identical to the incident beam direction $\underline{\Omega}_o$. A point within the uniform incoming beam profile is picked at random; this defines the position $\underline{r}_o$ on the target surface, where the neutron beam direction $\underline{\Omega}_o$ intersects the target. The distance $t_o(\underline{r}_o,\underline{\Omega}_1)$ is computed that the neutron must travel from $\underline{r}_o$ to the edge of the target in the direction $\underline{\Omega}_1$. Similarly at each collision point within the target, a distance $t_n(\underline{r}_{n-1},\underline{\Omega}_n)$ is calculated for the effective thickness as seen by a neutron travelling to the edge of the target in the direction $\underline{\Omega}_n$, <u>after</u> the $(n-1)^{th}$ collission at $\underline{r}_{n-1}$, or <u>before</u> the n^{th} collision.

The effective thickness t_o of the target as seen by the incoming

beam in the $\underline{\Omega}_o$ direction is the value of t_1 averaged over the beam profile. The probability of scatter per unit atom scatters under ideal conditions into the direction $\underline{\Omega}_D$, that is, in the absence of finite target corrections, is

$$P_I(\underline{\Omega}_o,\underline{\Omega}_D) = t_o \frac{d\sigma}{d\Omega}(\underline{\Omega}_o \rightarrow \underline{\Omega}_D)\Delta\Omega_D \tag{4.37}$$

which is simply the evaluation of equation (4.1).

Let the scattering and total cross sections be Σ_s and Σ_T, respectively. Then after the $(n-1)^{th}$ scattering event, the escape probability of the neutron travelling in the direction $\underline{\Omega}_n$ is simply $\exp(-\Sigma_T t_n)$, and the collision probability $1 - \exp(-\Sigma_T t_n)$. Hence the scattering probability is $\Sigma_s/\Sigma_T(1 - \exp(-\Sigma_T t_n))$. The scattering event is forced to occur at a distance $L_n \leq t_n$ from $\underline{r}_{n-1}$ in the direction $\underline{\Omega}_n$ by selecting a path length from the cumulative distribution function, equation (4.36). This is performed by choosing a random number R, $(0 \leq R \leq 1)$ such that the distance L_n is chosen from the modified exponential distribution, i.e.,

$$\frac{R}{1} = \frac{1 - \exp(-\Sigma_T L_n)}{1 - \exp(-\Sigma_T t_n)} \quad . \tag{4.38}$$

The statistical weight of the neutron at the n^{th} scatter is then given by

$$W_n = \frac{\Sigma_s}{\Sigma_T}(1 - \exp(-\Sigma_T t_n))\, W_{n-1} \tag{4.39}$$

where W_{n-1} is the neutron weight at the previous scatter. The use of statistical weights takes into account the probability of absorption and escape of neutrons, and allows the consideration only of scattered neutrons. The "worth" of the neutron at the n^{th} scattering event is simply given by

$$W_n = \prod_{j=1}^{n} \left[\frac{\Sigma_s}{\Sigma_T} (1 - \exp(-\Sigma_T t_j)) \right] . \tag{4.40}$$

After the n^{th} scattering event, a score $S_n(\underline{\Omega}_D)$ is computed for each detector D in turn. The distance $L_D(\underline{r}_n, \underline{\Omega}_D)$ from the scattering point $\underline{r}_n$ to the edge of the target in the detector direction $\underline{\Omega}_D$ is found in order to compute a transmission probability. The scattering angle from the direction $\underline{\Omega}_n$ to $\underline{\Omega}_D$ (and hence the corresponding wave vector change) is found in order to compute the differential scattering probability, $\Delta\Omega_D/\sigma \cdot \partial\sigma/\partial\Omega(\underline{\Omega}_n \rightarrow \underline{\Omega}_D)$, from the diffraction pattern. Then the score for the k^{th} neutron and the n^{th} scatter into the Θ scattering bank is

$$S_n^k(\Theta) = \sum_D U_D W_n \exp(-\Sigma_T L_D) \frac{\Delta\Omega_D}{\sigma} \frac{\partial\sigma}{\partial\Omega} (\underline{\Omega}_n \rightarrow \underline{\Omega}_D), \tag{4.41}$$

where the summation extends over all the detectors each with a relative statistical weight U_D in the bank of scattering angle Θ.

We now need to determine a new direction $\underline{\Omega}_{n+1}$. The cosine μ_n of the angle at the n^{th} scatter (viz., $\underline{\Omega}_n \cdot \underline{\Omega}_{n+1}$) is selected from the cumulative distribution of scattering angles, equation (4.34), which

may be written

$$f(\mu_n) = \frac{\int_{-1}^{\mu_n} \frac{\partial\sigma}{\partial\Omega} (\sqrt{2}\, k(1-\mu)^{1/2})\, d\mu}{\int_{-1}^{+1} \frac{\partial\sigma}{\partial\Omega} (\sqrt{2}\, k(1-\mu)^{1/2})\, d\mu} \tag{4.42}$$

This is performed by choosing a random number $R(0 \leq R \leq 1)$ to give momentum transfer Q by integration of the partially corrected diffraction pattern, i.e.,

$$\frac{R}{1} = \frac{\int_0^{Q_n} S(Q)\, QdQ}{\int_0^{2k} S(Q)\, QdQ} = \frac{2\pi}{\sigma_s(k)k^2} \int_0^{Q_n} \frac{\partial\sigma}{\partial\Omega}(Q)\, QdQ, \tag{4.43}$$

where

$$Q_n = 2k \sin \theta_n/2 = \sqrt{2}\, k\, (1-\mu_n)^{1/2}. \tag{4.44}$$

Hence, after selecting a random azimuthal angle (equation 4.35), a new direction $\underline{\Omega}_{n+1}$ is found.

This process is repeated until the weight W_n falls below a certain cut-off weight W_c, at which point a game of "Russian roulette" is played. There is a 50% probability that the neutron is thrown away and a new neutron history started, and a 50% probability that the neutron weight is increased by a factor of two and undergoes a further scatter. This procedure has the attraction of concentrating the low weighted events in a relatively small number of neutrons. Provided that the cut-off weight is sufficiently small, this does not introduce any biasing of the result. It is simply a means of ending of the neutron's

"lifetime" in the target, since it is forced always to undergo a scatter without escape.

The purpose of the Monte Carlo simulation is to provide values of $P_1(\theta)$ and $P_M(\theta)$, the probabilities of single and multiple scattering into a detector bank at angle θ, which are given by the average values of the scores $S_1(\theta)$ and $S_M(\theta)$ where

$$S_1(\theta) = \sum_{D(\theta)} U_D \frac{\Sigma_s}{\Sigma_r}(1 - \exp(-\Sigma_T t_1)) \frac{\Delta\Omega_D}{\sigma} \frac{\partial\sigma}{\partial\Omega}(\underline{\Omega}_1 \rightarrow \underline{\Omega}_D) \exp(-\Sigma_T L_D(\underline{r}_1, \underline{\Omega}_D)) \tag{4.45}$$

and

$$S_M(\theta) = \sum_{n=2}^{\infty} S_N(\theta), \tag{4.46}$$

where

$$S_N(\theta) = \sum_{D(\theta)} U_D \prod_{n=1}^{N} \left[\frac{\Sigma_s}{\Sigma_T} (1 - \exp(-\Sigma_T t_n)) \right] \frac{\Delta\Omega_D}{\sigma} \frac{\partial\sigma}{\partial\Omega} (\underline{\Omega}_N \rightarrow \underline{\Omega}_D) \exp(-\Sigma_T L_D(\underline{r}_N, \underline{\Omega}_D)). \tag{4.47}$$

It is interesting to compute the score $S_I(\theta)$ in the 'ideal' scattering experiment where there is no beam attenuation. For thin samples, the probability of an interaction is $\Sigma_s t_o$. Then

$$S_I(\theta) = \sum_{D(\theta)} U_D \Sigma_s t_o \frac{\Delta\Omega_o}{\sigma} \frac{\partial\sigma}{\partial\Omega} (\underline{\Omega}_o \rightarrow \underline{\Omega}_D). \tag{4.48}$$

With the substitution of

$$\Sigma_{s} t_{o} = \eta\sigma \,, \tag{4.49}$$

where η is the number of scattering per unit area, and after the summation over all detectors in a scattering bank, equation (4.48) becomes

$$P_{I}(\theta) = S_{I}(\theta) = \eta \frac{\partial\sigma}{\partial\Omega}(Q)\, \Delta\Omega_{D} \tag{4.50}$$

which is the same as equation (3.15).

The individual scores $S_{n}^{k}(\theta)$ are selected independently and randomly from an unknown probability distribution with a mean $P_{n}(\theta)$ and variance σ_{n}^{2}. Summations of the scores $S_{n}^{k}(\theta)$ over the total number K of neutron histories will yield average values of the scores

$$S_{n}(\theta) = \frac{1}{K} \sum_{k=1}^{K} S_{n}^{k}(\theta) \tag{4.51}$$

The sample mean $S_{n}(\theta)$ is the simulation estimate of $P_{n}(\theta)$, and provided K is large enough, $S_{n}(\theta) \rightarrow P_{n}(\theta)$. That is

$$P_{1}(\theta) = \lim_{K\to\infty} \frac{1}{K} \sum_{k=1}^{K} S_{1}^{k}(\theta) \tag{4.52}$$

$$P_{M}(\theta) = \lim_{K\to\infty} \frac{1}{K} \sum_{k=1}^{K} \sum_{n=2}^{\infty} S_{n}^{k}(\theta) \tag{4.53}$$

Since the summation is performed for neutrons with the same energy or wave number k, then these probabilities are a function of θ and k, which by equation (2.5) are related to the momentum transfer Q. Hence from

these values is found the multiple scattering correction factor

$$C_M^S(Q) = 1 + \frac{P_M}{P_1}(\theta,k) \tag{4.54}$$

An estimate of the variance σ_n^2 of the distribution of simulated scores $S_n(\theta)$ is given by

$$\sigma_{nK}^2 = \frac{1}{K-1}\left[\sum_{k=1}^{K}(S_n^k(\theta) - S_n(\theta))^2\right] \tag{4.55}$$

Then σ_{nK}^2/K is an estimate of the variance σ_{nP}^2 of the probability distribution $P_n(\theta)$ determined by the simulation.

In order to determine confidence limits to the estimated mean $S_n(\theta)$, the independent samples are divided into K_i groups of K_j histories each. The average scores for the single and multiple scatterings for the i^{th} group are

$$S_1^i(\theta) = \frac{1}{K_j}\sum_{k=1}^{K_j} S_1^k(\theta), \tag{4.56}$$

$$S_M^i(\theta) = \frac{1}{K_j}\sum_{k=1}^{K_j}\sum_{n=2}^{\infty} S_n^k(\theta) . \tag{4.57}$$

Each group i is regarded as an independent sample of the probability distribution. If K_j is large enough (~100), the distribution of these samples becomes approximately normal (gaussian) by the central limit theorem. Then for K_i groups, the average scores for single and multiple scatterings are

$$S_1(\theta) = \frac{1}{K_i}\sum_{i=1}^{K_i} S_1^i(\theta) \tag{4.58}$$

and

$$S_M(\theta) = \frac{1}{K_i} \sum_{i=1}^{K_i} S_M^i(\theta). \tag{4.59}$$

The variance of the distribution of group-averaged score $S_n^i(\theta)$ (the distributions being gaussian) is estimated by

$$\sigma_{nK_i}^2 = \frac{1}{K_i - 1}\left(\sum_{i=1}^{k_i} (S_n^i(\theta) - S_n(\theta))^2\right). \tag{4.60}$$

Then the measure of the deviation of the sample mean score $S_n(\theta)$ from the probabiltiy distribution mean $P_n(\theta)$ is the standard deviation σ_n of the group-averages scores

$$\sigma_n = \frac{1}{\sqrt{K_i}} \sigma_{nK_i}. \tag{4.61}$$

In order to apply a multiple scattering correction to the data, it would be useful to know how various functions involving P_1, P_M and $P_T (= P_1 + P_M)$ vary as a function of wave vector transfer Q, so that interpolation may be made on a function that is relatively smooth over the range of Q. To exhibit these variations in an easy manner, it is necessary to make some crude approximations. Assume that on the average all the scatters occur at a distance $t_o/2$ from the surface of the target, where t_o is effective target thickness as seen by the incoming beam. Neglect differences in the scores for detectors at different azimuthal angles. Then equations (4.45) through (4.47) may be averaged over a large number of neutrons to yield approximate

scattering probabilities given by

$$P_1(\theta) \simeq \frac{\Sigma_s}{\Sigma_T}(1 - \exp(-\Sigma_T t_o)) \frac{\Delta\Omega_D}{\sigma} \frac{\partial\sigma}{\partial\Omega}(\underline{\Omega}_1 \rightarrow \underline{\Omega}_D) \exp(-\Sigma_T t_o/2) \tag{4.62}$$

and

$$P_M(\theta) = \sum_{N=2}^{\infty} P_N(\theta), \tag{4.63}$$

where

$$P_N(\theta) \simeq \frac{\Sigma_s}{\Sigma_T}(1 - \exp(-\Sigma_T t_o)) \frac{\Delta\Omega_D}{\sigma} \frac{\partial\sigma}{\partial\Omega}(\underline{\Omega}_N \rightarrow \underline{\Omega}_D) \prod_{n=2}^{N} \left(\frac{\Sigma_s}{\Sigma_T}(1 - \exp(-\Sigma_T t_o/2)) \right) \exp(-\Sigma_T t_o/2) \tag{4.64}$$

These crude approximations may be reasonable for the case of diffraction from a slab of vanadium. Since the scattering is isotropic, the value of $(\Delta\Omega_D/\sigma)\,(\partial\sigma/\partial\Omega(\underline{\Omega}_N \rightarrow \underline{\Omega}_D))$ is a constant for all orders N of scatter. We shall call this probability p_D, for convenience. Then equations (4.62) and (4.63) reduce to

$$P_1(\theta) \simeq \frac{\Sigma_s}{\Sigma_T}(1-\exp(-\Sigma_T t_o))\, p_D \exp(-\Sigma_T t_o/2) \tag{4.65}$$

and

$$P_M(\theta) \simeq \frac{\Sigma_s}{\Sigma_T}(1-\exp(-\Sigma_T t_o))\, p_D \exp(-\Sigma_T t_o/2) \frac{\Sigma_s/\Sigma_T(1 - \exp(-\Sigma_T t_o/2))}{1 - \frac{\Sigma_s}{\Sigma_T}(1 - \exp(-\Sigma_T t_o/2))}. \tag{4.66}$$

The total probability of scatter $P_T(\theta)$ is given by

$$P_T(\theta) \simeq \frac{\Sigma_s}{\Sigma_T} \frac{(1 - \exp(-\Sigma_T t_o))p_D \exp(-\Sigma_T t_o/2)}{1 - \Sigma_s/\Sigma_T(1 - \exp(-\Sigma_T t_o/2))} . \quad (4.67)$$

It is found that the factors P_1/P_T and P_M/P_T change the least with respect to changes in Σ_T. Consequently it is believed that in general that these functions are the most useful for interpolation purposes when computing the multiple scattering corrections.

These crude approximations may not be reasonable for the case of diffraction from glassy carbon. Since forward angle scattering is predominant, the most probable scattering direction for all orders of scatter is very close to the incident direction $\underline{\Omega}_o$. Hence the probability $(\partial\sigma/\partial\Omega(\underline{\Omega}_N \rightarrow \underline{\Omega}_D))(\Delta\Omega_D/\sigma)$ of scattering into the detector direction is approximately a constant for all N. We shall call this probability p_D. On the other hand, the ratio of statistical weights before successive orders of scatter is certainly not constant, but this approximation is retained so that a simple calculation may be performed.

Since the absorption of neutrons is negligible for carbon, the scattering and total cross sections are approximately equal; so that $\Sigma_s/\Sigma_T \simeq 1$. Then equations (4 62) and (4.63) reduce to

$$P_1(\theta) \simeq (1 - \exp(-\Sigma_T t_o))p_D \exp(-\Sigma_T t_o/2) \quad (4.68)$$

and

$$P_M(\theta) \simeq (1 - \exp(-\Sigma_T t_o))p_D(1 - \exp(-\Sigma_T t_o/2)). \quad (4.69)$$

The total probability of scatter $P_T(\theta)$ is given by

$$P_T(\theta) = P_1(\theta) + P_M(\theta) = (1 - \exp(-\Sigma_T t_o))p_D \qquad (4.70)$$

It is found that the factors $P_1/P_T(\simeq e^{-\Sigma_T t_o/2})$ and $P_M/P_T(\simeq 1 - e^{-\Sigma_T t_o/2})$ change the least with respect to changes in Σ_T, which is a function of Q. Hence interpolation for multiple scattering purposes is made between values of the inverse of multiple scattering correction factor C_M; $(1 + P_M/P_1)^{-1}$ or (P_1/P_T). Values of the ratios have been smoothed using spline functions and are shown in Figure 4.8.

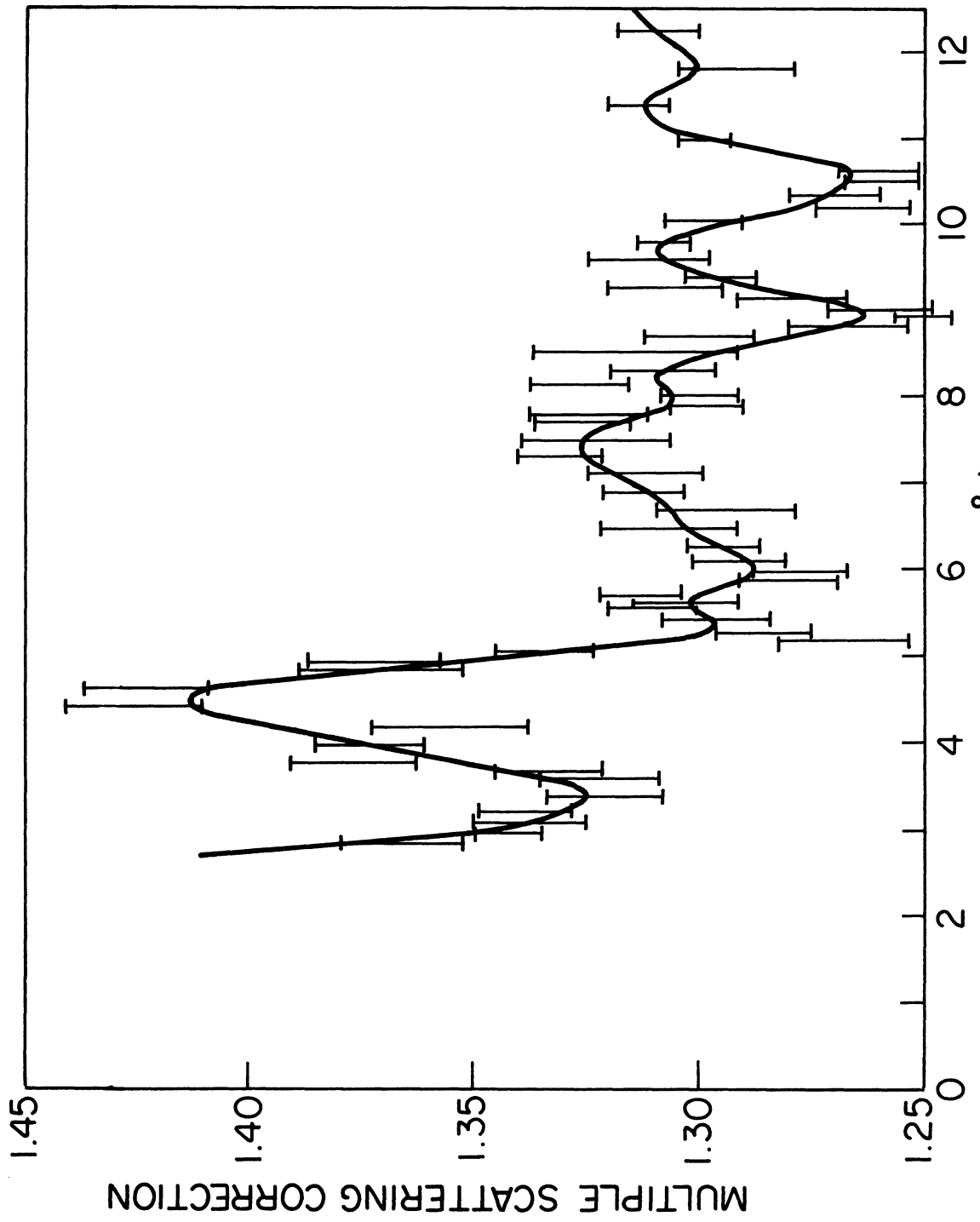

Figure 4.8. The smoothing of the multiple scattering correction factor.

4.7 INELASTIC SCATTERING CONTRIBUTIONS

In the analysis of the data, we have neglected contributions due to inelastic scattering, the cross-section for which is small, and have assumed that the total diffraction pattern may be treated as due to elastic scattering only; i.e., the static approximation has been invoked. If we consider the contributions from inelastic scattering then the count rate given by equation (3.2) becomes

$$C(\theta,t) = \int \phi(k_o)\, Nb^2 \frac{k}{k_o}\, S(\underline{Q},\omega)\, \Delta\Omega_D \eta(k)\, \delta\left(t - \left(\frac{L_o}{v_o} + \frac{L}{v}\right)\right) d\omega dk, \tag{4.71}$$

where $\underline{Q}$, k_o, k, ω, θ are related by the energy and momentun conservation equations in section 2.1. The computation of this integral is difficult; but if we neglect the wave number dependence of the neutron spectrum, $\phi(k_o)$, and assume that the detectors have an efficiency, $\eta(k)$, inversely proportional to k, then the static approximation is the result of integrating $S(\underline{Q},\omega)$ along a line of constant Q in Q-ω space.

Carpenter and Sutton (1972) have shown that the constant Q integration path in time-of-flight diffractometry is best approximated by equal flight paths. Typical integration paths for the UMTOFND machine are shown in Figure 4.9, where the flight paths are given by L_o = 2.37 m and L = 2.47 m. It can be seen that at the 90° bank, the static approximation is very good at high values of momentum transfer Q. It becomes less good at lower values of Q, though for a given Q the

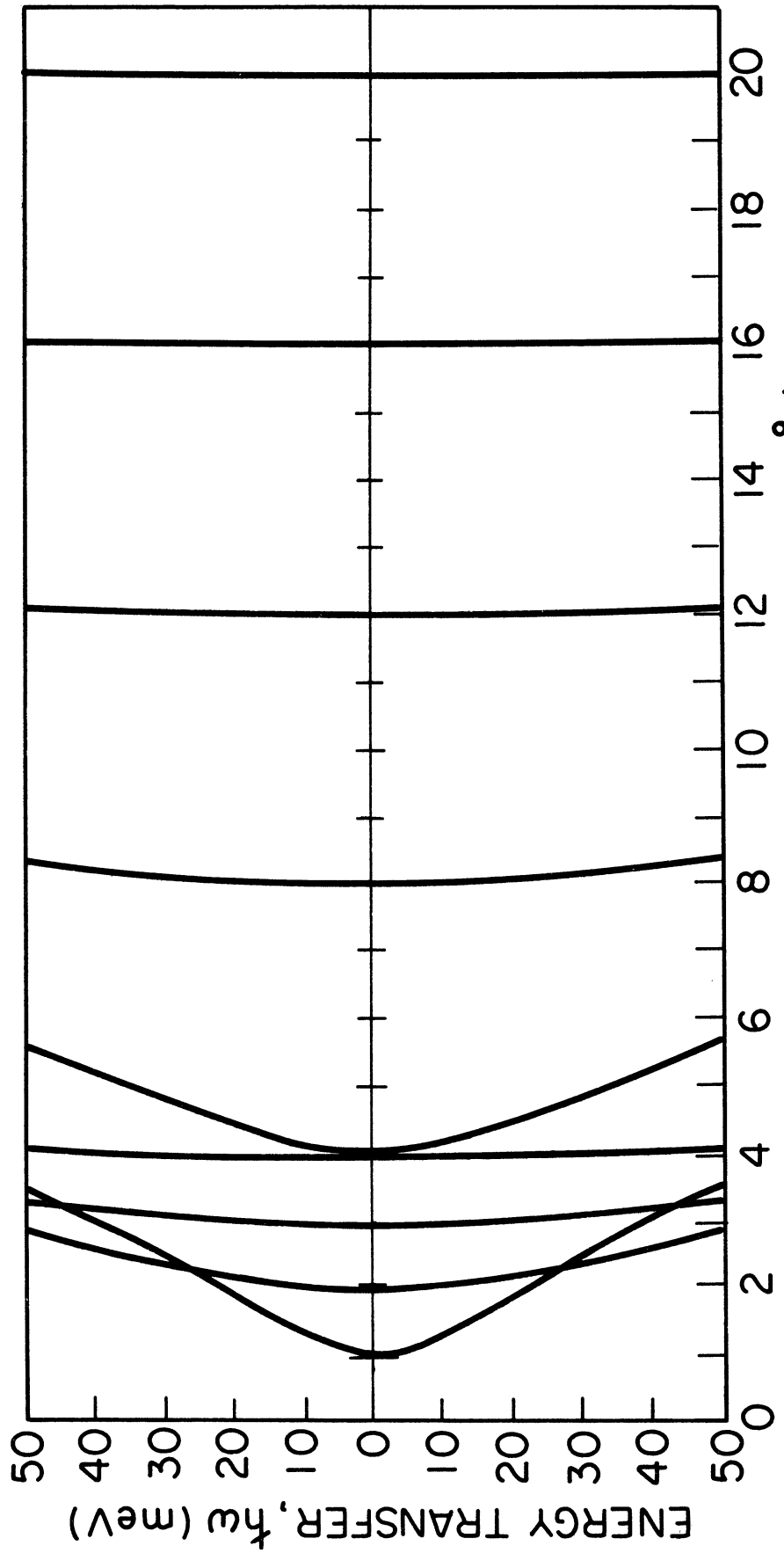

Figure 4.9. Typical integration paths in Q-ω space for the University of Michigan Time-of-Flight Neutron Diffractometer.

smaller angle provide a closer approach to the constant - Q condition, since the neutron wave number is higher (equation (2.5)). However within the range of Q values for the 20° scattering angle, the Q-ω integration paths are not as good as the 90° scattering bank's highest Q data. Fortunately most of the scattering is elastic, and the integration paths at $\omega = 0$ are a very good approximation to constant Q for all values of Q and θ.

Due to the relatively long scattered flight path for equal-path time-of-flight diffractometry, the counting rates are poor. Tomiyoshi et al. (1973) have shown that the counting rates may be improved without appreciable deterioration of the constant Q integration by using relatively short scattered flight paths. This is true for small scattering angles with low wavelength neutrons that are available from pulsed neutron sources, (Sinclair et al., 1973).

Deviations from the static approximation are accounted by applying Placzek corrections (Placzek, 1952; Wick, 1954) to the data, which involve energy moments of the scattering law $S(Q,\omega)$ and in consequence can be calculated only approximately. These are presumably minimized in measurements using the equal flight path configuration. This has been shown not to be the case for the calculable first moment corrections (Powles, 1973), since the integration is not only characterized by a path in Q-ω space, but is weighted by the neutron spectrum $\phi(k_o)$, and the detector efficiency $\eta(k)$. Consequently it may be that the equal

flight path arrangement is not the best.

The static approximation distortions in neutron time-of-flight diffractometry have been discussed in detail by Sinclair and Wright (1973). They show that the most dominant term in the Placzek corrections to the scattered intensity is decreased by shorter scattered flight paths. Consequently they conclude that the increased Placzek corrections required for the equal flight path arrangement may offset the improvement of having an integration path closely aligned to the static approximation. However in instances where independent detailed inelastic scattering measurements have been integrated to provide the exact structure factor, agreement within 2% statistical error has been found with measurement taken on UMTOFND (Carpenter, et al., 1973).

No Placzek corrections have therefore been applied to the glassy carbon data, though it is recognized that they are appropriate. To be able to perform these corrections accurately, it would be necessary to know the wave number dependence of the neutron spectrum and the detector efficiency. Additionally, Carpenter (1973) has measured the inelastic scattering from the same sample of carbon. The scattering law $S(Q,\omega)$ for frequencies $.6 < \omega$ 50 rad/ps, and wave vector transfers $1.3 < Q < 2.8$ Å^{-1} were examined. $S(Q,\omega)$ has a prominent elastically scattered component (Figure 4.10), which shows that the diffraction results will not be modified greatly by the application of Placzek corrections, though these adjustments will be greater at higher values of momentum transfer.

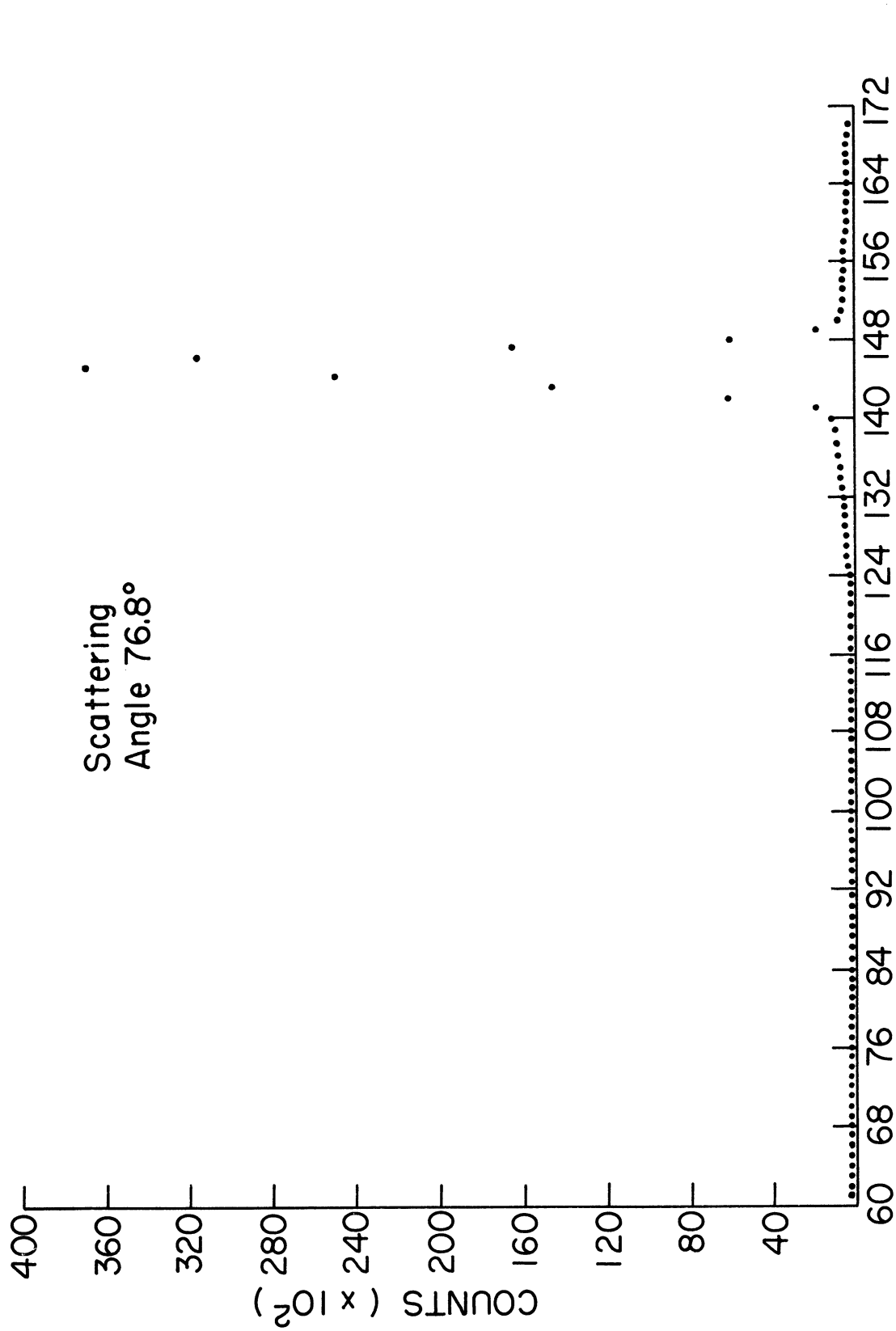

Figure 4.10. Typical data taken on the ANL time-of-flight spectrometer for a scattering angle.

4.8 ANALYSIS OF DIFFRACTION PEAKS

It is conventional in the characterization of carbons to describe a 'degree of graphitization' which is found by analysis of the diffraction peaks. The work of Short and Walker (1961) discusses the various formulae used in computing crystallite sizes from the line shapes. The first diffraction peak which is centered about $Q \sim 1.8$ $Å^{-1}$ and is analogous to the (00.2) peak in graphite (see Appendix A.2) provides values for the average plane spacing, d_c, and the mean crystallite height, L_c. Additionally the second diffraction peak which is centered about $Q \sim 3.0$ $Å^{-1}$ provides a value for the mean crystallite width L_a. The crystallite size dimensions refer to a right cylinder of diameter L_a and height L_c, and are introduced as a measure of the broadening of the appropriate X-ray diffraction peaks.

The crystallographic direction of the dimension L is perpendicular to the planes whose reflections are studied, and the relationship of L to the true mean crystallite dimension depends upon the distribution of the crystallite sizes. Scherrer (1918) has given the relationship between the crystallite dimension L and a measure of the broadening ΔQ of the peak as

$$L = K \frac{2\pi}{\Delta Q} \qquad (4.72)$$

where K is of the order of unity and is called the Scherrer constant. It has various numerical values depending on the shape of the crystals,

the indices of the reflecting planes, the precise definition of the crystallite dimensions and whether simple or integral line breadths are used. Though it is not clear what value of K should be used, it is relatively unimportant for these line broadening parameters should not be interpreted too literally since they apply to highly crystalline materials, and no allowance has been made for strain in the material (Ergun, 1973), or a possible distribution of layer spacings. However, they do provide a means of comparing various carbons. Several methods for extracting crystallite size parameters from line shapes are examined below.

The first diffraction peak is shown in Figure 4.11. The peak located at $Q = 1.80$ Å^{-1} provides a c-direction plane spacing $d_c = 2\pi/Q = 3.49$ Å. After base value subtraction, the full widths at half maximum and at three-quarters maximum are found to be 0.325 Å^{-1} and 0.17 Å^{-1}, respectively. Using $L_c = 1.78\ 2\pi/\Delta Q_{1/2}$ yields a value of 34.4 Å; whereas using $L_c = 1.02\ 2\pi/\Delta Q_{3/4}$ gives a value of 37.7 Å. An integral line width is that of a rectangular profile which has the same maximum and integral values of the observed line, using the formula

$$I_{max}\ \Delta Q = \int I(Q)\ dQ. \qquad (4.73)$$

This yields a value of $\Delta Q = 0.3716$ Å^{-1}, and using $L_c = 2\ 2\pi/\Delta Q$ gives a value of 33.8 Å. Hucke's analysis (1972) of wide angle X-ray diffraction using the full-width at three-quarters maximum formula after the subtraction of the base value gives a value of $L_c = 27.6$ Å and a spacing d_c of 3.57 Å. He notes that a lower value of d_c would be obtained if a

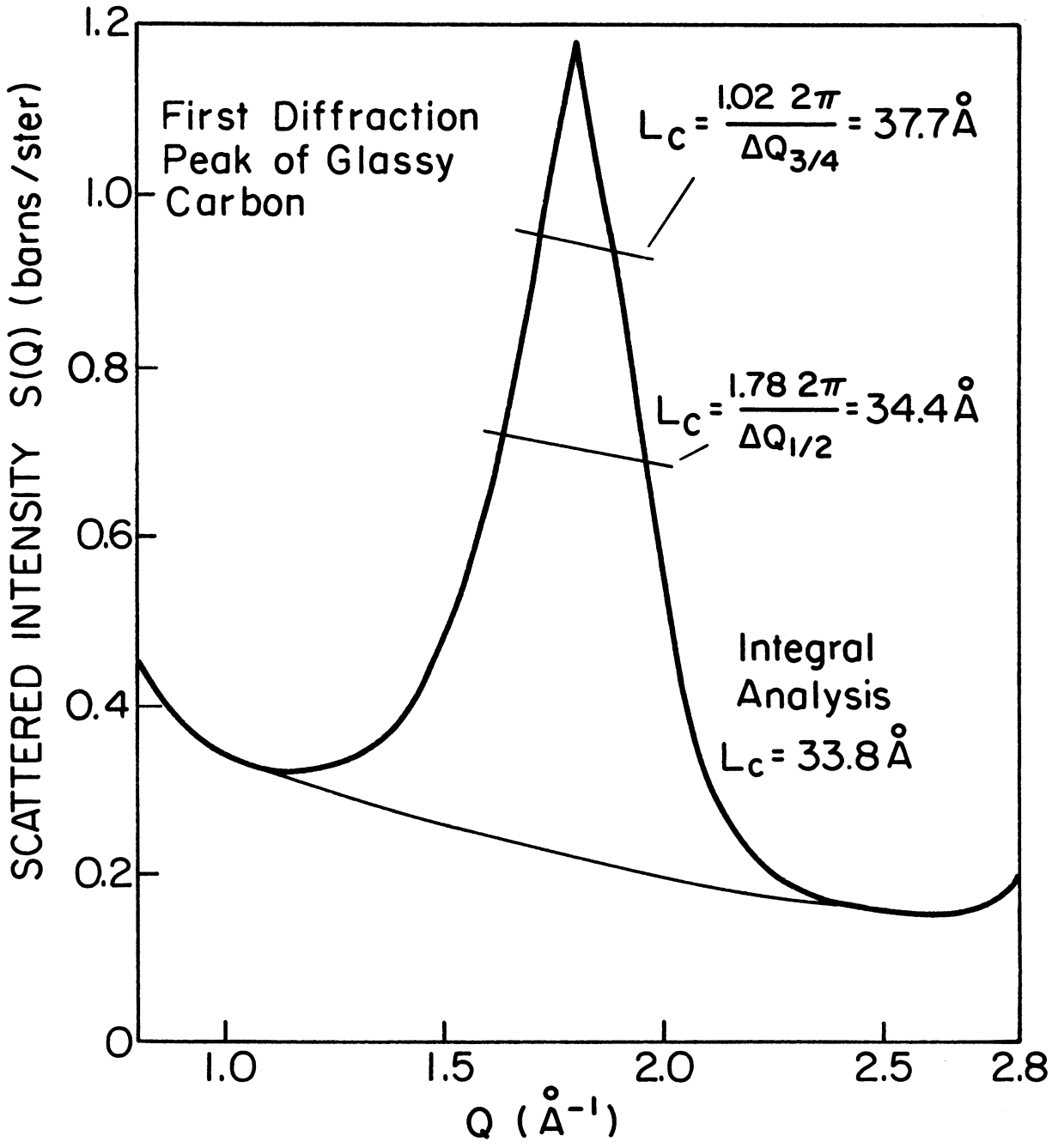

Figure 4.11. Analysis of the first diffraction peak of glassy carbon.

more rigorous analysis were employed.

If we use a more elaborate approach to the determination of the line shape of the first diffraction peak in the neutron data, it is found that the peak can be fitted very satisfactorily over a range $1.4 < Q < 2.2$ Å^{-1} by a Lorentzian. The peak is fitted to a function of the form

$$I(Q) = B_1 + \frac{B_2}{Q^2[(Q - Q_o)^2 + \Gamma^2]} \qquad (4.74)$$

with $Q_o = 1.816$ Å^{-1} and $\Gamma = 0.1793$ Å^{-1}. This gives a c-direction spacing of $d_c = 2\pi/Q_o = 3.46$ Å. The parameter Γ gives a measure of the crystallite height, L_c. The widths are approximately given by $\Delta Q_{1/2} = 2\Gamma$, and $\Delta Q_{3/4} = 2/\sqrt{3}\ \Gamma$. Use of the formulae, $L_c = 1.78\ 2\pi/\Delta Q_{1/2}$, and $L_c = 1.02\ 2\pi\ \Delta Q_{3/4}$ as above produce values of $L_c = 31.19$ Å and 30.96 Å, respectively. In addition the integral yields a value of $\Delta Q = 0.4485$ Å^{-1} which gives a value of $L_c = 28.0$ Å. Again it should be emphasized that these are only approximate values and give an idea of the range of ordering of planes.

The second diffraction peak is shown in Figure 4.12. It is analogous to the (10.0) and (10.1) peaks in graphite at $Q = 2.95$ and 3.14 Å^{-1}, respectively. The effect of peaks analogous to the (10.2) and (00.4) peaks in graphite at $Q = 3.49$ and 3.75 Å^{-1}, respectively, can be seen. A sloping base value yields values of $\Delta Q_{1/2} = 0.23$ Å^{-1} and $\Delta Q_{3/4} = 0.13$ Å^{-1}. Using the formulae, $L_a = 1.78\ 2\pi/\Delta Q_{1/2}$ and

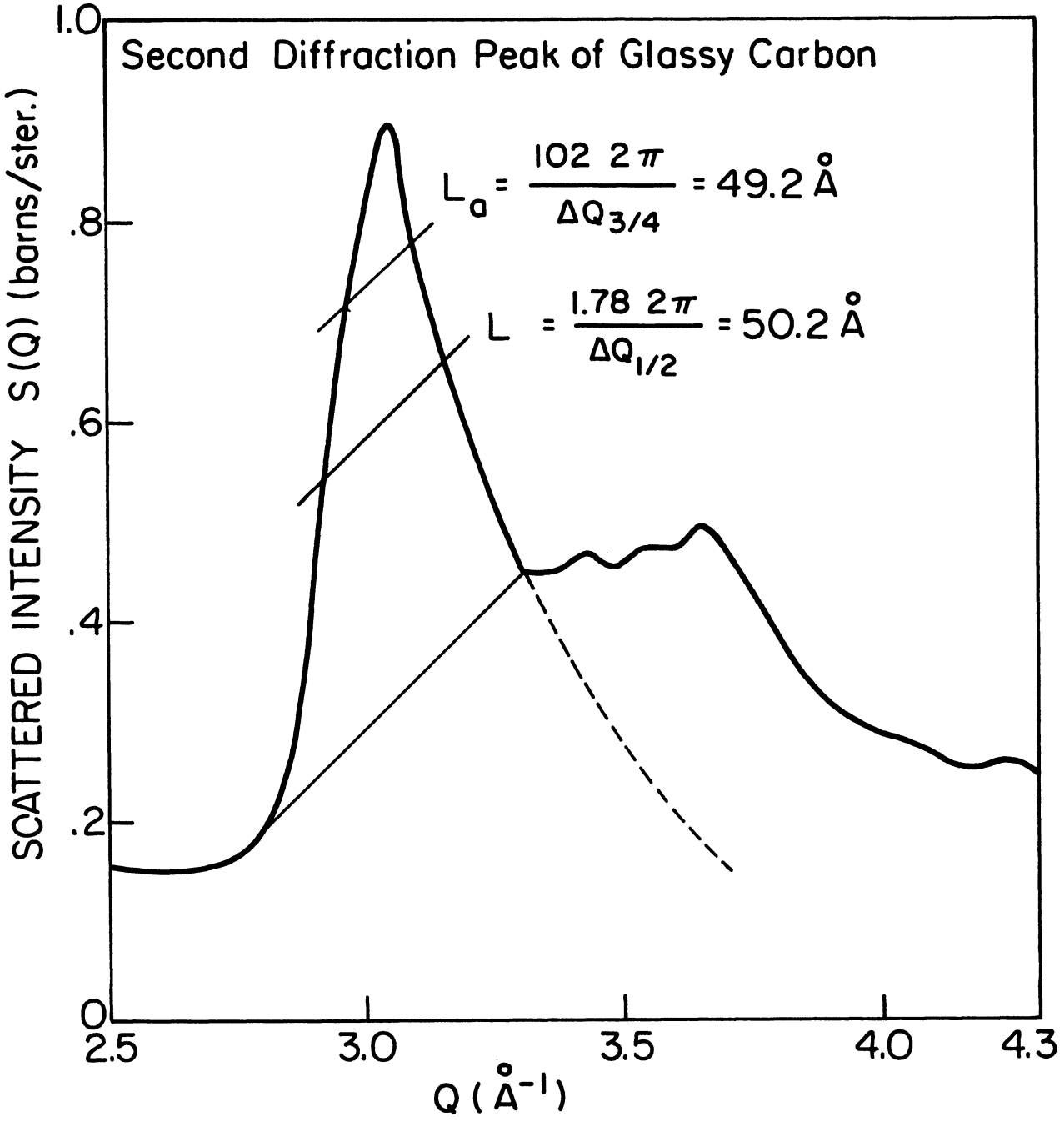

Figure 4.12. Analysis of the second diffraction peak of glassy carbon.

$L_a = 102\ 2\pi/\Delta Q_{3/4}$ as before, values of L_a are obtained as 50.2 $Å^{-1}$ and 49.2 $Å^{-1}$, respectively. The peak at $Q = 3.04\ Å^{-1}$ gives a value for $d_{10} = 2\pi/Q = 2.067$ Å. These values should be compared with the wide angle X-ray diffraction analysis (Hucke, 1972) which gave $L_a = 56.0$ Å and a spacing $d_{10} = 2.10$ Å.

It can also be seen from the diffraction pattern that there are numerous peaks which suggests that the carbon is not truly amorphous; that is; there is some ordering in the system. However, it is certainly not crystalline, as can be verified by comparison of the peak width with those in any of the calibration runs of the machine using crystalline samples. However, the analogy of the first two diffraction peaks with those found in graphite suggests that a closer examination of this analogy will be required. It should be pointed out that the first diffraction peak in cubic diamond is expected at $Q \sim 3.05\ Å^{-1}$ which is where the second peak in glassy carbon diffraction is found. The presence of some tetrahedral bonding might be expected to be felt because of the presence of this diffraction peak. However, no useful comparison of the higher-Q diffraction peaks with known diamond crystal reciprocal lattice vectors has been found.

4.9 SMALL Q SCATTERING

The small-Q diffraction pattern of this particular glassy carbon was obtained by Carpenter (1973) at the same time as the inelastic scattering data. The main features of the experiment will be presented here since further analysis has been made of the small-Q diffraction pattern. The measurements were performed on the Thermal Neutron Time-of Flight Spectrometer, TNTOFS (Kleb et al., 1973) at the Argonne National Laboratory. The incident monochromatic beam of neutrons have a wavelength λ_o = 4.06 Å, which was obtained by scattering from the (00.2) planes of pyrolytic graphite. By using a beryllium filter at liquid nitrogen temperature (77°K), which has a sharp drop in the scattering cross section for wavelengths greater than 3.96 Å, high order contamination (e.g., $\lambda_o/2$ = 2.03 Å) is eliminated.

The sample used in this experiment was a section cut from the same cylinder used in the large Q diffraction experiment, in the form of four discs, each 2.0 cm in diameter, and 0.267 gm/cm^2 (0.291) cm) thick. The total cross section as a function of neutron wave number (Figure 4.3) was obtained using the corrected data from TNTOFS and UMTOFND. For 4.06 Å wavelength neutrons (k_o = 1.55 Å^{-1}), the cross section is 10.3 barns/atom. The density of the carbon is 0.923 gm cc^{-1}, or 0.04628 atoms (barn-cm)$^{-1}$. Hence the probability of scatter of neutrons from this sample is 13%, and much of this is through small angles.

The elastic scattering was determined at angles between 2.40° and and 115.2°. Hence data were obtained for Q values between 0.065 Å^{-1}

and 2.613 $Å^{-1}$, to supplement the extended Q diffraction results from the UMTOFND machine. The detectors were calibrated against a vanadium standard scatterer, for which multiple scattering and attenuation corrections have been applied, so that absolute normalization is accomplished. The inelastic scattering and the background, mainly due to the aluminum sample support, were subtracted in the data reduction. It was found (Figure 4.10) for these small Q values, that the inelastic scattering was negligible compared to the elastic.

The Debye-Waller factor (equation 2.33)) is given by Marshall and Lovesy (1971)

$$W = \frac{h^2 Q^2}{2M} \frac{3k_B T}{(k_B \Theta_D)^2} \left[1 + \frac{1}{36} \left(\frac{\Theta_D}{T}\right)^2 - \frac{1}{3600} \left(\frac{\Theta_D}{T}\right)^4\right], \qquad (4.75)$$

where M is the mass of the scattering atom, and Θ_D is the Debye temperature of the substance, which for graphite 1550°K at a temperature T = 298°K (Gschneidner, 1964). Evaluating equation (4.75) we obtain the Debye-Waller factor

$$e^{-2W} = e^{-0.00232\, Q^2(Å^{-1})}. \qquad (4.76)$$

Since for Q = 1. $Å^{-1}$, the factor e^{-2W} is only .9977, it is reasonable to approximate the Debye-Waller factor as unity, and to consider the integrated elastic peak as essentially equal to the total scattering.

The small Q diffraction pattern, uncorrected for multiple scattering, has two main features; the first diffraction peak around Q ~ 1.8

$Å^{-1}$ and the small Q scattering to which, for $Q < 0.4\ Å^{-1}$, a good fit is an exponential of the form 280 exp(- 13.9 Q) barns/ster-atom. This small-Q diffraction data is joined to the large Q data as outlined in section 3.4 to provide a continuous diffraction pattern from which both approximate total cross sections (see section 4.3) and scattering probabilities (see section 4.6) may be obtained. The small Q scattering intensities were then corrected for attenuation and multiple scattering using Copley's (1973) modification of Bischoff's Monte Carlo multiple scattering simulation (1970), the elastic algorithm of which is similar to that of section 4.6.

Hence, the uncorrected data were used to correct the data themselves. The multiple scattering correction factor varies between 1.17 and 1.33 over the range of Q measured. The total cross section used in these corrections was 9.5 barns, obtained from the integral (equation (4.29)) of the uncorrected diffraction pattern, for a wave vector $k = 1.55\ Å^{-1}$ (equivalent to 4.06 Å neutrons). The value obtained from the sample-corrected diffraction pattern is 10.3 barns. Had this corrected cross section been used to generate a second iteration of the multiple scattering correction, about a 2% greater correction would have resulted.

The corrected small Q diffraction results are shown in Figure 4.13. The statistical errors are in fact smaller than the plotting symbols, though a normalization error exists of the order of 2%. The angular Q resolution of TNTOFS is negligible except at the smallest value of Q,

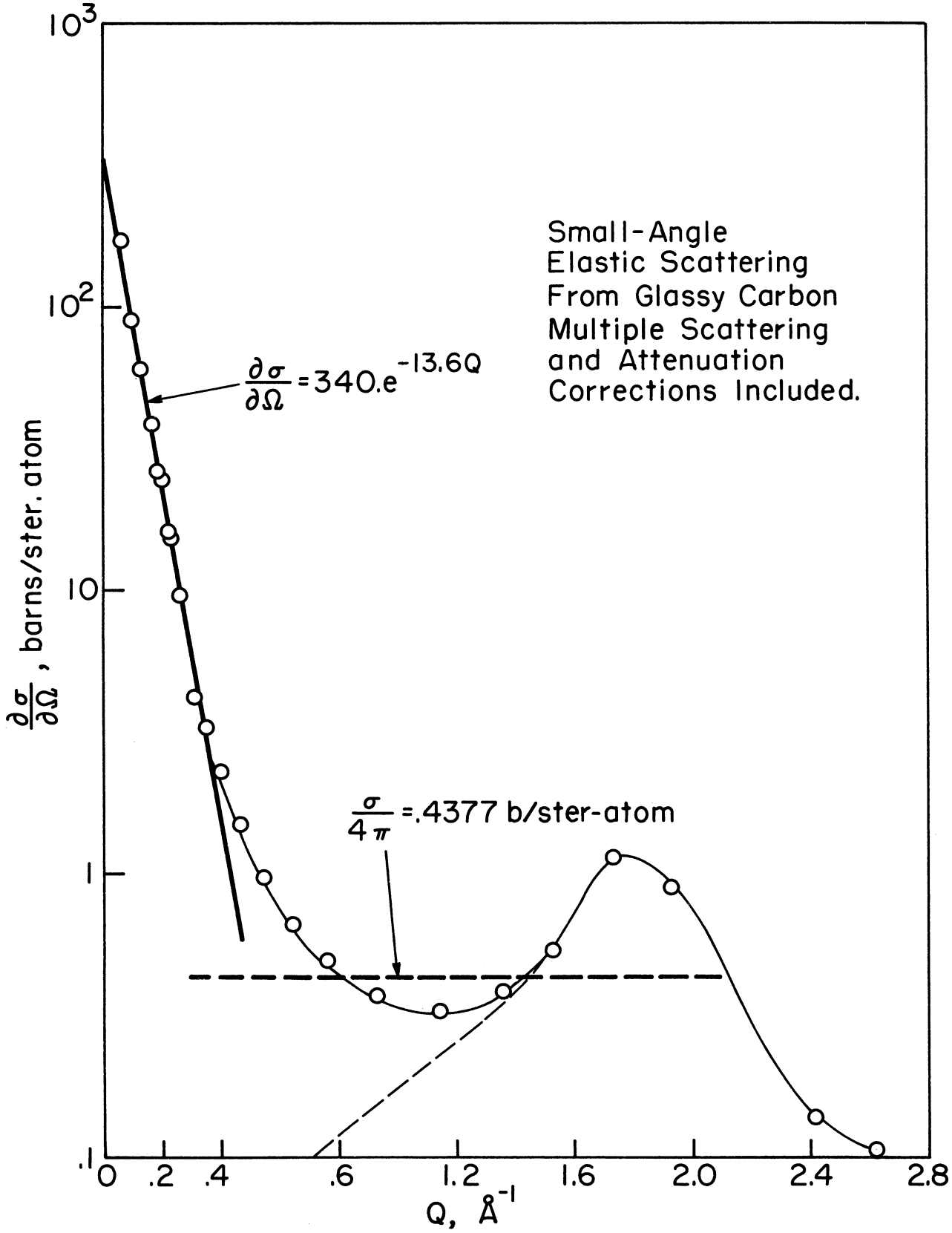

Figure 4.13. Small angle elastic scattering from glassy carbon.

viz., 0.065 $Å^{-1}$. The results have two main features. The scattering for $Q > 1$ $Å^{-1}$ overlaps the data obtained from UMTOFND, the practical range of which has a lower limit of 0.9 $Å^{-1}$. This overlap is necessary for the matching of data obtained from both machines to acquire the full diffraction pattern. Secondly, the intense scattering at small Q, which is characteristic of voids, appears to be well-fitted in the range 0.065 $Å^{-1}$ by the function

$$\frac{\partial\sigma}{\partial\Omega}\Big|_{\text{elastic}} = Ae^{-\alpha Q} \qquad (4.77)$$

where A is 340 barns $(\text{ster-atom})^{-1}$ and α is 13.6 Å. While the form of this function is simple and the fit very satisfactory over this range, it is not one of the conventional froms describing small-Q scattering.

Results of small Q X-ray diffraction (Hucke, 1973) show that the voids in this particular carbon are polydisperse, which suggests that there is interference between the scattering patterns of the small and large scale voids. It is therefore not too surprising that the small Q neutron elastic scattering may be fitted by a simple exponential function, $e^{-\alpha Q}$, where the parameter α will be interpreted as a scale length. for the small-scale void system. The interpretation of the small Q diffraction results will be presented in Chapter 6.

CHAPTER V. RADIAL DISTRIBUTION ANALYSIS

5.1 TERMINATION OF THE FOURIER INTEGRAL

The variation of the pair density g(r) from the average atomic density g_o as a function of interatomic distance r is found by Fourier inversion of the measured intensity distribution I(Q) using the Zernicke-Prins relation,

$$4\pi r(g(r) - g_o) = \frac{2}{\pi} \int_o^\infty Q\, i\,(Q) \sin Qr\, dQ, \qquad (2.46')$$

where i(Q) is the normalized intensity,

$$i(Q) = \frac{I(Q) - I(\infty)}{I(\infty)}, \qquad (2.44')$$

and $I(\infty)$ is the limiting value of the scattered intensity at very large wave vector transfers. The data are normalized by finely adjusting $I(\infty)$ (see section 4.4), which amounts to imposing a chosen value of g_o upon the transform.

Reliable data have therefore been obtained for our glassy carbon sample from two machines for wave vector transfers out to 25 $Å^{-1}$, the transformation of which gives a radial distribution function (RDF) as shown in Figure 5.1. Since the maximum extent of the diffraction pattern is $Q_{max} = 25\ Å^{-1}$, the spatial resolution in the RDF is given by $\Delta r = 2\pi/Q_{max} \sim 0.25\ Å^{-1}$. However using a unit modification function a delta function in the true RDF will have a width of $\Delta r = 3.78/Q_{max}$

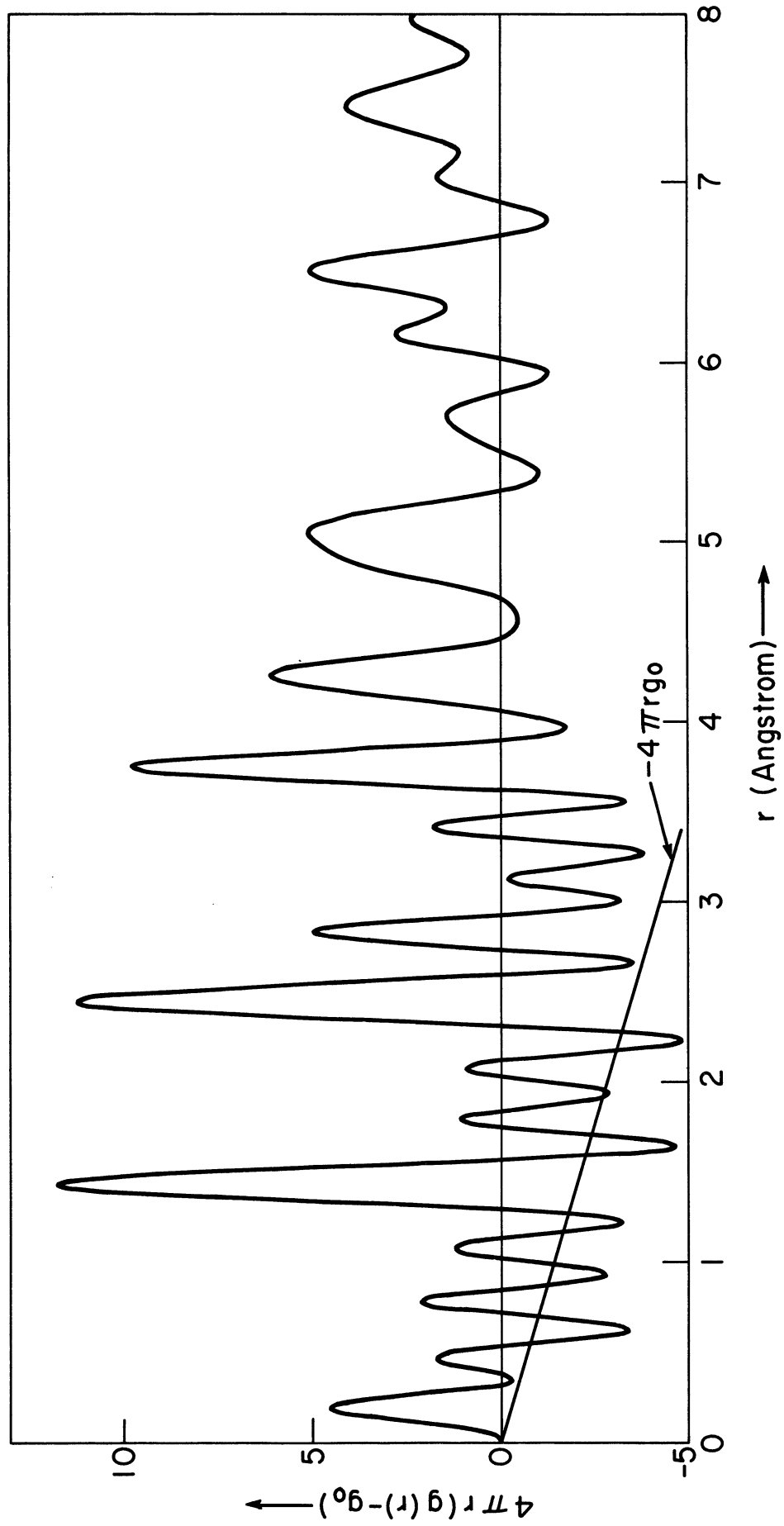

Figure 5.1. The radial distribution function for glassy carbon without termination error elimination.

~ 0.15 Å^{-1}. This is comparable to the difference between the tetrahedral bond length in diamond (1.54 Å) and the trigonal bond length in graphite (1.42 Å), which is about 0.12 Å. Hence it should prove possible to resolve the nearest neighbor peak into tetrahedral and trigonal parts. Moreover the resolution of the RDF can be improved by a technique which reproduces on a fitted function the limitations of the resolution caused by the truncation of the data at Q_{max} (Warren, 1969; Sutton, 1971).

Not only does the restricted range in Q of the diffraction pattern limit the spatial resolution of its Fourier transform, but it also produces termination ripples in the RDF. Since the diffraction pattern is given a value of $I(\infty)$ for $Q > Q_{max}$, the effect is to modify the true diffraction pattern by a function

$$\begin{aligned} M(Q) &= 1 \qquad \text{for } Q \leq Q_{max} \\ &= 0 \qquad Q > Q_{max} \,. \end{aligned} \tag{5.1}$$

Effectively this function causes the integration to be taken over the range from Q = 0 to Q_{max}, by giving zero weight to I(Q) for $Q > Q_{max}$, where no reliable data has in fact been taken. Unfortunately, this modification function causes the RDF to show spurious maxima and minima which will make the interpretation of g(r) difficult. A full discussion of the effects of modification functions is given by Waser and Schomaker (1953).

The Fourier transform r D(r) of Q i(Q) with a modification function M(Q) is the convolution of the RDF, r D(r), and the transform T(r) of the modification function; that is,

$$r\,D(r) = \frac{1}{2\pi^2}\int_0^\infty Q\,i(Q)\,M(Q)\,\sin Qr\,dQ \tag{5.2}$$

becomes

$$r\,D(r) = \frac{1}{4\pi^2}\int_{-\infty}^{\infty} r'D(r')\,T(r - r')\,dr' \tag{5.3}$$

where T(r) has the form $\sin(Q_{max}r)/Q_{max}r$ This function goes to zero when $Q_{max}r = n\pi$ (integer $n \neq 0$). Hence the transform has a full width of $2\pi/Q_{max}$ at its base, and has ripples of period $2\pi/Q_{max}$ with diminishing amplitude. Consequently we obtain

$$r\,D(r) = \frac{Q_{max}}{\pi}\int_0^\infty r'\,D(r')\,\{j_o(Q_{max}(r - r')) + j_o(Q_{max}(r + r'))\}dr' \tag{5.4}$$

To show the spurious effects caused by the truncation at Q_{max}, let us assume that there is an infinitesimal narrow peak in the RDF at r_o. That is, let

$$4\pi r'\,g(r') = \frac{1}{r'}\,\delta(r' - r_o); \tag{5.5}$$

and noting that

$$D(r) = 4\pi(g(r) - g_o), \qquad (2.43')$$

we obtain after substitution in equation (5.4)

$$4\pi r\, g(r) = \frac{Q_{max}}{\pi r_o} \{j_o(Q_{max}(r - r_o)) + j_o(Q_{max}(r + r_o))\}. \qquad (5.6)$$

Hence a peak which in theory has the appearance of a delta function in the RDF appears in the experimental RDF as a peak reduced in height with a full width at half-maximum of $3.78/Q_{max}$, and with satellite peaks having a period of $2\pi/Q_{max}$.

The spurious termination features may be greatly diminished by using an 'artificial temperature factor,' $e^{-\alpha Q^2}$. The modification function M(Q) becomes

$$M(Q) = e^{-\alpha Q^2} \quad \text{for } Q \leq Q_{max}$$

$$= 0 \qquad Q > Q_{max}. \qquad (5.7)$$

where $e^{-\alpha Q_{max}^2} = 0.1$.

This may be justified since equal weight should not be given to peaks and valleys in Q i(Q) at very large Q, where the resolution becomes poor. While this convergence factor reduces the false termination wiggles, it increases the resolution as defined by the full width at half-maximum; viz., $5/Q_{max}$. Other modification functions can be used to reduce the termination wiggles, but they also decrease the resolution of the RDF relative to that given by the unit of modification function (equation (5.1)).

Integrating equation (2.46) with respect to r from (r - Δr/2) to (r + Δr/2) gives

$$\int_{r-\Delta r/2}^{r+\Delta r/2} r\,D(r)\,dr = \frac{1}{2\pi^2}\int_{r-\Delta r/2}^{r+\Delta r/2} dr \int_{o}^{Q_{max}} Qi(Q)\sin Qr\,dQ. \tag{5.8}$$

Provided that $\Delta r \ll r$, we may consider the RDF to be a constant over the limits of the integration; that is, a sufficiently fine mesh in real space must be used. Integration of equation (5.8), neglecting terms in Δr relative to r, yields

$$r\,D(r) = \frac{1}{2\pi^2}\int_{o}^{Q_{max}} Qi(Q)\,\frac{\sin(\Delta rQ/2)}{(\Delta rQ/2)}\sin Qr\,dQ \tag{5.9}$$

Lorch (1969) has used this modification function which is given by

$$M(Q) = \frac{\sin(\Delta rQ/2)}{(\Delta rQ/2)} \qquad \text{for } Q \leq Q_{max}$$

$$= 0 \qquad Q > Q_{max} \tag{5.10}$$

where $\Delta r/2 = \pi/Q_{max}$. While this also reduces the termination ripples, the resolution is $6.28/Q_{max}$. Consequently it is believed that the unit modification function is probably the best to use provided that the spurious features can be identified.

In order to recognize the spurious termination peaks, we build a model of the RDF and transform it via equation (5.4) in an attempt to reproduce the wiggles caused by the truncation, viz.,

$$r\,D(r)_{calc} = \frac{1}{4\pi^2}\int_{-\infty}^{\infty} r'D(r')_{fit}\,\frac{\sin(Q_{max}(r - r'))}{Q_{max}(r - r')}\,dr'. \tag{5.11}$$

We compare values of the calculated RDF, $D(r)_{calc}$, obtained in this way with the observed RDF, $D(r)_{obs}$, acquired experimentally via equation (5.2); we alter the values of the fitted RDF, $D(r)_{fit}$, and iterate through equation (5.11). Eventually when a good comparison has been obtained between $D(r)_{calc}$ and $D(r)_{obs}$, we say that $D(r)_{fit}$ is a good equivalent of $D(r)_{true}$, the real RDF of the material.

We represent the fitted distribution as a series of delta functions,

$$D(r')_{fit} = \sum_n \frac{A_n}{r'^2} \delta(r' - r_n), \tag{5.12}$$

where $r_n = (n + 1/2)\Delta r$, and where Δr is a sufficiently small interval in r to show up details in D(r). Then the calculated distribution is obtained from equation (5.4); viz.,

$$rD(r)_{calc} = \frac{Q_{max}}{\pi} \sum_n \frac{A_n}{r_n} \{j_o(Q_{max}(r - r_n)) + j_o(Q_{max}(r + r_n))\} \tag{5.13}$$

Hence a set of $\{A_n\}$ is found for $D(r)_{fit}$ in order to obtain $D(r)_{calc}$ for comparison with $D(r)_{obs}$. These $\{A_n\}$ are easily adjusted to give a new $D(r)_{calc}$. The Bessel functions damp out reasonably rapidly in practice, so that adjustment of the values of $\{A_n\}$ is confined to a small interval in Δr.

This has been performed for the glassy carbon data, and the results are shown in Figure 5.2. Unfortunately not all of the termination errors have been eliminated. The largest peak adjacent to r = 0 has been very difficult to eliminate; it is probably due to a normalization

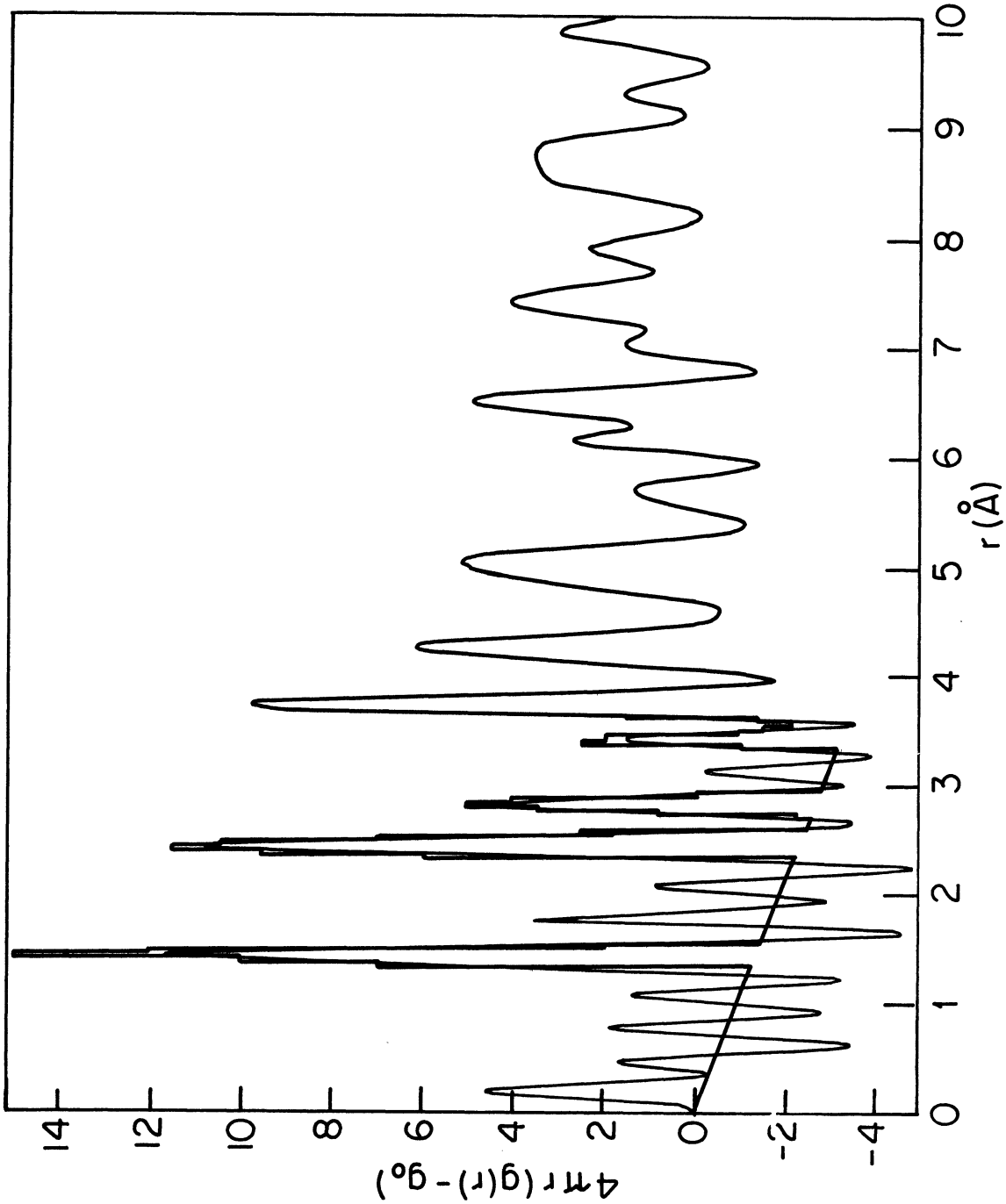

Figure 5.2. A fitted radial distribution function superimposed on the experimental function. Termination error removal is not complete.

error, especially since there are difficulties with the diffraction data at the highest Q. In this region it is probable that Placzek corrections are the most severe. Additionally, a unit modification function has been used which gives equal weighting for the high Q data, and the normalization procedure was such that values of I(Q) around Q_{max} were adjusted and this may be the cause of terminations effects around r = 0, well below the first peak in the RDF.

To see the effect on an improper normalization of the data, consider a small error $\Delta I(\infty)$ in the normalization, and its outcome on the function which is to be transformed; i.e.,

$$Q\ i(Q) = Q\left[\frac{I(Q) - I(\infty)}{I(\infty)}\right] . \tag{5.14}$$

By differentation we obtain

$$\frac{d\ (Q\ i(Q))}{d\ I(\infty)} = -Q\ \frac{I(Q)}{I(\infty)^2} = \frac{-Q}{I(\infty)}\left[\frac{I(Q) - I(\infty)}{I(\infty)}\right] - \frac{Q}{I(\infty)} . \tag{5.15}$$

Then

$$\Delta(Q\ i(Q)) = -\frac{\Delta I(\infty)}{I(\infty)}\ Q\ i(Q) - \frac{\Delta I(\infty)}{I(\infty)}\ Q . \tag{5.16}$$

If we now transform Q i(Q) + Δ(Q i(Q)) we obtain

$$\frac{2}{\pi}\int_o^{Q_{max}}\left\{Q\ i(Q)\left(1 - \frac{\Delta I(\infty)}{I(\infty)}\right) + \frac{\Delta I(\infty)}{I(\infty)}\ Q\right\}\sin Qr\ dQ =$$

$$4\pi r(g(r) - g_o)\left(1 - \frac{\Delta I(\infty)}{I(\infty)}\right) + \frac{2}{\pi}\frac{\Delta I(\infty)}{I(\infty)}\ Q_{max}^2\ j_1(Q_{max}r) . \tag{5.17}$$

Consequently the transform of the first term in equation (5.16) is proportional to the RDF, and gives a shift in scale. The transform of the second term gives an additional oscillatory error around $r = 0$, and which damps down with increasing r.

Values of $I(\infty)$ are very insensitive to the choice of g_o, and moreover, the value of g_o which is strictly compatible with the data is not well-known. This is due to the fact that the macroscopic density is influenced by the large-scale (~250 Å) pore system within this particular carbon, which must give rise to small-Q scattering in the range of $Q \lesssim 2\pi/250 \sim 0.025$ Å^{-1} which was not observed. Since the diffraction pattern includes some of the small-Q scattering due to small-scale voids, the value of g_o imposed on the normalization has therefore been chosen as that corresponding to the density measured by mercury porosimetry, viz., $g_o = 0.07471$ atom Å^{-3}, which is assumed to be the density of the material between the large scale voids (see section 6.2).

It should be noted that no resolution broadening factor has been unfolded from the observed scattered intensity. If the exact intensity I(Q) is broadened by a resolution function F(Q,Q'), then the observed intensity is given by

$$I_{obs}(Q) = \int dQ' \, F(Q,Q') \, I(Q'). \qquad (5.18)$$

A discussion of a method of correcting for resolution broadening is given by Sutton (1971). It is probable that there is little effect for

peaks in the RDF beyond a few Ångstroms, whereas the first few peaks may be slightly narrowed. The danger is to overestimate the effect of broadening, which will give false information about the RDF.

5.2 CARBON COORDINATION MODELS

It was proposed in section 1.4 that various models for glassy carbon in which trigonally and tetrahedrally bonded atoms are found could be checked against the areas under the peaks in the RDF. Let us signify a fourfold bonded carbon by D, since diamond is tetrahedrally bonded and a threefold bonded carbon by G, since graphite is trigonally bonded. Every D atom is surrounded by four atoms, and every G atom is surrounded by three atoms. If the total number of atoms is N, with a fraction x which being fourfold coordinated, there will be Nx atoms with sp^3 (fourfold) bonding, with four nearest neighbors, and N(1 - x) atoms with sp^2 (threefold) bonding, with three nearest neighbors. The total number of nearest neighbor pairs is 1/2(4Nx + 3N(1 - x)) or (N/2)(3 + x), and the area A_1 under the first peak of the RDF will be proportional to (3 + x); i.e., the average coordination number will be 3 + x. Hence the coordination of the first peak is linearly dependent on the proportion of fourfold bonded carbons atoms. This result is independent of the type of model used to describe glassy carbon since the scattering length is independent of the type of bonding. However, the type of nearest neighbor bonding will depend on the model.

On the other hand, the area A_2 under the second peak of the RDF will depend on the model for a given fraction x of fourfold bonded carbons, since the number of second nearest neighbours will depend on the type of nearest neighbors. Since $r_2(D) \sim r_2(G)$, that is, the second-

nearest neighbor distances for diamond and graphite are not too different, the second peak will include contributions from all the different combinations of trigonal and tetrahedral bondings which are available to second nearest neighbors. This might also be true for the third peak since some of third nearest neighbor distances for graphite and diamond are not too disimilar around 2.9 Å, and are less than the c-spacing distance of 3.35 Å in graphite. In fact, in all the models considered, except one, the second coordination number n_2 is $6(1 + x)$, so that the third coordination sphere should be considered.

Following the work of Betts et al. (1972), we consider some possible models for glassy carbon. At one extremity is the phase separated model in which glassy carbon has large regions of diamond-like (tetrahedrally-coordinated) carbon atoms seaparted by regions of graphitic (trigonally-coordinated) carbon atoms. These regions extend over lengths much greater than the inter-atomic distances, so we neglect the boundaries between regions. The D and G atoms are found in the proportion of x to $(1 - x)$. The coordination numbers are a linear combination of those for diamond-like and graphitic carbons in the proportion of the sample composition.

At the other extremity is the random coordinated model in which no chemical ordering is assumed, such that the numbers of D-D, G-G and D-G neighboring pairs are determined by the coordination numbers and the sample composition. There will be some considerable distortion of the

angles and distances between carbon atoms from those found in diamond and graphite. The net result will be for the first peak in the RDF to be very broad reflecting the difference in the bond lenghts between tetrahedrally and trigonally coordinated atoms.

Since the RDF has peaks whose postions correspond well to graphitic inter-atomic distances, the other models all have graphitic regions with a smaller proportion of tetrahedrally-coordinated atoms interspersed in some way. In the dilute linear fourfold coordinated model, all tetrahedrally bonded carbons are arranged in non-interconnecting linear chains within a graphitic structure. Thus the tetrahedrally coordinated carbons link graphitic regions with different orientations. The chain density is sufficiently dilute so that no two chains are within two nearest neighbors. This condition gives a maximum value to x of 1/4.

In the dilute fourfold coordinated model, tetrahedrally bonded carbons are sufficiently dilute such that there are no D-D nearest neighbors. This gives a maximum value to x of 3/7. In the very dilute fourfold coordinated model, no D-D second-nearest neighbors are allowed either so that the maximum value of x is 1/5. These dilute models might occur if tetrahedrally bonded carbons link regions of planes of graphitic layers having different orientations.

In the dilute double fourfold coordinated model, tetrahedrally bonded carbon atoms are found in pairs and might be used for linking graphitic layers of different orientation. The maximum value of x is 1/2. If no D-D second-nearest neighbors are allowed (the very dilute

double fourfold coordinated model), then the maximum value of x is 1/4.

The contributions from the various pairs of atoms to the first and second coordination sphere for the carbon models are shown in Table II. Additionally the coordination numbers for the third and fourth coordination spheres is given as a function of the proportion of tetrahedrally bonded carbon atoms. This is also illustrated in Figure 5.3. It should be pointed out that the numbers for n_3 and n_4 are probably not exact since it is difficult to assign distances in a mixture of trigonally and tetrahedral atoms to the third or fourth coordination sphere. However in all models, n_3 and n_4 should be 3 and 6 for $x = 0$ which is equivalent to graphitic layers. The dilute models are probably only accurate for $x < 0.2$, since all models should tend towards the diamond structure for $x \rightarrow 1$; i.e., both n_3 and n_4 approach 12.

TABLE II

CARBON COORDINATION MODELS

Tetrahedral and trigonal carbon atoms are in the proportion of x to (1-x), and all models have a first coordination number n_1 of (3-x)

Model	First Coordination Sphere			Second Coordination Sphere		
	G-G	G-D D-G	D-D	G-G	G-D D-G	D-D
Phase separated	$3(1-x)$	---	$4x$	$6(1-x)$	---	$12x$
Random coordinated	$3(1-x)^2$	$7x(1-x)$	$4x^2$	$3(1-x)^2(2+x)$	$7x(1-x)(2+x)$	$4x^2(2+x)$
Dilute linear 4-fold	$(3-5x)$	$4x$	$2x$	$\frac{2(9-27x+22x^2)}{3(1-x)}$	$\frac{8x(6-7x)}{3(1-x)}$	$2x$
Dilute 4-fold	$(3-7x)$	$8x$	---	$\frac{2(9-24x+31x^2)}{3(1+x)}$	$\frac{16x(3-7x)}{3(1-x)}$	$\frac{32x^2}{3(1-x)}$
Very dilute 4-fold	$(3-7x)$	$8x$	---	$\frac{2(9-24x+31x^2)}{3(1+x)}$	$\frac{16x(3-7x)}{3(1-x)}$	---
Dilute double 4-fold	$3(1-2x)$	$6x$	x	$\frac{3(2-5x+4x^2)}{(1-x)}$	$\frac{3x(5-7x)}{(1-x)}$	$\frac{3x^2}{(1-x)}$
Very dilute double 4-fold	$3(1-2x)$	$6x$	x	$\frac{3(2-5x+4x^2)}{(1-x)}$	$\frac{3x(5-6x)}{(1-x)}$	---

	n_2	n_3	n_4
Phase separated	$6(1-x)$	$3(1+3x)$	$6(1+x)$
Random coordinated	$(3+x)(2+x)$	$(3+4x+9x^2-12x^3+18x^4-7x^5-3x^6)$	$(6+8x+41x^2-61x^3+18x^4)$
Dilute linear 4-fold	$6(1+x)$	$(3+2x)$	$\frac{2(3+5x)(3+x)}{3(1-x)}$
Dilute 4-fold	$6(1+x)$	$(3-x)$	$6+22x$
Very dilute 4-fold	$6(1+x)$	$(3-x)$	$\frac{2(9+24x-49x^2)}{3(1-x)}$
Dilute double 4-fold	$6(1+x)$	$3(1-x)$	$3(2+9x)$
Very dilute double 4-fold	$6(1+x)$	$\frac{3-6x+4x^2}{(1-x)}$	$\frac{x(51-81x+24x^2)}{1-x}$

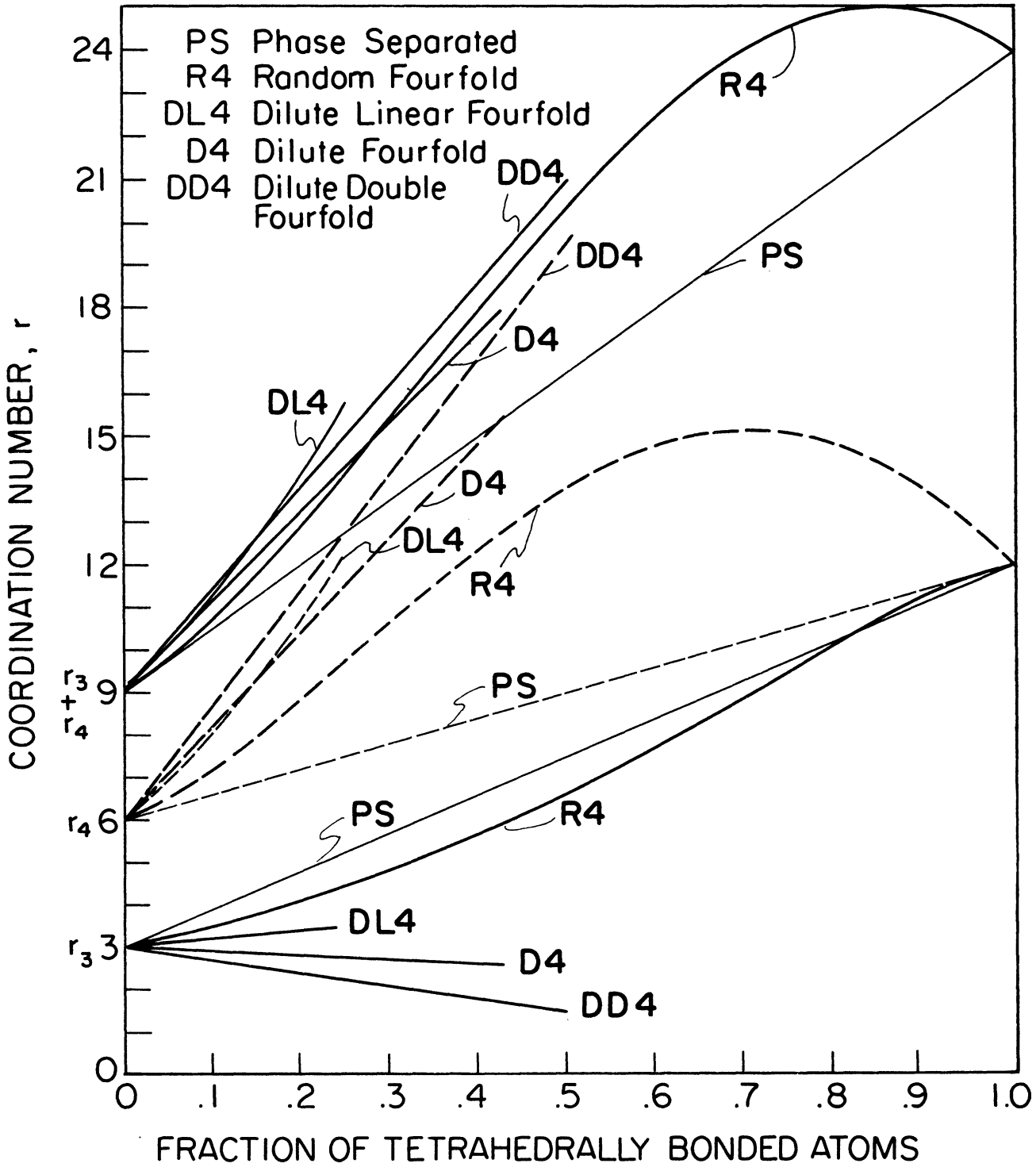

Figure 5.3. Coordination numbers for various carbon coordination models.

5.3 PEAK FUNCTION ANALYSIS

It can be seen from the RDF that the first real peak occurs at 1.425 Å which is close to the value found for the nearest neighbor distance in graphite. There is no evidence of a peak around 1.54 Å, the bond length in tetrahedrally bonded diamond. Moreover the area under this first peak corresponds to a coordination number around 3, as in trigonally-bonded graphite. Hence it is believed that there are no tetrahedral structural units as suggested by Noda and Inagaki (1964), but that graphitic units are linked by four-fold atoms of the order of a few per cent, which is unseen within the precision of the present measurements.

It is also found that there are additional peaks at higher distances which correspond also to graphite distances, as shown in Figure 5.4, the RDF from the partially corrected diffraction data (Mildner and Carpenter, 1972). These peaks have been analyzed by computing the area under each peak which should be proportional to the coordination number at that distance by equation (2.48). The results are shown on Figure 5.5 and the values for the first few real peaks are shown in Table III; values for graphite are also shown for comparison.

TABLE III

MILDNER (1973) 2000°C HUCKE SAMPLE

Coordination Sphere	Glassy Carbon		Graphite	
	r (Å)	n	r (Å)	n
1	1.425	2.99	1.42	3
2	2.45	6.10	2.46	6
3	2.83	3.28	2.84	3

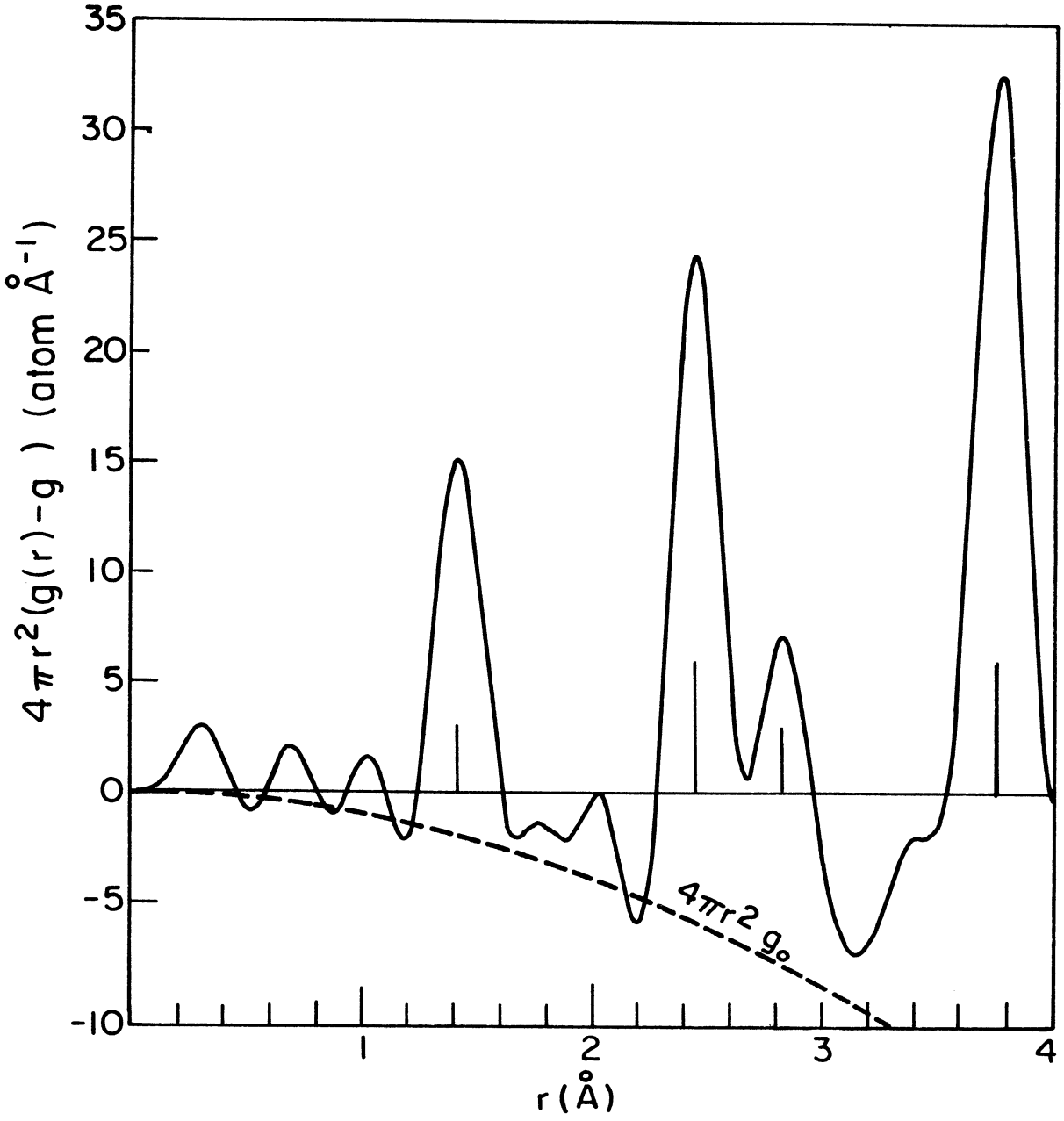

Figure 5.4. The RDF from partially corrected data showing the first four graphitic in-plane correlations. The heights correspond to the coordination numbers.

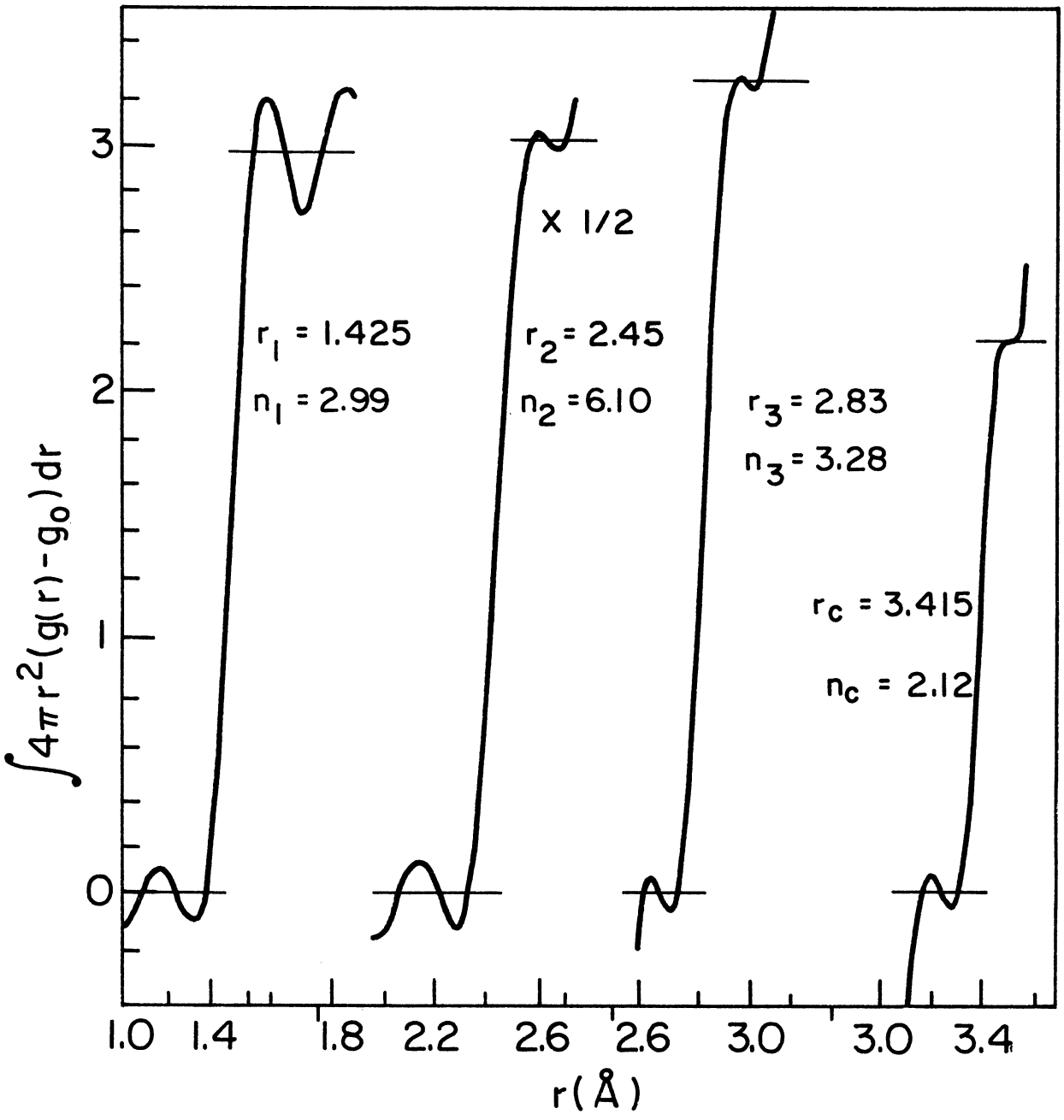

Figure 5.5. The integration of the peaks in the RDF giving the coordination numbers.

These numbers have been obtained by integrating the RDF without elimination of the termination errors. Consequently the error limits are difficult to access properly, and the values are only approximate, especially for larger coordination spheres. Additionally the fourth broad peak around 3.4 Å we attribute to an interplanar distance, though it is modified greatly by termination errors, since graphite has an interplanar distance of 3.35 Å.

Unfortunately it cannot be ascertained from these numbers which model in section 5.2 is uniquely defined, because the coordination numbers are not known accurately. Additionally we should expect n_1 to be greater than 3; and the value of n_2 gives a fraction of tetrahedrally coordinated atoms of between 1-2%. Hence it is believed that these atoms are in fact dilute. The value of n_3 suggests that for any model the fraction is less 10%; and it is conjectured that the true value is probably of the order of 5%, so that the bulk of the atoms in glassy carbon are linked trigonally as in graphite. Figure 5.6 shows in-plane correlations for graphite with artificial Gaussian widths. Many of the features of the RDF may be correlated with this figure.

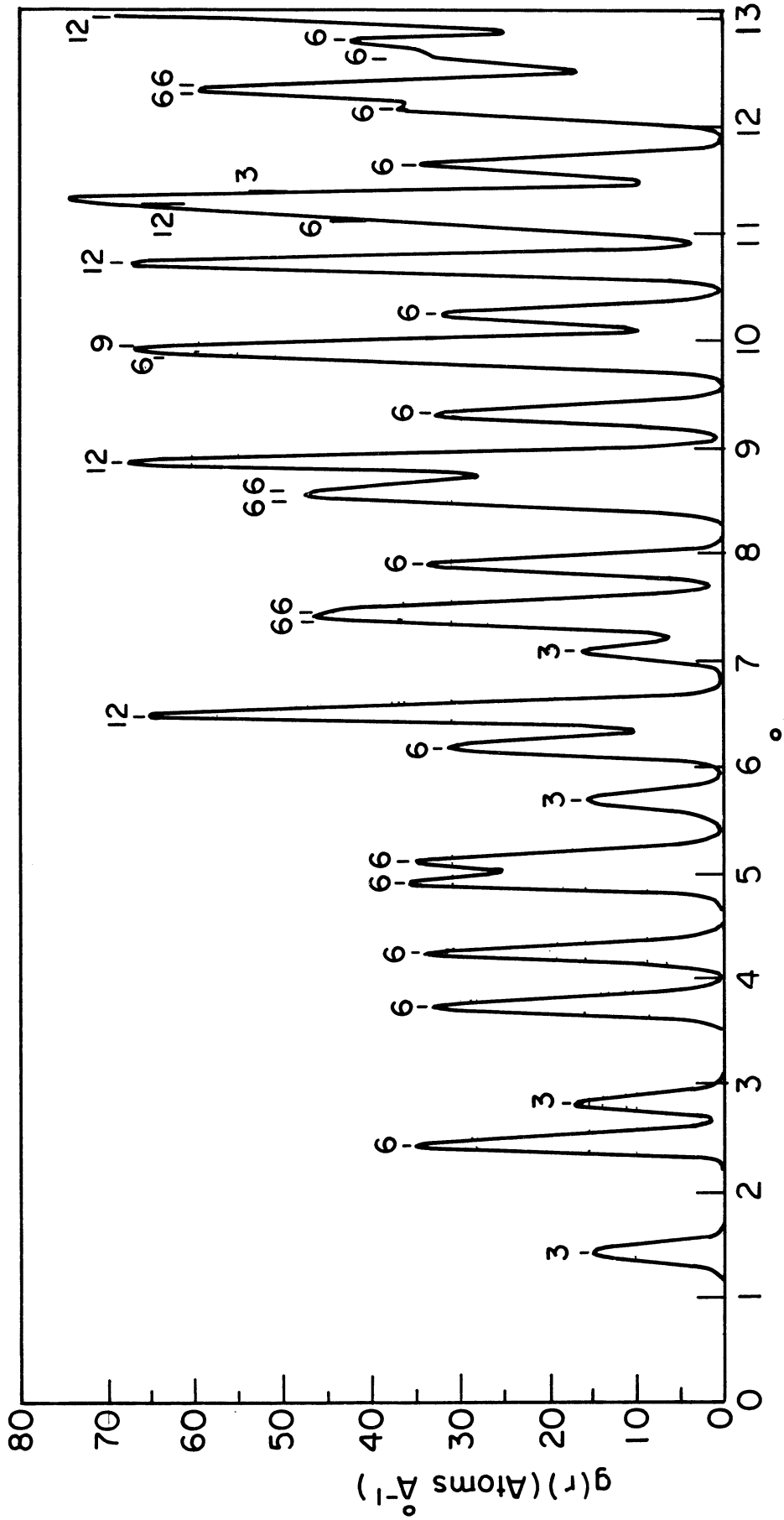

Figure 5.6. In-plane correlations for graphitic with artifical Gaussian widths.

5.4 TURBOSTRATIC MODEL

Since a comparison of the peak positions and areas in the RDF of glassy carbon can be made with the interatomic distances and coordination numbers of graphite (Figure 5.6), it would seem appropriate to consider models for glassy carbon which reflect some similarity to the hexagonal layers of graphite. Moreover the initial comparison with a single hexagonal layer was sufficiently good, that this may be extended by considering a large number of such layers. These layers certainly have no fixed orientation relative to each other, otherwise peaks in the RDF due to interplanar correlations would be apparent as for graphite. Consequently we consider these planes to be arranged randomly in orientation.

The theory of the diffraction pattern of a two-dimensional lattice which takes with equal probability all orientations in space was initially studied by Warren (1941). The reflections from a sample containing a large number of blocks of layers with random orientation are of the type (001), or the two-dimensional type (hk0); but there are no reflections of the type (hkl). It is this form of model of random layers that should be considered for comparison with glassy carbon.

The stacking of random layers yields an atomic density $g(\underline{r})$ as a function of interatomic distance r given by

$$g(r) = \frac{1}{N} \sum_{l,l'} \delta(|\underline{r}| - |\underline{r}_l - \underline{r}_{l'}|) \qquad (5.19)$$

where N is the total number of atoms, and $\underline{r}_l$, $\underline{r}_{l'}$ are the positions of the atoms marked l, l'. Now subdivide the summation index l into a plane index j and an atom-in-plane index i, so that equation (5.19) may also be subdivided into in-plane correlation and out-of-plane correlations. Hence

$$g(r) = \frac{1}{N} \sum_{j} \sum_{i,i'}' \delta(|\underline{r}| - |\underline{r}_{ij} - \underline{r}_{i'j}|) + \frac{1}{N} \sum_{j,j'}' \sum_{ii'} \delta(|\underline{r}| - |\underline{r}_{ij} - \underline{r}_{i'j'}|). \quad (5.20)$$

For out-of-plane correlations, let $\underline{z}_j$ be the position of the plane indexed j along the c-axis. Then

$$\underline{r}_{ij} - \underline{r}_{i'j'} = (\underline{z}_j - \underline{z}_{j'}) + (\underline{r}_{i(j)} - \underline{r}_{i(j')}). \quad (5.21)$$

Since the layers have no fixed orientation, there is no correlation between $\underline{r}_{i(j)}$ and $\underline{r}_{i(j')}$, and the distribution of $|\underline{r}_{i(j)} - \underline{r}_{i(j')}|$ depends on the mean density n_A of atoms in the plane. If N_P is the total number of planes each with N_A atoms, then

$$N = N_P N_A. \quad (5.22)$$

The sum over the indices i, i' for the out-of-plane correlations in equation (5.20) gives $n_A N_A$. Then performing the sum over planes for both types of correlations gives

$$g(r) = \frac{1}{N_A} \sum_{ii'} \delta(|\underline{r}| - |\underline{r}_{ii'}|) + n_A \sum_{j}' \delta(|\underline{z}| - |\underline{z}_j|), \quad (5.23)$$

where $\underline{r}_{ii'}$ is the vector distance between atoms marked i,i' in the same plane, and $\underline{z}_j$ is the vector distance between two planes, j layers apart.

Since the model is an isotropic arrangement of blocks of random layers, an orientation average must be applied to equation (5.23) in order to obtain an RDF. The first term represents the correlations of atoms in the same plane, and consequently is independent of the orientation of the particular layer, and the blocks of layers are oriented at random so that the averaging may be performed for many such blocks. Then equation (5.23) becomes

$$g(r) = \frac{1}{4\pi r^2 N_A} \sum'_{i,i'} \delta(r - r_{ii'}) + \frac{n_A}{2r} \int_{-r}^{+r} \sum'_j \delta(z - z_j)\,dz. \tag{5.24}$$

The second term, the density of atom pairs in distinct planes, is governed by the pair density of planes and mean atom density n_A of in a plane. Let $P(z)\,dz$ be the probability that a plane exists in dz about a distance z from a given plane; i.e., the plane-pair density function. The contribution to the RDF at dr about a distance r from a ring element of volume $2\pi\,dr\,dz$ at constant z with an atomic density n_A is $2\pi r\,dr\,dz\,n_A P(z)$. Consequently the radial distribution function for a turbostratic layered structure can be expressed in the form

$$4\pi r^2 g(r) = \frac{1}{N_A} \sum'_{ii'} \delta(r - r_{ii'}) + 2\pi r n_A \int_{-r}^{+r} P(z)\,dz. \tag{5.25}$$

Let $f_j(z)$ be the function giving the appropriate contribution to

the distribution P(z) from the plane indexed j. Then

$$P(z) = \sum_{j=-\infty}^{\infty}{}' f_j(z). \tag{5.26}$$

If the values of the distances between the planes are chosen from a Gaussian distribution with

$$W(z) = \frac{1}{(2\pi)^{1/2}\sigma_z} \exp\left(-\frac{(z - d_c)^2}{2\sigma_z^2}\right), \tag{5.27}$$

then the contribution from the plane indexed j is

$$f_j(z) = \frac{\sqrt{|j|}}{(2\pi)^{1/2}\sigma_z} \exp\left(-\frac{(z - jd_c)^2}{2|j|\sigma_z^2}\right), \tag{5.28}$$

where d_c is the average distance between the planes with a standard deviation σ_z. Then equation (5.25) becomes

$$4\pi r^2 g(r) = \frac{1}{N_A} \sum_{i,i'}{}' \delta(r - r_{ii'}) + \frac{2\pi r\, n_A}{(2\pi)^{1/2}\sigma_z} \int_{-r}^{+r} \sum_{j=-\infty}^{\infty} \sqrt{|j|} \exp\left(-\frac{(z - jd_c)^2}{2|j|\sigma_z^2}\right) dz. \tag{5.29}$$

This function should therefore be compared with the experimental RDF. The first three peaks will determine the validity of the parameters used to determine the in-plane correlations. For the turbostratic model of graphite, the average lattice parameters are taken as a_o = 2.46 Å and c_o = 3.35 Å. Lattice parameters for this model of glassy carbon are best obtained from the diffraction pattern of the sample itself (section 4.8).

The position of the (00.2) peak yields a distance d_c = 3.46 Å for

the mean layer spacing. The position of the (10) peak yields a distance d_{10} of 2.067 Å which corresponds to a lattice parameter a_o of 2.39 Å which is significantly different from that of graphite. X-ray analysis of the (10) peak gave d_{10} = 2.10 Å and therefore a_o = 2.43 Å. On the other hand, the RDF of the neutron diffraction pattern gave a value of a_o equal to 2.45 Å.

The in-plane correlations for the ideal graphitic model are given in Appendix A. 5, and hexagonal layers were constructed on the computer using a lattice parameter of 2.46 Å. In order to fit the peak widths in the RDF, the parametric value was taken as the peak in a Gaussian distribution of standard deviation σ_a = 0.03 Å. The orientation and positioning of adjacent layers were selected at random, with the constraint that the planes were parallel and that their distance apart was selected at random from a Gaussian distribution around 3.46 Å with a standard σ_c = 0.04 Å. Although an RDF of this model was constructed, it is believed that the artificial method used for broadening the diffraction peaks is unsatisfactory.

A more reasonable function for representing the pair density of planes is that suggested by the shape of the (00.2) peak of the diffraction pattern. That peak is of Lorenzian form, and is characterized by a plane spacing d_c and a mean crystallite height L_c. In the limit of large $|Z|$, $P(Z)$ approaches d_c^{-1}. Thus we assume a function which reasonably approximates the desired behavior, viz.;

$$P(z) = \sum_{j=-\infty}^{\infty}{}' \delta(z - jd_c)\, e^{-|z|/L_c} + \frac{1 - e^{-|z|/L_c}}{d_c} \tag{5.30}$$

The integral in equation (5.25) gives

$$\int_{-r}^{+r} P(z)\, dz = 2 \sum_{j=1}^{[r/d_c]} e^{-jd_c/L_c} + \frac{2r}{d_c} - \frac{2L_c}{d_c}\left(1 - e^{-r/L_c}\right), \tag{5.31}$$

where $[r/d_c]$ means the greatest integer in r/d_c. Since the limiting value of the density is given by

$$g_o = n_A/d_c, \tag{5.32}$$

then equation (5.25) becomes

$$4\pi r^2(g(r) - g_o) = \frac{1}{N_A} \sum_{i,i'}{}' \delta(r - r_{ii'}) + 4\pi r\, n_A \left\{ \frac{e^{-\frac{d_c}{L_c}[\frac{r}{d_c}]}}{e^{d_c/L_c} - 1} - \frac{L_c}{d_c}\left(1 - e^{-r/L_c}\right) \right\}. \tag{5.33}$$

5.5 RELAXED QUINOID COMPUTER MODEL

Though graphite was one of the first crystal structures to be determined, it may have a form beyond the two given in chapter 1, for the X-ray diffraction results of Lukesh (1955) showed that perhaps both ordinary and rhombohedral graphite had larger units of structure with lower symmetry. Pauling (1967) has suggested that perhaps the double bond of each carbon atom (which has a valence of four) does not resonate equally among all three covalent bonds. Since two of the valence electrons of carbons are identical, he proposed that it is likely that at least two of the bonds connecting each atom to its neighbors are equal in length. By symmetry the odd bond makes equal angles with the other two. If all the valence electrons hybridize to form three bonds equal in length, the structure is completely resonating. But if this third bond is not equal in length, the structure is quinoidal; that is, this theory assumes that this double bond is concentrated in one of the three.

This model of graphite, therefore, is a layered structure of carbon atoms with three neighboring atoms as before. In both hexagonal and rhombohedral graphite these atoms are 1.418 Å apart, with a lattice constant of 2.456 Å. However, in the quinoid structure, each carbon forms one stronger (double) bond, and two weaker (single) bonds. The structural characteristics of the quinoid model are given in Appendix C. Pauling suggests a number of advantages of the quinoid structure over the completely resonating structure. It permits a better packing

of the superimposed layers, a decrease in the inter layer spacing, and hence an increased stabilization through the stronger Van der Waals attraction between the layers He assigns the observed interlayer spacing of 3.354 Å to the quinoid structure, and the spacing of 3.44 Å and greater found in many graphitic carbons to the completely resonating structure.

Turbostratic graphite is a form of carbon which has graphitic layers superimposed upon each other, but with great disorder, and with inter-layer spacing between 3.44 Å and 3.70 Å. Presumably then, turbostratic graphite has the completely resonating structure, with all bonds equal in length.

The difficulty with the turbostratic model for glassy carbon is that there is no striking difference between it and a model for turbostratic graphite. And yet graphite is soft, whereas glassy carbon is hard, and does not cleave. The problem is to find particular properties that will differentiate glassy carbon from graphite. One solution, originally suggested by Ergun (1973), is to consider the quinoidal model created by Pauling (1967) to explain graphite. Since this model causes the inter layer distance to decrease compared to the completely resonating model, there is greater bonding between the layers, and hence greater strength.

Ergun's quinoidal model for glassy carbon is a quasi-crystalline two-dimensional model. In contrast, we have considered an 'amorphous

two-dimensional' model, in which the stronger or 'double' bond is selected at random, such that one bond out of three on every atom is shorter than the other two. This means that there is no ordering of the shorter bond in the individual plane.

A computer code has been written which generates a large plane of hexagonal arrays of atoms with random shorter bonds, and with periodic boundary conditions. The arrays are formed within cells in the shape of a rhombus, and of edge n times the lattice parameter a_o Consequently the two-dimensional cell contains $2n^2$ atoms. The algorithm is general and can cope with any n; the highest number of atoms in a plane produced by the program is 1250 atoms for n = 25.

The constraints are that each atom has one short and two long bonds, and that periodic boundary conditions apply at the cell boundary. Consequently any bond may be picked initially and assigned as a double bond; this labels four short bonds. The end of one of these joins is selected randomly as the next double bond, and so on It should be noted that often the selection of a particular bond to be short also determines other bonds to be short. Due to periodic boundary conditions, this allows arrays to be produced which are unable to comply with the first constraint. As a result, a number of arbortive efforts at completing an array are encountered.

For the cell of dimension n equal to unity, the periodic boundary conditions demand that the cell is unique, and all the short bonds are

aligned to give a '1-4 quinoid' structure. For cell dimension n equal to two, the cell may be one of two forms; a 1-4 quinoid structure (adequately defined by n = 1), and a 1-3 quinoid structure. The ratio of 1-3 quinoids to 1-4 quinoids is 3:1. However, for cell dimensions greater than two, the distorted hexagons may have anywhere between zero and three double bonds, though the total number of double bonds in the cell must be n^2. It is interesting to notice that there are clearly definite small scale patterns of the smaller bonds. An ensemble average of these should provide a useful comparison for the RDF.

Because of the strain introduced by these random stronger bonds, the atoms in the model of distorted hexagons are forced to move into new positions. The resulting atomic configuration within the cell is such that the energy within the bonds connecting the atoms is minimized, and the atoms are in equilibrium positions. This has been performed using a computer program constructed by Orlandea (1973) for the study of dynamic mechanical structures.

Central forces due to changes in bond length between nearest neighbors in two adjacent planes, and forces due to the bending of planes, which are proportional to the displacement of atoms in the c-direction, have been ignored. Consequently we have considered only a two-dimensional problem, in which atoms may move only within the layer plane. Young and Koppel (1965) have shown that this is probably a reasonable assumption for graphite, and consequently it should be better

for glassy carbon with a larger interlayer spacing; additionally it would be difficult to estimate useful force constants for these motions Forces due to changes in bond angles within the plane have been ignored and they are probably an order of magnitude lower than the bond streching force constants. Thus only central forces between nearest neighbors have been considered.

The equilibrium bond lengths used are those given by Ergun (1973) for his quinoid structure, viz., L_1 = 1.454 Å and L_2 = 1.356 Å. A discussion of the appropriate force constants is found in Appendix D. If it is assumed that the short bonds are double bonds, and the long bonds are single bonds, then the ratio of the force constants should be of the order of k_2/k_1 = 2.16. It is probably far too drastic an assumption that the short bonds are equivalent to double bonds, and we have arbitrarily chosen a ratio of 1.76 for the computer model. Consequently the force constants used are k_1 = 1.31 Mdyne/cm and k_2 = 2.31 Mdyne/cm, where the resonating bond force constant is 1.81 Mdyne/cm (Waser and Pauling, 1950).

The atoms in the plane are allowed to move in a harmonic potential function of a given force constant depending on the type of bond. Finally when the energy of the structure becomes minimal, the atomic positions are noted. This should be performed for many layer models since it has been observed that there are clearly small-scale patterns in the arrangement of the double bonds.

This relaxation method has been used for planes containing 18 different atoms, that is, starting with a rhombohedral lattice containing 3 x 3 unit cells of graphite, two atoms per cell, random double bonds are specified such that periodic boundary conditions are preserved. The small cell size has been used to reduce computational work, yet we feel it is indicative of the results of computing with a large cell. It can be seen that only four different types of structures can be generated for the 3 x 3 cell (their frequencies of occurrence are found assuming equal energy for all structures);

(a) a mixture of 1-3 and 1-4 quinoids (with a relative frequency of 7/16),

(b) a '3-2-1' structure (frequency 7/16),

(c) a 1-4 quinoid structure (frequency 1/16),

(d) a '3-3-0' structure (frequency 1/16).

The frequencies with which these various structures are generated for the 3 x 3 cell, is such that quinoids are produced as often as are structures containing a hexagon with three shorted bonds, though in general this is not true. The four 18-atom cells are shown in Figure 5.7.

These structures are relaxed by keeping atoms marked 1 through 4 as a fixed frame, so that an outer relaxation is performed in which the frame may be adjusted. It is found that the frame does not move by more than 0.1% for any of these structures (and for the 1-4 quinoid

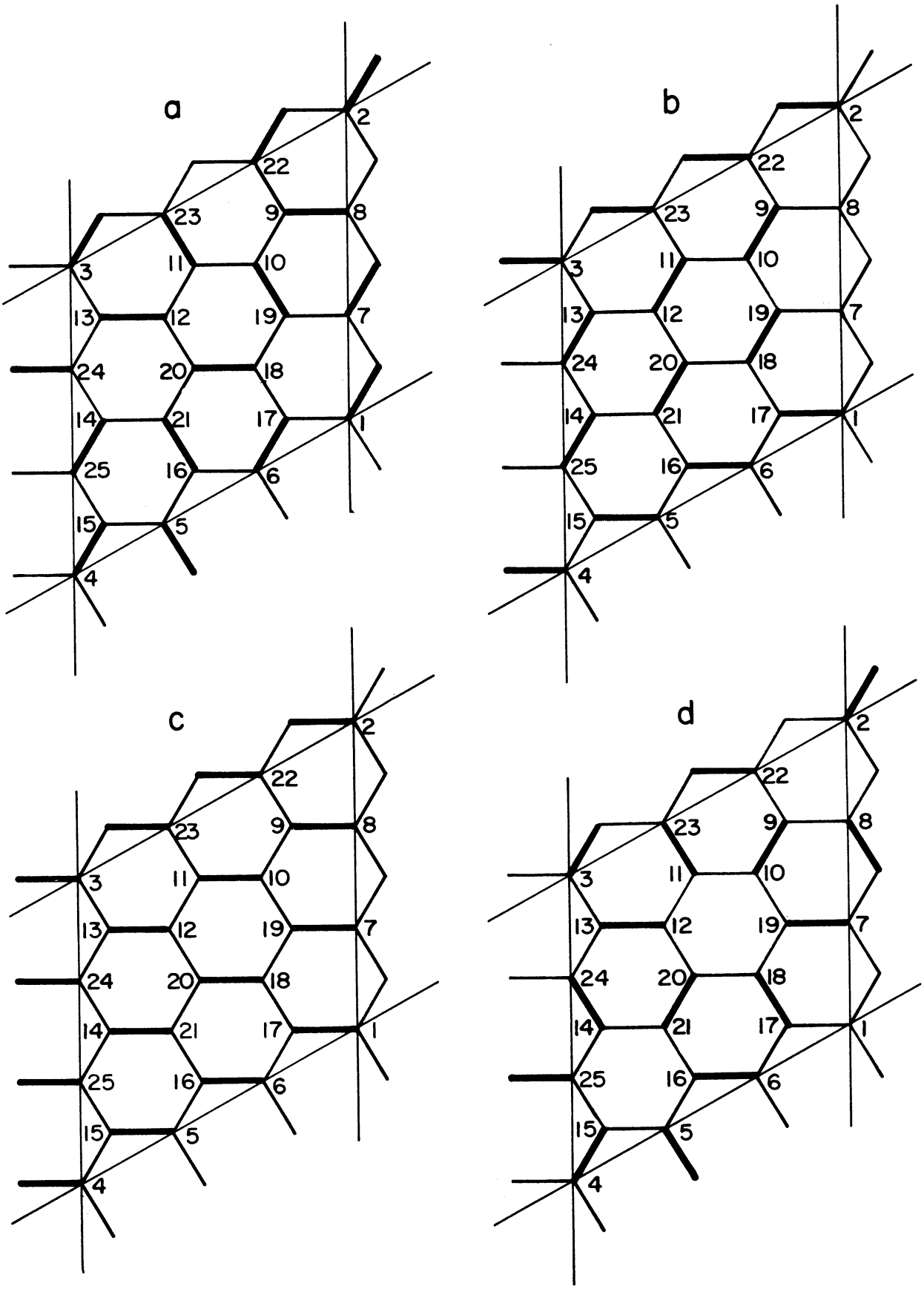

Figure 5.7. The four different types of structures that can be generated for the 18-atom cell.

structure, the structure does not move at all since the equilibrium bond length values were taken from Ergun's 1-4 quinoid graphite layers. The distances between the atoms in the relaxed planes are computed, so that the first term in equation (5.33) which represents the correlations of atoms in the same plane is computed as the ensemble average of the four distinct relaxed structures

The second term in this equation, which represents the out-of-plane correlations between atoms, requires values for the interlayer spacing d_c and the crystallite height L_c. We have taken d_c = 3.460 Å and L_c = 35.0 Å from the centroid and width of the first diffraction peak (section 4.8). In each of the relaxed structures, the cell was a 60° rhombus, 7.371 Å on a side (area 47.05 $Å^2$) containing 18 atoms. Thus the density of atoms in each plane is n_A = 0.3826 atoms/$Å^2$. Using equation (5.32), the average atomic density g_o is given as 0.1106 atoms/$Å^3$ which is to be interpreted as the microscopic atomic density, exclusive of any voids. Further discussion of the atomic density is to be found in Chapter 6.

The modeled radial distribution function (equation (5.33)) for the turbostratic, disordered layer structure is shown in Figure 5.8. The numbers above the peaks shows the coordination numbers contributing to the peaks. The non-zero value for g(r) below the interplanar distance (r = 3.46 Å), except for the peaks, is due to an artifact of the model for the out-of-plane correlations. For if we consider values of r in

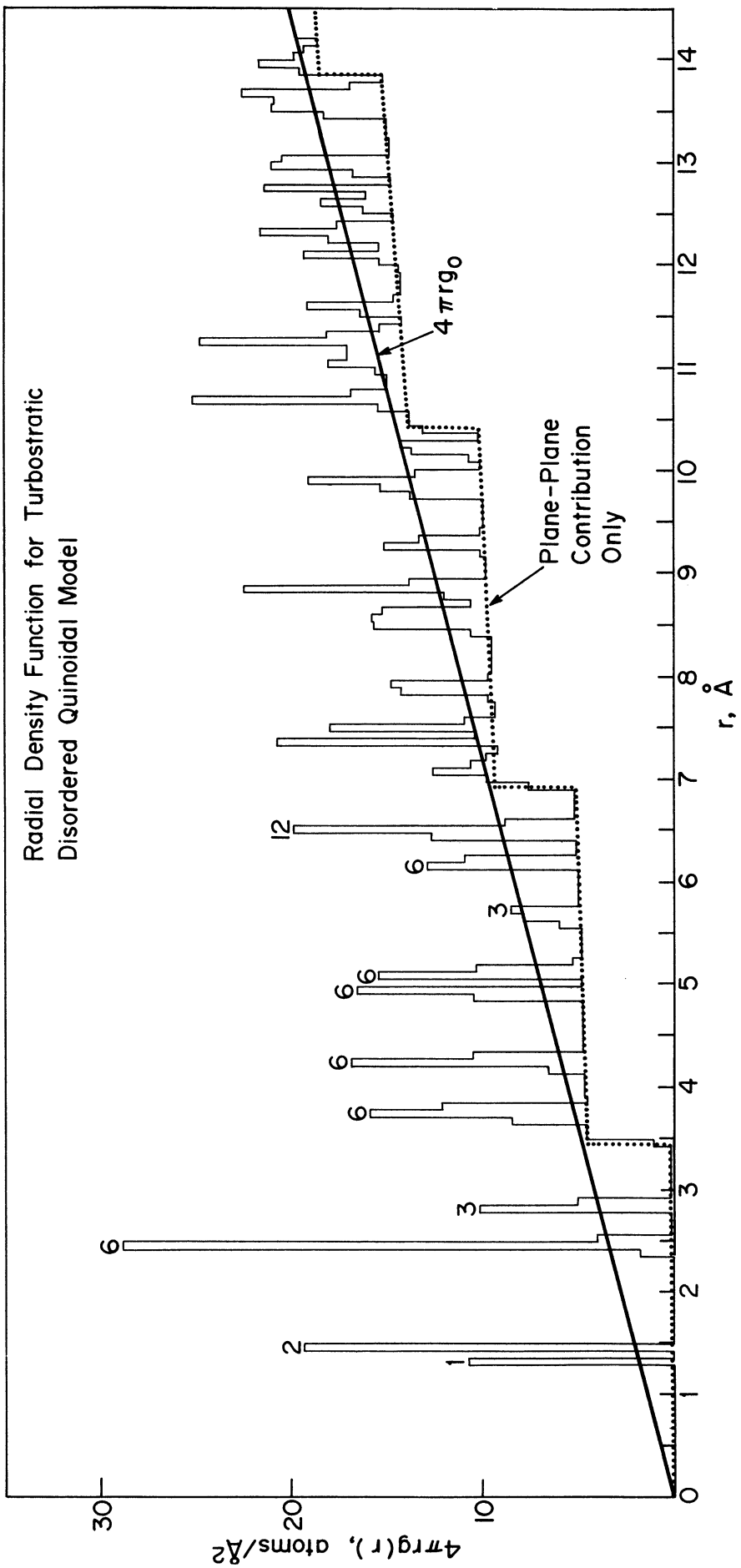

Figure 5.8. The modelled radial distribution function for the turbostratic disordered layer structure.

the region, $r < d_c \ll L_c$, and neglecting the in-plane correlations, equation (5.33) reduces to

$$4\pi r\, g(r) = 2\pi n_A \frac{r^2}{d_c L_c} . \tag{5.34}$$

Additionally at $r = d_c$, the difference between the average atomic density and the out-of-plane correlations is given by

$$4\pi r(g_o - g(r)) = 2\pi n_A \frac{d_c}{L_c} . \tag{5.35}$$

5.6 GRIGOROVICI-BELU MODEL

In the modelling of an amorphous substance, it is useful to consider a continuous network of atoms with the same type of covalent bonds as in the analogous crystal. Since glassy carbon appears to be a two-dimensional substance with trigonally bonded carbon atoms, it would be useful to construct a model with the constrains that the model is planar, and that each carbon atom has three diverging bonds. Grigorovici and Belu (1972) have built such a model using units consisting of three symmetrically diverging equal springs. They have formed a two-dimensional hexagonal crystal lattice containing only merged hexagons, and a continuous disordered network which consisted of merged pentagons, hexagons and heptagons.

The bond lengths, bond angles, and the RDF of both models were recorded under conditions of

(1) no stress,

(2) hydrostatic tension (equivalent to an outer relaxation),

(3) uniaxial stress.

The radial distribution analysis of the amorphous model showed that the 1st, 2nd, 4th, and 6th nearest neighbor distances of the lattice were present but with a definition which became worse with increasing distance; the 3rd, 5th, and 7th peaks were strongly broadened, shifted, or absent (see Figure 5.9). It was found that distances

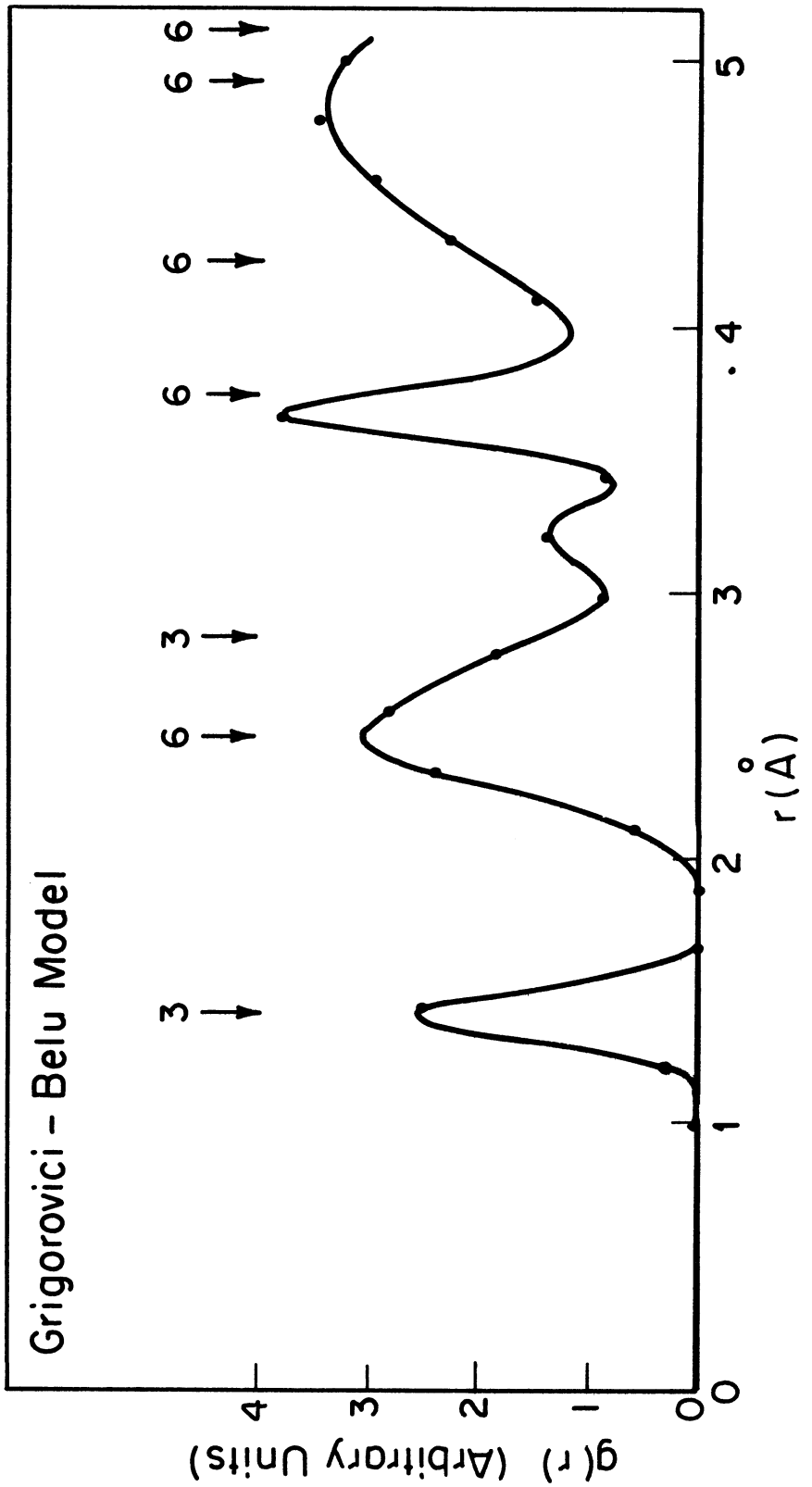

Figure 5.9. The radial distribution function of the Grigorovici-Belu disordered model. The arrows refer to the positions of the coordination spheres in the periodic lattice and their corresponding coordination numbers.

between atoms within the zig-zag chains were relatively well conserved in the amorphous model, whereas distances between atoms linked to the zig-zag chain by branched-off bonds were strongly changed and smeared out.

Uniform radial extension did not change the width of the bond length distribution in either model, but did change the width of the bond angle distribution in the amorphous model. Instead of a wide distribution of angles, there was a tendency to form angles which correspond to those of the regular polygons, the distorted form of which were present in the amorphous model. A uniaxal elongation shifted all the peaks in the RDF to higher distances; the second peak which is sensitive to changes in bond angles was broadened both strongly and asymmetrically.

No explanation is given for the peak around 3.2 Å which corresponds to no in-plane correlations for graphitic layers (see Appendix A.5). However atoms in regular heptagons have third nearest neighbor distances 3.19 Å. If the hexagons and heptagons are found in equal numbers, then this peak will be approximately twice as strong as that for hexagons (2.83 Å). The peak around 3.2 Å in our RDF (Figure 5.1) has been found to be a termination effect. Consequently the number of heptagons in reality must be small in comparison with the number of hexagons.

A network of planar hexagonal rings has been constructed on the computer by Cooper and Aubourg (1972), with the restrictions that each

atom has three adjacent atoms, and that all bond lengths are equal. Consequently the average bond angle is $2\pi/3$. The distribution of bond angles θ were restricted to the range $\pi/3 < \theta < \pi$ to avoid network overlap and reentrant angles. It was expected that the a priori distribution of bond angles would influence the pair correlation function and the final distribution of bond angles of the model. However, they found that the density and the determined distribution of angles were relatively insensitive to the initial distribution, but were sensitive rather to the limits of the distribution of θ. Consequently a self-consistent structure could be determined for a given angle of θ. They only report results for a uniform distribution in the range $\pi/3 < \theta < \pi$. Their histogram shows maxima at 1.42, 2.84, and 3.80 Å. However the limits of the range are unrealistic for carbon, and the model should be explored with a narrow distribution around $\theta \sim 2\pi/3$.

5.7 OTHER GLASSY CARBON DIFFRACTION PATTERNS

In this section we give the results of the more recently published data of radial distribution studies of glassy carbon. The original paper on the structure of glassy carbon was that of Noda and Inagaki (1964), who obtained a diffraction pattern of glassy carbon from Tokai out to $Q_{max} = 10.05$ Å^{-1}, using copper and molybdenum K_α radiation. They used an artificial temperature factor such that $\exp(-\alpha Q^2) = 0.1$ at $Q = Q_{max}$. Consequently this convergence factor gives a resolution in the RDF as defined by the full width at half-maximum of 0.5 Å. The RDF of the glassy carbon with a 2000°C heat treatment temperature is shown in Figure 5.10, and the peak positions and coordination numbers are given in Table IV. Peaks at approximately these same positions were found for the 900°C and 1500°C treated samples. The similarity with graphite is not apparent and their coordination numbers (obtained from Lindberg, 1969) are surprising low. The interlayer spacing of their 1800°C sample is given as 3.48 Å by Wright (1969).

TABLE IV

NODA-INAGAKI (1964) 2000°C TOKAI SAMPLE

Coordination Sphere	Glassy Carbon r (Å)	Glassy Carbon n	Graphite r (Å)	Graphite n
1	1.5	3.5	1.42	3
2	2.68	2.6	2.46	6
3			2.84	3
4			3.75	6
5	4.25	4.1	4.25	6
6	5.2	5.0	4.91	6
7			5.11	6

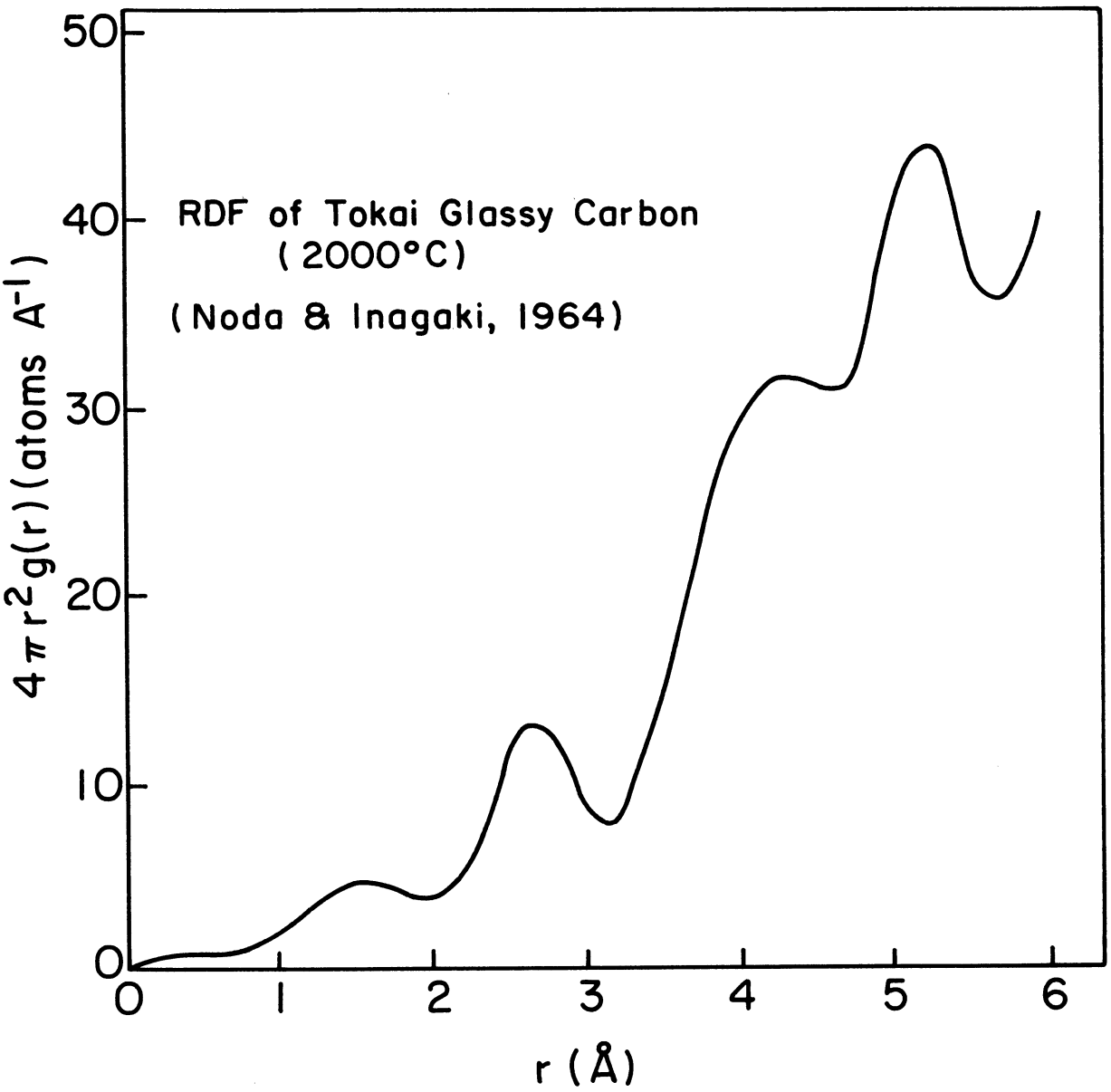

Figure 5.10. The radial distribution function of Tokai glassy carbon.

Further analysis was made of the first peak in the RDF, and is shown in Figure 1.1. It was assumed that the two types of coordination were present, and each had the same equilibrium distance as in the crystalline case. The peak was separated into these two components, each with a Gaussian form. This analysis suggested that the amount of trigonally coordinated atoms in glassy carbon increased with the heat treatment temperature. Although the resolution of their data is insufficient to support their analysis, their ideal of graphitic layers has been borne out by further experiments, except that the amount of tetrahedrally bonded atoms is probably much smaller than they suggest.

Lindberg (1969) took diffraction measurements on Lockheed glassy carbon with heat treatment temperatures of 1000°C, 2000°C, and 3000°C, out to $Q_{max} = 8.0$ Å^{-1} using copper K_{α} radiation. The scattered intensity showed peaks at $Q = 1.72$, 3.03, and 5.18 Å^{-1}. The RDF of the 2000°C sample is shown in Figure 5.11, and the peak positions and coordination numbers are given in Table V. No general trends were seen between the different heat treated temperature samples, in either the coordination numbers or peak distances; though this is not too surprising since the RDF had only a resolution of $\Delta r \sim 0.78$ Å. In addition, the value of g_o used to obtain the coordination numbers was 0.1078 atoms Å^{-3} which was obtained from an estimate of the density neglecting the small pores within the volume. Consequently these numbers need not be too accurate. However Lindberg concludes that glassy carbon has the

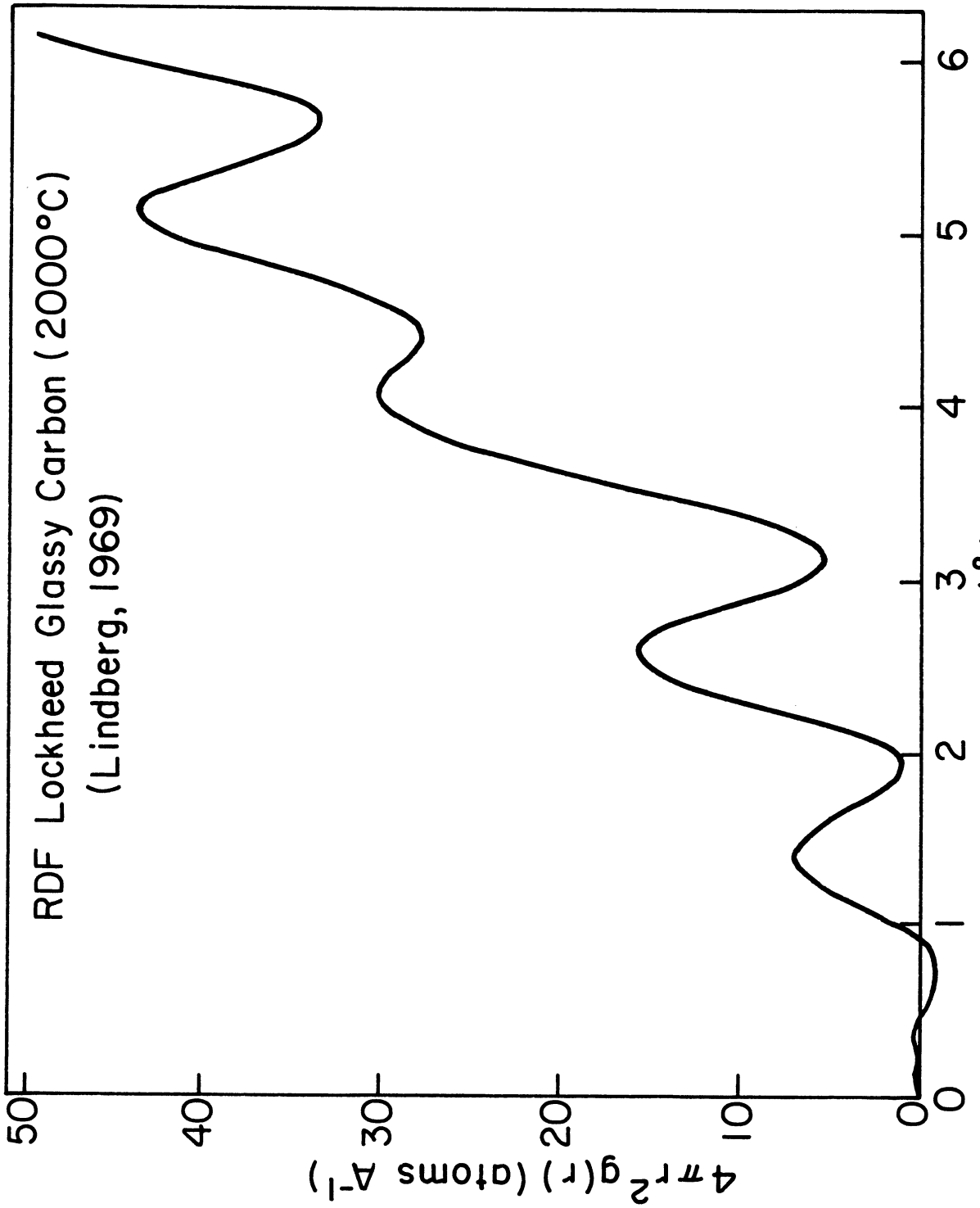

Figure 5.11. The radial distribution function of Lockheed 2000°C glassy carbon.

same nearest neighbor distances as graphite layers, and that the number of atoms at each distance is approximately the same as in graphitic layers.

TABLE V

LINDBERG (1969) 2000°C LOCKHEED SAMPLE

Coordination Sphere	Glassy Carbon r (Å)	Glassy Carbon n	Graphite r (Å)	Graphite n
1	1.43	3.3	1.42	3
2	2.60	9.6	2.46	6
3			2.84	3
4	4.05		3.75	6
5			4.25	6
6	5.12		4.91	6
7			5.11	6

Wright (1969) has obtained an X-ray diffraction pattern out to Q_{max} = 16 $Å^{-1}$ of a Plessy vitreous carbon as shown in Figure 5.12. The sample was prepared by thermal degradation of a phenolic resin, and was subjected to a maximum heat treatment temperature of 1800°C. The sample had a thickness of 2.556 mm, and a density of 1.5183 gm cm^{-3} (or 0.07613 atoms $Å^{-3}$), giving an X-ray transmission of 0.8. From the diffraction pattern, he also concludes that vitreous carbon is composed of units of parallel graphitic layers, with $L_c \sim 20$ Å, and $L_a \sim 30$ Å. A large amount of small angle scattering was found, but was not analyzed. The RDF is shown in Figure 5.13, and the peak positions are given in Table VI. In fact all the peaks out to 10 Å that are expected from

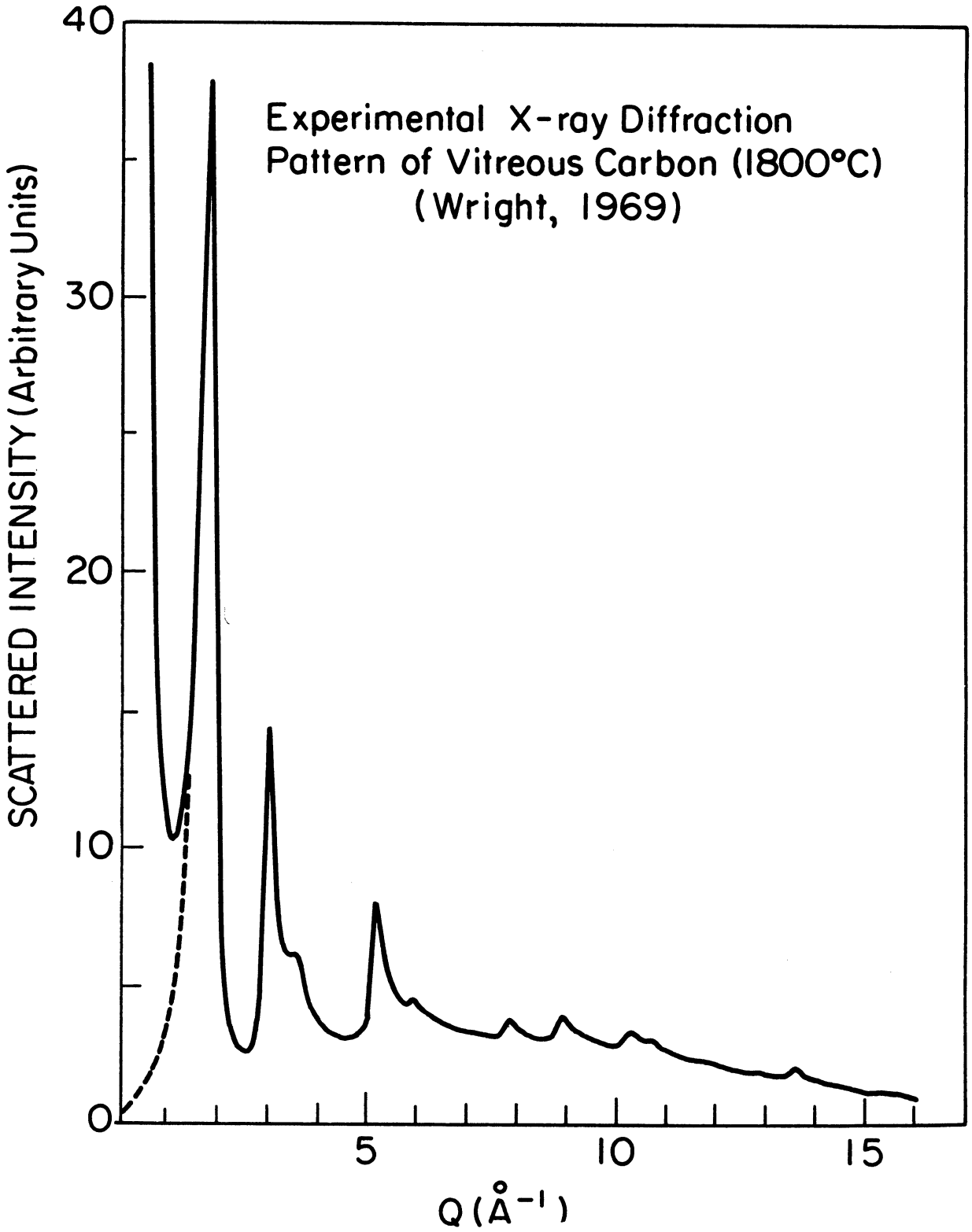

Figure 5.12. Experimental X-ray diffraction pattern of Plessey 1800°C vitreous carbon.

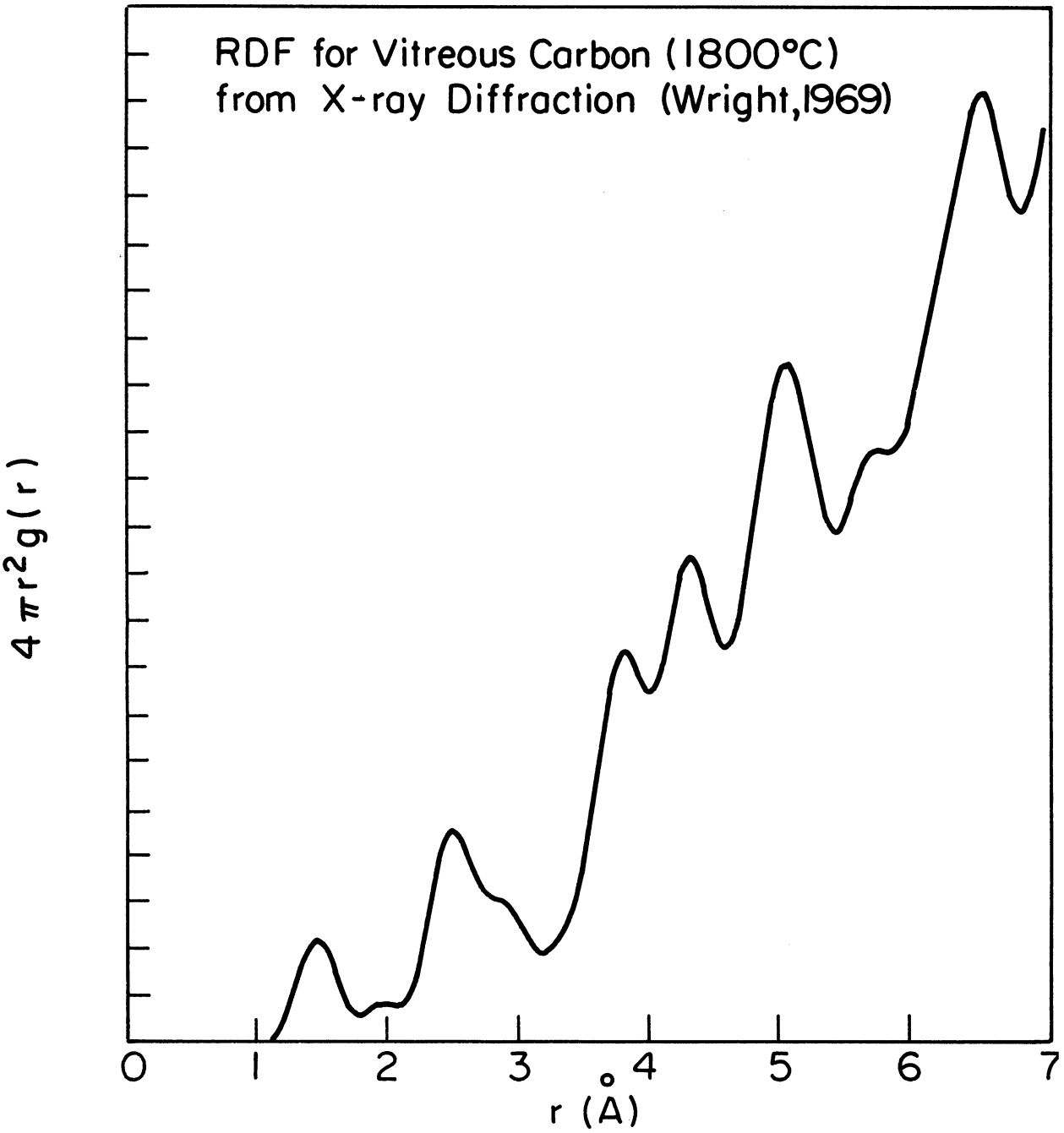

Figure 5.13. The radial distribution function of Plessey 1800°C vitreous carbon.

graphitic layers are believed to be seen with none extra. No coordination numbers are quoted. Apparently Lorch has obtained an unpublished neutron diffraction pattern of this particular sample (Leadbetter and Wright, 1973).

TABLE VI

WRIGHT (1969) 1800°C PLESSEY SAMPLE

Coordination Sphere	Vitreous Carbon r (Å)	Graphite r (Å)	n
1	1.44	1.42	3
2	2.47	2.46	6
3	shoulder	2.84	3
4	3.78	3.75	6
5	4.28	4.25	6
6	5.01	4.91	6
7		5.11	6

Duwez (1971) acquired a diffraction pattern out to $Q_{max} = 17.4$ Å^{-1} of a Beckwith vitreous carbon with a heat treatment temperature of 1800° C (Figure 5.14). The data were taken with copper and molybdenum K_α radiation, and no Compton corrections have been applied. The data is very similar to that of Wright. From the widths and positions of the first two diffraction we have obtained $L_c \sim 28$ Å, and $L_a \sim 34$ Å, and spacings $d_c = 3.59$ Å distance of 1.425 Å.

Ergun and Schehl (1973) have obtained a diffraction pattern of a glassy carbon sample of Fitzer produced from a polymer of furfuryl alcohol with a heat treatment temperature of 3000°C. The data were taken

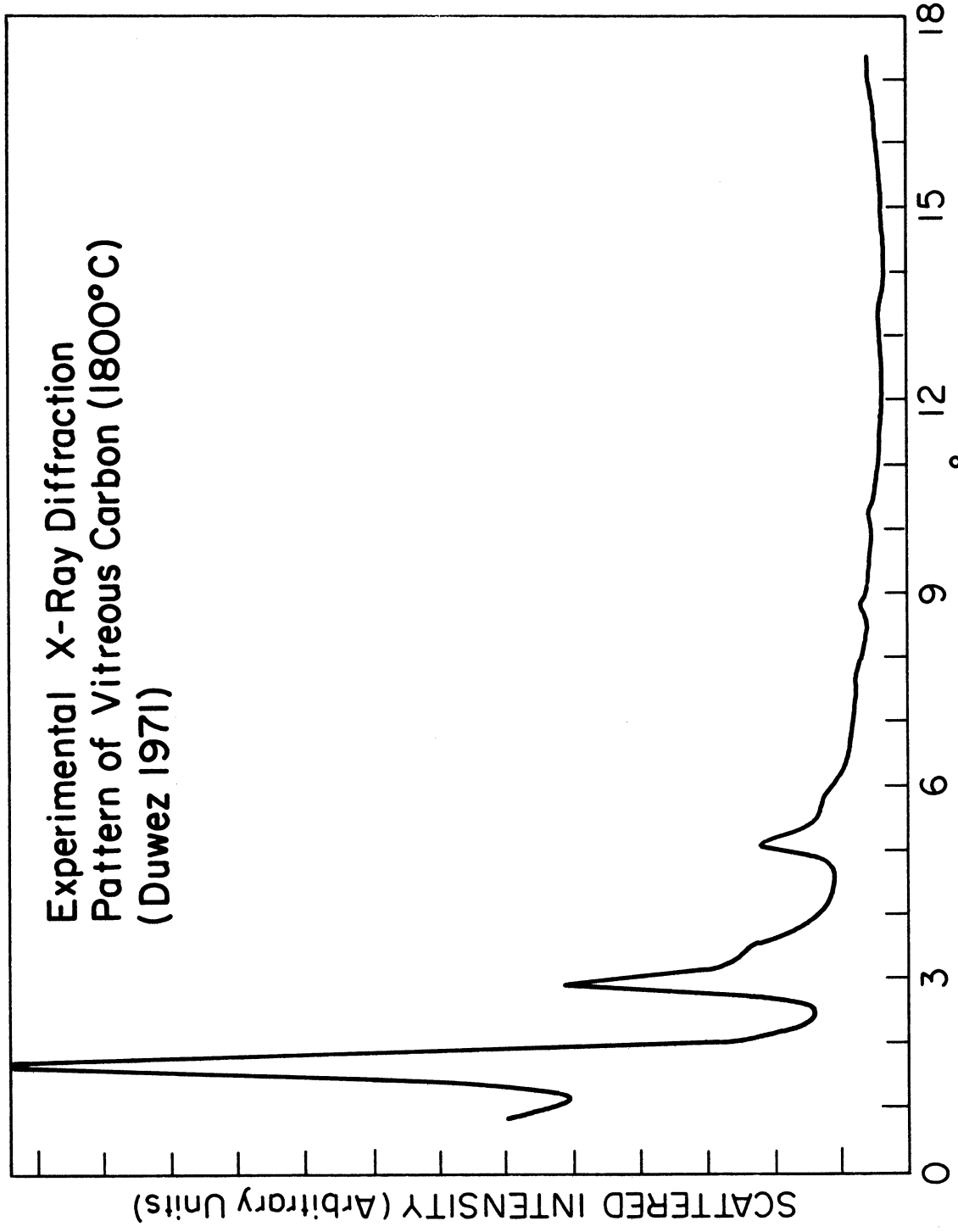

Figure 5.14. Experimental X-ray diffraction pattern of the Beckwith 1800°C vitreous carbon.

using silver K_α radiation. The corrected intensity function is shown in Figure 5.15. The position of the first diffraction peak gives the layer spacing of $d_c = 3.42$ Å $\pm$ 0.03 Å, and the width gives $L_c \sim 30$ Å. However, a detailed analysis of the Fourier transforms of the (ℓk0) reflections gives an interpretation of distorted hexagonal rings with considerable strain, and their conclusion is that these distortion effects outweigh the defect or layer size effects in the observed profiles of the (110) reflection. Ergun (1973) believes that folds are the cause of strain in the lattice and that in the vicinity of faults the possibility of the existence of quinoidal rings are very likely, since the distortion becomes less than in resonating rings. From a diffraction point of view folds constitute defects in the two-dimensional lattice. Ergun was the first to suggest that perhaps glassy carbon is composed of layers of quinoidal rings rather than hexagonal rings.

Wignall and Pings (1974) have most recently obtained a diffraction pattern out to $Q_{max} = 14.$ Å^{-1} of a sample of vitreous carbon from Vitreous Carbons (Beckwith) which has been subjected to a maximum temperature of 1800°C. The sample had a thickness of 1.28 mm, and a mean density of 1.484 gm cm^{-3}. The data were taken using molybdenum K_α radiation, and the corrected intensity function is shown in Figure 5.16. The RDF showed remarkable similarity to the correlations of carbon black (Ergun, 1968), and the nearest neighbor distance of 1.40 Å was obtained from the second diffraction peak. No significant amount of tetrahedral

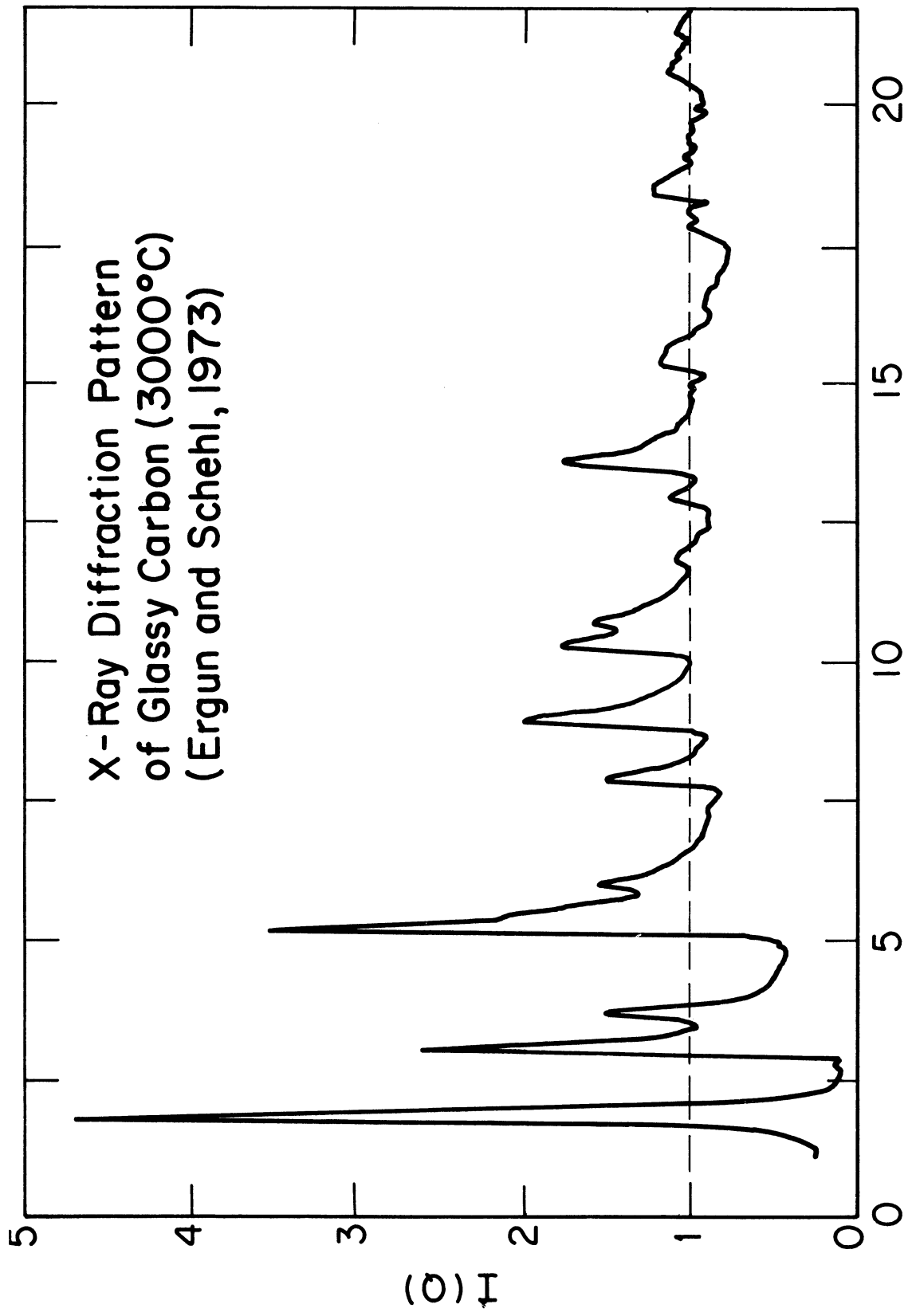

Figure 5.15. X-ray diffraction pattern of the Fitzer 3000°C glassy carbon.

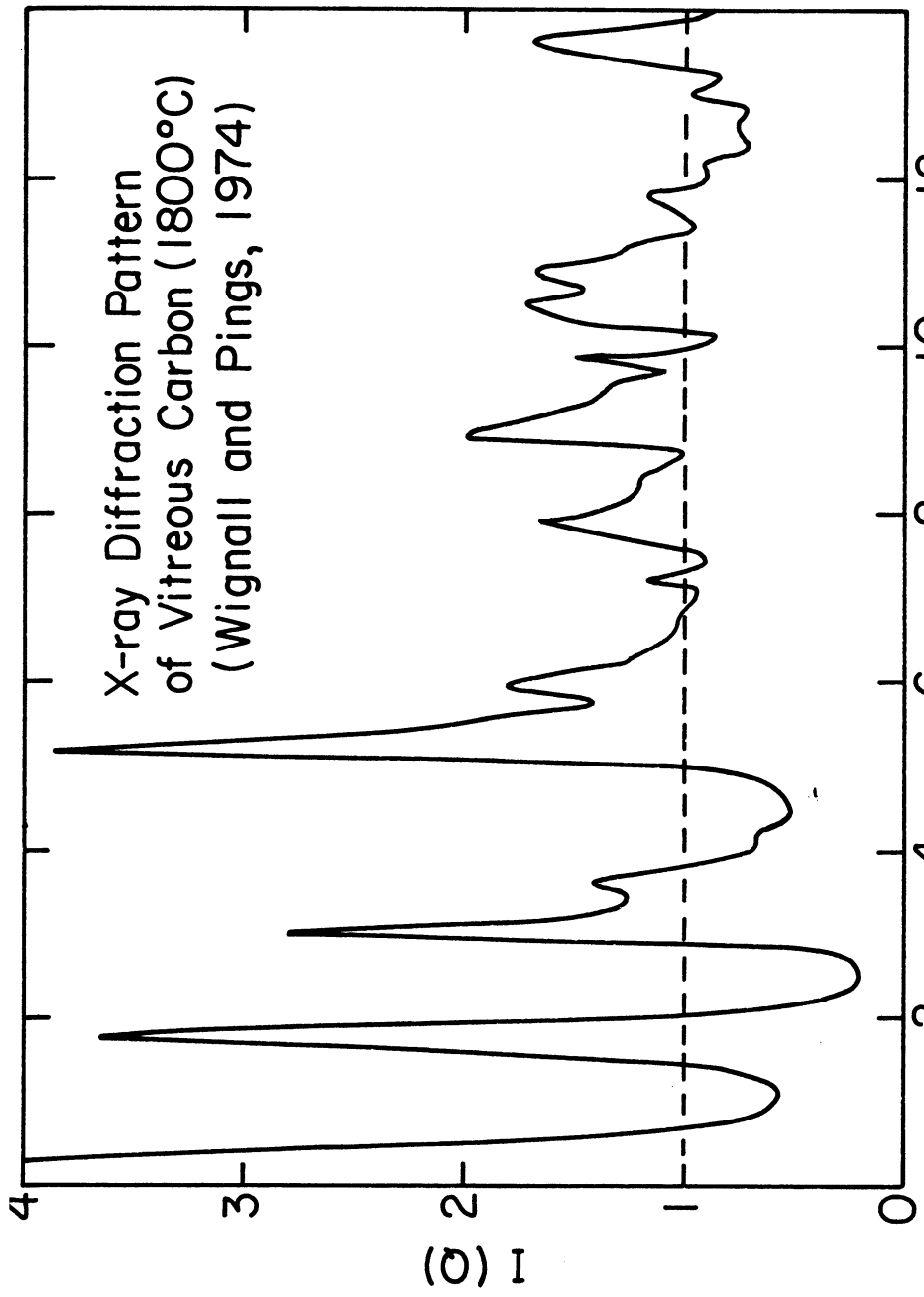

Figure 5.16. X-ray diffraction pattern of 1800°C vitreous carbon from Vitreous Carbons.

bonding was found. From the widths and positions of the diffraction peaks, they obtained $L_c \sim 15$ Å, and $L_a \sim 22$ Å, and a layer spacing of $d_c = 3.54$ Å. This spacing is higher than in graphite, and they attribute this to the fact that there is no correlation between adjacent parallel graphitic layers.

CHAPTER VI. SMALL Q DIFFRACTION

6.1 SMALL Q DIFFRACTION ANALYSIS

In this section, we consider possible explanations for the experimental forward angle scattering. We play the 'small Q game' of fitting the data to known theoretical forms for the size and shape of the pores to obtain an estimate of the local atomic density for comparison with bulk density measurements. All the formulae in this section will apply to a homogeneous medium; i.e., the voids are assumed identical and uniformly distributed throughout the system.

Applying formulae originally developed for small angle X-ray scattering, we consider integral relations of the diffracted intensity which describes scattering from voids (Guinier and Fournet, 1955). The void volume V_v and its characteristic length $\bar{l}$ (the mean length of all lines passing through every point of the void in all directions and ending on the surface of the void) are given by

$$\int_0^\infty Q^2\, i(Q)\, dQ = \frac{2\pi^2}{V_v}\, i(0), \tag{6.1}$$

and

$$\int_0^\infty Q\, i(Q)\, dQ = \frac{2\pi}{V_v}\, \bar{l}\, i(0). \tag{6.2}$$

Since the small Q diffraction (Figure 4.13) is more intense that the large Q diffraction, the whole pattern may be approximated by

$$S(Q) = Ae^{-\alpha Q} + b^2, \tag{6.3}$$

and

$$i(Q) = \frac{A}{b^2} e^{-\alpha Q}, \tag{6.4}$$

where $\alpha = 13.6$Å. This gives $\bar{l}$ from equations (6.1) and (6.2); i.e.,

$$\bar{l} = \pi/2\alpha = 21.36 \text{ Å}. \tag{6.5}$$

Hence if the small-Q scattering may be approximated by a simple exponential from, then the mean chord length may be determined from the slope of the intensity as a function of Q. It will be seen later however, that the scattered intensity is proportional to Q^{-3} (instead of Q^{-4}) in the wings of the small Q curve. Guinier and Fournet (1947) have shown that in this case the appropriate integrals become

$$1/2 \int_o^\infty Q\, i(Q)\, dQ = \frac{2\pi^2}{V_v} i(0), \tag{6.6}$$

and

$$1/\pi \int_o^\infty i(Q)\, dQ = \frac{2\pi}{V} \bar{l}\, i(0), \tag{6.7}$$

where

$$i(Q) = \frac{\pi}{2} Q\, i(Q). \tag{6.8}$$

Hence the simple exponential form $e^{-\alpha Q}$ gives $\bar{l}$ equal to α exactly. That is, the mean chord length is the characteristic void length; viz.,

$\bar{l}$ = 13.6 Å. The integrals also give a void volume,

$$V_v = 4\pi\alpha^3 = 3.16\ 10^4\ \text{Å}^3. \tag{6.9}$$

If equation (6.3) is transformed by the Zernicke-Prins relation (equation (2.47)), where

$$I(Q) = N\,S(Q) \tag{6.10}$$

and

$$I(\infty) = N\,S(\infty) = Nb^2, \tag{6.11}$$

N being the total number of scatterers exposed to the incoming beam, then

$$\begin{aligned} 4\pi r(g(r) - g_o) &= \frac{2}{\pi}\int_o^\infty Q\,\frac{A}{b^2}\,e^{-\alpha Q}\sin Qr\,dQ \\ &= \frac{2}{\pi}\frac{A}{b^2}\left(-\frac{\partial}{\partial\alpha}\right)\int_o^\infty e^{-\alpha Q}\sin Qr\,dQ \\ &= \frac{2}{\pi}\frac{A}{b^2}\,\frac{2\alpha r}{(\alpha^2 + r^2)^2}. \end{aligned} \tag{6.12}$$

This shows the deviation due to small-scale voids of the atomic density g(r) from its average value g_o. Note that at small r, g(r) approaches the local variation in atomic density which is obtained from the inversion of the extended diffraction pattern.

The variation in g(r) is given by

$$g(r) = g_o\left[1 + \frac{0.4188}{(1 + (r/13.6)^2)^2}\right] \tag{6.13}$$

and is shown in Figure 6.1. It may be fitted to a macroscopic parameter at infinite r. For at large r the value of g_o is given by 0.0747 atoms $Å^{-3}$, the atomic density corresponding to a density of 1.49 gm cc^{-1} obtained by mercury porosimetry, which method determines the bulk density neglecting the large scale pores. This yields a value of the local density of 0.1060 atom $Å^{-3}$ at zero r. Obviously a slightly different value would be obtained had not the structure factor S(Q) be approximated by equation (6.3), where the extended Q diffraction was assumed to be constant. However to be remarked is that the local density is very close to a local atomic density of 0.1106 atom $Å^{-3}$ which was obtained in section 5.5 by analogy with graphite using a plane spacing of 3.46 Å.

The slope of the small Q data depends on the void size, provided that the voids have a convex shape. It is important to note that the small Q neutron diffraction results do not appear to be obeyed by a conventional form for small angle scattering (Guinier, 1939). For example, Guinier's law for distinct globular voids with random orientation, widely distributed within a homogeneous material of constant atomic density, is given by

$$I(Q) \propto \exp(- Q^2 R_G^2/3) \qquad (6.14)$$

where R_G is the radius of gyration of the void, and the region of validity is $Q \lesssim 0.6\pi/R_G$. The characteristic void dimension is 13.6 Å, so that one might expect a Guinier law compliance for $Q < 0.14$ Å. The

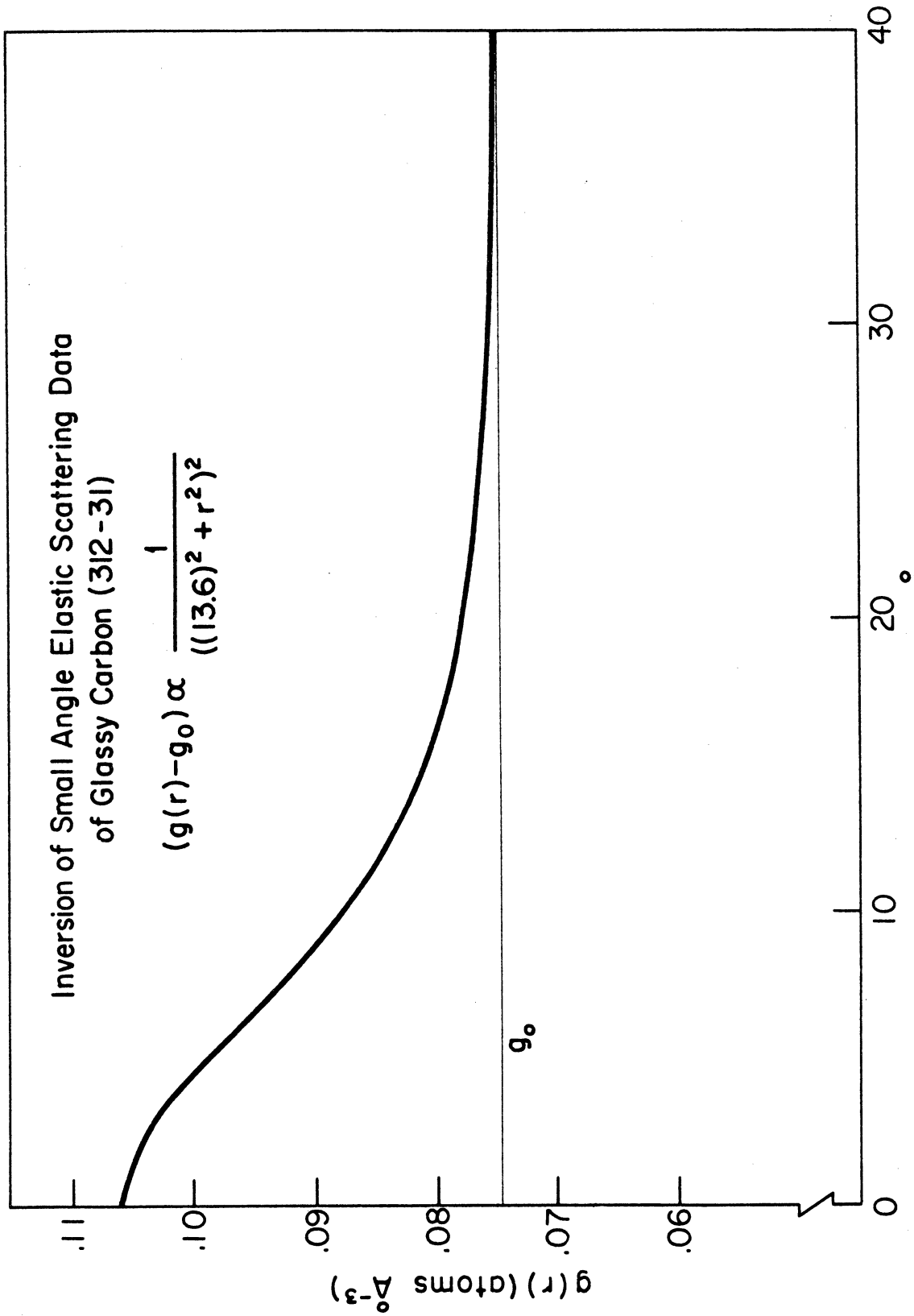

Figure 6.1. The transformation of the exponential fit to the small Q scattering, showing the variation of the average atomic density on function of atomic distance due to small scale voids.

lower limit of the small Q neutron diffraction results is $Q = 0.065$ Å^{-1}, and it is probable that there are deviations from the simple exponential form around this value.

Although the data are outside the limitations of the Guinier curve, one might expect in the wings that the intensity is given by Porod's law (1952). For at the large Q extremity of the small angle region, the scattered intensity is given by

$$I(Q) \propto Q^{-4} \tag{6.15}$$

This law is valid in the region $QL \gg 1$, and for any void shape provided that the orientation is random. If the data are plotted as log I(Q) versus log Q (see Figure 6.2), it will be seen that there is a range, 0.15 Å$^{-1} < Q < 0.6$ Å^{-1}, over which that data may be approximated by a straight line. It is obvious from the Porod plot that reasonable agreement is given by the relationship

$$I(Q) \propto Q^{-3}. \tag{6.16}$$

Moreover, if the scattering due to the first diffraction peak is extrapolated to smaller Q and subtracted from the higher intensity region, then equation (6.16) is a good fit for all $Q > 0.15$ Å^{-1} (Figure 6.3). The X-ray Porod plot for $Q > 0.15$ Å^{-1} is shown in Figure 6.4, and it also obeys a Q^{-3} law. Porod (1952) states that the straight line portion indicates a sharp density transition from one phase to another;

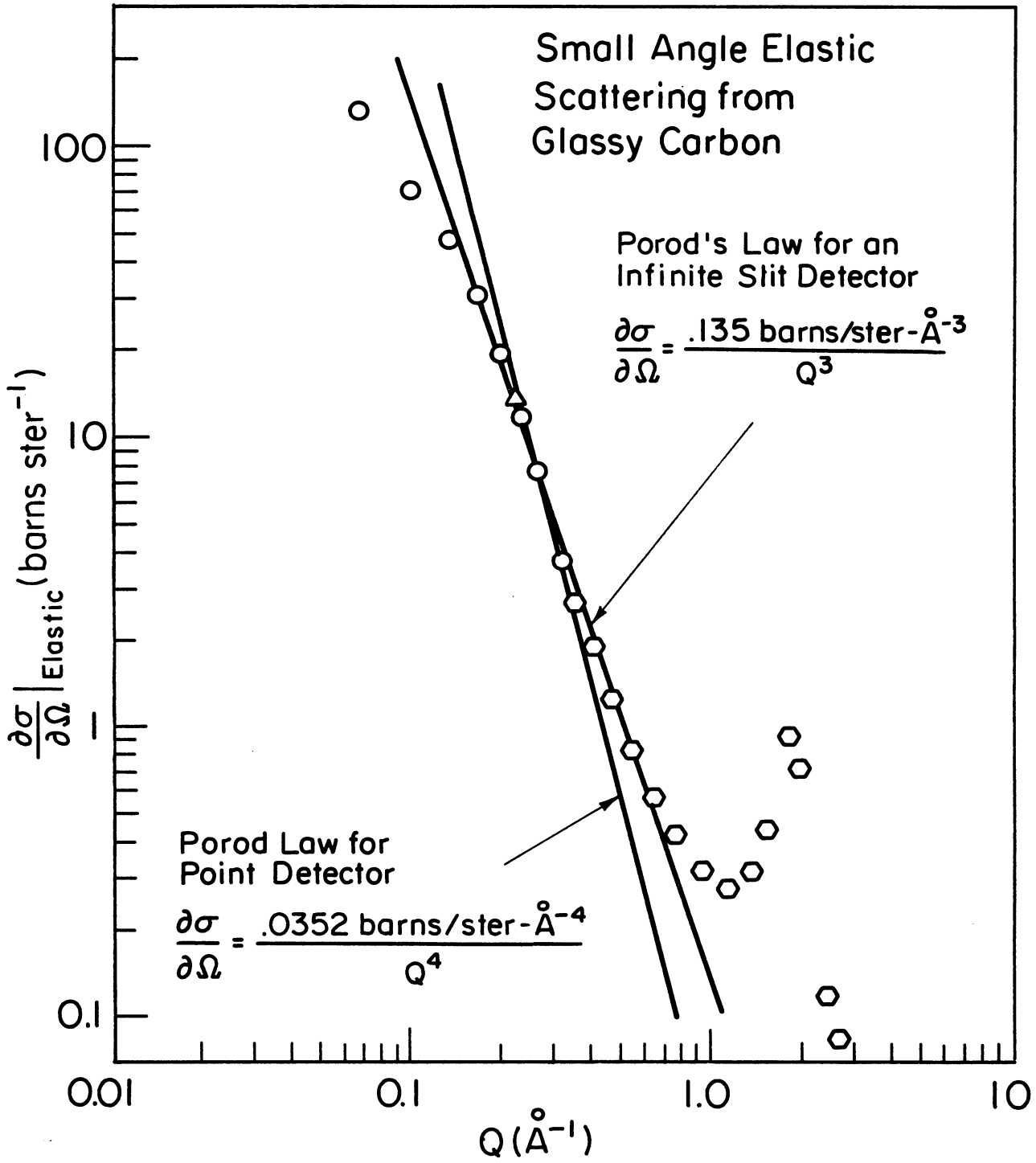

Figure 6.2. The Porod plot of the uncorrected small Q scattering of glassy carbon.

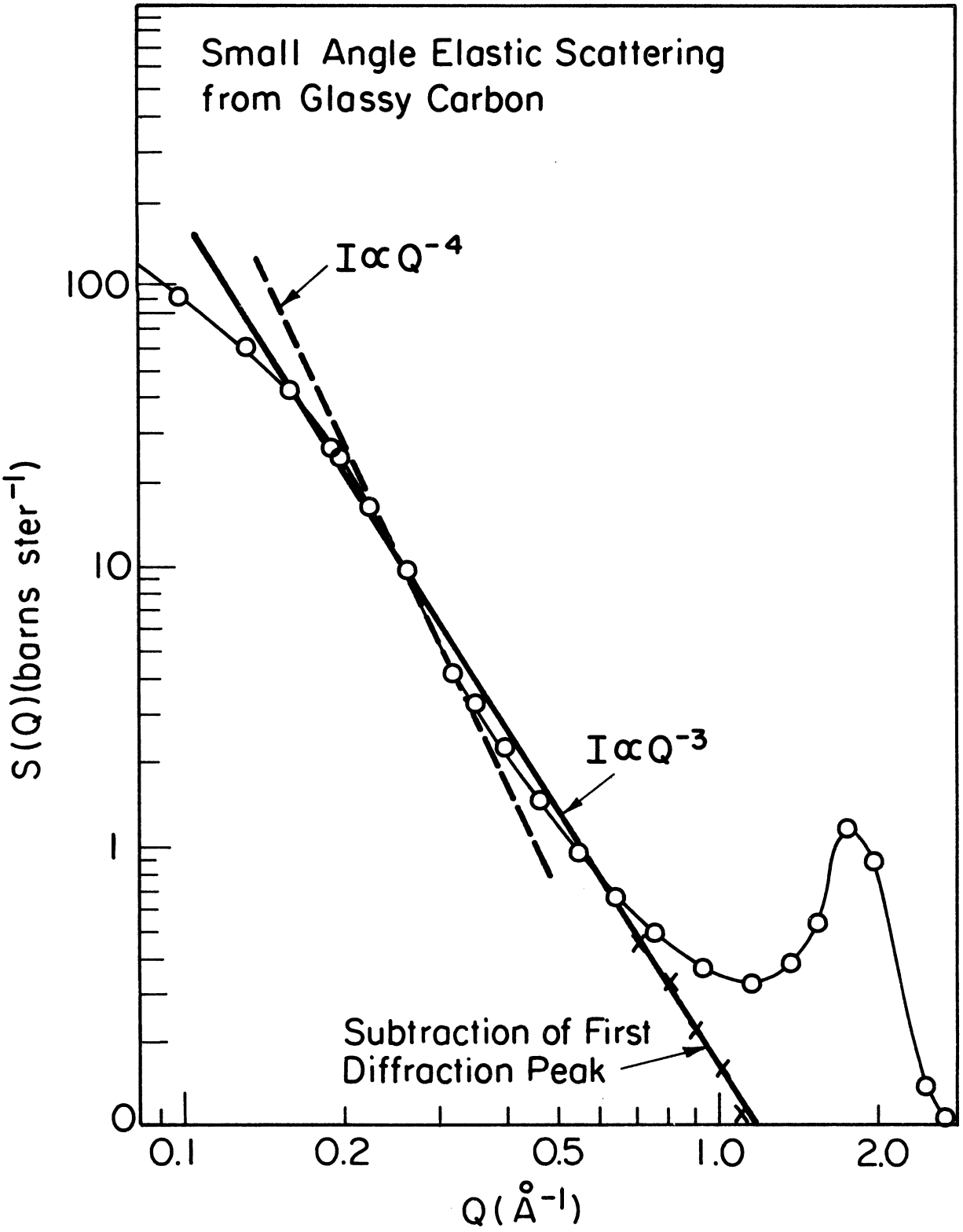

Figure 6.3. The Porod plot of the corrected small Q scattering of glassy carbon with the first diffraction peak subtracted as in Figure 4.13.

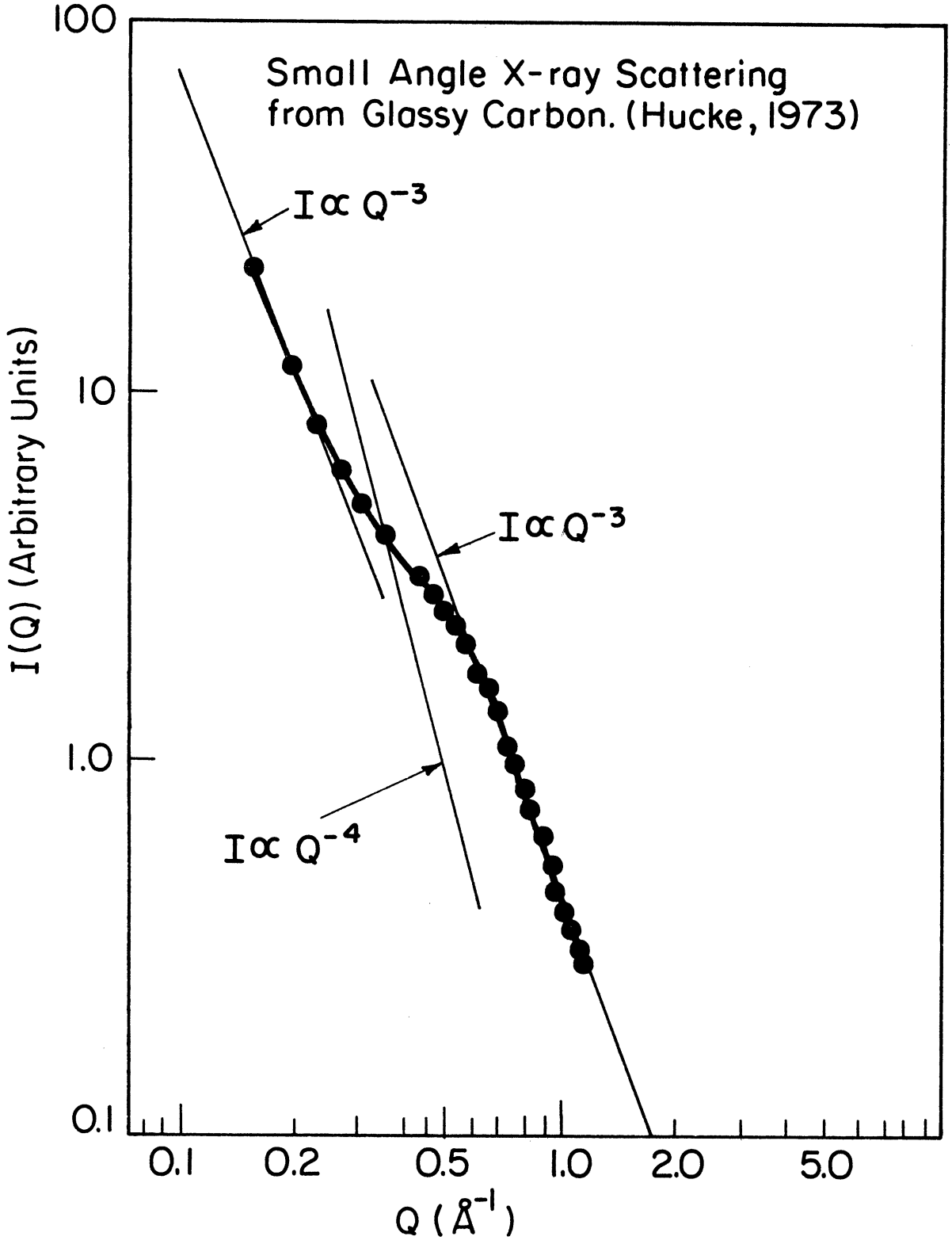

Figure 6.4. The Porod plot of the small angle X-ray scattering from glassy carbon.

i.e., void to material. Hence it is believed that the small scale voids are not interconnecting.

In general, small Q scattering experiments are capable not only of giving the size and shape of the voids, but also of giving the distribution of pores sizes. However if the voids are close together, important interference effects occur, especially if these voids have some form of regular arrangement as might be expected for glassy carbon. Schmidt (1958) has shown that at very low Q, interference effects between small and large-scale voids distort the Guinier relationship. The results of that part of the small Q X-ray diffraction measurements which covers a range will within the Guinier limitations (section 6.3) suggest that the voids are polydisperse (Hucke, 1973). It would seem therefore that interference effects between the small and large voids are apparent for $Q \sim 0.15$ $Å^{-1}$.

6.2 DIFFRACTION REGIONS

In the discussion of the diffraction from glassy carbon, it is found that the scattering can be separated into distinct regions because of the large and small-scale voids found within the sample. The three regions correspond to: (1) the very low Q diffraction characteristic of large-scale voids; (2) the samll Q diffraction characteristic of small-scale voids; and (3) the large Q diffraction characteristic of interference of neighboring atoms. Since mercury porosimetry measurements (Hucke, 1972) have shown that there are large scale voids of dimensions ~ 250 Å, the first region extends in wave vector transfer range, $0 < Q < Q_1 \simeq 0.025$ Å^{-1}. The second region is below the first diffraction peak at $Q \simeq 1.8$ Å, and has small-scale voids of characteristic length 13.6 Å within the dense material; the range of the region is $Q_1 < Q < Q_2 \simeq 1$ Å^{-1}. The third region has the range $Q > 1$ Å^{-1}, which is the normal diffraction region characteristic of interatomic spacings.

The normalized intensity i(Q) defined by equation (2.44) may be separated into three functions characteristic of each region, viz.,

$$i(Q) = i_1(Q) + i_2(Q) + i_3(Q). \tag{6.17}$$

The separation is fortuitously convenient because three scales of order exist, and we further make the assumption that the relative magnitudes of these functions are such that they differ by an order of magnitude for different regions in the diffraction pattern (see Figure 6.5). That is,

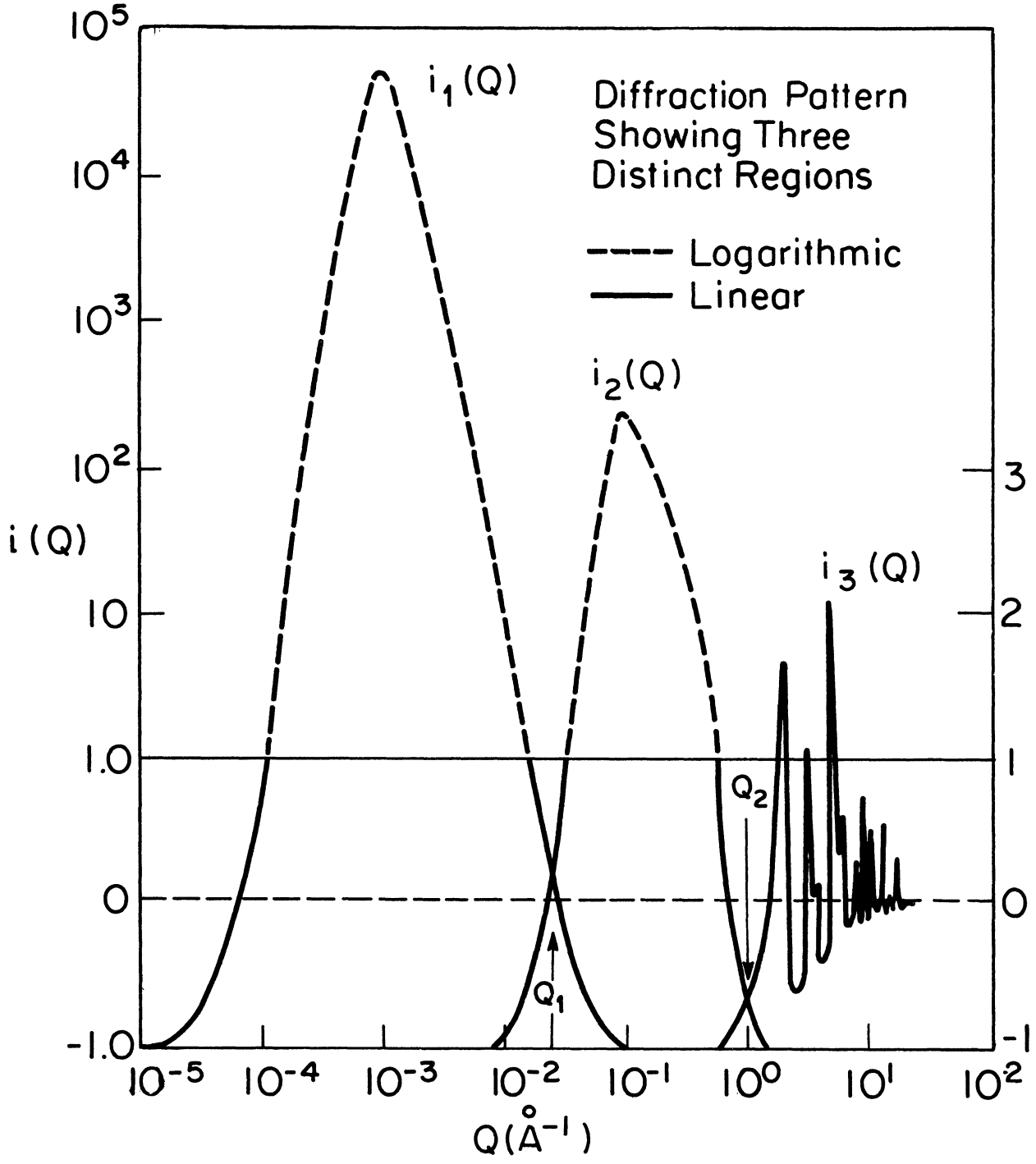

Figure 6.5. A schematic diffraction pattern of glassy carbon showing three distinct regions in wave vector transfer.

$$\text{(i)}\quad i_1(Q) \gg i_2(Q), \text{ for } Q \lesssim Q_1$$
$$i_1(Q) \ll i_2(Q), \text{ for } Q \gtrsim Q_1, \tag{6.18}$$

and

$$\text{(ii)}\quad i_2(Q) \gg i_3(Q), \text{ for } Q \lesssim Q_2$$
$$i_2(Q) \ll i_3(Q), \text{ for } Q \gtrsim Q_2. \tag{6.19}$$

Hence we may divide the diffraction pattern into three distinct regions within which the diffraction pattern is approximated by one of the three functions

$$(1)\ i(Q) \simeq i_1(Q), \text{ for } 0 < Q < Q_1, \tag{6.20}$$

$$(2)\ i(Q) \simeq i_2(Q), \text{ for } Q_1 < Q < Q_2, \tag{6.21}$$

$$(3)\ i(Q) \simeq i_3(Q), \text{ for } Q_2 < Q. \tag{6.22}$$

If we ignore all the small Q scattering, by extrapolating the first diffraction peak at low Q as in Figure 4.13, then i(Q) is approximated by $i_3(Q)$. Fourier inversion gives

$$4\pi r^2(g(r) - g_3) = \frac{2r}{\pi}\int_0^\infty Q\, i_3(Q) \sin Qr\, dQ, \tag{6.23}$$

where g_3 is an average local atomic density as introduced in section 2.6. It could be defined as the limiting atomic density on a 'local' scale as r becomes large, but smaller than the distance between the voids. That is, presumably for $r \ll 2\pi/Q_2 \sim 6$ Å. $i_3(Q)$ therefore is

the intensity shown in Figure 4.7 with the small Q scattering subtracted. The inversion of the extended Q diffraction only is shown in Figure 6.6. It therefore has the normalization as used previously; viz., the Krogh-Moe procedure with $g_o \equiv g_2$ in equation (3.32); though as before we note that the value of g_o is very sensitive to small changes in $I(\infty)$.

Since there is an effective exclusion of an atom from the immediate neighborhood of another atom, then $g(r) = 0$ for $r < R_1$, the first neighbor distance. Then equation (6.23) becomes

$$\int_o^\infty Q\, i_3(Q) \sin Qr\, dQ = -2\pi^2 r g_3. \tag{6.24}$$

Integration of equation (6.23) from $r = 0$ to $R < R_1$ gives

$$\begin{aligned} \int_o^R 4\pi r^2 (g(r) - g_3)\, dr &= \int_o^R - 4\pi r^2 g_3\, dr \\ &= - g_3 \tfrac{4}{3}\pi R^3, \end{aligned} \tag{6.25}$$

or

$$g_3 \simeq \bar{g}(R) = - \frac{1}{4/3\pi R^3} \int_o^R 4\pi r^2 (g(r) - g_3) dr. \tag{6.26}$$

The function $\bar{g}(R)$ determined from the transformed data is shown in Figure 6.7, but no useful value of g_3 can be estimated. The fact that $\bar{g}(R)$ rise to a value equal to g_3 obtained by analogy with graphite is entirely coincidental. Without termination wiggles which are most troublesome at small r, the function $\bar{g}(R)$ would be identically equal to g_3 for all $R < R_1$.

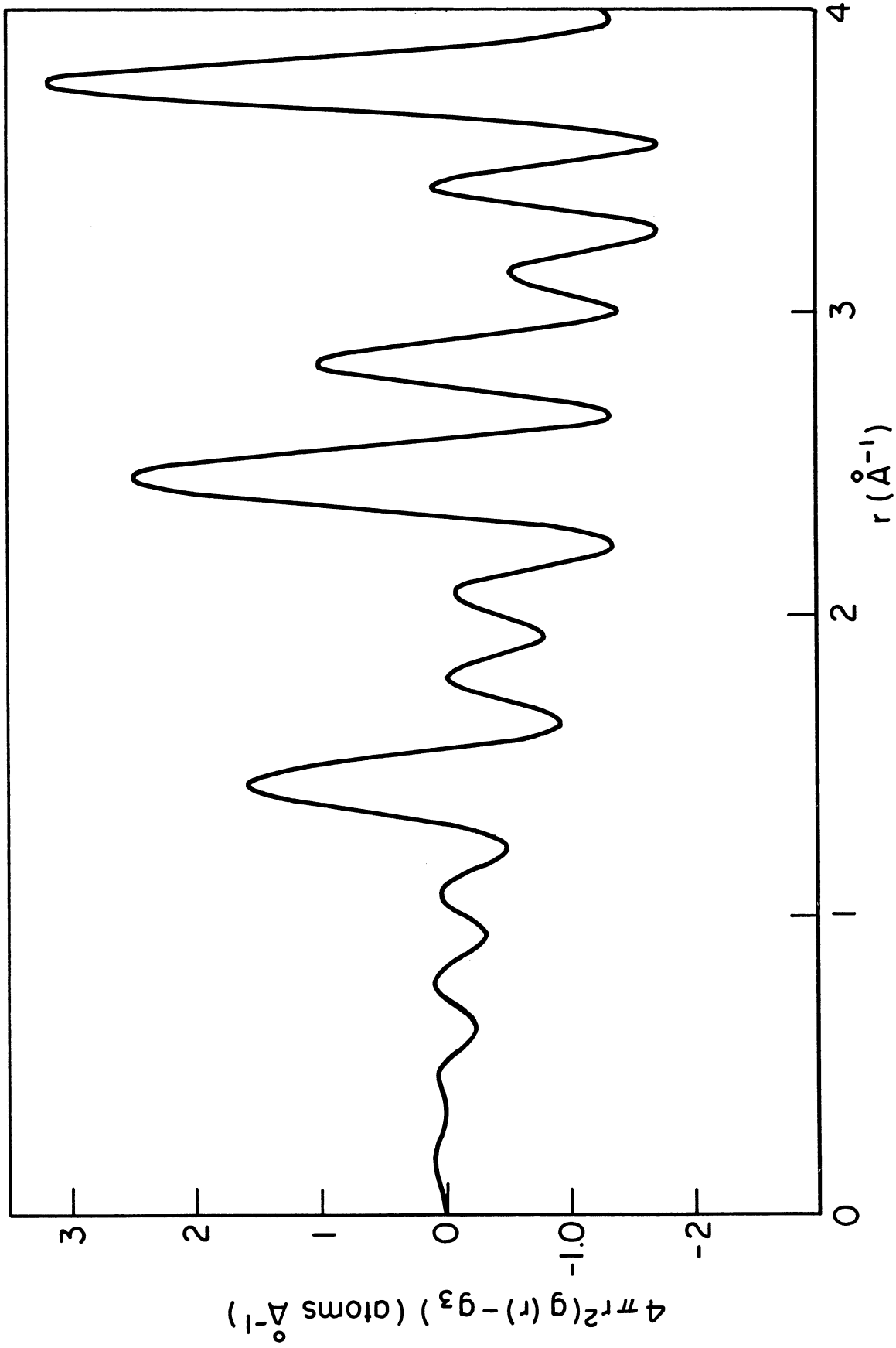

Figure 6.6. The Fourier inversion of the extended Q neutron diffraction pattern of glassy carbon only.

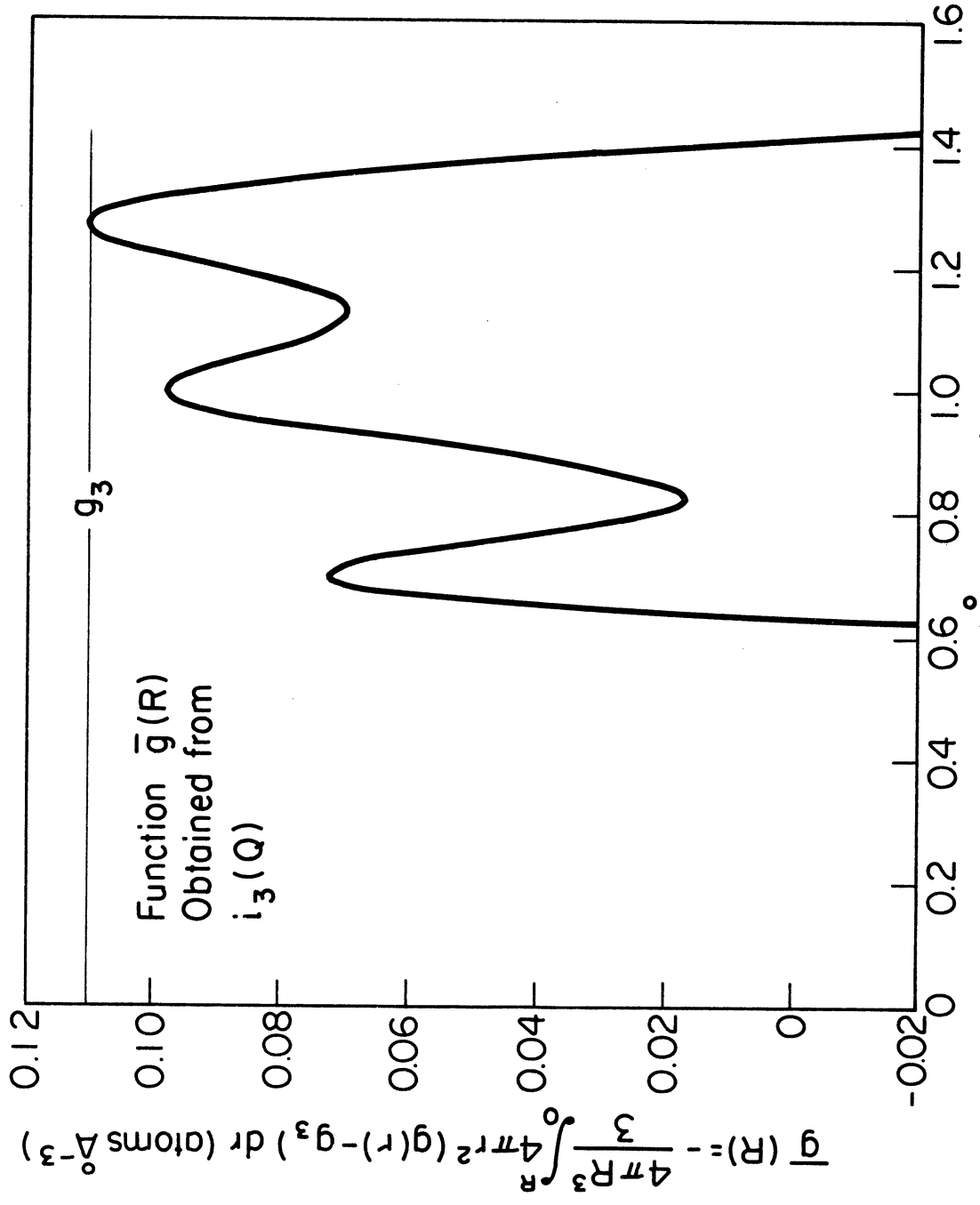

Figure 6.7. The function $\bar{g}(R)$ from the extended Q neutron diffraction pattern only. Termination errors prevent a determination of g_3.

If neighboring atoms are neglected, and i(Q) is approximated by $i_2(Q)$, then equation (6.12) is obtained where $g_o \equiv g_2$, the microscopic atomic density. Figure 6.1 shows the atomic density variation due to small scale voids. Note that the density decreases with increasing r, which shows the effect of voids in constrast to the Fourier transform of $i_3(Q)$. The same effect will be shown by the Fourier inversion of $i(Q) = i_1(Q)$; that is,

$$4\pi r^2(g(r) - g_1) = \frac{2r}{\pi} \int_o^\infty Q\, i_1(Q) \sin Qr\, dQ. \tag{6.27}$$

This gives the atomic density variations due to the larger scale interconnecting voids. Its limiting value g_1 may be determined from the macroscopic density of 0.923 gm cc^{-1} determined by mercury immersion.

Now combine all three functions

$$\begin{aligned} g(r) - g_o &= \frac{1}{2\pi^2 r} \int_o^\infty Q\, i(Q) \sin Qr\, dQ \\ &= \frac{1}{2\pi^2} \left[\int_o^\infty Q^2 i_1(Q) \frac{\sin Qr}{Qr}\, dQ + \right. \\ &\quad \left. \int_o^\infty Q^2 i_2(Q) \frac{\sin Qr}{Qr}\, dQ + \int_o^\infty Q^2 i_3(Q) \frac{\sin Qr}{Qr}\, dQ\right], \end{aligned} \tag{6.28}$$

where $g_o \equiv g_1$, the macroscopic atomic density (schematically shown in Figure 6.8). There will be two natural divisions in the radial distribution function due to the assumptions originally made for i(Q). These will occur at $r_1 \sim 2\pi/Q_1$, and $r_2 \sim 2\pi/Q_2$ giving three regions of interest. For $0 < r \lesssim r_2$, the RDF will show the local ordering of atoms with a mean value of g_3, the local atomic density. For $r_2 \lesssim r \lesssim r_1$, the

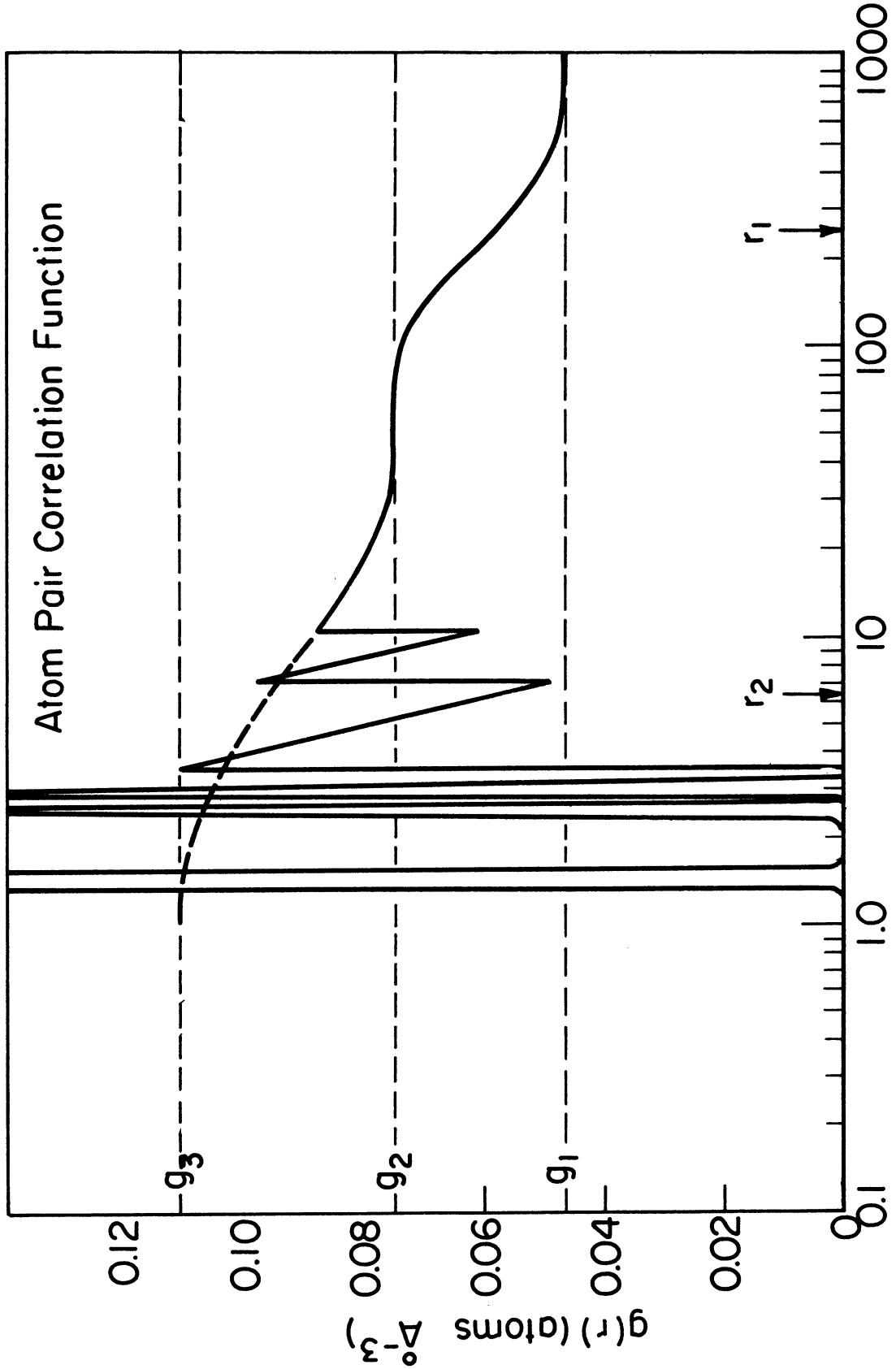

Figure 6.8. A schematic atom-pair correlation function showing three distinct regions. The first region only shows the first three in-plane correlations and the first three variations due to out-of-plane correlations. The other regions correspond to small and large-scale voids.

value of $g(r)$ will tend towards g_2, the microscopic atomic density, and for $r \gtrsim r_1$, the value tends towards g_1, the macroscopic atomic density.

Hence with the above assumptions about the relative effects of the small and large scale voids, the radial distribution function may be estimated. The local ordering of atoms in the glassy carbon is determined from the large Q diffraction pattern which was measured by neutron time-of-flight diffraction out to $Q < 25$ Å, while the longer range variations are resolved by small Q diffraction. In practice the first diffraction region given by $i_1(Q)$ is considerably modified by multiple scattering, and in fact has not been measured. Hence we have transformed only the other two parts (see section 5.1).

6.3 SMALL SCALE LAMELLAR VOIDS

Kratky and Porod (1949) have given relations analogous to the Guinier equation (6.14) for the small Q scattering from lamellar voids whose radii of gyration are given by $R_1 \sim R_2 \ll R_3$, where $R_3^2 = H^2/12$, H being the disc thickness, and $R_1 < R_2 = R/2$, R being the disc radius; viz.,

$$I(Q) \propto \frac{1}{Q^2} \exp(- R_3^2 Q^2), \tag{6.29}$$

in the region, $2\pi/R_1 \lesssim Q \lesssim 0.6\pi/R_3$, and

$$I(Q) \propto \exp(- R_1^2 Q^2), \tag{6.30}$$

in the region, $Q \lesssim 2\pi/R_1$. A plot of log $[Q^2\ I(Q)]$ versus Q^2 for the neutron small Q data is shown in Figure 6.9. The straight portion for $0.024\ \text{Å}^{-2} \lesssim Q^2 \lesssim 0.1\ \text{Å}^{-2}$ has a slope which gives $R_3^2 = 11.7\ \text{Å}^2$, or an average thickness, H, of the lamellae of 11.8 Å. The experimental upper limit of the validity of this equation is $Q = 0.32\ \text{Å}^{-1}$, which is well within the theoretical limit of $Q \lesssim 0.6\pi/R_3 = 0.55\ \text{Å}^{-1}$.

In addition, integral relation analysis (section 6.1) gives a void volume of $3.16\ 10^4\ \text{Å}^3$. For a lamellar thickness, H, of 11.8 Å, the radius of the lamellar disc is 29.2 Å. Hence the diameter of these voids is 58.3 Å, which is a remarkably close fit to the crystallite size, $L_a \sim 50$ Å by neutrons, and 56 Å by X-rays, from the (10) diffraction peak.

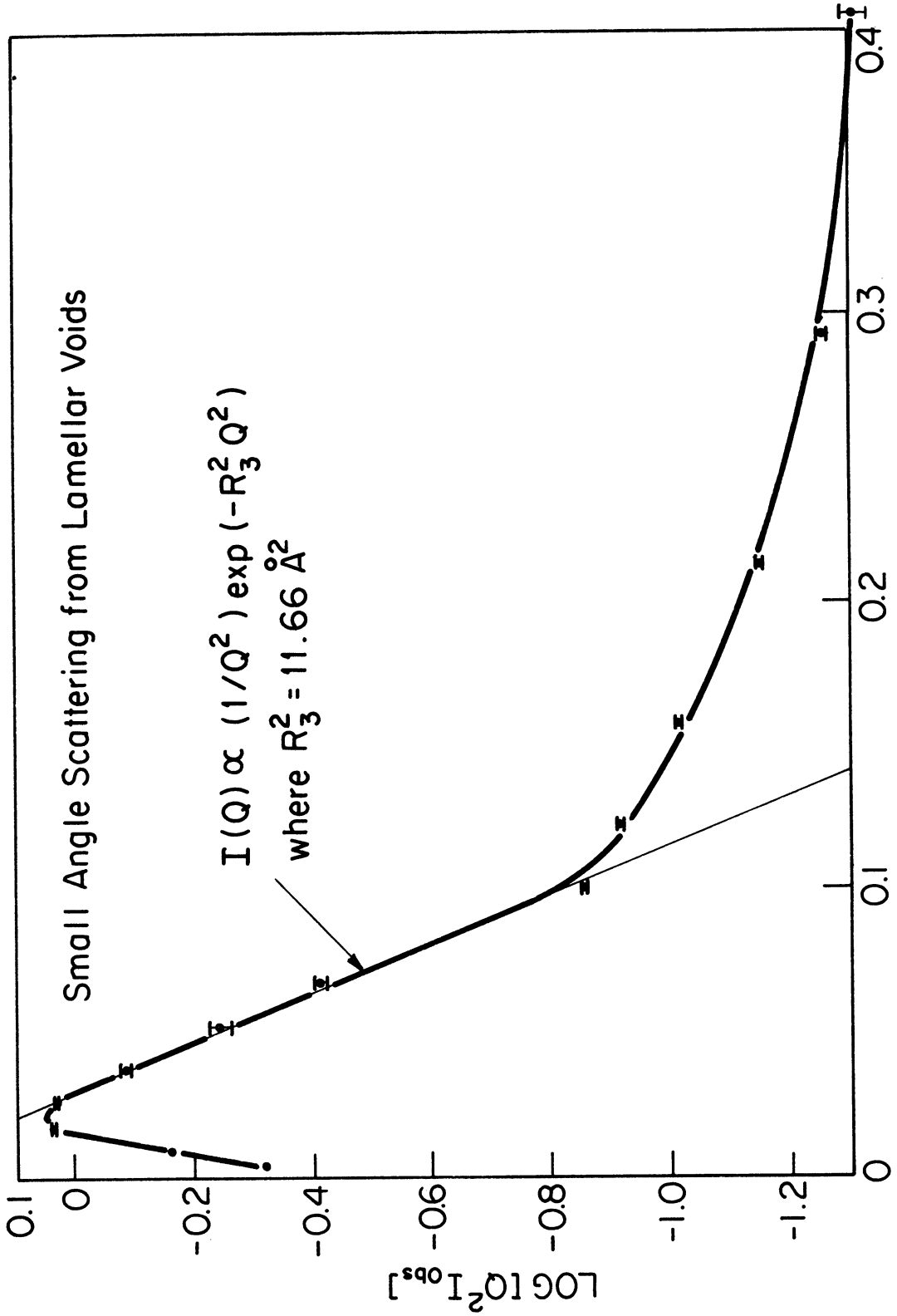

Figure 6.9. The Guinier plot for lamellar voids for the small Q neutron scattering from glassy carbon.

Since the experimental lower limit of the Guinier fit is $Q \sim 0.155$ $Å^{-1}$, then $R_1 \gtrsim 40.5$ Å, giving the average radius of the lamellar disc, $R \sim 81$ Å. Presumably the diameter, ~ 160 Å, should be compared with platelet distances found by electron micrography which were originally found to be between 200 Å and 500 Å, though a later measurement gave distances of the order of 150 Å (Hucke, 1972). Additionally dark field electron microscopy gave a distance greater than 100 Å in the (100) direction. The discrepancy of these distances with the void diameter found by the Guinier fit for lamellae may be explained either by interference effects or inhomogeneity. However, we shall assume that these voids are wedge-shaped between adjacent crystallites, and lie perpendicular to the (00.2) direction of the crystallites.

In order to interpret the small Q scattering data extrapolated to $Q = 0$ given by equation (4.77), it is necessary to consider the total number of scattering nuclei; vix., $g_2 V$. Then

$$I(0) = A g_2 V. \tag{6.31}$$

If we assume that there are N_v identical voids of volume V_v, then the intensity of scatter is given by equation (2.55). The maximum intensity occurs at $Q = 0$ and is given by

$$I(0) = N_v b^2 g_3^2 V_v^2. \tag{6.32}$$

The void fraction Φ is given by

$$\phi = \frac{N_V V_V}{V} = 1 - \frac{g_2}{g_3} . \qquad (6.33)$$

And finally we assume that there exists on the average one thin void per crystallite with cross section similar to the crystallite size in the (10.0) direction. Then

$$\frac{V_V}{\frac{\pi}{4} L_a^2 L_c} = \frac{\phi}{1-\phi} = \frac{g_3}{g_2} - 1, \qquad (6.34)$$

where L_a and L_c are the crystallite sizes obtained from the diffraction peaks, and correspond to a right cylinder of diameter L_a and height L_c (see section 4.8).

The combination of the last four equations gives the intensity per scattering nucleus in the limit of $Q \to 0$; i.e.,

$$A = \frac{\pi}{4} L_a^2 L_c b^2 g_3 \left(\frac{g_3}{g_2} - 1\right)^2, \qquad (6.35)$$

or

$$g_3^3 - 2g_3^2 g_2 + g_3 g_2^2 - \frac{4A g_2^2}{\pi b^2 L_c^2 L_c} = 0. \qquad (6.36)$$

The large Q diffraction data give values of L_a and L_c equal to 50 Å and 28 Å, respectively. These are similar to values obtained by select area X-ray diffraction. The small Q diffraction gives a value of A equal to 340 barn $ster^{-1}$. Substituting these values into equation (6.36), and using $g_2 = 0.0747$ atom $Å^{-3}$ as before, gives $g_3 = 0.103$ atom $Å^{-3}$.

Hence our model assumes that there are large grains of atomic density g_2 which are composed of many crystallites of atomic density g_3,

and that these crystallites may be considered as similar to turbostratic graphite with lamellar pores between the planes of adjacent crystallites. Consequently the small pore fraction is approximately

$$\phi = 1 - \frac{g_2}{g_3} = \frac{H}{L_c + H}, \qquad (6.37)$$

where H is the thickness of the pores. If we relax the assumption that these lamellar voids are regular in shape, then crystallites within a given grain need not be aligned. Consequently the grains themselves will be isotropic, though the individual crystallites give rise to diffraction peaks corresponding to each reflection in the reciprocal lattice.

While the neutron small Q diffraction data does not extend much lower than the point of breakdown of equation (6.29), the X-ray small Q measurements have been made on this sample in the experimental range $0.1\ \text{Å}^{-1} < Q < 0.01\ \text{Å}^{-1}$ (Hucke, 1973). This may be within the Guinier law limitations for globular voids (equation (6.14)), depending on the size of the voids. If the distribution of pore sizes is reasonably narrow, then the plot of log I(Q) versus Q^2 will be a straight line, the slope of which yields a value of the Guinier radius R_G. However for a wide distribution of pore sizes, the slope of I(Q) versus Q^2 varies for values of Q, and the sample is described as polydisperse. In fact, in the analysis of polydisperse systems of equal numbers (Guinier and Fournet, 1955), the scattering from pores with the larger radius of gyration is dominant for most Q values.

The Guinier plot of the X-ray small Q diffraction data shown in Figure 6.10 suggest that the carbon sample is indeed polydisperse. These results which used slit collimation gave a Guinier radius, R_G, of 26.6 Å from the slope. Using pinhole collimation, the value of R_G is 31.6 Å. Assuming globular voids, this gives a value of 40.8 Å to the average radius of the pores. Then the region of validity of this analysis is $Q \lesssim 0.6\pi/R_G = 0.06$ Å^{-1}, which is below the straight portion of the plot.

While this discrepancy may be explained by polydisperseness, there may be an overlap of small-scale lamellar voids and larger scale globular voids. The Guinier plot for lamellar voids (equation (6.30)) yields a radius to the voids of ~ 63 Å. The region of validity of this equation is $Q \lesssim 2\pi/R_1 \sim 0.2$ Å^{-1}, which includes the straight portion of the plot. This results lends support to the idea that the small scale voids are lamellar in shape. Interestingly, there is also a range, 0.025 Å$^{-1} \lesssim Q \lesssim .10$ Å^{-1}, for which these X-ray results may be fitted to an exponential (Figure 6.11) with a characteristic length of 32.3 Å. This may have some connection with the mean granulation diameter of 35 Å found by bright field microscopy.

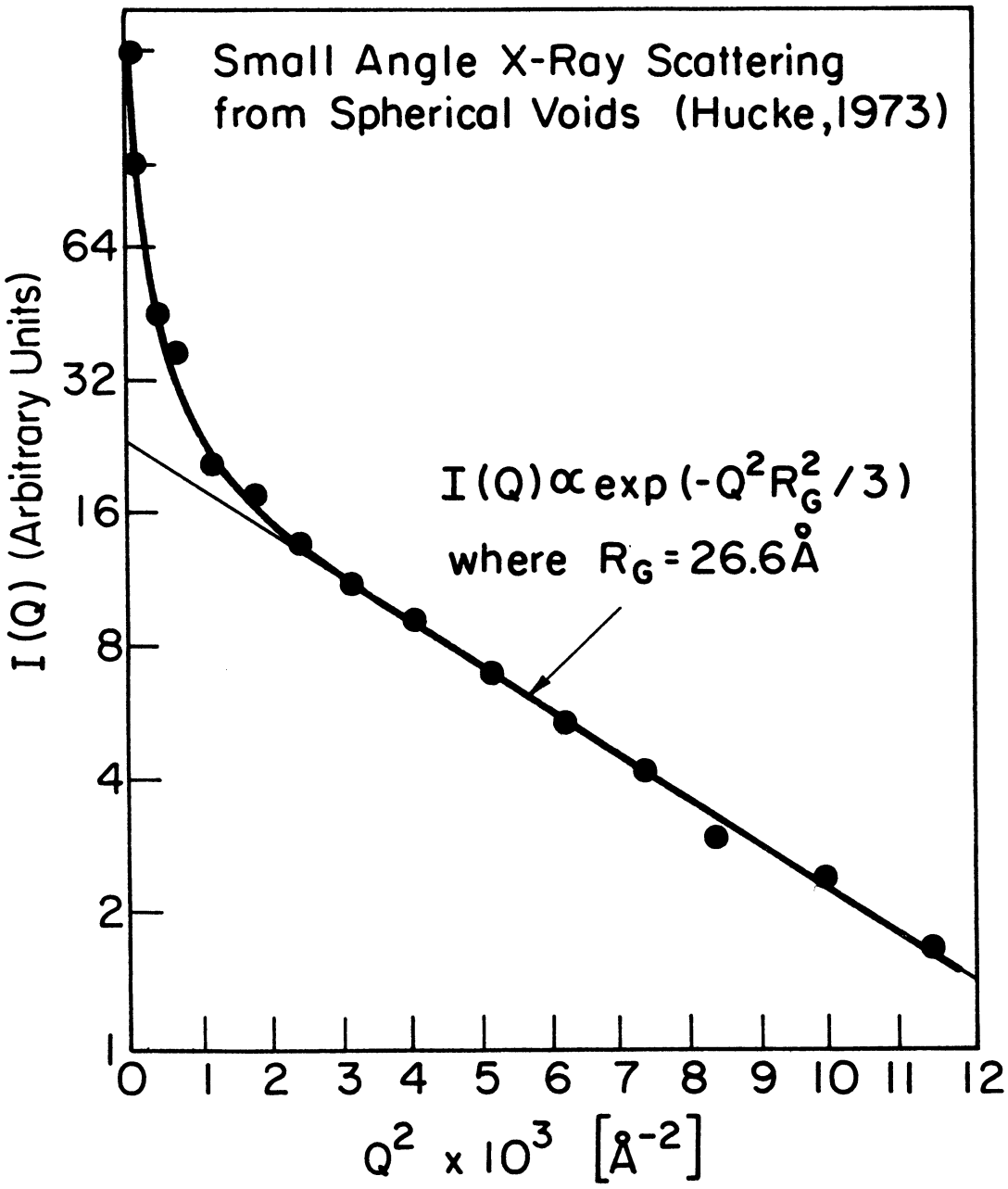

Figure 6.10. The Guinier plot for spherical voids for the small Q X-ray scattering from glassy carbon.

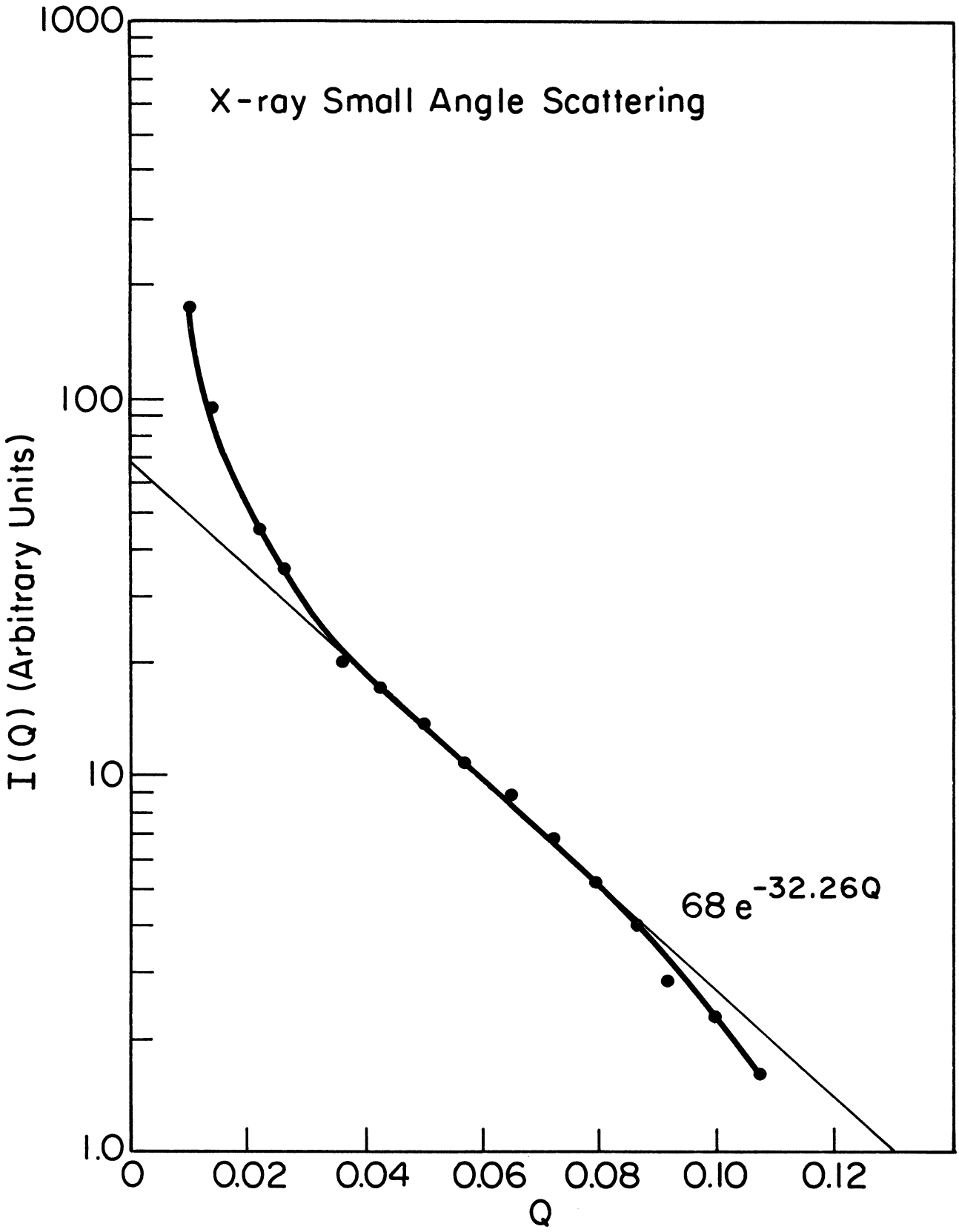

Figure 6.11. An exponential plot of small Q X-ray scattering from glassy carbon.

6.4 POLYDISPERSE VOIDS

The inability to determine uniquely the long-range order of this carbon suggests that perhaps the voids are not identical but have a random distribution of shapes as required by the Debye theory. Since the material itself is homogeneous, then the intensity of scatter of given by equation (2.65), or

$$I(Q) = \frac{c}{(1 + a^2Q^2)^2} . \tag{6.38}$$

A Debye plot, which is a graph of $I(Q)^{-1/2}$ versus Q^2, gives a value of the value of the correlation length a from the square root of the slope-intercept ratio. Debye et al. (1957) have shown that the correlation length and the void fraction ϕ can give characteristic lengths, $\bar{l}_v$ and $\bar{l}_s$, of the voids and of the solid material respectively, by

$$\bar{l}_v = \frac{a}{1 - \phi} , \tag{6.39}$$

and

$$\bar{l}_s = \frac{a}{\phi} . \tag{6.40}$$

The Debye plot of the neutron small Q data is shown in Figure 6.12, and gives a correlation length a of 7.80 Å. Using equation (6.33) we obtain characteristic lengths, $\bar{l}_v \sim 11.6$ Å and $\bar{l}_s \sim 24$ Å. The characteristic length in the voids agrees well with thickness derived from the Guinier plot for disc-shaped voids. The characteristic length in the solid agrees well with the crystallite size L_c found from the

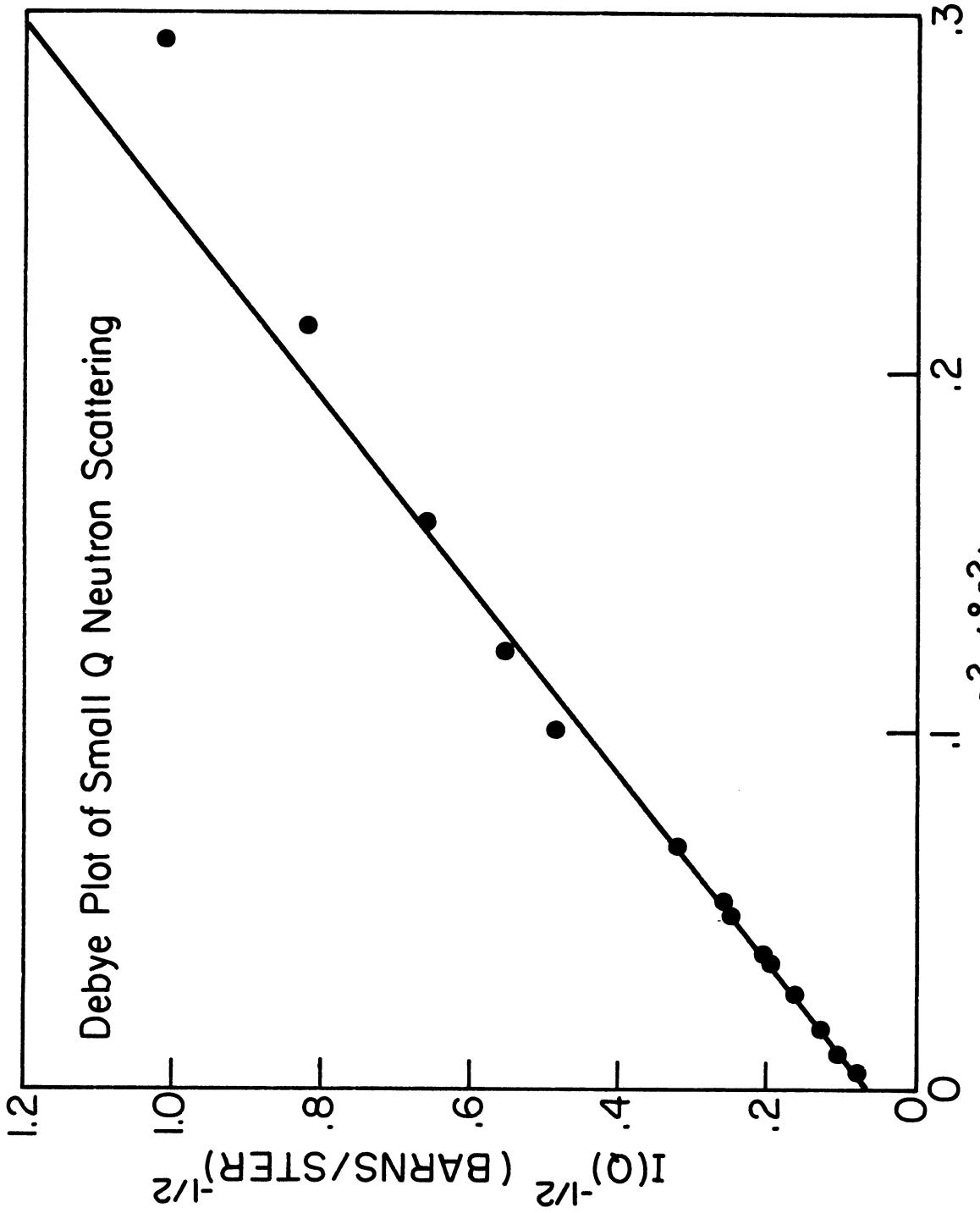

Figure 6.12. The Debye plot of small Q neutron scattering from glassy carbon.

first diffraction peak.

The Debye plot of the X-ray small Q data is shown in Figure 6.13, and gives a correlation length a of 17.8 Å. It should be noticed that these data are in a different Q range from the neutron data. The characteristic length $\bar{l}_v$ in the voids is 26.4 Å, and the characteristic length $\bar{l}_s$ the solid is 54.9 Å. These values have a reasonable agreement with the crystallite parameters, L_c and L_a, determined from the extended Q diffraction pattern, where L_c is interpreted as the distance between pores, and L_a as the distance across regions of two-dimensional ordering. It seems as though disc-shaped voids of average thickness about 11.6 Å act as spacers between crystalline cylinders of height L_c and diameter L_a. This analysis is entirely consistent with the previous concept of separated lamellar pores. In addition the slope appears to increase for $Q < .025$ Å^{-1}, which corresponds to large-scale voids of dimensions 250 Å. These general ideas have been confirmed recently by Wignall and Pings (1974) for Beckwith vitreous carbon using X-ray diffraction techniques.

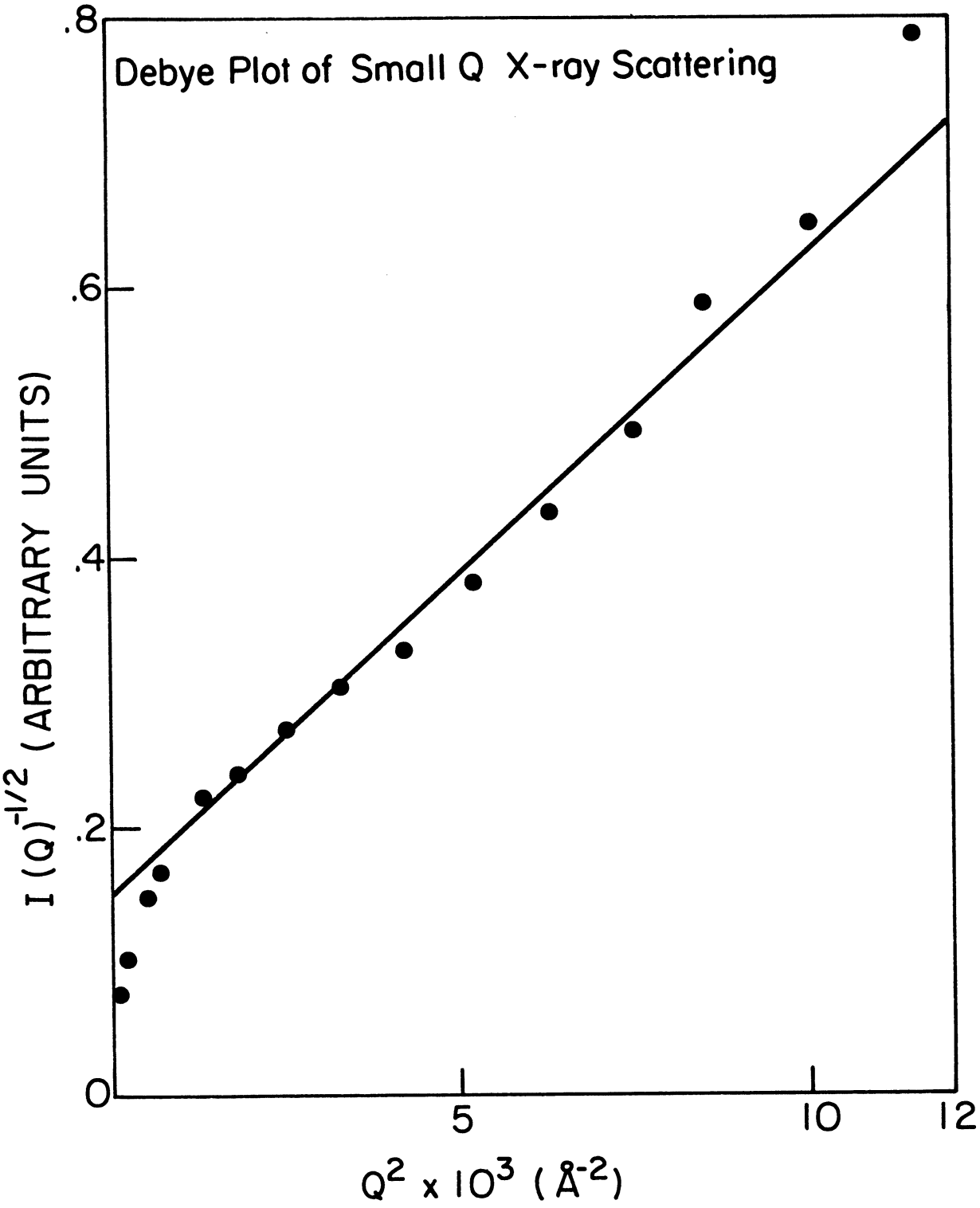

Figure 6.13. The Debye plot of small Q X-ray scattering from glassy carbon.

6.5 VERY LOW Q DIFFRACTION

The range of wave vector transfer over which the small Q neutron diffraction measurements have been taken does not extend sufficiently low to be able to define a value of Q_1, the boundary between the diffraction effects of short and long range voids. However mercury porosimetry measurements suggest that the interconnected pore systems have a mean diameter of ~ 250 Å which should have dominant effects in the range of $Q \lesssim 0.025$ Å^{-1}. Additionally the small Q X-ray data suggest more intense scattering below this value. Not having any further clues to the value of Q_1, we shall assume that is is around this estimate.

In the range of Q very close to zero, it is possible that refractive effects may become important, and even overshadow the diffracted intensity. This is due to multiple scattering near the boundaries between the voids and the material, so that severe corrections may be necessary in the first diffraction region. We will calculate a value of the critical wave vector transfer Q_c, below which refraction must be considered.

For neutrons of wave length λ and a material of atomic density g and scattering length b, the refractive index n is given (Goldberger and Seitz, 1947) by

$$n = 1 - \frac{\lambda^2 gb}{2\pi} \quad . \tag{6.41}$$

Hence for a positive scattering length, the refractive index is less than unity, so that total internal reflection is possible if the glancing angle is less than the critical angle θ_c given by $\cos \theta_c = n$. Since n is very close to unity, all angles are very small for refractive effects to occur. Then the critical glancing angle is given by

$$\theta_c = \lambda \left(\frac{gb}{\pi} \right)^{1/2} \tag{6.42}$$

and the critical wave vector transfer is given by

$$Q_c = \frac{4\pi}{\lambda} \theta_c = (16\pi gb)^{1/2} \tag{6.43}$$

which is independent of neutron wavelength. This analysis will only be valid if the boundary between the voids and the crystallites is relatively flat which is the case for lamellar voids. This may also be true for globular voids whose radius of curvature is very much greater than the incident radiation wavelength. The appropriate number density is that overaged over a few mean free paths at the boundary between the voids and the material; that is, $g_3 \sim 0.1106$ atom $Å^{-3}$. Hence the critical wave vector transfer Q_c is about 0.019 $Å^{-1}$. However the depth of penetration of radiation reflected at grazing incidence is given by

$$d = (4\pi gb)^{-1/2} \tag{6.44}$$

and total reflection will be seriously influenced by inhomogeneties at distances less than $d \sim 100$ Å from the void surfaces, which is about

twice the crystallite size L_a. Hence it is believed that the refractive effect corrections may not be too severe in the first diffraction region.

Since we have had great success in transforming a simplified function (equation 6.3)) for the second and third regions, we now attempt the same procedure for the first region, also. We assume that the diffraction pattern may be approximated as a constant over all ranges of Q, except at very small Q where the Guinier approximation (equation (6.14)) is valid; that is:

$$S(Q) \simeq B \exp(- R^2Q^2/5) + b^2 \tag{6.45}$$

where R is the average radius of the large-scale pores. Then

$$4\pi r(g(r) - g_1) = \frac{2}{\pi} \int_o^\infty Q\, B \exp\left(-\frac{R^2Q^2}{5}\right) \sin Qr dr \tag{6.46}$$

or

$$g(r) = g_1 + B\left(\frac{5}{4\pi R^2}\right)^{3/2} e^{-4r^2/5R^2}. \tag{6.47}$$

The results from the transform should be fitted to the following macroscopic results. The density measured by mercury immersion is given as $\rho_1 = 0.923$ gm cc^{-1}, which is averaged over the large -scale voids. Hence the atomic density $g_1 = 0.0463$ Å^{-3} for $r \to \infty$. The density measured by mercury porosimetry is given as $\rho_2 = 1.49$ gm cc^{-1} which neglects the large-scale voids. Hence the atomic density g_2 is

0.0747 Å^{-3} as $r \to \infty$. For spherical voids of radius R ~ 125 Å, the first diffraction region gives a density function

$$g(r) = g_1(1 + 0.614 \exp\{-(0.00716r)^2\}) \qquad (6.48)$$

which falls to 1/e of its maximum at r = 116 Å (see Figure 6.9).

Clement (1972) has discussed the distribution of path lengths through a porous material assuming that there are no correlations in the sizes of the pores and the distances between the pores. The assumption in equation (6.41) is that the large-scale void sizes are much smaller than the distances between the pores; that is, the material is rather like a Swiss cheese. To test this hypothesis, consider a continuous system with voids distributed uniformly throughout the material with a void number density n_v, Since the effective cross section of a void in any direction is πR^2, then the probability of traversing a distance ℓ without encountering a void is given by

$$p(\ell) = \exp(-\pi R^2 n_v \ell) = \exp(-\ell/L_v) \qquad (6.49)$$

where L_v is the mean "void-free" mean free path. The fraction of volume occupied by the voids is

$$\phi_v = (4/3\pi R^3)n_v = \frac{4R}{3L_v} \qquad (6.50)$$

The large scale pore volume ϕ_v is given by

$$\phi_v = 1 - \frac{g_1}{g_2}, \qquad (6.51)$$

and is 0.38 using the bulk measurements of density. The mean diameter of the interconnected pore system is 250 Å, as determined by the mercury porosimetry measurements. Then $R \sim 125$ Å, and $1/L_v \simeq 2.3\ 10^{-3}$ Å^{-1}, which is within the first diffraction region, and the 'void-free' mean free path, L_v, has a value about 440 Å. Unfortunately this is not significantly greater than the large-scale pore diameter, which suggests that there will be interference between the scattering from the grains and the large-scale pores. This is in addition to the interference between the interconnecting large scale pores.

Because of these difficulties and the inability to make measurements within this region, our structural determinations have ignored $i_1(Q)$ altogether. While no neutron diffraction measurements have been taken in this region, it would certainly be interesting to explore it using neutrons of very long wavelength at small scattering angle. Such low Q neutron diffraction measurements may be performed for $Q > 0.001$ Å^{-1} at Grenoble (Maier, 1973).

CHAPTER VII. CONCLUSION

The neutron diffraction pattern of the Hucke glassy carbon treated at 2000°C is similar to the X-ray diffraction patterns of other glassy carbons. This has been found by comparison with data from Ergun of the Fitzer glassy carbon treated at 3000°C, and from Wignall and Pings of a 1800°C treated sample from Vitreous Carbons.

It is believed that the structure of glassy may be described by two-dimensional graphitic layers, and the arrangement of these planes may be found from the diffraction pattern. The position of the first peak gives the interplanar spacing of 3.46 Å, and the position of the second peak gives an interatomic distance of about 1.4 Å based on the hexagonal lattice. The widths of these diffraction peaks are interpreted as corresponding to crystallite sizes of $L_c \sim 31$ Å and $L_a \sim 50$ Å. These numbers have been confirmed by wide angle X-ray diffraction.

The radial distribution function has peak positions and coordination numbers which correspond to those expected for graphitic planes. However, there is no peak corresponding to interplanar correlations, so that there is no regular arrangement in the stacking of the planes as in graphite. There is no evidence of a peak corresponding to tetrahedrally bonded carbon atoms as suggested in the double peak distribution for Noda and Inagaki.

The small angle neutron diffraction has been examined using a number of traditional means. While none is clearly the best, there is no disagreement in the results from each method. The solid regions of two-dimensional ordering have dimensions which agree with those obtained from the diffraction pattern. These regions may be joined in the direction of the planes by tetrahedrally bonded atoms, the amount of which is estimated at less than 8%, though this is too small to be seen in the RDF. The crystallites are stacked end to end with thin non-interconnecting voids which act as spacers between the solid regions. The voids have a mean thickness of about 12 Å, and a mean diameter of about 50 Å.

There are also much larger pores with dimensions of the order of 250 Å. These voids give rise to very low Q diffraction. Consequently the diffraction pattern has been separated into three distinct diffraction regions which reflect the solid regions and the two scales of voids. The transforms of each diffraction region have been correlated with the atomic densities on the local level and those taking into account the two scales of voids.

APPENDIX A.1. CUBIC DIAMOND STRUCTURE AND DIFFRACTION

Each carbon atom is surrounded by four equidistant neighbours at the corners of a regular tetrahedron. The unit cell is cubic, and the structure has eight atoms arranged in the following positions:

$$(0,0,0),\ (0,1/2,1/2),\ (1/2,0,1/2),\ (1/2,1/2,0),\ (1/4,1/4,1/4),$$
$$(1/4,3/4,3/4),\ (3/4,1/4,3/4),\ (3/4,3/4,1/4).$$

The cube length or lattice constant a_o is given as 3.56679 Å at a temperature 20°C. The reciprocal lattice vector has a length,

$$|\underline{b}| = 2\pi/a_o = 1.7616\ \text{Å}^{-1}.$$

A typical reflection (h,k,l) has an associated wave vector transfer

$$\underline{q}_{hkl} = 2\pi/a_o\ (h,k,l),$$

with a magnitude

$$|\underline{q}_{hkl}| = |\underline{b}|\ (h^2+k^2+l^2)^{1/2}.$$

The structure factor F_{hkl} for a given reflection (h,k,l) may be given by

$$F_{hkl} = [1+\exp(-\pi/2i(h+k+l)]$$
$$[1+\exp(-\pi i(k+l)) + \exp(-\pi i(h+l)) + \exp(-\pi i(h+k))]$$

Hence $F_{hkl} = 0$, if

(1) $(h+k+l) \bmod 4 = 2$, or

(2) h,k,l are mixed indices.

With the above restrictions, the only allowed reflections have structure factors of either

8 for $(h+k+l) \bmod 4 = 0$, or

$4(1 \pm i)$ for $(h+k+l) \bmod 4 = 1,3$.

The first few reflections are shown below:

Plane	$h^2+k^2+l^2$	Multiplicity	$\lvert F_{hkl} \rvert^2$	$\lvert q_{hkl} \rvert$ ($Å^{-1}$)
111	3	4	32	3.051
220	8	6	64	4.983
311	11	12	32	5.843
400	16	3	64	7.046
331	19	12	32	7.611
422	24	12	64	8.630
511	27	12	32	9.154
333	27	4	32	9.154
440	32	6	64	9.965
531	35	24	32	10.422
620	40	12	64	11.141
533	43	12	32	11.552
444	48	4	64	12.205

APPENDIX A.2. HEXAGONAL GRAPHITE STRUCTURE AND DIFFRACTION

Each carbon atom is surrounded by three equidistant neighbours to form an hexagonal array. The unit cell is a prism of dimensions a_o = 2.456 Å and c_o = 6.696 Å, with four atoms arranged in the following positions

$$(0,0,0),\ (0,0,1/2),\ (1/3,2/3,0)\ (2/3,1/3,1/2)\ .$$

The reciprocal lattice vectors have lengths

$$|\underline{b}_1| = |\underline{b}_2| = 2\pi/a_o \cdot 2/\sqrt{3} = 2.954\ \text{Å}^{-1},$$

and

$$|\underline{b}_3| = 2\pi/c_o = 0.9383\ \text{Å}^{-1}.$$

A typical reflection (h,k,l) has an associated wave vector transfer

$$\underline{q}_{hkl} = 2\pi(-(h+k)/a_o,\ +(h-k)/\sqrt{3}\ a_o,\ +l/c_o)$$

with a magnitude

$$|\underline{q}_{hkl}| = (|\underline{b}_1|^2(h^2+hk+k^2) + |\underline{b}_3|^2\ l^2)^{1/2}.$$

The structure factor F_{hkl} for a given reflection (h,k,l) may be given by

$$F_{hkl} = 1 + \exp(-\pi i l) + \exp(-2\pi i/3(h + 2k))$$

$$+ \exp(-\pi i l)\exp(-2\pi i/3(2h + k))$$

Hence $F_{hkl} = 0$ when both $l \bmod 2 = l$ (i.e., l is odd), and $(h^2 + hk + k^2) \bmod 3 = 0$. The only allowed reflections have structure factors of either

1 for $l \bmod 2 = 0$ (l even) and $(h^2 + hk + k^2) \bmod 3 \neq 0$, or

4 for $l \bmod 2 = 0$ (l even) and $(h^2 + hk + k^2) \bmod 3 = 0$, or

$\pm i\sqrt{3}$ for $l \bmod 2 = l$ (l odd) and $(h^2 + hk + k^2) \bmod 3 \neq 0$.

The first few reflections are shown below in hexagonal units, and equivalent 4-axis units:

Plane		Multiplicity	$\lvert F_{hkl}\rvert^2$	$\lvert \underline{q}_{hkl}\rvert$ (Å^{-1})
hexagonal units (hkl)	4-axis units ($a_1a_2a_3 \cdot c$)			
00.2	000.2	1	16	1.877
10.0	10$\bar{1}$.0	3	1	2.954
10.1	10$\bar{1}$.1	6	3	3.100
10.2	10$\bar{1}$.2	6	1	3.501
00.4	000.4	1	16	3.753
10.3	10$\bar{1}$.3	6	3	4.081
10.4	10$\bar{1}$.4	6	1	4.776
11.0	11$\bar{2}$.0	3	16	5.117
11.2	11$\bar{2}$.2	6	16	5.450
10.5	10$\bar{1}$.5	6	3	5.544
00.6	000.6	1	16	5.630
20.0	20$\bar{2}$.0	3	1	5.908
20.1	20$\bar{2}$.1	6	3	5.982
20.2	20$\bar{2}$.2	6	1	6.199
11.4	11$\bar{2}$.4	6	16	6.346
10.6	10$\bar{1}$.6	6	1	6.358
20.3	20$\bar{2}$.3	6	3	6.544

Plane		Multiplicity	$\lvert F_{hkl} \rvert^2$	$\lvert \underline{q}_{hkl} \rvert$ ($Å^{-1}$)
hexagonal units (hkl)	4-axis units ($a_1a_2a_3.c$)			
20.4	$20\bar{2}.4$	6	1	6.999
10.7	$10\bar{1}.7$	6	3	7.202
00.8	000.8	1	16	7.507
20.5	$20\bar{2}.5$	6	3	7.544
11.6	$11\bar{2}.6$	6	16	7.607
21.0	$21\bar{3}.0$	12	1	7.816
21.1	$21\bar{3}.1$	12	3	7.872
21.2	$21\bar{3}.2$	12	1	8.038
10.8	$10\bar{1}.8$	6	1	8.067
20.6	$20\bar{2}.6$	6	1	8.161
21.3	$21\bar{3}.3$	12	3	8.307
21.4	$21\bar{3}.4$	12	1	8.670
20.7	$20\bar{2}.7$	6	3	8.834
30.0	$30\bar{3}.0$	3	16	8.862
10.9	$10\bar{1}.9$	6	3	8.946
30.2	$30\bar{3}.2$	6	16	9.059
11.8	$11\bar{2}.6$	6	16	9.084
21.5	$21\bar{3}.5$	12	3	9.116
00.10	000.1C	1	16	9.383
20.8	$20\bar{2}.8$	6	1	9.553
30.4	$30\bar{3}.4$	6	16	9.624
21.6	$21\bar{3}.6$	12	1	9.632
10.10	$10\bar{1}.1C$	6	1	9.837
21.7	$21\bar{3}.7$	12	3	10.209
22.0	$22\bar{4}.0$	3	16	10.233
20.9	$20\bar{2}.9$	6	3	10.306
22.2	$22\bar{4}.2$	6	16	10.404
30.6	$30\bar{3}.6$	6	16	10.499
31.0	$31\bar{4}.0$	6	1	10.651

APPENDIX A.3. RHOMBOHEDRAL GRAPHITE STRUCTURE AND DIFFRACTION

Each carbon atom is surrounded by three equidistant neighbours to form an hexagonal array. The unit cell is a rhombohedron with dimensions $a_o = 3.635$ Å and $\alpha = 39°30'$, with two atoms at locations

$$(1/6,1/6,1/6),\ (-1/6,-1/6,-1/6).$$

The reciprocal lattice vector has a length

$$|\underline{b}| = \frac{2\pi}{a_o} \frac{\cot \alpha/2}{(3 - 4 \sin^2 \alpha/2)^{1/2}} = 3.019 \text{ Å}^{-1}$$

A typical reflection (h,k,l) has an associated wave vector transfer

$$\underline{q}_{hkl} = \frac{2\pi}{a_o}\left(\frac{(h+k-2l)}{2\sqrt{3} \sin \alpha/2}, \frac{(h-k)}{2 \sin \alpha/2}, \frac{(h+k+l)}{(9 - 12 \sin^2 \alpha/2)^{1/2}}\right)$$

with a magnitude

$$|\underline{q}_{hkl}| = \left(|\underline{b}|^2(h+k+l)^2 - \left(\frac{2\pi}{a_o}\right)^2 \frac{(hk+kl+hl)}{\sin^2 \alpha/2}\right)^{1/2}$$

The structure factor F_{hkl} for a given reflection (h,k,l) may be given by

$$F_{hkl} = 2 \cos(\pi/3 \cdot (h+k+l)).$$

Hence all (h,k,l) planes reflections are allowed with structure factors of either

2 for $(h+k+l) \bmod 3 = 0$, or

1 for $(h+k+l) \bmod 3 \neq 0$.

In addition rhombohedral graphite may be viewed with an hexagonal pseudounit of dimensions a' = 2.456 Å, and c = 10.044 Å, with six atoms arranged in the following positions:

$$(0,0,0),\ (1/3,2/3,0),\ (0,0,1/3),\ (2/3,1/3,1/3),$$
$$(1/3,2/3,2/3),\ (2/3,1/3,2/3).$$

The first few reflections are shown below in rhombohedral units, hexagonal units, and the equivalent planes for hexagonal graphite.

Planes		Equivalent			
rhombohedral units (hkl)	hexagonal units (hkl)	Hexagonal Graphitic Planes	Multiplicity	$\lvert F_{hkl}\rvert^2$	$\lvert \underline{q}_{hkl}\rvert$ (Å^{-1})
111	00.3	00.2	1	4	1.876
100	10.1	(10.2/3)	3	1	3.020
110	10.2	(10.4/3)	3	1	3.208
222	00.6	00.4	1	4	3.752
211	10.4	(10.8/3)	3	1	3.871
221	10.5	(10.10/3)	3	1	4.302
1$\bar{1}$0	11.0	11.0	3	4	5.116
322	10.7	(10.14/3)	3	1	5.282
210	11.3	11.2	6	4	5.450
333	00.9	00.6	1	4	5.628
332	10.8	(10.16/3)	3	1	5.811
1$\bar{1}$1	20.1	(20.2/3)	3	1	5.941
200	20.2	(20.4/3)	3	1	6.039
321	11.6	11.4	6	4	6.349

Notice that the rhombohedral graphite reflections do not include all the hexagonal graphite reflections; conversely, there are some rhombohedral graphite reflections which have no corresponding hexagonal graphite reflections.

APPENDIX A.4. HEXAGONAL DIAMOND STRUCTURE AND DIFFRACTION

Each carbon atom is surrounded by four equidistant neighbours at the corners of a regular tetrahedron. The unit cell is a prism and the structure has four atoms arranged in the following positions:

$$(0,0,0),\ (1/3,2/3,1/2),\ (0,0,u),\ (1/3,2/3,u+1/2)$$

in hexagonal coordinates.

The unit lengths are $a_o = 2.5235$ Å and $c_o = 4.1134$ Å, with an axial ratio $c_o/a_o \simeq 1.63$, and $u = 0.375$, found by assuming an interatomic distance of 1.5444 Å.

The reciprocal lattice vectors have lengths

$$|\underline{b}_1| = |\underline{b}_2| = 2\pi/a_o \cdot 2/\sqrt{3} = 2.875\ \text{Å}^{-1}$$

and

$$|\underline{b}_3| = 2\pi/c_o = 1.527\ \text{Å}^{-1}.$$

A typical reflection (h,k,l) has an associated wave vector transfer

$$\underline{q}_{hkl} = 2\pi(-(h+k)/a_o,\ +(h-k)/\sqrt{3}a_o,\ +l/c_o)$$

with a magnitude

$$|\underline{q}_{hkl}| = (|\underline{b}_1|^2(h^2+hk+k^2) + |\underline{b}_3|^2 l^2)^{1/2}.$$

The structure factor F_{hkl} for a given reflection (h,k,l) may be given by

$$F_{hkl} = [1 + \exp(-2\pi i u l)][1 + \exp(-\pi i/3(2h + 4k + 3l)] .$$

Hence $F_{hkl} = 0$, if

(1) $(2ul) \bmod 2 = 1$; i.e., $l = 4, 12$, etc.

(2) $(2h + 4k + 3l) \bmod 6 = 3$; i.e., there are some reflections missing when l is odd.

Since $u = 0.375$, the only allowed reflections have structure factors of

4	for $l \bmod 8 = 0$ and $(h + 2k) \bmod 3 = 0$
$1 \pm \sqrt{3}i$	for $l \bmod 8 = 0$ and $(h + 2k) \bmod 3 \neq 0$
$2(1 \pm i)$	for $l \bmod 4 = 2$ and $(h + 2k) \bmod 3 = 0$
$1/2(1 \pm i)(1 \pm \sqrt{3}i)$	for $l \bmod 4 = 2$ and $(h + 2k) \bmod 3 \neq 0$
$\sqrt{3}/2(\sqrt{3} \pm i)(1 + (1 + i)/\sqrt{2})$	for $l \bmod 8 = 3,5$
$\sqrt{3}/2(\sqrt{3} \pm i)(1 - (1 + i)/\sqrt{2})$	for $l \bmod 8 = 1,7$.

The first few reflections are shown below:

(hkl) Planes	Equivalent Cubic Planes	Multiplicity	$\lvert F_{hkl} \rvert^2$	$\lvert \underline{q}_{hkl} \rvert$ (Å^{-1})
10.0		3	4	2.876
00.2	111	1	8	3.051
10.1		6	1.7574	3.256
10.2		6	2	4.192
11.0	220	3	16	4.983
10.3		6	10.2426	5.406
20.0		3	4	5.754
11.2	311	6	8	5.843
20.1		6	1.7574	5.952
20.2		6	2	6.513
20.3		6	10.2426	7.352

(hkl) Planes	Equivalent Cubic Planes	Multiplicity	$\lvert F_{hkl} \rvert^2$	$\lvert q_{hkl} \rvert$ ($Å^{-1}$)
21.0	331	6	4	7.611
21.1		12	1.7574	7.762
10.5		6	10.2426	8.152
21.2		12	2	8.200
30.0	422	3	16	8.630
21.3		12	10.2426	8.881
30.2	511	6	8	9.154
00.6	333	1	8	9.154
20.5		6	10.2426	9.555
10.6		6	2	9.595

Note that the 00.4 reflection (equivalent to the 222 reflection in cubic diamond) is missing. Also none of the forbidden reflections in cubic diamond are found in hexagonal diamond.

APPENDIX A.5. IDEAL GRAPHITE IN-PLANE CORRELATIONS

We consider a graphitic layer in which atoms are located on lattice size of a regular hexagonal array which the graphitic unit cell dimension a_o = 2.456 Å. Distances between the atoms are given by

$$r' = \frac{a_o}{\sqrt{3}} (p^2 + pq + q^2),$$

where p and q are integers, such that $p > 0$, and $p \geq q \geq 0$. The in-plane atomic density correlations are given

$$g(r) = n(r)\, \delta(r-r')$$

where n(r) is given by

3 if q = 0, and p mod 3 ≠ 0

6 if q = 0, and p mod 3 = 0

6 if q = p

6 if p ≠ q ≠ 0, and (p-q) mod 3 ≠ 0

12 if p ≠ q ≠ 0, and (p-q) mod 3 = 0

and is undefined elsewhere.

The first few in-plane correlation distances are shown below:

p	q	p^2+pq+q^2	Distance (Å)	Coordination r
1	0	1	1.418	3
1	1	3	2.456	6
2	0	4	2.836	3
2	1	7	3.752	6
3	0	9	4.254	6
2	2	12	4.912	6
3	1	13	5.113	6
4	0	16	5.672	3
3	2	19	6.181	6
4	1	21	6.498	12
5	0	25	7.090	3
3	3	27	7.368	6
4	2	28	7.503	6
5	1	31	7.895	6
6	0	36	8.508	6
4	3	37	8.625	6
5	2	39	8.855	12
6	1	43	9.298	6
4	4	48	9.824	6
5	3	49	9.926	6
7	0			3
6	2	52	10.225	6
7	1	57	10.705	12
5	4	61	11.075	6
6	3	63	11.255	12
8	0	64	11.344	3
7	2	67	11.607	6
8	1	73	12.115	6
5	5	75	12.280	6
6	4	76	12.362	6
7	3	79	12.603	6
9	0	81	12.762	6
8	2	84	12.996	12
6	5	91	13.527	6
9	1			6
7	4	93	13.674	12
8	3	97	13.965	6

APPENDIX B.1. ALUMINUM STRUCTURE AND DIFFRACTION

Aluminum has a close-packed cubic structure with a lattice constant a_o of 4.04958 Å at a temperature of 25°C. The unit cell has four atoms arranged in the following positions:

$$(0,0,0),\ (0,1/2,1/2),\ (1/2,0,1/2),\ (1/2,1/2,0).$$

The reciprocal lattice vector has a length

$$|\underline{b}| = 2\pi/a_o = 1.55156\ \text{Å}^{-1}.$$

A typical reflection (hkl) has an associated wave vector transfer

$$q_{hkl} = 2\pi/a_o(h,k,l)$$

with a magnitude

$$|\underline{q}_{hkl}| = 2\pi/a_o\ (h^2+k^2+l^2)^{1/2}.$$

The structure factor F_{hkl} for a given reflection (h,k,l) may be given by

$$F_{hkl} = 1 + \exp(-\pi i(h+k)) + \exp(-\pi i(h+l)) + \exp(-\pi i(k+l)).$$

Hence $F_{hkl} = 0$, if any two of $(h+k)$, $(h+l)$, and $(k+l)$ are odd; i.e., if h,k,l are mixed indices. Otherwise, $F_{hkl} = 4$.

The first few reflections are shown below:

Plane	Multiplicity	$h^2+k^2+l^2$	Distance (Å)	$\lvert q_{hkl} \rvert$ ($Å^{-1}$)
111	4	3	2.33803	2.68739
200	3	4	2.02479	3.10313
220	6	8	1.43174	4.38849
311	12	11	1.22099	5.14596
222	4	12	1.16901	5.37478
400	3	16	1.01240	6.20626
331	12	19	0.92904	6.76311
420	12	20	0.90551	6.93880
422	12	24	0.82662	7.60108
333	4	27	0.77934	8.06217
511	12	27		
440	6	32	0.71587	8.77698
531	24	35	0.68450	9.17918
442	12	36	0.67493	9.30939
600	3	36		
620	12	40	0.64029	9.81296
533	12	43	0.61756	10.17429
622	12	44	0.61050	10.29192
444	4	48	0.58451	10.74955
551	12	51	0.56705	11.08039
711	12	51		
640	12	52	0.56158	11.18849
642	24	56	0.54115	11.61084
553	12	59	0.52721	11.91779
731	24	59		
800	3	64	0.50620	12.41245
733	12	67	0.49473	12.70010
644	12	68	0.49108	12.79453
820	12	68		
660	6	72	0.47725	13.16546
822	12	72		
555	4	75	0.46761	13.43694
751	24	75		
662	12	76	0.46452	13.52623
840	12	80	0.45276	13.87761
753	24	83	0.44450	14.13543
911	12	83		
842	24	84	0.44185	14.22033
664	12	88	0.43169	14.55497
931	24	91	0.42451	14.80098
844	12	96	0.41331	15.20217
755	12	99	0.40700	15.43787
771	12	99		
933	12	99		

APPENDIX B.2. LEAD STRUCTURE AND DIFFRACTION

Lead has a close-packed cubic structure with a lattice constant a_o of 4.9505 Å. The unit cell has four atoms arranged in the following positions:

$$(0,0,0),\ (0,1/2,1/2),\ (1/2,0,1/2),\ (1/2,1/2,0)\ .$$

The reciprocal lattice vector has a length

$$|\underline{b}| = 2\pi/a_o = 1.2692\ \text{Å}^{-1}\ .$$

A typical reflection (hkl) has an associated wave vector transfer

$$\underline{q}_{hkl} = 2\pi/a_o(h,k,l)$$

with a magnitude

$$|\underline{q}_{hkl}| = 2\pi/a_o\ (h^2+k^2+l^2)^{1/2}\ .$$

The structure factor is given by

$$F_{hkl} = 1 + \exp(-\pi i(k+l)) + \exp(-\pi i(h+l)) + \exp(-\pi i(h+k))\ .$$

Hence $F_{hkl} = 0$ if any two of $(k+l)$, $(h+l)$, and $(h+k)$ are odd; i.e., if h,k,l are mixed indices. Otherwise, the structure factor is constant.

The first few reflections are shown below:

Plane	Relative Multiplicity	$\lvert F_{hkl} \rvert^2$	$\lvert \underline{q}_{hkl} \rvert$ ($Å^{-1}$)
111	4	16	2.198
200	3	16	2.538
220	6	16	3.590
311	12	16	4.209
222	4	16	4.397
400	3	16	5.077
331	12	16	5.532
420	12	16	5.676
422	12	16	6.218

APPENDIX B.3. VANADIUM STRUCTURE AND DIFFRACTION

Vanadium has a body-centered cubic structure with a lattice constant $a_o = 3.024$ Å. The unit cell has two atoms at positions

$$(0,0,0,), (1/2,1/2,1/2).$$

The reciprocal lattice vector has a length

$$|\underline{b}| = 2\pi/a_o = 2.0778 \text{ Å}^{-1}.$$

A typical reflection (hkl) has an associated wave vector transfer

$$\underline{q}_{hkl} = 2\pi/a_o \, (h,k,l)$$

with a magnitude

$$|\underline{q}_{hkl}| = 2\pi/a_o \, (h^2+k^2+l^2)^{1/2}.$$

The structure factor is given by

$$F_{hkl} = 1 + \exp(-\pi i(p+q+r)).$$

Hence $F_{hkl} = 0$ whenever $(p+q+r) \bmod 1 = 1$ or $(p+q+r)$ is odd; and $F_{hkl} = 2$ whenever $(p+q+r)$ is even.

The first few peaks are:

Plane	Multiplicity	Distance (Å)	$\lvert \underline{q}_{hkl} \rvert$ (A^{-1})
110	12	2.138	2.938
200	6	1.512	4.156
211	24	1.235	5.089
220	12	1.069	5.877
310	24	0.956	6.570
222	8	0.873	7.198
321	48	0.839	7.492
400	6	0.756	8.311
330	12	0.713	8.815
420	24	0.617	9.292
332	24	0.645	9.746

APPENDIX C. QUINOID STRUCTURE OF GRAPHITE

The structural unit has orthorhombic symmetry with dimensions, a_o = 2.461 Å, b_o = 4.263 Å, and c_o = 6.708 Å, and with eight atoms arranged at the following positions:

$$(0,0,0),\ (1/2+u,1/2,0),\ (0,0,1/2),\ (1/2-u,1/2,1/2),$$

$$(0,v,0),\ (1/2+u,1/2+v,0),\ (0,-v,1/2),\ (1/2-u,1/2-v,1/2),$$

where v = 0.318, and $u \simeq 0$.

The reciprocal lattice vectors have lengths

$$|\underline{b}_1| = 2\pi/a_o = 2.553\ \text{Å}^{-1},$$

$$|\underline{b}_2| = 2\pi/b_o = 1.474\ \text{Å}^{-1},$$

and

$$|\underline{b}_3| = 2\pi/c_o = 0.937\ \text{Å}^{-1}.$$

A typical reflection has an associated wave vector transfer

$$\underline{q}_{hkl} = 2\pi(h/a_o, k/b_o, l/c_o)$$

with a magnitude

$$|\underline{q}_{hkl}| = (h^2|\underline{b}_1|^2 + k^2|\underline{b}_2|^2 + l^2|\underline{b}_3|^2)^{1/2}.$$

Notice that the 1-4 quinoid structure is given when $v < 1/3$, and $u = 0$. The structure factor F_{hkl} for a reflection (hkl) may be given by

$$F_{hkl} = [1 + \exp(-\pi i(h+k))]\,[(1 + \exp(-2\pi ikv)) + \exp(-\pi il)(1 + \exp(+2\pi ikv))]$$

Hence $F_{hkl} = 0$, if

(1) $(h+k) \bmod 2 = 1$ (or h,k are mixed indices)

(2) $l \bmod 2 = 0$ (l even) and $2kv \bmod 2 = 1$

(3) $l \bmod 2 = 1$ (l odd) and $2kv \bmod 1 = 0$.

Note that if $v = 1/3$ (exactly equivalent to hexagonal graphite)

$$F_{hkl} = [1 - \exp(-\pi i(h+k))]\,[(1 + \exp(-2\pi ik/3)) + \exp(-\pi il)(1 + \exp(+2\pi ik/3))]$$

Hence $F_{hkl} = 0$, if

(1) $(h+k) \bmod 2 = 1$

(2) $l \bmod 2 = 1$ (l odd) and $k \bmod 3 = 0$.

The first reflections are shown below:

Planes		Multiplicity	$\lvert F_{hkl} \rvert^2$	$\lvert \underline{q}_{hkl} \rvert$ ($Å^{-1}$)
orthorhombic units (hkl)	equivalent hexagonal units (hkl)			
002	00.2	1	64	1.873
110	10.0	3	5.49	2.948
020			1.89	
111	10.1	6	13.25	3.093
021			9.10	
112	10.2	6	5.49	3.493
022			1.89	
004	00.4	1	64	3.747
113	10.3	6	13.25	4.073
023			9.10	
114	10.4	6	5.49	4.768
024			1.89	
200	11.0	3	64	5.106
130			61.37	
202	11.2	6	64	5.439
132			61.37	
115	10.5	6	13.25	5.534
025			9.10	
006	00.6	1	64	5.620
220	20.0	3	1.89	5.896
040			11.89	
221	20.1	6	9.10	5.970
041			15.70	
222	20.2	6	1.89	6.186
042			11.89	
204	11.4	6	64	6.333
134			61.37	
116	10.6	6	5.49	6.346
026			1.89	

Note that each reflection has a corresponding hexagonal graphite reflection.

Notice also that the 1-3 quinoid structure is given when $v > 1/3$, and $u \neq 0$.

APPENDIX D. FORCE CONSTANTS FOR DISTORTED MODELS

For elements in the solid state, Waser and Pauling (1950) have given an empirical law, analogous to Badger's rule for molecules in the gaseous state (1935), for the relationship between the force constant k (in Mdyne/cm) of a bond and its equilibrium distance r (in Å); viz.,

$$k^{-1/3} = a(r - b). \qquad (D.1)$$

The constants for solid carbon are a = 2.89, and b = 1.13 Å. A graph of this relationship is shown in Figure D.1, and the force constant k for a particular bond of length r may be estimated using Badger's rule from this figure.

We also estimate the equilibrium bond length using a method analogous to that suggested by Pauling (1960) for molecules. Let r_1, r_2, r_n be the equilibrium interatomic distances for a single bond, a double bond, and a bond of intermediate type with a bond number n. Assume that the potential function of the resonating bond may be expressed as the sum of the two parabolic functions representing the potentials of the single and double bonds, weighted by the proportion of each type; viz., (2 - n) and (n - 1). This potential function is

$$V(r) = \frac{1}{2}(2-n)\, k_1 (r_n - r_1)^2 + \frac{1}{2}(n-1) k_2 (r_n - r_2)^2 . \qquad (D.2)$$

The equilibrium value for a given bond number n is at the minimum of the

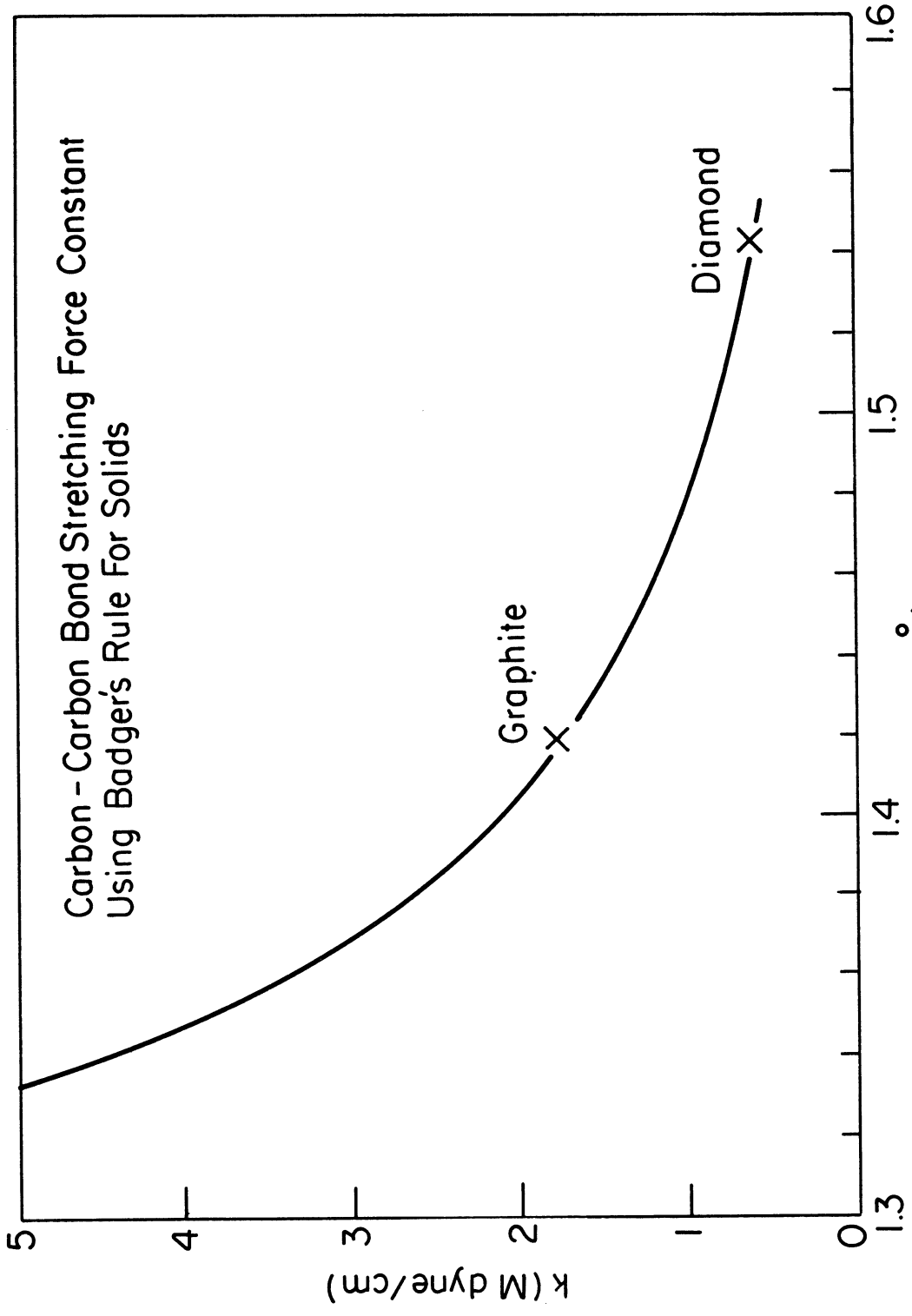

Figure D.1. Carbon-carbon bond stretching force constant using the analogous Badger's rule for solids.

potential function. Thus

$$r_n = r_1 + \frac{(r_2 - r_1)(n-1)\, k_2/k_1}{(2-n) + (n-1)\, k_2/k_1} \,. \qquad (D.3)$$

To use this relationship, we need to estimate a value of k_2/k_1. Consequently we substitute the following values into equation (D.3); $r_1 = 1.542$ Å for diamond, $r_2 = 1.334$ Å obtained from X-ray diffraction of crystals, and $r_n = 1.421$ Å for $n = 4/3$ as in graphite. This gives

$$\frac{k_2}{k_1} = 2.78 \,, \qquad (D.4)$$

which may be compared to $k_2/k_1 = 8.24$ given by equation (D.1). However the simple Badger relationship only holds good when the bond type remains constant during compression. Since we know that bonding in diamond is sp^3 and in graphite is sp^2, this relationship is invalid over such a large range of r.

We have used in our computer model (section 5.5) equilibrium bond lengths found by Ergun (1973) for the quinoid structure of graphite; viz., $L_1 = 1.454$ Å for the single bonds, and $L_2 = 1.356$ Å for the double bonds. Using Badger's rule, which may be valid over this limited range, we obtain force constants, $k_1 = 1.28$ Mdyne/cm and $k_2 = 3.59$ Mdyne/cm. However the ratio of these, $k_2/k_1 = 2.95$ is close to that for Pauling's method (equation (D.4)) for quite different bond lengths. An estimate values of k_1 and k_2 may be obtained form the observed compressibility of graphite in its basal plane.

Consider a system with n atoms per unit cell, and assume that each atom has three bonds, each with an associated energy and degree of freedom. Then for N unit cells, the total energy U is given by

$$U = Nn \sum_{i=1}^{3} \frac{1}{2} k_i (\underline{r}_o - \underline{r}_i)^2 \qquad (D.5)$$

where k_i is the bond force constant and $\underline{r}_i$ is the position vector of the neighboring atom of the typical atom whose position vector is $\underline{r}_o$. Then

$$\frac{d^2U}{dr^2} = Nn(k_1 + k_2 + k_3) . \qquad (D.6)$$

The compressibility K is defined by

$$\frac{1}{K} = V \frac{d^2U}{dV^2} = V \frac{d^2U}{dr^2} \left(\frac{dr}{dV}\right)^2 \qquad (D.7)$$

where V signifies the volume of the system. Hence the force constants may be estimated from the compressibility of the material.

For the benzenoid (resonating) structure all three bonds are considered equivalent with a force constant k_o. The structure is that of hexagonal graphite, with lattice parameters a_o and c_o, and 4 atoms per unit cell. Then for N cells, the volume of the system is

$$V = N \frac{\sqrt{3}}{2} a_o^2 c_o . \qquad (D.8)$$

Substitution into equation (D.7) gives the planar compressibility

$$\frac{1}{K} = \frac{2k_o}{\sqrt{3}\, c_o} \qquad (D.9)$$

The observed compressibility of a single crystal of graphite along its basal plane is given as 0.32 10^{-13} cm^2/dyne (Lynch and Drickamer, 1966). Waser and Pauling (1966) used equation (D.9) to obtain a stretching force constant k_o of 1.81 Mdyne/cm for graphite. Pauling notes that this value is smaller than the expected value.

For a quinoid system; two bonds are equivalent with a force constant k_1, and the other bond is stronger with a force constant k_2. Then equation (D.6) becomes

$$\frac{d^2U}{dr^2} = Nn\,(2k_1 + k_2). \qquad (D.10)$$

L_1 and L_2 are the equilibrium lengths of these two types of bonds.

The 1-4 quinoid structure is orthorhombic with 8 atoms per unit cell, with lattice parameters, a_o, b_o, c_o, given by

$$a_o = 2L_1 \sin\alpha,$$

$$b_o = 2L_2 - 2L_1 \cos\alpha \quad (\text{with } \alpha > \pi/2). \qquad (D.11)$$

For N cells, the volume of the system is

$$V = N\,a_o b_o c_o = 4Nc_o L_1 \sin\alpha(L_2 - L_1\cos\alpha). \qquad (D.12)$$

Substitution into equation (D.7) gives

$$\frac{1}{K} = \frac{2(2k_1 + k_2)}{c_o \sin\alpha} \quad \frac{(L_2/L_1 - \cos\alpha)}{(1 + L_2/L_1 - 2\cos\alpha)^2} \qquad (D.13)$$

In general for quinoid structures, there is no definite relationships between the bond angles and lengths. However regular quinoid structures may also form hexagonal symmetry which does provide such a relationship. If α is the angle between the short and longer bonds, and β is the angle between the longer bonds, then

$$\beta + 2\alpha = 2\pi. \tag{D.14}$$

The 1-4 quinoid structure has the relationship

$$2L_1 \sin(\beta/2) = (L_1^2 + L_2^2 - 2L_1L_2 \cos\alpha)^{1/2} \tag{D.15}$$

which, for $L_1 = 1.454$ Å, and $L_2 = 1.356$ Å, gives a value of α equal to 122.21°. Then equation (D.12) becomes

$$\frac{1}{K} = \frac{2k_1 + k_2}{17.39}, \tag{D.16}$$

and $(2k_1 + k_2) = 5.435$ Mdyne/cm. If we assume that Badger's rule is a reasonably good approximation to the slope of $k^{-1/3}$ versus r only for values of r arond the graphitic equilbrium value, then we obtain the following values of the equilibrium constants for the 1-4 quinoid structure,

$$k_1 = 1.305 \text{ Mdyne/cm}$$

$$k_2 = 2.83 \text{ Mdyne/cm} \tag{D.17}$$

The 1-3 quinoid structure is also orthorhombic with 8 atoms per unit cell with dimensions given by

$$a_o = L_2 \sin\alpha - L_1 \sin\beta$$

$$b_o = 2L_1 - 2L_2 \cos\alpha \quad (\text{with } \alpha > \pi/2) \tag{D.18}$$

For N cells, the volume of the system is

$$V = N a_o b_o c_o = 2Nc_o (L_2 \sin\alpha - L_1 \sin\beta)(L_1 - L_2 \cos\alpha). \tag{D.19}$$

It also has the relationship

$$L_1 - 2L_2 \cos\alpha = L_1 - 2L_1 \cos\beta \tag{D.20}$$

which, for $L_1 = 1.454$ Å and $L_1 = 1.356$ Å, gives a value of α equal to 120.76°. Then equation (A.7) reduces to

$$\frac{1}{K} = \frac{2k_1 + k_2}{17.37}, \tag{D.21}$$

and $(2k_1 + k_2) = 5.429$ Mdyne/cm. In the same way as for the 1-4 quinoid, we arrive at the following values of the equilibrium constants for the 1-3 quinoid structure,

$$k_1 = 1.305 \quad \text{Mdyne/cm}$$

$$k_2 = 2.82 \quad \text{Mdyne/cm} \tag{D.22}$$

Hence for a model in which all carbon atoms have three bonds, two

single bonds of length L_1 and one double bond of length L_2, then the ratio of the force constants should be of the order of

$$\frac{k_2}{k_1} = 2.16 \ . \qquad \text{(D.22)}$$

It is probably unrealistic to find force constants that differ so much in a hexagonal lattice; consequently we have chosen values of k_1 and k_2 symmetrically about k_o; viz., $k_1 = 1.31$ Mdyne/cm, and $k_2 = 2.31$ Mdyne/cm. Additionally neutron inelastic scattering measurements (Carpenter, 1973) suggest that glassy carbon is dynamically similar to graphite, with frequencies on the glass generally lower than in the crystal.

REFERENCES

BADGER, R. M., (1935), J. Chem. Phys., 3, 710. See also 2, 128.

BETTS, F., BIENENSTOCK, A., KEATING, D. T., and DeNEUFVILLE, J. P., (1972), J. Non-Cryst. Solids, 7, 417.

BERNAL, J. D., (1924), Proc. Roy. Soc. (London), 106A, 749.

BISCHOFF, F. G., (1970), "Generalized Monte Carlo Methods for Multiple Scattering Problems in Neutron and Reactor Physics," Ph.D. thesis Rensselaer Polytechnic Institute. Also BISCHOFF, F. G., YEATER, M. L., and MOORE, W. E., (1972), Nucl. Sci. Eng., 48, 266. Monte Carlo methods are also described by GOERTZEL, G., and KALOS, M. H., (1958), Progress in Nuclear Energy, Series 1, Physics and Mathematics, Volume 2; editors, Hughes, D. J., Sanders, J. E., and Horowitz, J., Pergamon Press.

BRAGG, R. H., and HAMMOND, M. L., (1965), Carbon, 3, 340.

BRAGG, W. H., and BRAGG, W. L., (1913), Proc. Roy. Soc. (London), 89A, 277.

BOKROS, J. C., (1972), private communication.

CARPENTER, J. M., (1967), Nucl. Instr. Meth., 47, 179.

CARPENTER, J. M., and SUTTON, J. D., (1972), Nucl. Instr. Meth., 99, 453.

CARPENTER, J. M., (1973); see MILDNER, D.F.R., and CARPENTER, J. M., (1973).

CARPENTER, J. M., MILDNER, D.F.R., PELIZZARI, C. A., SUTTON, J. D., and GUNNING, J. E., (1973), Nucl. Instr. Meth., 114, to be published.

CLEMENT, C. F., (1972), J. Phys. D. Appl. Phys., 5, 793.

COOPER, A. R., and AUBOURG, P. R., (1972), "Mathematical Model of One- and Two-Dimensional Amorphous Structures," in "Amorphous Materials," editors, Douglas, R. W., and Ellis, B., Wiley Interscience.

COPLEY, J.R.D., (1973), Comp. Phys. Comm., to be published.

REFERENCES (Continued)

DEBYE, P., ANDERSON, H. R., Jr., and BRUMBERGER, H., (1957), J. Appl. Phys., 28, 679.

DEBYE, P., and BUECHE, A. M., (1949), J. Appl. Phys., 20, 518.

DUWEZ, P. E., (1971), private communication.

ERGUN, S., and ALEXANDER, L. E., (1962), Nature, 195, 765.

ERGUN, S., (1968), Carbon, 6, 141.

ERGUN, S., and SCHEHL, R. R., (1973), Carbon, to be published.

ERGUN, S., (1973), Acta Cryst., A29, 605, and Carbon (1973) to be published.

FITZER, E., SCHÄFER, W., and YAMADA, S., (1969), Carbon, 7, 643.

FRANKLIN, R. E., (1950), Acta Cryst., 3, 107.

FURUKAWA, K., (1964), J. Cryst. Japan, 6, 101.

GRIGOROVICI, R., and BELU, A., (1972), "Structural Modelling in Amorphous Semiconductors," presented at the Eleventh International Conference on the Physics of Semiconductors, Warsawa, Poland.

GOLDBERGER, M. L., and SEITZ, F., (1947), Phys. Rev., 71, 294.

GSCHNEIDNER, K. A., Jr., (1964), Solid State Phys., 16, 3701; obtained from KEESON, P. H., and VAN DER HOEVEN, B.J.C., Jr., (1963), Phys. Rev., 130, 1318.

GUINIER, A., (1939), Ann. Phys., 12, 161.

GUINIER, A., and FOURNET, G., (1947), J. Phys. Radium, 8, 345.

GUINIER, A., and FOURNET, G., (1955), "Small Angle Scattering of X-rays," Wiley.

GUINIER, A., (1963), "X-ray Diffraction in Crystals, Imperfect Crystals and Amorphous Bodies," Freeman & Co.

REFERENCES (Continued)

HUCKE, E. E., (1972), "Glassy Carbon," ARPA report 1824, The University of Michigan.

HUCKE, E. E., (1973), "Glassy Carbon," ARPA report 1824, The University of Michigan.

HUGHES, D. J., and SCHWARTZ, R. L., (1957), U.S.A.E.C. document, BNL-325, 1st edition.

HUGHES, D. J., and SCHWARTZ, R. L., (1958), U.S.A.E.C. document, BNL-325, 2nd edition.

KAMMERECK, R., and NAKAMIZO, M., (1973), "Laser Raman Studies on Carbons," in "Glassy Carbon, Alloys," Walker, P. L., Jr., ARPA report, The Pennsylvania State University.

KAKINOKI, J., KATADA, K., HANAWA, T., and INO, T., (1960), Acta Cryst., 13, 171.

KAKINOKI, J., (1965), Acta Cryst., 18, 578.

KASATOCHKIN, V. I., KORSHAK, V. V., KUDRYAVTSEV, Yu. P., SLADKOV, A. M., and STERENBERG, I. E., (1973), Carbon, 11, 70.

KLEB, R., OSTROWSKI, G. E., PRICE, D. L., and ROWE, J. M., (1973), Nucl. Instr. Meth., 106, 221.

KRATKY, O., and POROD, G., (1949), J. Colloid Sci., 4, 35.

KROGH-MOE, J., (1956), Acta Cryst., 9, 951. See also RAHMAN, A., (1964).

LEADBETTER, A. J., (1973), "Structure and Atomic Motion in Glasses," in "Chemical Applications of Thermal Neutron Scattering," editor, Willis, B.T.M., Oxford University Press. See also LEADBETTER, A. J., WRIGHT, A. C., and APLING, A. J., (1972), "Neutron Scattering in Amorphous Materials," editors Douglas, R. W., and Ellis, B., Wiley Interscience.

LEADBETTER, A. J., and WRIGHT, A. J., (1973), private communication. Lorch's neutron diffraction data were obtained in 1968.

LINDBERG, R. W., (1969), "Radial Distribution Analysis of Glassy Carbon," M.Sc. thesis, Stanford University.

LINGUS, C., and LEYCHAUD, F. E., (1974), private communication.

REFERENCES (Continued)

LIPSON, H., and STOKES, A. R., (1942), Proc. Roy. Soc. (London), 181A, 101.

LOMER, W. M., and LOW, G. G., (1965), "Introductory Theory," in "Thermal Neutron Scattering," editor, Egelstaff, P. A., Academic Press.

LORCH, E. A., (1969), J. Phys. C. Solid State Phys., 2, 229.

LUKESH, J. S., (1950), Phys. Rev., 80, 226. See also 84, 1068 (1951).

LYNCH, R. W., and DRICKAMER, H. C., (1966), J. Chem. Phys., 44, 181.

MAIER, B., (1973), "Neutron Beam Facilities at the ILL High Flux Reactor," Grenoble, France.

MARSHALL, W., and LOVESY, S. W., (1971), "Theory of Thermal Neutron Scattering," Oxford University Press. See also BOYTER, J. K., and BRUGGER, R. M., (1968), "Introductory Computer Programs for Neutron Diffraction," IN-1214, Idaho Nuclear Corporation.

MILDNER, D.F.R., and CARPENTER, J. M., (1972), Bull. Am. Phys. Soc., 17, 596.

MILDNER, D.F.R., and CARPENTER, J. M., (1972), presented at the Fifth International Conference on Amorphous, and Liquid Semiconductors, Garmisch-Partenkirchen Germany; to be published by Taylor & Francis.

MILDNER, D.F.R., CARPENTER, J. M., and PELIZZARI, C. A., (1974), Rev. Sci. Instr., to be published.

NODA, T., and INAGAKI, M., (1964), Bull. Chem. Soc. Japan, 37, 1534.

NODA, T., INAGAKI, M., and YAMADA, S., (1968), Bull. Chem. Soc. Japan, 41, 3023; see also NODA, T., INAGAKI, M., and YAMADA, S., (1969), J. Non-Cryst. Solids, 1, 285.

NICKLOW, R., WAKABAYASHI, N., and SMITH, H. G., (1972), Phys. Rev., B5, 4951.

ORLANDEA, N., (1973), "Node-Analogous Sparcity-Oriented Methods for Simulation of Mechanical Dynamics Systems," Ph.D. thesis, The University of Michigan. The program was adapted for our purposes.

REFERENCES (Continued)

PAULING, L., (1960), "The Nature of the Chemical Bond," 3rd edition, Cornell University Press.

PAULING, L., (1966), Proc. Nat. Acad. Sci., U.S., 56, 1646.

PERRET, R., and RULAND, W., (1972), J. Appl. Cryst., 5, 183.

PICKLES, J. R., and HAZLEWOOD, R., (1961), Harwell report, AERE X/PR/2357.

PLACZEK, G., (1952), Phys. Rev., 86, 377.

POROD, G., (1952), Kolloid. Z., 125, 51 and 109. See also 124, 83 (1951).

POWLES, J. G., (1973), Mol. Phys., to be published.

RAHMAN, A., (1964), J. Chem. Phys., 42, 3540.

ROWE, J. M., (1973), program found in COPLEY, J.R.D., PRICE, D. L., and ROWE, J. M., (1973), Nucl. Instr. Meth., 107, 501.

ROTHWELL, W. S., (1968), J. Appl. Phys., 39, 1840.

SALINGER, G. L., (1973), private communication.

SAXENA, R. R., and BRAGG, R. H., (1973), Carbon, to be published.

SCHERRER, P., (1918), Nachr. Gottingen Gessell, 98.

SCHMIDT, P. W., (1958), Acta Cryst., 11, 674.

SHORT, M. A., and WALKER, P. L., Jr., (1961), Carbon, 1, 3.

SINCLAIR, R. N., JOHNSON, D.A.G., DORE, J. C., CLARKE, J. H., and WRIGHT, A. C., (1973), Nucl. Instr. Meth., to be published.

SINCLAIR, R. N., and WRIGHT, A. C., (1973), Nucl. Instr. Meth., to be published.

STEDMAN, R., (1961), Chalk River Report, CRRP-931.

REFERENCES (Continued)

SUMMERFIELD, G. C., CARPENTER, J. M., and LURIE, N. A., (1968), "Introduction to the Theory of Slow-Neutron Scattering," unpublished report, The University of Michigan.

SUTTON, J. D., (1971), "A Study of the Structure and Motions of Vitreous Silica by Thermal Neutron Scattering Techniques," Ph.D. thesis, The University of Michigan.

TAKAHASHI, Y., and WESTRUM, E. F., Jr., (1965), presented at the first Japanese Calorimetry Conference, Osaka.

TOMIYOSHI, K., WATANABE, N., MISAWA, M., KAI, K., and KIMURA, M., (1973), Japan J. Appl. Phys., 12, 1119.

TURBERFIELD, K. C., (1970), "Time-of-Flight Diffractometry" in "Thermal Neutron Diffraction," editor Willis, B.T.M., Oxford University Press.

VAN HOVE, L., (1954), Phys. Rev., 95, 249.

VINEYARD, G. H., (1954), Phys. Rev., 96, 93.

WARREN, B. E., (1941), Phys. Rev., 59, 693.

WARREN, B. E., (1969), "X-Ray Diffraction," Addison-Wesley.

WARREN, B. E., and BISCOE, J., (1941), Phys. Rev., 59, 688.

WASER, J., and PAULING, L., (1950), J. Chem. Phys., 18, 747.

WASER, J., and SCHOMAKER, V., (1953), Rev. Mod. Phys., 25, 671.

WICK, G. C., (1954), Phys. Rev., 94, 1228.

WIGNALL, G. D., and PINGS, C. J., (1974), Carbon, to be published.

WILLIS, B.T.M., (1973), "Chemical Applications of Thermal Neutron Scattering," Oxford University Press.

WINDSOR, C. G., (1973), "Basic Theory of Thermal Neutron Scattering by Condensed Materials," in "Chemical Applications of Thermal Neutron Scattering," Willis B.T.M., editor, Oxford University Press.

REFERENCES (Concluded)

WRIGHT, A. C., (1969), "The Structure of Five Simple Glasses," D. Phil. thesis, University of Bristol.

WRIGHT, A. C., (1974), Adv. Struct. Res. Diffr. Meth., 5, to be published.

WHITTAKER, A. G., and WOLTEN, G. M., (1972), Science, 178, 54.

YAMADA, S., (1968), "A Review of Glasslike Carbon," DCIC report 68-2, Defense Ceramic Information Center. See also NODA, T., INAGAKI, M., and YAMADA, S., (1969), J. Non-Cryst. Solids, 1, 285.

YOUNG, J. A., and KOPPEL, J. U., (1965), J. Chem. Phys., 42, 357.

ZERNICKE, F., and PRINS, J. A., (1927), Z. Phys., 41, 184.